INL/MIS-23-71867-Revision-1

Depletion Chain Simplification With Pseudo-Nuclides to Model Decay Effects

June 2023

Olin W Calvin

Changing the World's Energy Future

INL is a U.S. Department of Energy National Laboratory operated by Battelle Energy Alliance, LLC

INL/MIS-23-71867-Revision-1

Depletion Chain Simplification With Pseudo-Nuclides to Model Decay Effects

Olin W Calvin

June 2023

Idaho National Laboratory
Idaho Falls, Idaho 83415

http://www.inl.gov

Prepared for the
U.S. Department of Energy
Under DOE Idaho Operations Office
Contract DE-AC07-05ID14517

Depletion Chain Simplification With Pseudo-Nuclides to Model Decay Effects

A Dissertation
Presented in Partial Fulfillment of the Requirements for the
Degree of Doctor of Philosophy
with a
Major in Nuclear Engineering
in the
College of Graduate Studies
University of Idaho
by
Olin William Calvin

Approved by:
Major Professor: R. A. Borrelli, Ph.D.
Committee Members: Mark D. DeHart, Ph.D.; Michael Haney, Ph.D.; Michael McKellar, Ph.D.;
Mauricio E. Tano Retamales, Ph.D.; Vincent M. Laboure, Ph.D.
Department Administrator: I. Charit, PhD

August 2023

Abstract

This work introduces the novel usage of pseudo-nuclides to model decay effects in nuclear fission reactor systems which are otherwise absent from simplified depletion libraries. Pseudo-nuclides are artificial nuclides which, when added to a simplified depletion library, can preserve quantities of interest, such as decay energy release or decay photon activity, which are otherwise significantly under-predicted by simplified libraries. Several dozen pseudo-nuclides are capable of accurately modeling decay effects of hundreds of short-lived radionuclides. The computational resources needed to model the decay effects in depletion systems with simplified depletion libraries with pseudo-nuclides are significantly less than those needed when using simplified depletion libraries without pseudo-nuclides. When compared to the similar method of decay heat precursors for a given system, pseudo-nuclides allow for smaller depletion libraries to be generated because of their ability to more accurately model the fission product irradiation effect on decay heat.

Acknowledgements

I would like to thank Dr. Yaqi Wang from Idaho National Laboratory for their support in implementing the functionality presented in this work into Griffin. This work was funded, in part, through the Idaho National Laboratory Directed Research & Development Program and, in part, through the Nuclear Energy Advanced Modeling and Simulation program managed by the Department of Energy Office of Nuclear Energy, both of which are under DOE Idaho Operations Office Contract DE-AC07-05ID14517. Accordingly, the U.S. Government retains a nonexclusive, royalty-free license to publish or reproduce the published form of this contribution, or allow others to do so, for U.S. Government purposes. This research made use of the resources of the High Performance Computing Center at Idaho National Laboratory, which is supported by the Office of Nuclear Energy of the U.S. Department of Energy and the Nuclear Science User Facilities under Contract No. DE-AC07-05ID14517.

Table of Contents

List of Tables

List of Figures

Statement of Contribution

This work includes journal articles which were multi-author works. The contributions of these multi-author articles are delineated with CRediT author statements below.

Chapter 2: Introduction of the Adding and Doubling Method for Solving Nuclear Fuel Depletion

Olin W. Calvin: Methodology, Software, Formal Analysis, Investigation, Data Curation, Writing - Original Draft, Writing - Review & Editing, and Visualization.
Barry D. Ganapol: Conceptualization, Software, Formal Analysis, and Writing - Review & Editing.
R. A. Borrelli: Methodology, Writing - Review & Editing, and Supervision.

Chapter 3: Evaluation Quantities of Interest Other than Nuclide Densities in the Bateman Equations

Olin W. Calvin: Conceptualization, Methodology, Software, Validation, Formal Analysis, Investigation, Data Curation, Writing - Original Draft, Writing - Review & Editing, and Visualization.
Micah D. Gale: Conceptualization, Methodology, Formal Analysis, Writing - Original Draft, Writing - Review & Editing, Supervision, Project Administration, and Funding Acquisition.
Sebastian Schunert: Conceptualization, Methodology, Writing - Original Draft, and Writing - Review & Editing.

Chapter 4: Depletion Chain Simplification Using Pseudo-Nuclides

Olin W. Calvin: Sole Author

Chapter 5: Pseudo-Nuclides for Modeling Decay Photons

Olin W. Calvin: Sole Author

Chapter 1: Introduction

1.1. Nuclear Power Plants

Nuclear reactors are systems which are designed to sustain either nuclear fission or nuclear fusion reactions. When developed in the context of a nuclear power plant (NPP), the goal of a nuclear reactor is to release energy via exothermic nuclear fission or nuclear fusion reactions. This energy is released as heat which can then be used in a power cycle, similar to the operation of coal and natural gas power plants. Currently, all commercial NPPs rely on nuclear fission in order to produce electricity as existing nuclear fusion systems have not been demonstrated to be commercially viable. Consequently, for the remainder of this work references to nuclear reactors refer specifically to nuclear reactors which operate using nuclear fission.

1.1.1. History

The history of NPPs begins with the Experimental Breeder Reactor-I (EBR-I), a liquid metal fast reactor (LMFR), when, on December 20, 1951, EBR-I provided enough electricity to light four lightbulbs. After this accomplishment, the output of EBR-I was increased to 100 kWe (kilowatts of electricity), providing electricity to the building which housed the reactor until EBR-I was decommissioned in 1964 [6]. While numerous nuclear reactors were constructed and achieved criticality prior to EBR-I, the first being Chicago Pile-1 in 1942 [7], these reactors were built either for research purposes or for producing fissile material for nuclear weapons. EBR-I represented a shift away from nuclear reactors for the purposes of nuclear weapons and towards a peaceful application of electricity generation from NPPs. Other notable firsts in nuclear power generation include:

- USS Nautilis: Constructed in the US and commissioned in 1954, it was the first nuclear-powered submarine [8].
- Obninsk Nuclear Power Plant: Constructed in the USSR and commissioned in 1954, it was the first NPP connected to an electrical grid and produced a net 5 MWe [9].
- Calder Hall Nuclear Power Station: Constructed in the UK and commissioned in 1956, it was the first full-scale commercial NPP, designed to produce weapons-grade plutonium and 60 MWe [9].
- Shippingport Atomic Power Station: Constructed in the US and commissioned in 1958, it was the first full-scale NPP "devoted exclusively to peacetime uses" and its initial core produced 60 MWe [10].

After the achievement of these initial milestones, NPPs expanded dramatically, increasing global installed capacity from less than 1 GWe in 1960 to almost 400 GWe today as shown in Figure 1.1.

1.1.2. Present-Day

According to the International Atomic Energy Agency (IAEA), as of 2022 there are 422 nuclear power reactors in operation for a total net nameplate capacity of 378 GWe and, over the past three years, the average global energy availability factor of operating nuclear power reactors has been roughly 80% [4]. Consequently, it can be determined that, on average, nuclear power reactors annually provide roughly 2,649 TWh of electricity. With global electricity generation estimated to be 28,466 TWh of electricity in 2021 [11], the electricity generation of nuclear power reactors corresponds to 9.3% of total electricity generation, the second-largest source of low-carbon electricity after hydropower. This means that NPPs play a vital role in reducing CO_2 emissions in order to combat

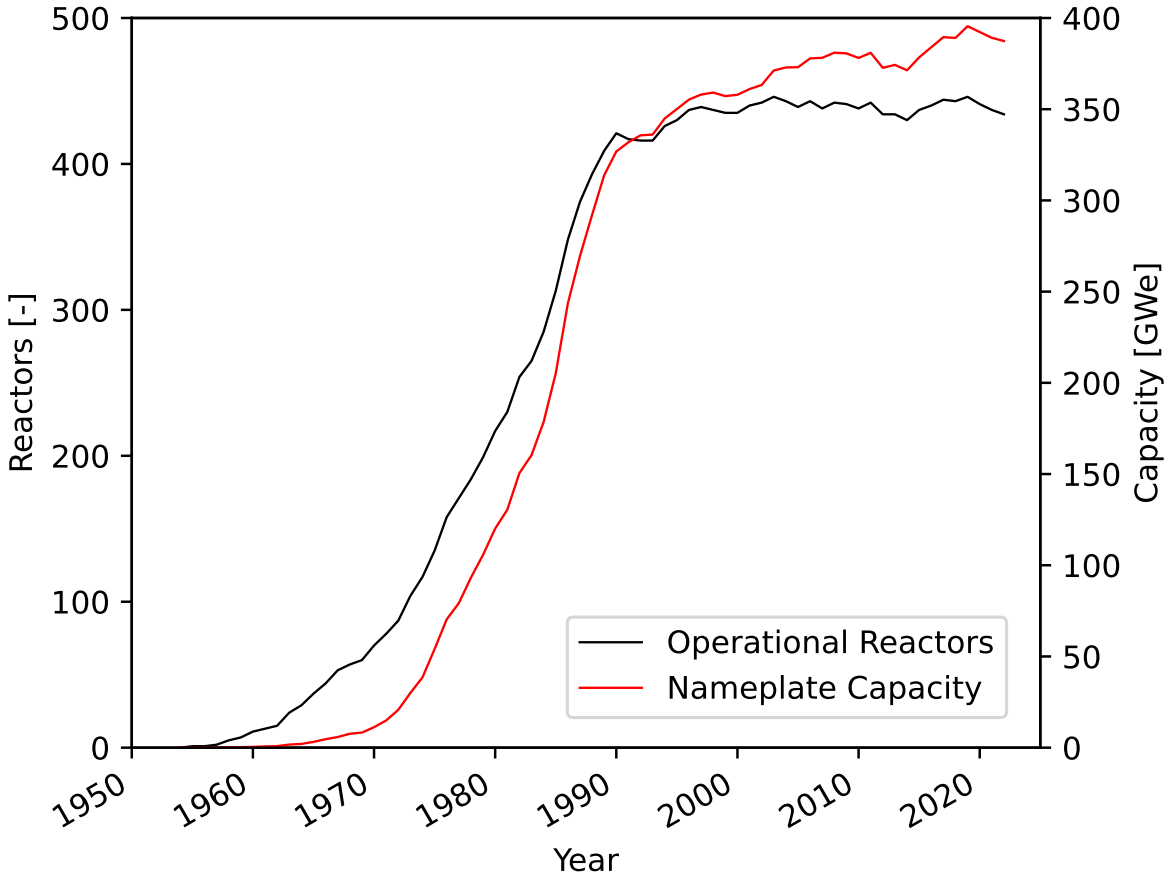

Figure 1.1: Number of operational nuclear reactors and electrical capacity. Data from the IAEA [4].

climate change. In order to maintain and expand the deployment of NPPs as a source of low-carbon electricity, accurate modeling and simulation of the depletion of nuclear fuel in various nuclear reactor designs, many of which are entirely novel with limited applicable operational experience, is critical to ensuring an economical fuel cycle for the NPP, minimizing the potential proliferation of weapons-grade nuclear material to bad actors, and assessing the radiological hazard posed by the NPP during normal operation and during accident scenarios.

1.2. Reactor Analysis

Early in the nuclear industry the primary means of testing new reactor designs was to simply build a prototype reactor, perform experiments on the prototype to gather the necessary data, and then use the experimental data to inform the design and construction of commercial reactors. However, as time progressed the costs, in terms of both time and money, of building prototype reactors increased, dissuading the construction of entire nuclear reactor systems for the purposes of conducting only a small number of experiments.

Many examples of these prototype reactors with short operational periods were constructed at what is today Idaho National Laboratory (INL), formerly the National Reactor Testing Station, where dozens of nuclear reactors were constructed. Many of these reactors were used in destructive tests which contributed to their short-lived operational lifetimes, as was the case for Boiling Water Reactor Reactor Experiment (BORAX) No. 1 [12]. While the data obtained from reactor experiments, including the BORAX series, has been invaluable to the nuclear industry, the increasing costs and regulatory restrictions have limited the ability of the nuclear industry to perform experimental analysis in the same way it had previously.

Fortunately, as the costs of physical reactor experiments have increased, the costs of high-fidelity computational modeling and simulation of reactors have decreased. This decrease in computational costs has largely been driven by the increase in computational power in accordance with Moore's law [13]. In addition to the increase in computational power, improvements have been made regarding the computational modeling of neutron transport [14, 15] and measurements of nuclear data [5, 16–18] which have improved the accuracy of high-fidelity reactor models. One such tool capable of computational reactor analysis is Griffin, which is jointly developed by INL and Argonne National Laboratory (ANL) [2]. All functionality mentioned in this work was implemented and tested in Griffin.

1.2.1. Cross Sections

In nuclear engineering, the term cross section (XS) refers to the probability of a given particle interacting with a given nucleus. While XSs exist for all types of particles (photons, protons, etc.), neutron XSs are the primary focus of reactor analysis as it is the probability of a neutron being absorbed, and potentially causing fission, which determines whether or not a given reactor system can achieve criticality.

XSs are expressed in units of area, which for neutron cross sections is typically in units of barns (b) [19] where:

$$1\text{ b} = 10^{-24}\text{ cm}^2 = 10^{-30}\text{ m}^2 \tag{1.1}$$

XSs of this type are typically referred to as microscopic XSs (σ) as they correspond to the effective cross sectional area of a given nucleus, which is quite small in absolute terms. As an example of how XSs determine the rate at which neutron-nuclei reactions occur, consider some fictional nuclide X which has a microscopic fission XS ($\sigma_{\text{f,X}}$) of 10 b for all neutrons and a nuclide number density (NND) of 0.0335 $\frac{\text{atoms}}{\text{b}\cdot\text{cm}}$, which is roughly

the molecular number density of liquid water at 0°C and atmospheric pressure. The macroscopic fission XS (Σ_{f}) of a homogeneous system containing X can then be calculated:

$$\Sigma_{\mathrm{f}} = \sigma_{\mathrm{f,X}} N_{\mathrm{X}} = 10\ \mathrm{b} \cdot 0.0335 \frac{\mathrm{atoms}}{\mathrm{b} \cdot \mathrm{cm}} = 0.335\ \mathrm{cm}^{-1} \tag{1.2}$$

The macroscopic XS has units of inverse length (typically cm^{-1}) and describes the probability of a given neutron interaction occurring in a given material. If it is assumed that there is an infinite system composed of material X, and there is a constant neutron flux (ϕ) of $10^4\ \frac{\mathrm{neutrons}}{\mathrm{cm}^2 \cdot \mathrm{s}}$ throughout the system, then the fission rate density in the material can be calculated:

$$\Sigma_{\mathrm{f}} \phi = 0.335\ \mathrm{cm}^{-1} \cdot 10^4 \frac{\mathrm{neutrons}}{\mathrm{cm}^2 \cdot \mathrm{s}} = 3350 \frac{\mathrm{fissions}}{\mathrm{cm}^3 \cdot \mathrm{s}} \tag{1.3}$$

In real-world systems, it is more difficult to calculate the total fission rate in a reactor, as will be shown. However, the principles are essentially the same. Calculating the fission rate of a reactor system is necessary as fission is a highly exothermic process and is responsible for producing most of the heat which is required to run the power cycle of the NPP that the reactor is a part of. If the fission rate increases beyond the specifications of a reactor system then the reactor will produce heat faster than it can be removed resulting in an increase in material temperature in the core and, eventually, core melting. Alternatively, if the fission rate decreases below specifications, then the reactor is producing less heat, and subsequently less electricity, than it is capable of safely producing. This results in economic inefficiencies which can potentially render an NPP noncompetitive with other energy sources.

As mentioned previously, XSs are units of probability, however, the units describing XSs are units of length which, when applied to a given neutron flux, give an exact reaction rate instead of a statistical distribution. The reason for this is because of the magnitude of the quantities involved in nuclear engineering. The typical number density of solid materials in a reactor is usually on the order of $10^{22}\ \frac{\mathrm{atoms}}{\mathrm{cm}^3}$ or more and the neutron flux is on the order of $10^{12}\ \frac{\mathrm{neutrons}}{\mathrm{cm}^2 \cdot \mathrm{s}}$. These large quantities (in absolute terms) result in very good statistical convergence in accordance with the law of large numbers [20] which allows XSs to be expressed in units of area and length. Additionally, any statistical uncertainties which may be present in transmutation reaction rates are likely to be overshadowed by the experimental uncertainty in neutron XS measurements [21]. However, probabilities can still be applicable when dealing with very small quantities as it is not possible to have fractional reactions or fractions of atoms. If in Eq. 1.3 the neutron flux was reduced to only $1\ \frac{\mathrm{neutron}}{\mathrm{cm}^2 \cdot \mathrm{s}}$, then the fission rate density would reduce to $0.335\ \frac{\mathrm{fissions}}{\mathrm{cm}^3 \cdot \mathrm{s}}$ which could more accurately be interpreted as a 33.5% probability of a fission event occurring in a given cubic centimeter of material in a given second.

1.2.2. Neutron Transport

At the core of nuclear engineering is the neutron transport equation (NTE) which can be used to calculate the change in the neutron population of a given reactor system. Nuclear engineers operating nuclear reactors must have a good understanding of the changing neutron population of the reactor such that the number of neutrons can increase during reactor startup to the level necessary to produce the rated thermal power output of the reactor via nuclear fission and other exothermic neutron-nuclei interactions. Once this neutron population is achieved, it is crucial that the neutron population be maintained such that the number of neutrons does not increase, which would result in the reactor producing more power than it is rated for and potentially causing an accident scenario. The neutron population also should not decrease, which would result in the reactor producing less power than it is rated for which damages both the economics of the NPP and the population which relies on the power produced

by the NPP. The "classical" NTE is shown in Eq. 1.4 adapted from Ref. [22]. Note that even Eq. 1.4 still makes some simplifications regarding neutron behavior in the system, such as no decay of free neutrons (free neutrons have a half-life of 613.9 s [5]), no neutrons produced from photon-nuclei interactions such as photofission, no neutron-neutron collisions, and no temperature-dependence of microscopic XSs from Doppler broadening [23].

$$\begin{aligned}\frac{1}{v(E)}\frac{\partial\psi(\vec{r},E,\vec{\Omega},t)}{\partial t} &= -\vec{\Omega}\cdot\vec{\nabla}\psi(\vec{r},E,\vec{\Omega},t) - \sum_i N_i(\vec{r},t)\sigma_{\mathrm{t},i}(E)\psi(\vec{r},E,\vec{\Omega},t) \\ &+ \sum_i N_i(\vec{r},t)\int_0^\infty dE'\int_{4\pi} d\vec{\Omega}'\sigma_{\mathrm{s},i}(E'\to E,\vec{\Omega}'\to\vec{\Omega})\psi(\vec{r},E',\vec{\Omega}',t) \\ &+ \frac{1}{4\pi}\sum_i N_i(\vec{r},t)\int_0^\infty dE'\nu_{\mathrm{p},i}(E')\sigma_{\mathrm{f},i}(E')\chi_{\mathrm{p},i}(E'\to E)\phi(\vec{r},E',t) \\ &+ \frac{1}{4\pi}\sum_i \nu_{\mathrm{d},i}\lambda_{\mathrm{d},i}N_i(\vec{r},t)\chi_{\mathrm{d},i}(E) \\ &+ S_{\mathrm{ext}}(\vec{r},E,\vec{\Omega},t)\end{aligned} \tag{1.4}$$

where

$\vec{r}$	spatial position vector
E	kinetic energy of the neutron
t	time
$\vec{\Omega}$	neutron direction
v	neutron velocity
ψ	angular neutron flux
ϕ	scalar neutron flux
N_i	position-dependent and time-dependent NND of nuclide i
$\sigma_{\mathrm{t},i}$	microscopic total XS of nuclide i
$\sigma_{\mathrm{s},i}$	microscopic scattering XS of nuclide i
$\nu_{\mathrm{p},i}$	average number of prompt neutrons produced from the neutron-induced fission of nuclide i
$\sigma_{\mathrm{f},i}$	microscopic fission XS of nuclide i
$\chi_{\mathrm{p},i}$	prompt neutron energy spectrum from the neutron-induced fission of nuclide i
$\nu_{\mathrm{d},i}$	average number of neutrons emitted per delayed neutron emission of nuclide i
$\lambda_{\mathrm{d},i}$	decay constant of delayed neutron emission of nuclide i
$\chi_{\mathrm{d},i}$	delayed neutron energy spectrum from the delayed neutron emission of nuclide i
S_{ext}	external neutron source term.

Several assumptions and simplifications can be made to Eq. 1.4 in order to formulate the infinite medium neutron multiplication factor.

$$k = \frac{\nu\Sigma_{\mathrm{f}}}{\Sigma_{\mathrm{a}}} \tag{1.5}$$

where

k	neutron multiplication factor
ν	average number of neutrons released per fission in the material
Σ_{f}	macroscopic fission XS of the material
Σ_{a}	macroscopic absorption (non-scattering) XS of the material.

The process of deriving the infinite medium multiplication factor from the NTE is shown in Eqs. A.1–A.9. The infinite medium multiplication factor is the factor by which the neutron population of the infinite medium considered changes with each subsequent neutron generation. If $k = 1$ then the population of neutrons in the system with not change from one neutron generation to another, $k = 0.5$ will result in the neutron population halving from one generation to the next, and $k = 2$ will result in the neutron population doubling from one generation to the next. During operation, the amount of power produced by a nuclear reactor is directly proportional to the neutron population in the reactor as the neutron population determines the rate at which nuclear fission occurs as shown in Eq. 1.3. As a result, accurately calculating the neutron multiplication factor is crucial during reactor operation. Since the NNDs of the system, which impact the macroscopic XS as shown in Eq. 1.2, will change as a result of depletion in the system, accurate modeling of the neutron multiplication factor requires accurate modeling of depletion.

1.3. Depletion

In nuclear engineering, depletion is the process by which the concentration of nuclides, often expressed in terms of NNDs, in a system changes as the result of radioactive decay and neutron transmutation. The term depletion, which implies a decrease in some quantity, is used because in nuclear reactor fuel neutron transmutation results in some of the fissionable nuclides in the system undergoing nuclear fission, destroying the parent nuclide and replacing it with two (or more) daughter nuclides known as fission products (FPs). Even if there is no neutron transmutation occurring in the system, the overall concentration of fissionable nuclides in a system will decrease as the fissionable nuclides (nuclides with Z $\geq$ 88) either undergo radioactive decay to non-fissionable nuclides. All fissionable nuclides are radioactive as shown in Figure 1.2.

Theoretically, non-fissionable nuclides can undergo neutron transmutation in order to become fissionable nuclides, which would increase the concentration of fissionable nuclides in the system. In practice, the number of neutron transmutation events required to transmute naturally-occurring non-fissionable nuclides, such as ^{209}Bi, to a fissionable nuclide, such as ^{223}Ra, is prohibitive, with a minimum 14 neutron absorption events necessary. Additionally, Figure 1.2 shows that most isotopes of polonium have relatively short half-lives and many of these isotopes decay via alpha emission, which reduces the A-number of the nuclide by 4. Thus it can be assumed that the concentration of fissionable nuclides in any real-world nuclear reactor system will decrease over time as depletion occurs, barring external processes such as refueling.

Aside from the fissionable nuclide concentration decreasing over time as depletion occurs, for many reactor systems the excess reactivity of the system also continuously decreases over time as the concentration of fissile nuclides (fissionable nuclides capable of sustaining a fission chain reaction) decreases over time as fissile nuclides are more likely to undergo fission relative to other fissionable nuclides. However, this is not always the case as some reactor designs, such as the sodium fast reactor (SFR) and molten salt reactor (MSR), can achieve conversion

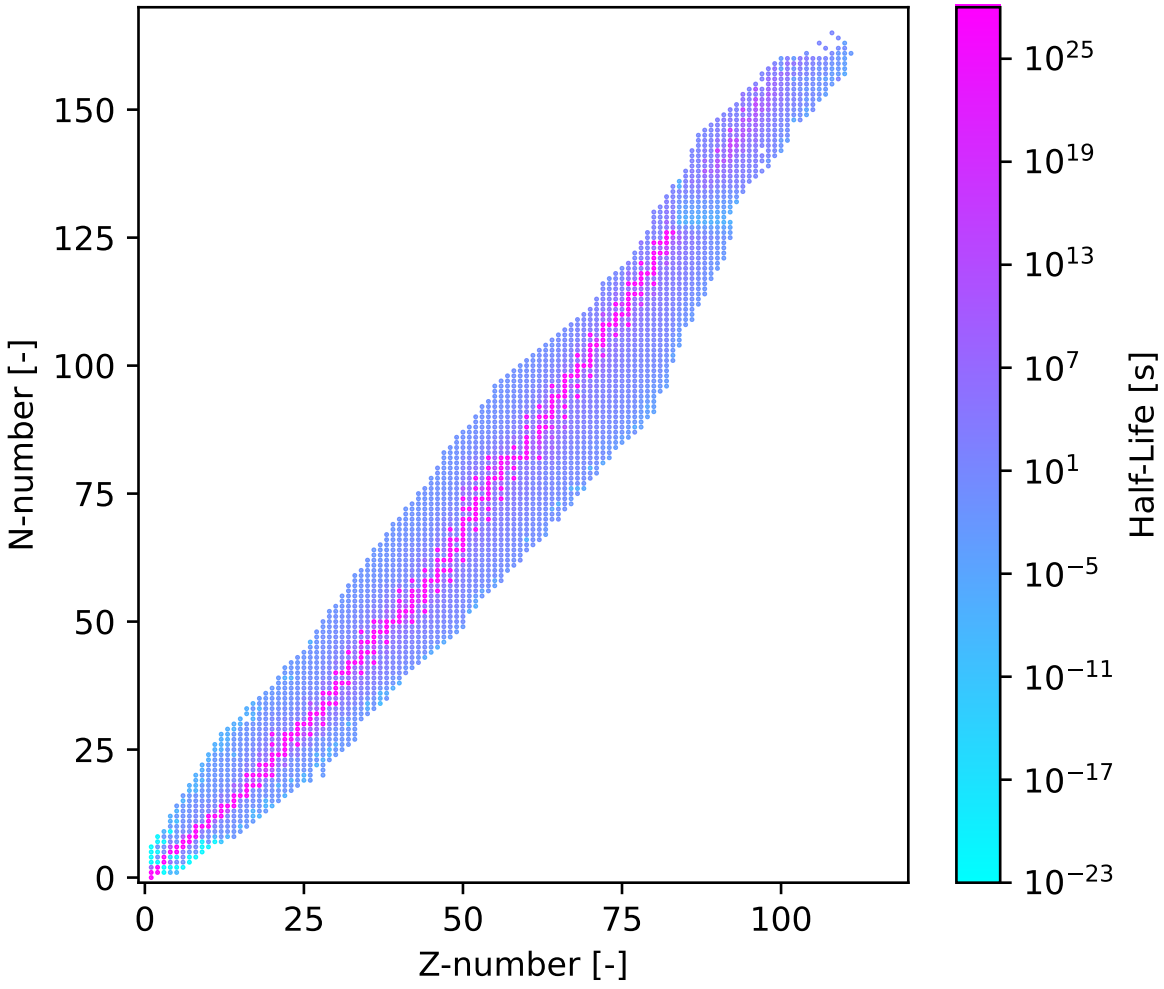

Figure 1.2: Half-lives of ground-state nuclides with respect to Z-number and N-number. Stable nuclides are assumed to have a half-life of 10^{28} s for plotting purposes. Data from the Evaluated Nuclear Data File (ENDF) library, specifically ENDF-B/VIII.0 [5].

ratios greater than 1.0, meaning they produce more fissile material than they consume during operation. Note that this conversion comes from the neutron transmutation of fertile nuclides, such as ^{238}U, into fissile nuclides, such as ^{239}Pu. While the conversion of fertile material into fissile material can increase the reactivity of a system, the overall concentration of fissionable nuclides does not change as a result of this conversion and reactors such as the SFR and MSR will still experience a decrease in the total concentration of fissionable nuclides as they deplete.

Depletion impacts the NNDs of all nuclides in the system, not just the fissionable NNDs. As shown in Eqs. 1.4 and 1.5, the NNDs of all nuclides in the system impact the neutron multiplication factor of the system, which must be accurately modeled. Additionally, the NNDs of the fuel determine other quantities of interest, such as decay heat and radiological hazard. While fission does not occur outside of the reactor fuel, other materials in the reactor, such as the fuel cladding and coolant, will also undergo depletion as they experience neutron transmutation and radioactive decay. For fuel cladding in particular, this depletion can be significant as transmutation products can significantly contribute to the radiation damage the cladding experiences [1, 24], degrading its performance and shortening its operational lifetime under reactor conditions.

1.3.1. The Bateman Equations

Mathematician Harry Bateman formulated the mathematical model to describe the change in the NNDs in a system as radioactive decay occurs over time [25]. Despite the absence of neutron transmutation terms in the original Bateman equation, it is relatively trivial to add these terms resulting in the Bateman equation used to describe nuclear fuel depletion. This is shown in Eq. 1.6 adapted from Ref. [26] with spatial and neutron energy dependencies added.

$$\begin{aligned}\frac{dN_i(\vec{r},t)}{dt} &= \sum_{j\neq i} b_{j\to i}\lambda_j N_j(\vec{r},t) + \int_0^\infty \sum_{j\neq i} \sigma_{j\to i}(E)\phi(\vec{r},E,t)N_j(\vec{r},t)dE \\ &+ \int_0^\infty \sum_{j\neq i} \sigma_{\mathrm{f},j}(E)\gamma_{\mathrm{f},j\to i}(E)\phi(\vec{r},E,t)N_j(\vec{r},t)dE + \sum_{j\neq i}\lambda_{\mathrm{sf},j}N_j(\vec{r},t)\gamma_{\mathrm{sf},j\to i} \\ &- \lambda_i N_i(\vec{r},t) - \int_0^\infty \sigma_{\mathrm{a},i}(E)\phi(\vec{r},E,t)N_i(\vec{r},t)dE\end{aligned} \tag{1.6}$$

where

t	time
E	incident neutron energy
$\vec{r}$	position with the system
λ_j	decay constant of nuclide j
$b_{j\to i}$	probability of nuclide j to produce nuclide i by a decay mode other than spontaneous fission (SF)
N_i	NND of nuclide i
$\sigma_{j\to i}$	microscopic XS for nuclide j which produces nuclide i excluding production of nuclide i from neutron-induced fission of nuclide j
ϕ	scalar neutron flux
$\sigma_{\mathrm{f},j}$	microscopic fission XS of nuclide j
$\gamma_{\mathrm{f},j\to i}$	FPYF of nuclide i from the neutron-induced fission of nuclide j
$\gamma_{\mathrm{sf},j\to i}$	FPYF of nuclide i from the SF of nuclide j
$\lambda_{\mathrm{sf},j}$	SF decay constant of nuclide j
$\sigma_{\mathrm{a},i}$	microscopic non-scattering (absorption) XS of nuclide i

Griffin relies on the multigroup approximation for both neutron transport and depletion calculations. Additionally, Griffin relies on discrete spatial depletion zones, rather than modeling a continuous spatial NND distribution. Applying these two approximations allows Eq. 1.6 to be simplified as shown in Eq. 1.7 for a single discrete depletion zone where g represents the index of a given neutron energy group.

$$\begin{aligned}\frac{dN_i(t)}{dt} = &\sum_{j\neq i} b_{j\to i}\lambda_j N_j(t) + \sum_{g=1}^{G}\sum_{j\neq i}\sigma_{g,j\to i}\phi_g(t)N_j(t) + \sum_{g=1}^{G}\sum_{j\neq i}\sigma_{\mathrm{f},g,j}\gamma_{\mathrm{f},g,j\to i}\phi_g(t)N_j(t)\\ &+\sum_{j\neq i}\lambda_{\mathrm{sf},j}N_j(t)\gamma_{\mathrm{sf},j\to i} - \lambda_i N_i(t) - \sum_{g=1}^{G}\sigma_{\mathrm{a},g,i}\phi_g(t)N_i(t)\end{aligned} \tag{1.7}$$

As Eq. 1.7 applies to a single nuclide i, the total number of Bateman equations that must be solved for a single spatial depletion zone is equal to the number of nuclides in the system. If attempting to track all known nuclides which can be produced in nuclear reactor fuel, the number of nuclides per depletion zone containing reactor fuel can be upwards of 1,700. The reason for the large number of nuclides which must be tracked in reactor fuel is driven by the spectrum of FPs which fissionable nuclides can produce. The various FPYFs for ^{235}U are shown in Figure 1.3. Note that the FPs produced immediately after nuclear fission occurs typically have too many neutrons to be stable, as shown in Figure 1.2. Additionally, FPs can also undergo neutron transmutation. As a result, it becomes necessary to track not only the FPs themselves, but also the decay and transmutation products which can be produced from the FPs.

Another challenge in solving Eq. 1.7 is because of the potential for a given nuclide X to be produced by nuclides Y and Z, while nuclide X is also capable of producing nuclides Y and Z. This results in a series of coupled differential equations. If solving for a system undergoing pure radioactive decay, the Bateman equations are much simpler to solve as radionuclides decay into their decay products and there are no pathways for a decay product to produce its decay parent. However, when neutron transmutation is considered, this poses challenges. Consider the reactions shown in Eq. 1.8 which illustrate a potential transmutation "loop."

$$\begin{aligned}{}^{2}\mathrm{H} + {}^{1}\mathrm{n} &\to {}^{3}\mathrm{H} + {}^{0}\gamma\\ {}^{3}\mathrm{H} + {}^{1}\mathrm{n} &\to {}^{2}\mathrm{H} + 2\,{}^{1}\mathrm{n}\end{aligned} \tag{1.8}$$

Deuterium is capable of undergoing an (n,γ) reaction to produce tritium; tritium is then capable of undergoing an (n,2n) reaction which results in the production of deuterium. This introduces a cyclic dependency in the NNDs of deuterium and tritium making it more complicated to solve for the NNDs of systems which experience neutron transmutation when compared to systems which only experience radioactive decay.

1.3.2. The Depletion Matrix

In order to solve Eq. 1.7 for a system with several or more nuclides, it is convenient to group the decay and transmutation terms into a matrix (referred to as the "depletion matrix") and express Eq. 1.7 in matrix-vector notation. Every nuclide has a corresponding Bateman equation in order to calculate its changing NND which can be inserted as a row into a matrix alongside all other Bateman equations for all other nuclides.

$$\frac{d\vec{N}}{dt} = \mathbf{A}\vec{N} \tag{1.9}$$

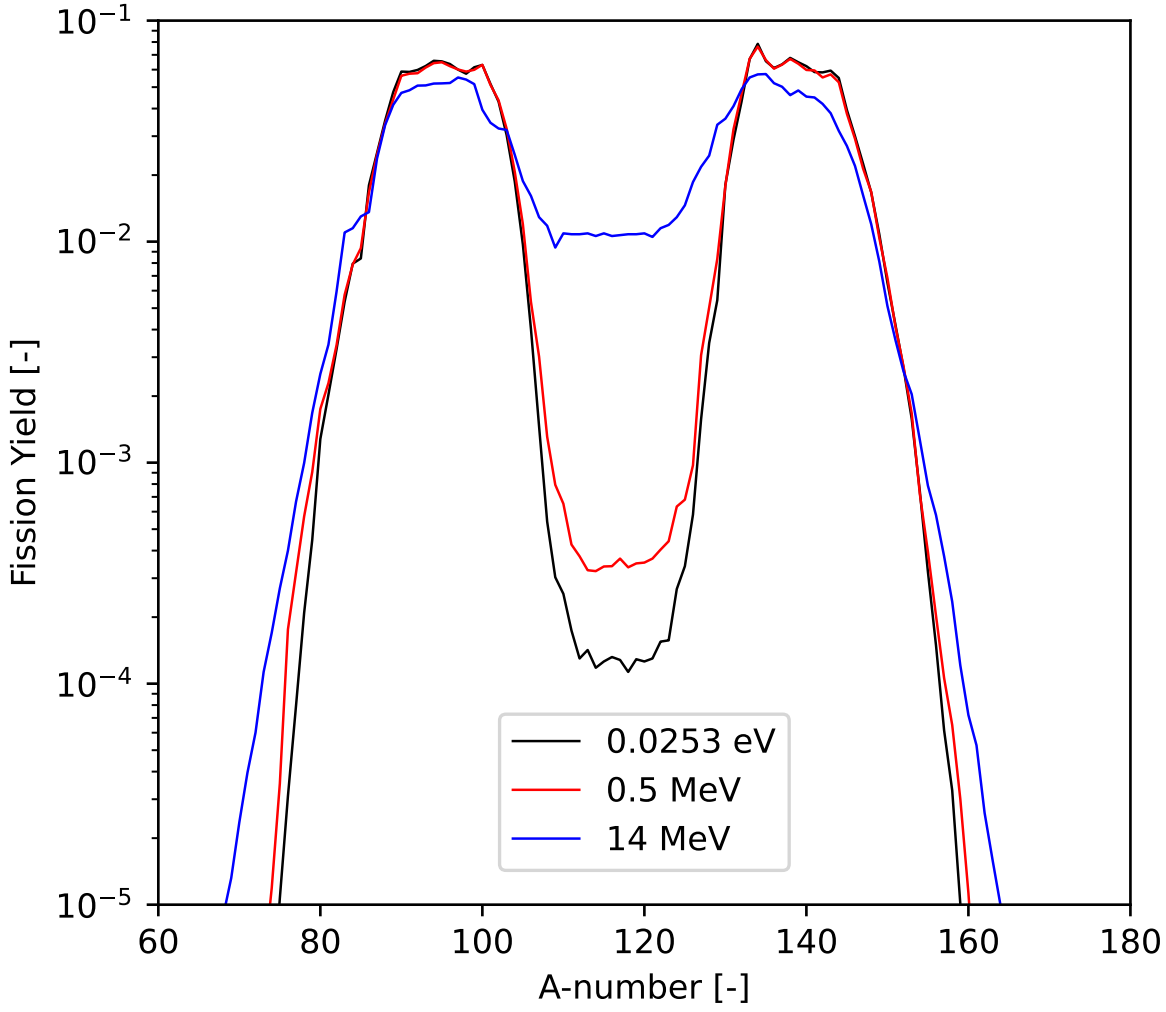

Figure 1.3: Neutron energy-dependent FPYFs of ^{235}U for FPs with specific A-numbers. Note that multiple FP nuclides can be produced with the same A-number, such as ^{135}Te, ^{135}I, and ^{135}Xe. Data from the ENDF-B/VIII.0 [5].

where

$\frac{d\vec{N}}{dt}$	vector of the change in the NNDs of all nuclides in the system
$\mathbf{A}$	depletion matrix containing all decay and transmutation terms for all nuclides
$\vec{N}$	vector of all NNDs in the system.

Eq. 1.9 can be rewritten in the form of the exponential of a matrix.

$$\vec{N}(t) = \vec{N}_0 e^{\mathbf{A}t} \tag{1.10}$$

where

$\vec{N}_0$	vector of the initial NNDs in the system
t	length of the depletion interval.

Recall that the definition of the matrix exponential is a power series [27].

$$e^{\mathbf{A}} = \sum_{k=0}^{\infty} \frac{\mathbf{A}^k}{k!} = \mathbf{I} + \mathbf{A} + \frac{\mathbf{A}^2}{2!} + \frac{\mathbf{A}^3}{3!} \cdots \tag{1.11}$$

Because of the potential stiffness of the depletion matrix, which is driven in large part by the large decay constants of very short-lived nuclides, many traditional methods [27] of solving the power series directly are inadequate because of the time and/or computational precision required to converge to an acceptable answer [28]. As a result several methods have been developed specifically for solving the exponential of the depletion matrix, such as the Chebyshev rational approximation method (CRAM) [28] and the Adding and Doubling Method (ADM) [29].

1.3.3. The Computational Costs of Depletion

While Griffin supports several different methods of solving Eq. 1.10, CRAM is used for the entirety of this work because of its well-documented performance in terms of accuracy and runtime [30–32], although the ADM is investigated as a competitor to CRAM. When using CRAM, the runtime needed scales linearly with the number of non-zeroes in the depletion matrix. In general, this can be inferred to mean that the runtime of CRAM scales linearly with the number of nuclides as nuclides typically introduce a similar number of non-zeroes to the depletion matrix. The exceptions to this are nuclides which can be produced as secondary particles from decay and transmutation events, such as ^{1}H produced from (n,p) reactions and ^{4}He produced from decay via α emission, and fissionable nuclides which can produce hundreds of different FPs. However, since the vast majority of nuclides are not fissionable or produced as secondary particles, it can generally be assumed that the runtime of CRAM scales linearly with the number of nuclides in the system.

Previous testing of the CRAM implementation in Griffin yields a runtime of 19 ms at Approximation Order 16 for a system with about 1,600 nuclides for the processor tested, with Approximation Order 16 generally accepted as accurate enough for most depletion analyses [29, 30]. The total runtime of the CRAM depletion calculation

will scale relatively linearly with the number of depletion zones per processor core available and the number of depletion intervals to solve for.

$$0.019 \frac{\text{s}}{\text{CRAM solve}} \times \frac{X \text{ depletion zones}}{Y \text{ processor cores}} \times Z \text{ depletion intervals} \tag{1.12}$$

As an example, a system with 2 million depletion zones, 1,600 nuclides, and 50 depletion intervals performed on 1,000 processor cores would take about half an hour purely for the depletion calculation. If the number of depletion zones increased by a factor of ten, the runtime would also increase by a factor of ten to about five hours.

Regarding random-access memory (RAM) usage, all depletion-capable applications must store the NNDs of all nuclides for all unique depletion zones in the system. Assuming double-precision, the RAM usage can be calculated as shown in Eq. 1.13.

$$8 \frac{\text{bytes}}{\text{nuclide}} \times X \text{ nuclides} \times Y \text{ depletion zones} \tag{1.13}$$

Consequently, for a system with 1,600 nuclides per depletion zone and 2 million depletion zones, which has been used previously in published research [33], the total RAM usage is 25.6 GB. If the number of depletion zones increased by a factor of ten, the RAM usage would similarly increase by a factor of ten to 250 GB. The disk storage needed for the results of the depletion calculation is equal to the RAM usage multiplied by the number of depletion intervals. If the NNDs are solved for 50 depletion intervals for the same system then the total disk storage is 1.3 TB for the 2 million depletion zone case and 13 TB for the 20 million depletion zone case.

As shown by Eqs. 1.12 and 1.13, the computational costs associated with high-fidelity depletion calculations can be quite large. While modern supercomputers, such as Frontier, may have hundreds of thousands of processor cores and petabytes of RAM available [34], it is still desirable to reduce the computational costs of high-fidelity reactor models as not every researcher may have access to a powerful supercomputer and researchers with access to powerful supercomputers will desire reduced runtimes and RAM usage so that multiple permutations of a model can be run simultaneously and the turnaroud time of individual models will be reduced. Additionally, the growing interest in applying machine learning and neural networks to reactor modeling and simulation will result in a need for comprehensive reactor models which are computationally inexpensive in order to train neural networks which may require thousands or millions of training generations [35]. Another concern is that, for multiphysics simulations, the depletion calculation is only one component of a multifaceted simulation. In order for multiphysics simulations to be viable, all portions of the simulation, such as fluid mechanics, material performance, depletion, and neutron transport, must be optimized when it comes to computational resource usage, otherwise the simulation may become bottlenecked by a particular slow portion of the model or the computational resources used by one portion of the model may limit the resources available for other portions of the model.

In order to reduce the computational costs of depletion calculations, I propose reducing the number of nuclides tracked during the depletion calculation while preserving quantities of interest to the analyst modeling the system with the use of pseudo-nuclides (PNs). Since short-lived nuclides which are often excluded from depletion calculations can have a significant impact on the decay effects of the system, simply removing these nuclides is not appropriate when analyzing systems where these decay effects must be accurately modeled. Pseudo-nuclides may be capable of preserving these decay effects while reducing the overall number of nuclides tracked in the system.

1.4. Objectives

The objectives of this work are to:

1. Investigate an alternative method to CRAM for solving the Bateman equations which does not have the same shortcomings as CRAM [36].
2. Determine the significance of calculating non-nuclide, but otherwise NND-dependent, quantities such as displacements per atom (DPA), fissions per initial heavy metal atom (FIMA), and kinetic energy released per unit mass (KERMA) in the Bateman equations.
3. Develop a method for reducing the number of nuclides in a system based on user-defined criteria.
4. Investigate the suitability of using a simplified depletion library generated using a given set of depletion conditions to a system which experiences different depletion conditions spatially and temporally.
5. Determine if a size reduction of the nuclide library can be achieved when adding PNs to model decay effects and if the size reduction merits implementation of the functionality for existing depletion-capable tools.

The first objective was achieved by developing a modified version of the well-known "scaling and squaring" method of solving the matrix exponential [27] which was tailored specifically for solving the Bateman equations. ADM was developed, implemented in Griffin, and demonstrated comparable performance in terms of run time relative to CRAM for systems with 300 or fewer nuclides, however, because the run time of ADM increases rapidly with increasing numbers of nuclides when compared to CRAM, it is overall a slower method for larger depletion systems. Nevertheless, ADM serves as an independent method to verify CRAM which was demonstrated to sometimes calculate negative NNDs when too low of an approximation order was used.

The second objective was achieved by adding several non-nuclide quantities to track in the depletion matrix in Griffin including the total damage energy released in the system (used to calculate radiation in units of DPA), the total number of fissions that have occurred in the system (used to calculate fuel burnup in units of fissions per initial heavy metal atom (FIMA)), and the total energy released in the system, also referred to as KERMA. The calculation of these values in the Bateman equations was compared to the traditional forward Euler (FE) finite difference method which demonstrated that solving for these quantities in the Bateman equations was superior to using FE, particularly for decay-related quantities such as decay energy release.

The third objective was achieved by developing a simple heuristic method where the user specifies a set of depletion conditions (neutron flux and depletion interval lengths) and tolerance levels for the macroscopic XS and target nuclides. The heuristic method then calculates reference values for the macroscopic XS and target nuclide quantities using the unmodified depletion library given by the user. The heuristic method then attempts to simplify the depletion library by iteratively removing nuclides from the system and recalculating the macroscopic XS and target NNDs after a nuclide has been removed. If the calculated quantities are within the user-defined tolerances over all depletion intervals specified by the user then the nuclide remains removed from the simplified library and the method attempts to remove the next nuclide. If the user-defined tolerances are exceeded, then the nuclide is added back into the simplified depletion library and the method attempts to remove the next nuclide.

The fourth objective was accomplished by performing depletion calculations using the simplified depletion libraries for varying neutron flux levels. Based on these calculations it was determined that the results calculated by the simplified depletion libraries are sensitive to increases in the neutron flux experienced by the system, resulting in the results calculated by simplified depletion libraries diverging from the results calculated by the reference depletion library in excess of the user-specified tolerances during the simplification process.

The fifth objective was accomplished by adding decay energy release and decay photon activity as target quantities to preserve during the simplification process. This resulted in a significant increase in the number of nuclides in the simplified depletion library in order to preserve these quantities. The addition of PNs allowed for more nuclides to be removed and an overall decrease in the number of nuclides tracked in the simplified depletion libraries while preserving the decay quantities of interest.

1.5. Dissertation Overview

The remainder of this dissertation is broken into four self-contained journal articles which discuss the fulfillment of the objectives outlined in Section 1.4 as well as concluding remarks and a discussion of future work to build off of the research accomplished in this work.

1. Chapter 2 consists of a journal article which discusses the development of ADM as a method for solving the Bateman equations where accuracy and run-time comparisons are made between ADM and CRAM.

2. Chapter 3 consists of a journal article which relates the calculation of certain non-nuclide quantities, such as DPA, to the Bateman equations used to calculate the NNDs of a system and the implementation of tracking said quantities in the depletion matrix, specifically quantities which are dependent on the NNDs of the system.

3. Chapter 4 consists of a journal article which introduces the heuristic simplification method and the concept of pseudo-nuclides for modeling decay energy release. Testing is performed using a 0D infinite homogeneous region with one-group and two-group microscopic XS libraries used.

4. Chapter 5 consists of a journal article which applies the previously introduced heuristic simplification method to a 2D SFR core with homogenized assemblies divided into varying levels of spatial refinement with a 33-group microscopic XS library used. Pseudo-nuclides are once again used to model decay energy release as well as model the decay photon activity contribution from removed nuclides.

5. Chapter 6 presents concluding remarks regarding the research presented in Chapters 2 to 5 and makes recommendations to the users and developers of depletion-capable reactor analysis applications.

6. Chapter 7 discusses future research topics of interest discovered during the course of the research performed for this dissertation.

Chapter 2: Introduction of the Adding and Doubling Method for Solving Bateman Equations for Nuclear Fuel Depletion

Olin W. Calvin, Barry D. Ganapol, and R. A. Borrelli, 2023. Introduction of the Adding and Doubling Method for Solving Bateman Equations for Nuclear Fuel Depletion. Nuclear Science and Engineering 197(4), 558. doi:10.1080/00295639.2022.2129950.

2.1. Abstract

This paper introduces and evaluates the Adding and Doubling Method (ADM) for solving the Bateman equations for depletion systems with varying numbers of nuclides and compares it to the Chebyshev rational approximation method (CRAM), both implemented in the reactor physics analysis application Griffin. ADM, when applied to the Crank-Nicolson Finite Difference method, can produce results comparable in accuracy and precision to CRAM with comparable run times for systems with 35 or 297-nuclides. For systems with more than 300 nuclides, the matrix-matrix operations required by ADM are significantly more costly than the matrix-vector operations required by CRAM, making CRAM the more efficient method for systems with large numbers of nuclides. ADM is an accurate method that maintains other advantages over CRAM in that it does not depend on pre-generated coefficients or require complex number operations. ADM also manages to outperform CRAM by a factor of more than 250 in terms of run time for depletion systems which require multiple Bateman solves while the depletion matrix and time step size remain constant over all depletion intervals.

2.2. Introduction

The Bateman equations, named after mathematician Harry Bateman, form the mathematical model describing the abundances of various nuclides in a system as time passes and radioactive decay occurs, transforming radioactive nuclides into their decay products [25]. While the Bateman equations originally only considered radioactive decay, they can be modified to account for the neutron transmutation that occurs in nuclear systems. This is shown in Eq. 2.1 adapted from Ref. [26]:

$$\begin{aligned}\frac{dN_i(t)}{dt} = &\sum_j \gamma_{j,i}\sigma_{f,j}N_j(t)\phi(t) + \sum_k \Big(\sum_r \sigma_{r,k\to i}N_k(t)\phi(t)\Big) \\ &+ \sum_l \lambda_{l\to i}N_l(t) - \sigma_{a,i}N_i(t)\phi(t) - \lambda_i N_i(t)\end{aligned} \tag{2.1}$$

where

$\frac{dN_i(t)}{dt}$	time-dependent rate of change in the number density of nuclide i
$\gamma_{j,i}$	probability that nuclide i will be produced as a fission product as a result of the neutron-induced nuclear fission of nuclide j
$\sigma_{f,j}$	monoenergetic microscopic fission cross section of nuclide j
$N_j(t)$	time-dependent number density of nuclide j
$\phi(t)$	time-dependent monoenergetic neutron flux within the system
$\sigma_{r,k\to i}$	monoenergetic microscopic non-scattering, non-fission reaction cross section of reaction type r of nuclide k, which produces nuclide i

$N_k(t)$	time-dependent number density of nuclide k
$\lambda_{l \to i}$	the decay constant of nuclide l, which produces nuclide i
$N_l(t)$	time-dependent number density of nuclide l
$N_i(t)$	time-dependent number density of nuclide i
$\sigma_{a,i}$	monoenergetic microscopic absorption (nonscattering) cross section of nuclide i
λ_i	decay constant of nuclide i.

When tracking systems with more than one nuclide, matrix-vector notation is convenient to describe the change in nuclide number densities:

$$\frac{d\mathbf{N}}{dt} = \mathbf{A}(t)\mathbf{N}(t) \tag{2.2}$$

where

$\mathbf{N}(t)$	time-dependent vector of the number densities of all nuclides in the system
$\frac{d\mathbf{N}}{dt}$	time-dependent vector of the rate of change of the number densities of all nuclides in the system
$\mathbf{A}(t)$	time-dependent matrix of the terms from Eq. 2.1 for each nuclide in the system, also known as the "depletion matrix."

When expressed in matrix-vector notation, the number densities of all nuclides at any point in time can be determined by solving the matrix exponential, where $\mathbf{A}$ for some length of time t is constant (i.e., microscopic cross sections and neutron flux are constant) and the initial number densities of all nuclides in the system $\mathbf{N}_0$ are known:

$$\mathbf{N}(t) = e^{\mathbf{A}t}\mathbf{N}_0 \tag{2.3}$$

The definition of a matrix exponential being a power series:

$$e^{\mathbf{A}t} = \sum_{i=0}^{\infty} \frac{(\mathbf{A}t)^i}{i!} \tag{2.4}$$

Depending on the nuclides being considered, the depletion matrix can become extraordinarily stiff when considering the decay constants of long- and short-lived nuclides, such as ^{209}Bi (half-life of 6.3×10^{26} s) and ^{4}H (half-life of 1.9×10^{-22} s) that have roughly 48 orders of magnitude difference in their half-lives. While this is an extreme example, it is not uncommon to consider depletion systems where there may be a 30 or 40 order of magnitude difference between the largest and smallest terms in the depletion matrix, which presents numerical challenges for many traditional matrix exponential solvers, such as solving the power series directly [27].

In this paper, we evaluate a numerical method, referred to as the Adding and Doubling Method (ADM), in order to determine how accurately and efficiently it can solve the Bateman equations when compared to one of the more prolific methods: the Chebyshev rational approximation method (CRAM).

2.2.1. Nuclide Number Densities

Throughout this work, the unit for the number density of a nuclide is atoms per barn per centimeter ($\frac{\text{atoms}}{\text{b}\cdot\text{cm}}$). This enables high-concentration nuclides in certain materials to be defined without very large or very small exponential terms. As an example, the number density of liquid water at 0°C and atmospheric pressure is roughly $0.0335\ \frac{\text{atoms}}{\text{b}\cdot\text{cm}}$ or $0.0556\ \frac{\text{mol}}{\text{cm}^3}$. The reason for using number density rather than molarity is that it is computationally much easier to work with the number density directly, and microscopic neutron cross sections are expressed in units of barns, making arithmetic operations simpler:

$$1\frac{\text{atoms}}{\text{b}\cdot\text{cm}} = 10^{30}\frac{\text{atoms}}{\text{m}^3} = 10^{24}\frac{\text{atoms}}{\text{cm}^3} \approx 1.66\frac{\text{mol}}{\text{cm}^3} \tag{2.5}$$

2.3. Chebyshev Rational Approximation Method

This section provides a brief overview of CRAM (Refs. [28] and [30]) as well as documentation of its benefits and shortcomings. CRAM was developed by Pusa and Leppänen specifically to solve Bateman equations and was first deployed in Serpent, a Monte Carlo particle transport code developed at the VTT Technical Research Centre of Finland [37]. Since then, CRAM has been deployed in other applications capable of performing depletion analyses, such as the Oak Ridge Isotope GENeration (ORIGEN) code, developed at Oak Ridge National Laboratory (ORNL) [38], and Griffin, developed at INL and ANL [2] [39].

CRAM relies on a min/max approximation theory applied to the scalar exponential, which leads to a partial fraction decomposition (PFD) that is a sum of K rational partial fractions of order unity, where K is also the polynomial degree. The approximation requires $\frac{K}{2}$ matrix inversions. The large number of required matrix inversions was one of the primary shortcomings of CRAM. Further development work on CRAM yielded two major improvements:

- The application of sparse Gaussian elimination (SGE) to the CRAM equations resulted in the ability to avoid performing a direct matrix inversion (DMI), which enabled a significant run-time reduction for a system with 1600 nuclides while preserving numerical accuracy [31].
- The use of incomplete partial fraction (IPF) decomposition by forming a second-order rational partial fraction by combining two partial fractions, which resulted in a reduced roundoff error and the ability to perform solves at higher approximation orders [32].

These two improvements resulted in four different "versions" of CRAM that can be deployed, any of which can be referred to as CRAM despite their differences:

- PFD with DMI, which was the first form of CRAM developed
- PFD with SGE
- IPF decomposition with DMI
- IPF decomposition with SGE, which is the most modern version of CRAM and the version currently deployed in Serpent.

Note that each of the above versions of CRAM also require a specified approximation order, with approximation orders for CRAM with PFD known up to Approximation Order 20 and the approximation orders for CRAM with IPF known up to Approximation Order 48 because of data limitations.

To our knowledge, CRAM with IPF and SGE is the most modern and efficient version. It benefits from the improvements of IPF over PFD, which enabled higher approximation orders and a reduced error without any increase in run time when comparing IPF and PFD at the same approximation order. It also benefits from the use of SGE over DMI, which reduced the run time by avoiding the need to perform costly matrix inversions. Consequently, for the rest of this work when comparisons to CRAM are made or referenced (e.g., "CRAM-16") we are referring to CRAM with IPF and SGE at the given approximation order to ensure that the most optimal version of CRAM is used and a fair comparison made between ADM and CRAM.

Before proceeding, we highlight two primary drawbacks to CRAM. The first being that CRAM is dependent on the use of published coefficients for each approximation order, as deriving the coefficients for a given approximation order of CRAM is not trivial, which is why the coefficients were published. Since there may be errors in the published coefficients (or the coefficients may not be published to a desired level of numerical precision), this can cause issues for users working with greater than double precision. The second drawback of CRAM is its numerical inconsistency, $\Delta t \rightarrow 0$, which has been documented previously [36]. However, this time inconsistency can be resolved for practical purposes by increasing the CRAM approximation order.

Based on the drawbacks of CRAM, we can consider ADM a useful method if it does not possess these drawbacks even if it does not outperform CRAM in terms of run time.

For completeness, the equations used to solve CRAM with PFD and CRAM with IPF are included here:

Partial Fraction Decomposition:

$$\mathbf{N}(t) = \alpha_0 \mathbf{N}_0 + 2\text{Re}\Big(\sum_{i=1}^{k/2} \alpha_i (\mathbf{A}t - \theta_i \mathbf{I})^{-1} \Big) \mathbf{N}_0 \tag{2.6}$$

Incomplete Partial Fraction:

$$\begin{aligned} &\mathbf{y} = \mathbf{N}_0 \\ &\text{for } i = 1, 2, ..., k/2 \text{ do} \\ &\mathbf{y} = 2\text{Re}(\alpha_i (\mathbf{A}t - \theta_i \mathbf{I})^{-1} \mathbf{y}) + \mathbf{y} \\ &\text{end for} \\ &\mathbf{y} = \alpha_0 \mathbf{y} \\ &\mathbf{N}(t) = \mathbf{y} \end{aligned} \tag{2.7}$$

where

t	length of the time step depletion occurs over
k	approximation order of the CRAM solve being used
$\mathbf{N}_0$	number densities of all nuclides at the beginning of the time step
$\mathbf{N}(t)$	time-dependent vector of the number densities of all nuclides in the system at time t
$\mathbf{A}$	depletion matrix, which is constant over time t
$\mathbf{I}$	identity matrix with the same dimensions as matrix $\mathbf{A}$
α_i, θ_i, α_0	constants provided in the CRAM documentation for the given approximation order k.

2.4. Adding and Doubling Method

This section presents ADM in detail for the CNFD response algorithm. We consider a finite difference scheme in order to avoid explicitly evaluating the matrix exponential. We do not consider two other common finite difference schemes, forward Euler (FE) and backward Euler, because they are only first-order approximations while CNFD is a second-order approximation. Additionally, limited testing showed overall worse performance for both methods compared to CNFD, which is to be expected. While FE and backward Euler are slightly faster methods than CNFD, the significant degradation in accuracy, when compared to CRAM, of both methods was considered unacceptable. Consequently, we do not discuss either method further in this work and consider CNFD only.

Two key assumptions are made for the application of CNFD to the depletion matrix. The first is that $\mathbf{I} + \mathbf{A}h$ or $\mathbf{I} - \mathbf{A}h$ (where h is a discrete time interval) will not have a noticeably worse condition number than $\mathbf{A}$. For the depletion matrix $\mathbf{A}$, this is typically a valid assumption as $\mathbf{A}$ has terms significantly greater than 1, because of short-lived nuclides and nuclides with very large cross sections, and terms significantly less than 1, because of long-lived nuclides and nuclides with very small cross sections. The second assumption is that $\det(\mathbf{I} - \mathbf{A}h) \neq 0$, thus $\mathbf{I} - \mathbf{A}h$ is invertible. For all test cases we considered, we never encountered this issue, and thus we assume for most real-world nuclear systems this will hold true. It is possible to define depletion systems where $\det(\mathbf{I} - \mathbf{A}h) = 0$, but this is expected to be only for depletion matrices specifically constructed to be purely upper triangular, meaning that should $(\mathbf{A}h)_{ii} = 1$ a zero on the diagonal will occur resulting in the determinate of the upper triangular matrix being zero and the matrix being non-invertible. Since real-world depletion matrices encountered by analysts are not purely upper triangular this is not expected to be a concern and, in the rare instances that $\mathbf{I} - \mathbf{A}h$ is upper triangular and $(\mathbf{A}h)_{ii} = 1$, it is expected that since h is a discrete time interval, a slightly different discrete time interval could be selected such that $(\mathbf{A}h)_{ii} \neq 1$ for all diagonal entries, thereby guaranteeing a nonzero determinant for upper triangular matrices and thus guaranteeing that such matrix is invertible.

2.4.1. Crank-Nicolson Finite Difference

In order to arrive at a CNFD response matrix, we express the matrix exponential as

$$e^{\mathbf{A}h} = e^{\frac{\mathbf{A}h}{2}} \left(e^{-\frac{\mathbf{A}h}{2}} \right)^{-1} \tag{2.8}$$

Before continuing, we use a scalar x such that $x = \mathbf{A}h$ (and $1 = \mathbf{I}$) for the sake of simplicity and generality. Consider the following rational function, which is a Padé (1,1) approximant for the exponential:

$$r_{1,1}(x) = \left[1 + \frac{x}{2}\right] \left[1 - \frac{x}{2}\right]^{-1} \tag{2.9}$$

which (if expressed in the form of a series) is also

$$r_{1,1}(x) = \left[1 + \frac{x}{2}\right] \sum_{i=0}^{\infty} \left[\frac{x}{2}\right]^{i} \tag{2.10}$$

Therefore,

$$r_{1,1}(x) = 1 + x + \frac{x^2}{2} + O(x^3) \tag{2.11}$$

Note that the power series of the matrix exponential has the identical representation

$$e^x = 1 + x + \frac{x^2}{2} + O(x^3) \tag{2.12}$$

Now we subtract Eq. 2.11 from both sides of Eq. 2.12 while using the form from Eq. 2.9 on the left-hand side.

$$e^x - \left[1 + \frac{x}{2}\right]\left[1 - \frac{x}{2}\right]^{-1} = O(x^3) \tag{2.13}$$

Substituting $\mathbf{A}h$ for x and $\mathbf{I}$ for 1 into Eq. 2.13 yields

$$\begin{aligned} e^{\mathbf{A}h} &= \left[\mathbf{I} + \frac{\mathbf{A}h}{2}\right]\left[\mathbf{I} - \frac{\mathbf{A}h}{2}\right]^{-1} + O((\mathbf{A}h)^3) \\ \mathbf{P}_{CN}(\mathbf{A}h) &= \left[\mathbf{I} + \frac{\mathbf{A}h}{2}\right]\left[\mathbf{I} - \frac{\mathbf{A}h}{2}\right]^{-1} \\ e^{\mathbf{A}h} - \mathbf{P}_{CN}(\mathbf{A}h) &= O((\mathbf{A}h)^3) \end{aligned} \tag{2.14}$$

Thus $\mathbf{P}_{CN}(\mathbf{A}h)$ is a second-order approximation method with the consideration that order for truncation methods is asserted to be k in the error term $O(h^{k+1})$, which for CNFD $k = 2$.

Higher-order versions of CNFD can be derived using more terms from the power series.

$$\begin{aligned} x &= \mathbf{A}h \\ e^x &= e^{\frac{x}{2}}\left(e^{-\frac{x}{2}}\right)^{-1} \\ e^x &\approx \left[1 + \frac{x}{2} + \frac{x^2}{8}\right]\left[1 - \frac{x}{2} + \frac{x^2}{8}\right]^{-1} \\ e^{\mathbf{A}h} &\approx \left[\mathbf{I} + \frac{\mathbf{A}h}{2} + \frac{(\mathbf{A}h)^2}{8}\right]\left[\mathbf{I} - \frac{\mathbf{A}h}{2} + \frac{(\mathbf{A}h)^2}{8}\right]^{-1} \end{aligned} \tag{2.15}$$

2.4.2. Evaluating a Time Step

For CNFD, $\mathbf{P}(\mathbf{A}h)$ is

$$\begin{aligned} \mathbf{P}(\mathbf{A}h) &= \tilde{\mathbf{P}}(\mathbf{A}h)\left[\mathbf{I} + O((\mathbf{A}h)^\alpha)\right] \\ \alpha &= 3 \end{aligned} \tag{2.16}$$

The exact solution, denoted by $\mathbf{N}(t)$ for 2^j discretizations, is found by consecutive multiplication of the response matrix $\mathbf{P}$ 2^j number of times:

$$\mathbf{N}(t) = \prod_{i=1}^{2^j} \mathbf{P}(\mathbf{A}h(t,j))\mathbf{N}_0 = \mathbf{P}_j(\mathbf{A}h(t,j))\mathbf{N}_0 \tag{2.17}$$

where

$$\begin{aligned} \mathbf{P}_j(\mathbf{A}h(t,j)) &= \left[\mathbf{P}(\mathbf{A}h(t,j))\right]^{2^j} \\ h(t,j) &= \frac{t}{2^j} \end{aligned} \tag{2.18}$$

Eq. 2.17 is equivalent to a standard finite difference solution. If, for example, $j = 10$, there are $2^{10} = 1024$ discretizations; that many multiplications of a large matrix, say $n = 1600$, would be extremely costly for a single time t. Additionally, the limits of double precision result in a dramatic increase in truncation error as j increases because of the large number of arithmetic operations and subsequent rounding after each operation. A more efficient method of evaluating Eq. 2.17 is necessary, which requires the principle of doubling.

One such efficient multiplication is to first determine $\mathbf{N}(t_1)$ and then at indices 2^q for $q = 1, 2, ..., j$ as follows:

$$\begin{aligned}
\mathbf{N}(t_1) &= \mathbf{P}(\mathbf{A}h(t,j))\mathbf{N}_0 \\
\mathbf{N}(t_2) &= \mathbf{P}(\mathbf{A}h(t,j))\mathbf{N}(t_1) = \Big[\mathbf{P}(\mathbf{A}h(t,j))\mathbf{P}(\mathbf{A}h(t,j))\Big]\mathbf{N}_0 \\
\mathbf{N}(t_4) &= \Big[\mathbf{P}(\mathbf{A}h(t,j))\mathbf{P}(\mathbf{A}h(t,j))\Big]\mathbf{N}(t_2) \\
&= \Big(\Big[\mathbf{P}(\mathbf{A}h(t,j))\mathbf{P}(\mathbf{A}h(t,j))\Big]\Big[\mathbf{P}(\mathbf{A}h(t,j))\mathbf{P}(\mathbf{A}h(t,j))\Big]\Big)\mathbf{N}_0 \\
\mathbf{N}(t_8) &= (\mathbf{P}(\mathbf{A}h(t,j)))^4\mathbf{N}(t_4) = \Big[(\mathbf{P}(\mathbf{A}h(t,j)))^4(\mathbf{P}(\mathbf{A}h(t,j)))^4\Big]\mathbf{N}_0 \\
\mathbf{N}(t_{2^q}) &= (\mathbf{P}(\mathbf{A}h(t,j)))^{2^{q-1}}\mathbf{N}(t_{2^{q-1}}) = \Big[(\mathbf{P}(\mathbf{A}h(t,j)))^{2^{q-1}}(\mathbf{P}(\mathbf{A}h(t,j)))^{2^{q-1}}\Big]\mathbf{N}_0 \\
\mathbf{N}(t_{2^j}) &= (\mathbf{P}(\mathbf{A}h(t,j)))^{2^{j-1}}\mathbf{N}(t_{2^{j-1}}) = (\mathbf{P}(\mathbf{A}h(t,j)))^{2^j}\mathbf{N}_0
\end{aligned} \tag{2.19}$$

We call this process doubling to t. The advantage of doubling is that, instead of requiring 2^j matrix-matrix multiplications, only j matrix-matrix multiplications are necessary. The principle of doubling here is identical to the process used by the "scaling and squaring" method commonly used to evaluate the matrix exponential [27].

Each use of ADM requires the specification of j (which we refer to as the approximation power) when determining the size of the discrete subinterval $h(t,j) = \frac{t}{2^j}$. Thus when we refer to a given solve for ADM, we may refer to it as ADM–10, which would refer to ADM with $j = 10$ resulting in a discrete subinterval of length $h(t,10) = \frac{t}{2^{10}} = \frac{t}{1024}$.

We now introduce the principle of "adding," which involves undoing some of the implementation of doubling. The final "stage" of doubling for a given approximation power j is

$$(\mathbf{P}_{j-1}(\mathbf{A}h(t,j)))^2\mathbf{N}_0 = \mathbf{P}_{j-1}(\mathbf{A}h(t,j))\mathbf{P}_{j-1}(\mathbf{A}h(t,j))\mathbf{N}_0 = \mathbf{P}_j(\mathbf{A}h(t,j))\mathbf{N}_0 = \mathbf{N}(t) \tag{2.20}$$

There are two ways to solve Eq. 2.20 once $\mathbf{P}_{j-1}(\mathbf{A}h(t,j))$ is known. A single matrix-matrix multiplication can be performed to calculate $\mathbf{P}_j(\mathbf{A}h(t,j))$ and then perform a matrix-vector multiplication to calculate $\mathbf{P}_j(\mathbf{A}h(t,j))\mathbf{N}_0 = \mathbf{N}(t)$. Alternatively, two matrix-vector multiplications could be performed instead:

$$\mathbf{P}_{j-1}(\mathbf{A}h(t,j))(\mathbf{P}_{j-1}(\mathbf{A}h(t,j))\mathbf{N}_0) = \mathbf{N}(t) \tag{2.21}$$

We refer to this process as adding because through the matrix-vector multiplication operations we are effectively sequentially adding the results of two substeps together. Two matrix-vector multiplication operations are less computationally expensive than performing one matrix-matrix multiplication and one matrix-vector multiplication, thus it is always preferable to not perform the final matrix-matrix multiplication in favor of matrix-vector multiplication. Additionally, earlier matrix-matrix multiplications could be avoided in favor of matrix-vector multiplication as follows:

$$\mathbf{P}_{j-2}(\mathbf{A}h(t,j))\Big\{\mathbf{P}_{j-2}(\mathbf{A}h(t,j))\Big[\mathbf{P}_{j-2}(\mathbf{A}h(t,j))\big(\mathbf{P}_{j-2}(\mathbf{A}h(t,j))\mathbf{N}_0\big)\Big]\Big\} = \mathbf{N}(t) \tag{2.22}$$

Now we are replacing one matrix-matrix multiplication and two matrix-vector multiplications with four matrix-vector multiplications. We show the relationship between the number of matrix-matrix multiplications and matrix-vector operations required by ADM in Eq. 2.23:

$$\begin{aligned} j &= m + v \\ \text{MMM} &= m \\ \text{MVM} &= 2^v \end{aligned} \tag{2.23}$$

where

j	the approximation power of ADM
MMM	the number of matrix-matrix multiplications
MVM	the number of matrix-vector multiplications.

When we perform the ADM comparisons, we first investigate with $m = j$, which represents "pure" doubling and no adding ($v = 0$). After we have determined a suitable approximation power, we will investigate varying m and v values to arrive at the optimal number of matrix-matrix and matrix-vector operations, or in other words, the optimal ratio of adding to doubling.

For the remainder of this work, we will only consider applying ADM to the original CNFD method, as higher-order forms of CNFD suffer from numerical stability issues in raising the depletion matrix to a given power, which can result in the method failing because of the limits of working in double precision with a potentially stiff matrix, with failure in this instance resulting in the calculation of significantly different number densities from CRAM as well as negative number densities. Even more concerning, higher-order forms of CNFD only failed for some of the systems tested, making these higher-order forms dangerously inconsistent and thus not suitable for deployment in analysis tools that operate in double precision, such as Griffin. Hence when we refer to ADM for the rest of this work we are referring to ADM applied with CNFD.

2.4.3. Numerical Implementation of ADM and CRAM

Here we considered a simple numerical implementation of ADM and determined the length of the discrete interval $h(t, j)$ based on the approximation power ADM-j specified and the length of the depletion interval t specified

$$h(t,j) = \frac{t}{2^j} \tag{2.24}$$

and then solved for the initial response matrix $\mathbf{P}(\mathbf{A}h(t, j))$. Once the response matrix was calculated, we performed j matrix-matrix multiplications to calculate $(\mathbf{P}(\mathbf{A}h(t, j)))^{2^j}$. If $j = 4$, the process is

$$
\begin{aligned}
(\mathbf{P}(\mathbf{A}h(t,j))^{2^1} &= \mathbf{P}(\mathbf{A}h(t,j))\mathbf{P}(\mathbf{A}h(t,j)) \\
(\mathbf{P}(\mathbf{A}h(t,j)))^{2^2} &= (\mathbf{P}(\mathbf{A}h(t,j)))^{2^1}(\mathbf{P}(\mathbf{A}h(t,j)))^{2^1} \\
(\mathbf{P}(\mathbf{A}h(t,j)))^{2^3} &= (\mathbf{P}(\mathbf{A}h(t,j)))^{2^2}(\mathbf{P}(\mathbf{A}h(t,j)))^{2^2} \\
(\mathbf{P}(\mathbf{A}h(t,j)))^{2^4} &= (\mathbf{P}(\mathbf{A}h(t,j)))^{2^3}(\mathbf{P}(\mathbf{A}h(t,j)))^{2^3} \\
\mathbf{P}_4(\mathbf{A}h(t,j)) &= (\mathbf{P}(\mathbf{A}h(t,j)))^{2^4} \\
h(t,j=4) &= \frac{t}{2^4} = \frac{t}{16}
\end{aligned}
\tag{2.25}
$$

After finding the final response matrix, we performed a matrix-vector multiplication with an example for $j = 4$

$$
\mathbf{N}(t) = \mathbf{P}_4(\mathbf{A}h(t,4))\mathbf{N}_0 = \mathbf{P}_4\Big(\frac{\mathbf{A}t}{16}\Big)\mathbf{N}_0 \tag{2.26}
$$

When testing varying the number of matrix-matrix and matrix-vector multiplications, we followed the process explained in Sec. 2.4.2.

For performing matrix-matrix and matrix-vector multiplications, we used sparse matrix multiplication routines implemented in Griffin [2]. For performing any matrix inversions, which are needed for ADM, we used the DGETRF and DGETRI routines from LAPACK [40]. We note that the LAPACK routines are dense matrix operations, meaning that there is the potential for using an optimized sparse matrix inversion operation to reduce the cost of the matrix inversions required by ADM. However, for all practical uses of ADM, we anticipated that the matrix-matrix multiplication operations will be the more expensive part of the ADM solve.

For solving CRAM, we used the optimized SGE algorithms specified in Ref. [31], the IPF algorithm defined in Eq. 2.7, and sparse back-substitution, all implemented in Griffin.

2.5. Test Cases

We considered five different nuclide libraries to evaluate the performance of CRAM and ADM.

1. A 297-nuclide library from the DRAGON5 application for a beginning-of-life (BOL) pressurized water reactor (PWR) fuel pin [41].

2. A 1450-nuclide library from ORIGEN for a BOL PWR fuel pin [38].

3. A 1599-nuclide library that is the same as the 1450 ORIGEN library with some additional short-lived nuclides of light elements (hydrogen to aluminum) added from the ENDF decay library [5]. These short-lived nuclides are asserted to be produced as fission products from uranium as no other transmutation pathways existed for the nuclides to be produced.

4. A 35-nuclide library that uses nuclides tracked from an Organization of Economic Co-operation and Development (OECD) SFR benchmark with decay and cross-section data taken from the DRAGON5 297-nuclide library [42].

5. A 693-nuclide library that uses the same library as the 1599-nuclide library but with all nuclides with decay constants greater than 10^{-4} s^{-1} removed from the system and their decay chains commuted. As an example, consider the nuclide ^{4}H which has an extraordinarily short half-life. When ^{4}He undergoes an (n,p) reaction, instead of producing ^{4}H which then rapidly decays to hydrogen-3, we remove ^{4}H from the

system and assume that hydrogen-3 is directly produced from ^{4}He undergoing an (n,p) reaction. This was done in order to generate a reduced library to serve as an intermediate between the 297- and 1450-nuclide libraries. Commuting short-lived nuclides (i.e., nuclides with large decay constants) is preferred since most nuclides of interest are either stable or have decay constants smaller than 10^{-4} s^{-1}.

These test cases test two libraries from applications used within the nuclear engineering field as well as a 1599-nuclide library, which closely matches the size of the libraries used for testing CRAM in its various publications, and a 35-nuclide library, which closely resembles the nuclides tracked for an extensively tested SFR benchmark problem. A 693-nuclide library serves as an intermediate size between 297 and 1450. Numerically, the smaller the depletion matrix becomes the easier solving the Bateman equations should be since a smaller matrix requires fewer arithmetic operations. Additionally, smaller depletion matrices are expected to be less stiff since shrinking the depletion matrix often means ignoring short-lived nuclides, which are the main source of stiffness in the depletion matrix. However, when considering systems that only experience radioactive decay, small matrices may remain very stiff within a single decay chain, such as the ^{232}Th and ^{238}U decay series.

In terms of time periods, we considered depletion intervals of 1 s, 1 h (3600 s), and 1000 hours (3.6×10^{6} s). All systems are treated as an infinite homogeneous region irradiated with a constant neutron flux of 10^{15} $\frac{\text{neutrons}}{\text{cm}^2 \cdot \text{s}}$.

In order to measure how well methods compare to one another in terms of accuracy, we considered the simple standards of maximum nuclide absolute relative difference (MNARD) and average nuclide absolute relative difference (ANARD). MNARD corresponds to the number density of a single nuclide where the magnitude of the relative difference (RD) between the number density calculated by the two methods being compared is the greatest. ANARD corresponds to the average of the absolute RD values of all nuclides between the two methods. Should the average and maximum differences differ significantly for a given method then there are specific nuclides that one or both methods have difficulty accurately calculating the number density of. If both MNARD and ANARD are similar, one method has a given level of precision in comparing to another method for all nuclides considered. Last, for methods where it is relevant, we considered negative nuclide number density (NNND), or the number of nuclides with number densities less than zero. These values, when they occur, are clearly non-physical and serve as another way to determine how valid a method is for solving the Bateman equations. NNND information is only included in a given table if there were negative number densities calculated by the method. If the column is omitted from a table, no nuclides were calculated to have negative number densities. MNARD and ANARD are always provided.

Initial number densities somewhat represented a homogenized region of light-water reactor UO_2 fuel with light-water coolant with no cladding. The initial number densities used for each test case are shown in Table 2.1.

Nuclide	Density [$\frac{\text{atoms}}{\text{b}\cdot\text{cm}}$]	Nuclide	Density [$\frac{\text{atoms}}{\text{b}\cdot\text{cm}}$]
^{1}H	0.049457000000000	^{234}U	$8.4512220988817 \times 10^{-6}$
^{16}O	0.046688131274253	^{235}U	0.0010518948891610
^{17}O	$1.7748234213217 \times 10^{-5}$	^{238}U	0.022292593642974

Table 2.1: Initial number densities ($\mathbf{N}_0$) for all test cases representing a homogenized PWR fuel pellet with light-water coolant.

2.6. Results

We now compare CRAM to ADM. For the purposes of fair comparison, we implemented both ADM and CRAM into Griffin [2]. The first reason for this is that Griffin is written in C++ and the original testing for CRAM

was performed in Serpent, which is written in C, meaning the performance should be similar between Griffin and the published CRAM numbers derived from Serpent (barring differences in processor speed). The second reason is that both methods involve a significant number of matrix operations, and it can be difficult to accurately assess the run time in something such as MATLAB, which has heavily optimized routines that cannot be easily deployed in production codes. These heavily optimized routines can be implemented in C++ but not without significant effort.

All results were generated using a 12-core 2.70 GHz Intel Xeon E5-2697 with all calculations performed in serial. While Griffin can be run in parallel, all calculations for this work were performed in serial to remove any potential overhead from parallelization. Even running in serial, run-time fluctuations of roughly 10% appeared when running the same problem multiple times.

Since CRAM and ADM will converge, we did not provide a high-precision reference solution for the problems we considered since the odds of two disparate methods like ADM and CRAM converging to same erroneous result is practically zero.

There are three criteria by which we compared ADM to CRAM:

1. *Precision of the solution*: If ADM can provide a solution of similar precision to CRAM, it, at a minimum, has value as a reference solution.

2. *Run time to obtain the solution*: If ADM can produce a solution in less than or equal time as CRAM, it may supplant CRAM in analysis tools because of ADM's increased efficiency.

3. *Lines of code*: If ADM can function with significantly fewer lines of code than CRAM then it is desirable because of the simplicity of implementing and maintaining the functionality.

The CRAM run time increases as the approximation order of the method increases. Similarly, the ADM run time will increase as the size of the discretization $h(t, j) = \frac{t}{2^j}$ decreases and j increases since the number of matrix-matrix multiplications will increase.

For all tests, we compared the results calculated after one depletion interval with a length of one second (which is the time unit used by default in Griffin) by both ADM and CRAM. We then repeat this process 100 times for each test case in order to estimate the standard deviation of the ADM and CRAM run times. Once the run time has been evaluated, we then performed ADM and CRAM solves for 1- and 1000-h depletion intervals and compared the results in order to determine how changing the size of the depletion interval impacts the solution calculated by ADM. We do not provide run-time analyses on these longer time step solves as the depletion interval length does not have an effect on ADM or CRAM run times, which was expected. The run times of the 3600- and 3.6×10^6-s depletion intervals are identical to 1.0-s depletion interval run times for similar approximation powers of ADM and similar approximation orders of CRAM.

2.6.1. 297-Nuclide Test Case

We first considered the 297-nuclide test case as it provides a balance between the number of nuclides and stiffness of the matrix. In general, the ADM behavior determined using the 297-nuclide test case can then determine how to improve ADM before applying it to other systems with different numbers of nuclides and different depletion matrices.

2.6.1.1 Testing CRAM at Different Approximation Orders

Before comparing CRAM to ADM, we first compared CRAM to itself. As the CRAM approximation order increases, the accuracy of the solution provided by CRAM increases as well. To test this, we compared various CRAM approximation orders to the CRAM-48 solution, which is the highest approximation order of CRAM available based on published coefficients [32].

Comparisons for the 297-nuclide test case for the tested approximation orders is shown in Table 2.2. The run times demonstrate a linear relationship between run time and increasing CRAM approximation order. The absolute RD between various approximation orders and Order 48 are shown in Figure 2.1 with the x-axis corresponding to the number density of each nuclide as calculated by CRAM at Approximation Order 48. We drew two conclusions from Figure 2.1, the first that the comparison between Order 24 and Order 48 is markedly different than the rest of the comparisons. This is attributed to issues specifically for CRAM Order 24, which is potentially an issue with the published coefficients, since all other comparisons exhibited similar behavior. The second conclusion is that with an increasing order, the results produced by CRAM do converge with an extremely high degree of precision. This confirms that the implementation of CRAM in Griffin is performing as expected and confirms previously published results from CRAM. Finally, we considered the number of nuclides with negative number densities calculated by each CRAM approximation order shown in Table 2.2, which clearly shows that a large number of negative values are calculated at very low approximation orders, but these disappear with an increasing order. It is also important to note that even the negative value with the greatest magnitude $\left(-3.81 \times 10^{-35} \frac{\text{atoms}}{\text{b·cm}}\right)$ is still quite small in absolute terms, corresponding to less than one ten-thousandth of a "negative atom" per cubic meter.

Order	Time [ms]	MNARD	ANARD	NNND
4	1.190 ± 0.046	9.87×10^{7}	3.58×10^{5}	38
8	1.861 ± 0.059	2.65×10^{4}	1.53×10^{2}	25
12	2.536 ± 0.070	7.02×10^{2}	3.18×10^{0}	10
16	3.228 ± 0.094	4.08×10^{0}	1.73×10^{-2}	1
20	3.868 ± 0.087	1.16×10^{-2}	4.70×10^{-5}	0
24	4.534 ± 0.094	6.67×10^{-5}	3.88×10^{-5}	0
28	5.208 ± 0.106	2.42×10^{-8}	9.32×10^{-11}	0
32	5.872 ± 0.112	2.23×10^{-11}	8.90×10^{-14}	0
36	6.535 ± 0.142	1.46×10^{-14}	7.32×10^{-16}	0
40	7.175 ± 0.148	7.63×10^{-15}	7.04×10^{-16}	0
44	7.863 ± 0.145	9.84×10^{-15}	2.61×10^{-15}	0
48	8.499 ± 0.162	-	-	0

Table 2.2: 297-nuclide 1.0-s test case comparison of different CRAM approximation orders to the CRAM-48 solution.

Based on the run-time results of various CRAM orders as well as the convergence of the solutions of various CRAM approximation orders as the approximation order increases, we concluded that using CRAM at Approximation Order 48 is valid for comparing to ADM. CRAM Order 48 provides the most accurate results, although its run time is roughly 33% greater than that of Order 36, which provides a comparable level of precision for the 297-nuclide test case. Consequently, should ADM, or any algorithm, slightly outperform CRAM-48 in terms of run time, comparisons between other CRAM approximation orders may be necessary.

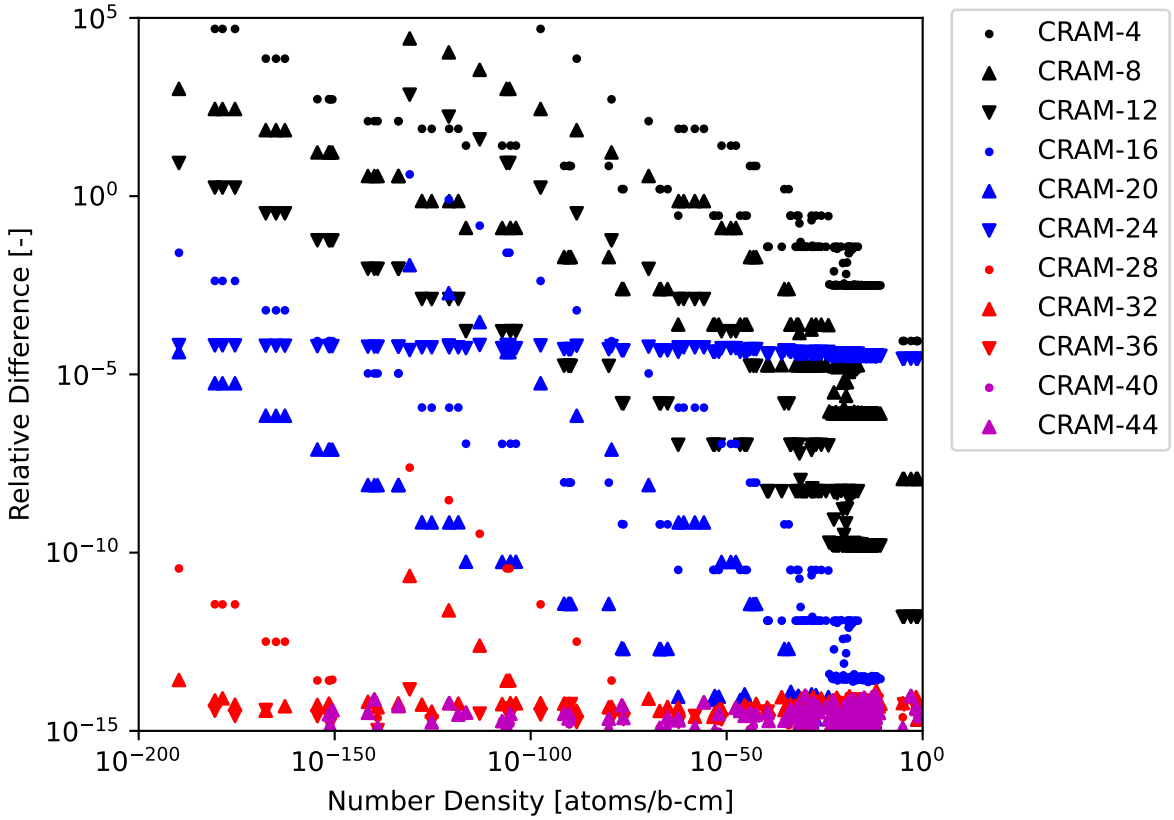

Figure 2.1: 297-nuclide 1.0-s test case RDs computed for various CRAM approximation orders relative to the CRAM-48 solution

2.6.1.2 ADM to CRAM Comparison

We now compare ADM to the CRAM-48 solution. The first set of results for ADM are shown in Table 2.3 and Figure 2.2 and indicate that, with increasing approximation power, ADM converges to the CRAM-48 solution to within about 10 decimal places of accuracy as Power 20 is reached. However, Figure 2.2 shows that, as the approximation power increases, the RD between CRAM-48 and ADM increases for large number density nuclides. This trend is attributed to a compounding error from operations performed in double-precision as the ADM-20 solution requires a total of one matrix inversion and 21 matrix-matrix multiplications to calculate the response matrix for the final matrix-vector operation. By contrast, while CRAM requires multiple Gaussian elimination operations, these operations do not compound upon one another in the same way as when calculating the response matrix for ADM. Also, ADM never produces any negative number densities.

Table 2.3 reveals that the run time for ADM is greater than CRAM-48 for all approximation powers and the ADM-20 solution requires a run time 40 times greater than the CRAM run time. The main cause of this difference is the need to perform a matrix inversion coupled with several matrix-matrix multiplications while CRAM only requires matrix-vector operations. Additionally, ADM's requirement of multiple matrix-matrix multiplications results in each subsequent matrix becoming denser, resulting in each subsequent matrix-matrix multiplication being more costly. One proposal to improve the run time of ADM-CNFD is to apply a numerical tolerance or "cutoff" to the matrices considered, treating values below this cutoff as zero whenever such a value is calculated. This reduces the number of arithmetic operations that must be performed when multiplying matrices and is expected

to improve run time. From a practical perspective, we are only concerned with nuclides with number densities greater than 10^{-30} $\frac{\text{atoms}}{\text{b·cm}}$ (or 1 $\frac{\text{atom}}{\text{m}^3}$), thus applying a cutoff is valid as long as we preserve the numerical accuracy of nuclides with number densities greater than 10^{-30} $\frac{\text{atoms}}{\text{b·cm}}$.

We did not consider applying a numerical cutoff to CRAM as testing showed that CRAM does not significantly benefit from applying a numerical cutoff because of its matrix-vector operations. The depletion matrix, while having small values that may be zeroed, used for solving CRAM does not appreciably increase in density when performing sparse Gaussian elimination. By contrast, the matrix-matrix multiplications required by ADM can result in extraordinarily small non-zero values in the matrix, which can significantly increase the density of the ADM response matrix without those small values significantly affecting the final number density values, thus ADM's run time can be significantly reduced by using a numerical cutoff while CRAM does not experience a similar benefit.

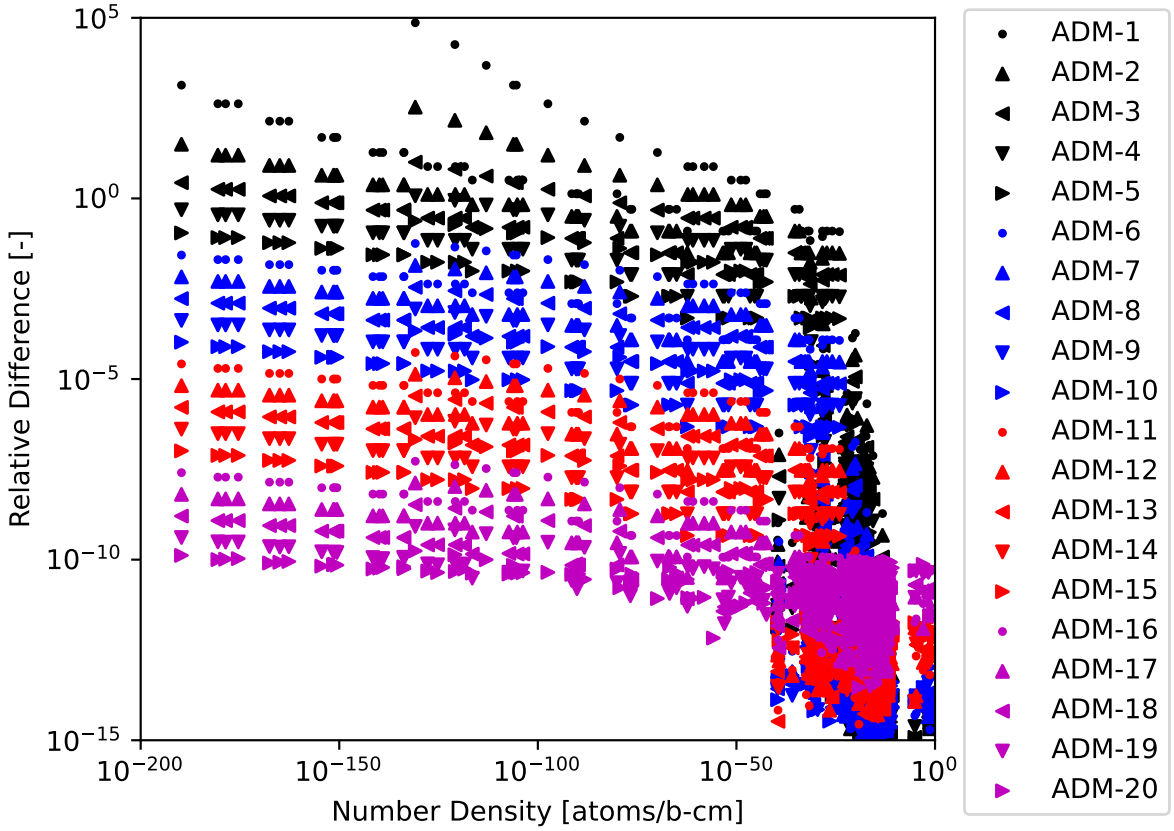

Figure 2.2: 297-nuclide 1.0-s test case RDs computed for various ADM approximation powers to the CRAM-48 solution.

Table 2.4 shows the number of nuclides that have number densities calculated by CRAM-48 to have concentrations below the given cutoffs. Tables 2.5, 2.6, 2.7, and 2.8 as well as Figure 2.3 show the impact of applying a numerical cutoff to the ADM calculation. As expected, run time improves as the numerical cutoff increases, with the ADM-20 solution with a numerical cutoff of 10^{-50} taking roughly twice as long as the CRAM-48 solution. However, MNARD and ANARD for number densities above the cutoff increased, particularly for the cutoffs of 10^{-100} and 10^{-50}. Instead of considering all nuclides with number densities greater than 10^{-50} $\frac{\text{atoms}}{\text{b·cm}}$, we specifically consider nuclides with number densities greater than 10^{-30} $\frac{\text{atoms}}{\text{b·cm}}$ and evaluate MNARD and ANARD for

Power	Time [ms]	MNARD	ANARD	Power	Time [ms]	MNARD	ANARD
1	28.102 ± 3.781	7.31×10^{4}	3.47×10^{2}	11	209.533 ± 4.456	5.42×10^{-5}	1.69×10^{-6}
2	49.388 ± 5.535	3.37×10^{2}	2.67×10^{0}	12	225.029 ± 3.715	1.36×10^{-5}	4.22×10^{-7}
3	66.955 ± 4.822	1.01×10^{1}	1.74×10^{-1}	13	239.717 ± 5.471	3.39×10^{-6}	1.06×10^{-7}
4	88.117 ± 6.205	1.18×10^{0}	3.09×10^{-2}	14	256.733 ± 6.293	8.48×10^{-7}	2.64×10^{-8}
5	106.092 ± 6.144	2.39×10^{-1}	7.11×10^{-3}	15	272.353 ± 6.443	2.12×10^{-7}	6.59×10^{-9}
6	123.549 ± 6.542	5.66×10^{-2}	1.74×10^{-3}	16	288.142 ± 7.339	5.30×10^{-8}	1.65×10^{-9}
7	142.001 ± 6.557	1.39×10^{-2}	4.33×10^{-4}	17	301.846 ± 7.313	1.32×10^{-8}	4.16×10^{-10}
8	158.481 ± 6.102	3.48×10^{-3}	1.08×10^{-4}	18	315.530 ± 7.611	3.31×10^{-9}	1.10×10^{-10}
9	172.409 ± 4.459	8.68×10^{-4}	2.70×10^{-5}	19	332.502 ± 7.635	8.32×10^{-10}	4.24×10^{-11}
10	193.101 ± 5.045	2.17×10^{-4}	6.75×10^{-6}	20	346.539 ± 8.824	1.75×10^{-10}	3.71×10^{-11}

Table 2.3: 297-nuclide 1.0-s test case comparison of various approximation powers of ADM to the CRAM-48 solution.

these nuclides in Table 2.9. This indicates that a very good agreement is achieved for nuclides with number densities greater than 10^{-30} $\frac{\text{atoms}}{\text{b·cm}}$, with 10 digits of precision achieved at Approximation Power 16 for all nuclides that exceed 10^{-30} $\frac{\text{atoms}}{\text{b·cm}}$ while using a numerical cutoff of 10^{-50}. With a run time of 14.7 milliseconds, ADM-16 is still almost double the CRAM-48 run time. Additionally, we can estimate that each additional matrix-matrix multiplication adds roughly 0.6 milliseconds and that the matrix inversion takes roughly 4.8 milliseconds, which corresponds to one-third of the ADM-16 solve run time meaning that an optimized matrix inversion method would potentially reduce the ADM-16 run time but not make it faster than CRAM-48.

Cutoff	Nuclides Below Cutoff	Cutoff	Nuclides Below Cutoff
10^{-200}	0	10^{-50}	52
10^{-150}	11	10^{-30}	79
10^{-100}	29	—	—

Table 2.4: 297-nuclide 1.0-s test case number of nuclides with CRAM-48 calculated number densities below the given numerical cutoffs.

Power	Time [ms]	MNARD	ANARD	Power	Time [ms]	MNARD	ANARD
1	12.805 ± 0.585	7.31×10^{4}	3.47×10^{2}	11	71.406 ± 0.769	5.42×10^{-5}	1.69×10^{-6}
2	19.527 ± 0.295	3.37×10^{2}	2.67×10^{0}	12	76.391 ± 0.780	1.36×10^{-5}	4.22×10^{-7}
3	26.225 ± 0.453	1.01×10^{1}	1.74×10^{-1}	13	81.803 ± 0.893	3.39×10^{-6}	1.06×10^{-7}
4	32.257 ± 0.438	1.18×10^{0}	3.09×10^{-2}	14	86.383 ± 0.980	8.48×10^{-7}	2.64×10^{-8}
5	38.442 ± 0.588	2.39×10^{-1}	7.11×10^{-3}	15	91.313 ± 0.805	2.12×10^{-7}	6.59×10^{-9}
6	44.211 ± 0.509	5.66×10^{-2}	1.74×10^{-3}	16	96.251 ± 0.803	5.30×10^{-8}	1.65×10^{-9}
7	50.078 ± 0.621	1.39×10^{-2}	4.33×10^{-4}	17	102.088 ± 1.673	1.32×10^{-8}	4.16×10^{-10}
8	55.918 ± 0.650	3.48×10^{-3}	1.08×10^{-4}	18	106.656 ± 1.916	3.31×10^{-9}	1.10×10^{-10}
9	61.595 ± 0.783	8.68×10^{-4}	2.70×10^{-5}	19	109.628 ± 0.770	8.32×10^{-10}	4.24×10^{-11}
10	65.964 ± 0.636	2.17×10^{-4}	6.75×10^{-6}	20	113.387 ± 1.009	1.75×10^{-10}	3.71×10^{-11}

Table 2.5: 297-nuclide 1.0-s test case comparison of various approximation powers of ADM with a cutoff of 10^{-200} to the CRAM-48 solution for nuclides with number densities greater than 10^{-200} $\frac{\text{atoms}}{\text{b·cm}}$.

We did not consider numerical cutoffs above 10^{-50} since we see an impact on number densities that are greater than but still close to the cutoff meaning that applying a cutoff of 10^{-30} or even 10^{-40} could impact the results of number densities with concentrations greater than 10^{-30} $\frac{\text{atoms}}{\text{b·cm}}$. For all other test cases, we used a cutoff of 10^{-50} in order to benefit from the decreased run time of ADM with said cutoff.

We now attempted to optimize the ratio of adding and doubling by varying the number of matrix-matrix operations (m) and matrix-vector operations (2^v). Results are shown in Table 2.10. We achieved a minimum run time of 11.4 milliseconds for $v = 6$. This is now roughly 33% greater than the run time of CRAM-48. Changing m and v results in the same ADM solution, although, as $m \to 0$, the number of matrix-vector operations can

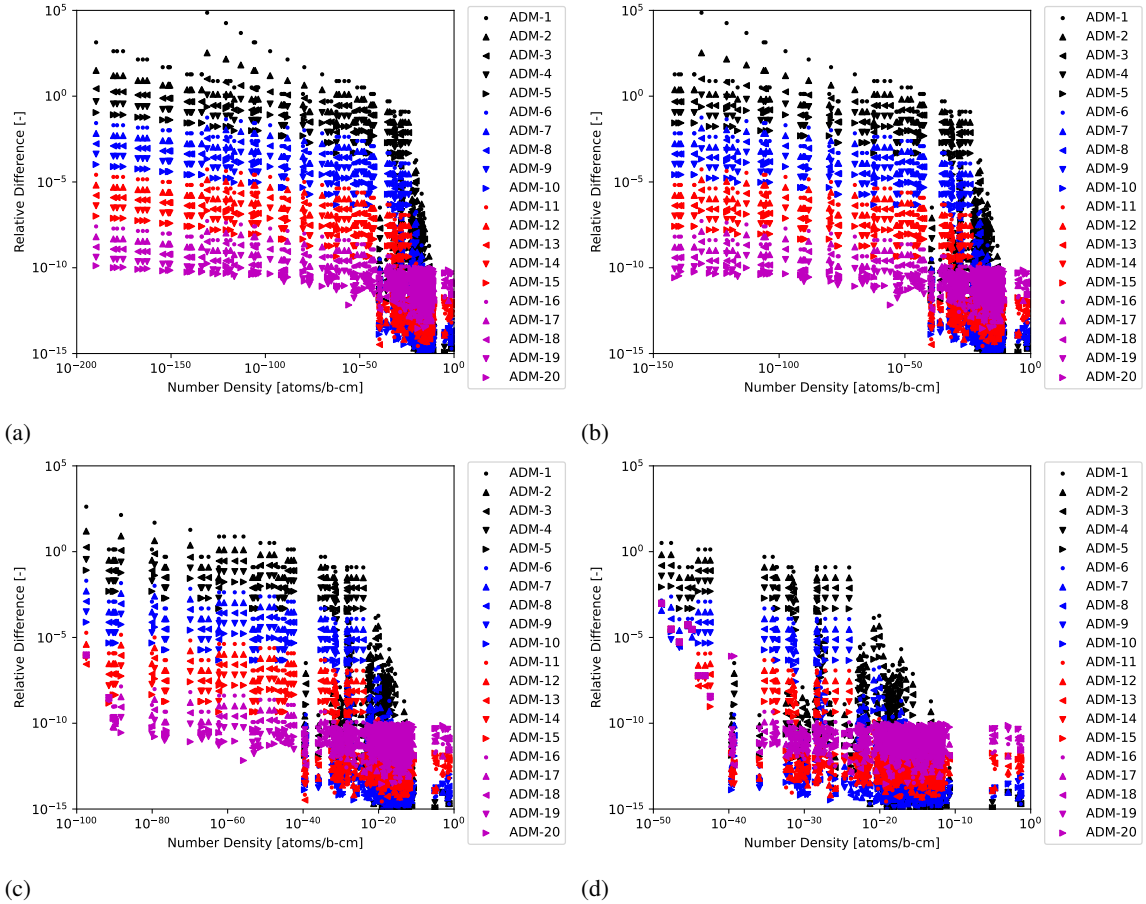

Figure 2.3: 297-nuclide 1.0-s test case RDs computed for various ADM approximation powers with various cutoffs to the CRAM-48 solution: a cutoff of 10^{-200}, b cutoff of 10^{-150}, c Cutoff of 10^{-100}, and d cutoff of 10^{-50}.

Power	Time [ms]	MNARD	ANARD	Power	Time [ms]	MNARD	ANARD
1	7.963 ± 0.446	7.31×10^{4}	3.49×10^{2}	11	28.045 ± 0.547	5.42×10^{-5}	1.16×10^{-6}
2	10.170 ± 0.515	3.37×10^{2}	2.35×10^{0}	12	30.439 ± 0.783	1.36×10^{-5}	2.91×10^{-7}
3	12.274 ± 0.542	1.01×10^{1}	1.30×10^{-1}	13	31.418 ± 0.632	3.39×10^{-6}	7.28×10^{-8}
4	14.815 ± 0.541	1.18×10^{0}	2.17×10^{-2}	14	33.176 ± 0.699	8.48×10^{-7}	1.82×10^{-8}
5	16.672 ± 0.467	2.39×10^{-1}	4.93×10^{-3}	15	35.028 ± 0.695	2.12×10^{-7}	4.55×10^{-9}
6	18.972 ± 0.572	5.66×10^{-2}	1.20×10^{-3}	16	36.596 ± 0.746	5.30×10^{-8}	1.14×10^{-9}
7	20.752 ± 0.572	1.39×10^{-2}	2.99×10^{-4}	17	38.026 ± 0.614	1.32×10^{-8}	2.88×10^{-10}
8	22.644 ± 0.487	3.48×10^{-3}	7.46×10^{-5}	18	39.563 ± 0.746	3.31×10^{-9}	7.75×10^{-11}
9	24.624 ± 0.726	8.68×10^{-4}	1.86×10^{-5}	19	40.754 ± 0.856	8.32×10^{-10}	3.45×10^{-11}
10	26.567 ± 0.805	2.17×10^{-4}	4.66×10^{-6}	20	42.389 ± 0.779	1.75×10^{-10}	3.50×10^{-11}

Table 2.6: 297-nuclide 1.0-s test case comparison of various approximation powers of ADM with a cutoff of 10^{-150} to the CRAM-48 solution for nuclides with number densities greater than 10^{-150} $\frac{\text{atoms}}{\text{b·cm}}$.

introduce a loss of precision because of the large number of resulting arithmetic operations (reflected in the significant increase in run time when $m = 0$).

Now that we have identified the optimal conditions for ADM in terms of precision and run time for the 1 second depletion case, we considered ADM-16 applied to the 297-nuclide test case for a depletion period of 3,600 s (1 h) and 3.6×10^{6} s (1000 h). The main motivation for testing longer depletion intervals is two-fold. First, depletion intervals for normal reactor operation are generally on the order of hours or days, with short depletion

Power	Time [ms]	MNARD	ANARD	Power	Time [ms]	MNARD	ANARD
1	6.978 ± 0.517	4.18×10^{2}	2.53×10^{0}	11	20.694 ± 0.558	1.87×10^{-5}	3.30×10^{-7}
2	8.526 ± 0.505	1.58×10^{1}	1.56×10^{-1}	12	21.761 ± 0.615	3.96×10^{-6}	7.98×10^{-8}
3	10.050 ± 0.486	1.79×10^{0}	2.53×10^{-2}	13	23.058 ± 0.593	8.94×10^{-7}	1.73×10^{-8}
4	11.446 ± 0.513	3.51×10^{-1}	5.67×10^{-3}	14	23.872 ± 0.630	6.46×10^{-7}	6.46×10^{-9}
5	12.638 ± 0.434	8.23×10^{-2}	1.38×10^{-3}	15	25.324 ± 0.781	8.77×10^{-7}	4.27×10^{-9}
6	14.070 ± 0.512	2.03×10^{-2}	3.42×10^{-4}	16	26.250 ± 0.733	9.34×10^{-7}	3.74×10^{-9}
7	15.633 ± 0.698	5.04×10^{-3}	8.54×10^{-5}	17	27.248 ± 0.575	9.49×10^{-7}	3.61×10^{-9}
8	16.615 ± 0.518	1.26×10^{-3}	2.13×10^{-5}	18	28.295 ± 0.593	9.52×10^{-7}	3.59×10^{-9}
9	17.862 ± 0.385	3.14×10^{-4}	5.33×10^{-6}	19	29.581 ± 0.598	9.53×10^{-7}	3.59×10^{-9}
10	19.169 ± 0.496	7.77×10^{-5}	1.33×10^{-6}	20	30.271 ± 0.666	9.53×10^{-7}	3.60×10^{-9}

Table 2.7: 297-nuclide 1.0-s test case comparison of various approximation powers of ADM with a cutoff of 10^{-100} to the CRAM-48 solution for nuclides with number densities greater than 10^{-100} $\frac{\text{atoms}}{\text{b·cm}}$.

Power	Time [ms]	MNARD	ANARD	Power	Time [ms]	MNARD	ANARD
1	5.484 ± 0.194	3.22×10^{0}	5.31×10^{-2}	11	12.470 ± 0.492	9.74×10^{-4}	4.48×10^{-6}
2	6.201 ± 0.192	6.70×10^{-1}	1.20×10^{-2}	12	12.636 ± 0.323	9.76×10^{-4}	4.48×10^{-6}
3	7.005 ± 0.247	1.58×10^{-1}	2.89×10^{-3}	13	13.283 ± 0.418	9.77×10^{-4}	4.47×10^{-6}
4	7.777 ± 0.375	3.91×10^{-2}	7.14×10^{-4}	14	13.839 ± 0.435	9.77×10^{-4}	4.48×10^{-6}
5	8.972 ± 0.420	9.73×10^{-3}	1.75×10^{-4}	15	14.390 ± 0.436	9.77×10^{-4}	4.48×10^{-6}
6	8.941 ± 0.196	2.41×10^{-3}	4.07×10^{-5}	16	14.734 ± 0.246	9.77×10^{-4}	4.48×10^{-6}
7	9.594 ± 0.199	5.79×10^{-4}	1.01×10^{-5}	17	15.396 ± 0.415	9.77×10^{-4}	4.48×10^{-6}
8	10.632 ± 0.443	8.27×10^{-4}	5.67×10^{-6}	18	16.131 ± 0.468	9.77×10^{-4}	4.48×10^{-6}
9	11.033 ± 0.428	9.39×10^{-4}	4.58×10^{-6}	19	16.359 ± 0.452	9.77×10^{-4}	4.48×10^{-6}
10	11.380 ± 0.208	9.67×10^{-4}	4.49×10^{-6}	20	16.888 ± 0.402	9.77×10^{-4}	4.48×10^{-6}

Table 2.8: 297-nuclide 1.0-s test case comparison of various approximation powers of ADM with a cutoff of 10^{-50} to the CRAM-48 solution for nuclides with number densities greater than 10^{-50} $\frac{\text{atoms}}{\text{b·cm}}$.

periods generally restricted to specific short-term transient modeling. Second, ADM relies on increasing its accuracy by reducing the substep size for calculating the response matrix since $O((Ah)^3) \to 0$ as $h \to 0$ where $h = \frac{t}{2^j}$. As the time step length t increases, the time discretization h for a given ADM approximation power j increases, which results in a decrease in precision.

The results of ADM-16 compared to CRAM-48 for the 297-nuclide test case for 3,600 seconds and 3.6×10^6 seconds are shown in Figure 2.4 and Table 2.11. For the 3,600 second depletion interval, there were 255 nuclides with number densities above 10^{-50} $\frac{\text{atoms}}{\text{b·cm}}$ and 240 nuclides with number densities above 10^{-30} $\frac{\text{atoms}}{\text{b·cm}}$. For the 3.6×10^6 second depletion interval, there were 268 nuclides with number densities above 10^{-50} $\frac{\text{atoms}}{\text{b·cm}}$ and 258 nuclides with number densities above 10^{-30} $\frac{\text{atoms}}{\text{b·cm}}$. As expected, there is a reduction in the precision of the ADM-

Power	MNARD	ANARD	Power	MNARD	ANARD
1	1.25×10^{-1}	2.68×10^{-3}	11	1.19×10^{-7}	2.56×10^{-9}
2	3.13×10^{-2}	6.71×10^{-4}	12	2.98×10^{-8}	6.40×10^{-10}
3	7.81×10^{-3}	1.68×10^{-4}	13	7.45×10^{-9}	1.60×10^{-10}
4	1.95×10^{-3}	4.19×10^{-5}	14	1.86×10^{-9}	4.06×10^{-11}
5	4.88×10^{-4}	1.05×10^{-5}	15	4.66×10^{-10}	1.10×10^{-11}
6	1.22×10^{-4}	2.62×10^{-6}	16	1.19×10^{-10}	5.37×10^{-12}
7	3.05×10^{-5}	6.55×10^{-7}	17	3.31×10^{-11}	4.68×10^{-12}
8	7.63×10^{-6}	1.64×10^{-7}	18	2.07×10^{-11}	8.39×10^{-12}
9	1.91×10^{-6}	4.09×10^{-8}	19	4.91×10^{-11}	2.01×10^{-11}
10	4.77×10^{-7}	1.02×10^{-8}	20	9.44×10^{-11}	3.45×10^{-11}

Table 2.9: 297-nuclide 1.0-s test case comparison of various approximation powers of ADM with a cutoff of 10^{-50} to the CRAM-48 solution for nuclides with number densities greater than 10^{-30} $\frac{\text{atoms}}{\text{b·cm}}$.

m	v	Time [ms]	m	v	Time [ms]
16	0	14.734 ± 0.246	7	9	15.471 ± 0.300
15	1	13.989 ± 0.273	6	10	21.639 ± 0.384
14	2	13.329 ± 0.297	5	11	34.539 ± 0.570
13	3	12.677 ± 0.289	4	12	60.035 ± 0.894
12	4	12.083 ± 0.239	3	13	111.901 ± 1.042
11	5	11.569 ± 0.195	2	14	215.705 ± 1.624
10	6	11.405 ± 0.257	1	15	419.896 ± 4.308
9	7	11.788 ± 0.389	0	16	832.604 ± 3.376
8	8	12.754 ± 0.255	-	-	-

Table 2.10: 297-nuclide 1.0-s test case run time comparisons for ADM-16 with a cutoff of 10^{-50} with varying m and v numbers.

16 solution as the length of the depletion interval increases, meaning that, for longer depletion intervals, it may be necessary to increase the approximation power of ADM in order to maintain the desired precision.

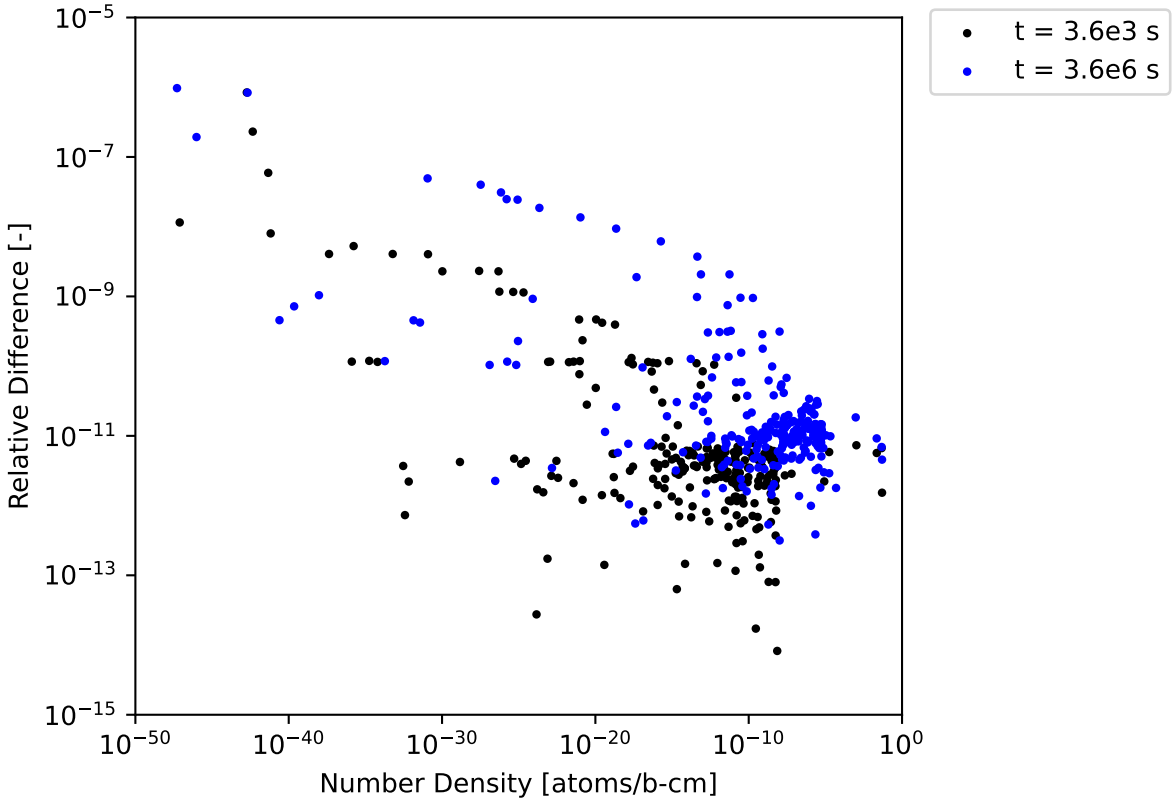

Figure 2.4: 297-nuclide 3,600 and 3.6×10^6 second test cases RDs computed for ADM-16 with a cutoff of 10^{-50} to the CRAM-48 solution.

2.6.2. 1450-Nuclide Test Case

Now we considered a 1450-nuclide test case, which is based on a combined 1-group cross section and decay library for a BOL PWR fuel assembly from ORIGEN [38].

Depletion Interval [s]	MNARD	ANARD
3,600	2.32×10^{-9}	5.92×10^{-11}
3.6×10^{6}	4.00×10^{-8}	7.03×10^{-10}

Table 2.11: 297-nuclide 3,600 and 3.6×10^{6} second test cases comparison of ADM-16 with a cutoff of 10^{-50} to the CRAM-48 solution for nuclides with number densities greater than 10^{-30} $\frac{\text{atoms}}{\text{b·cm}}$.

2.6.2.1 Testing CRAM at Different Approximation Orders

First we checked all CRAM approximation orders against the CRAM-48 solution. The results are shown in Figure 2.5 and Table 2.12. The behavior overall appears similar to the 297-nuclide case with the caveats that convergence is slower with an increasing order, and the number of approximation orders that produce negative number densities is larger. Additionally, we see negative number densities are calculated by all approximation orders up to 28. This once again highlights the need to use a higher CRAM approximation order to ensure that physical number densities are calculated.

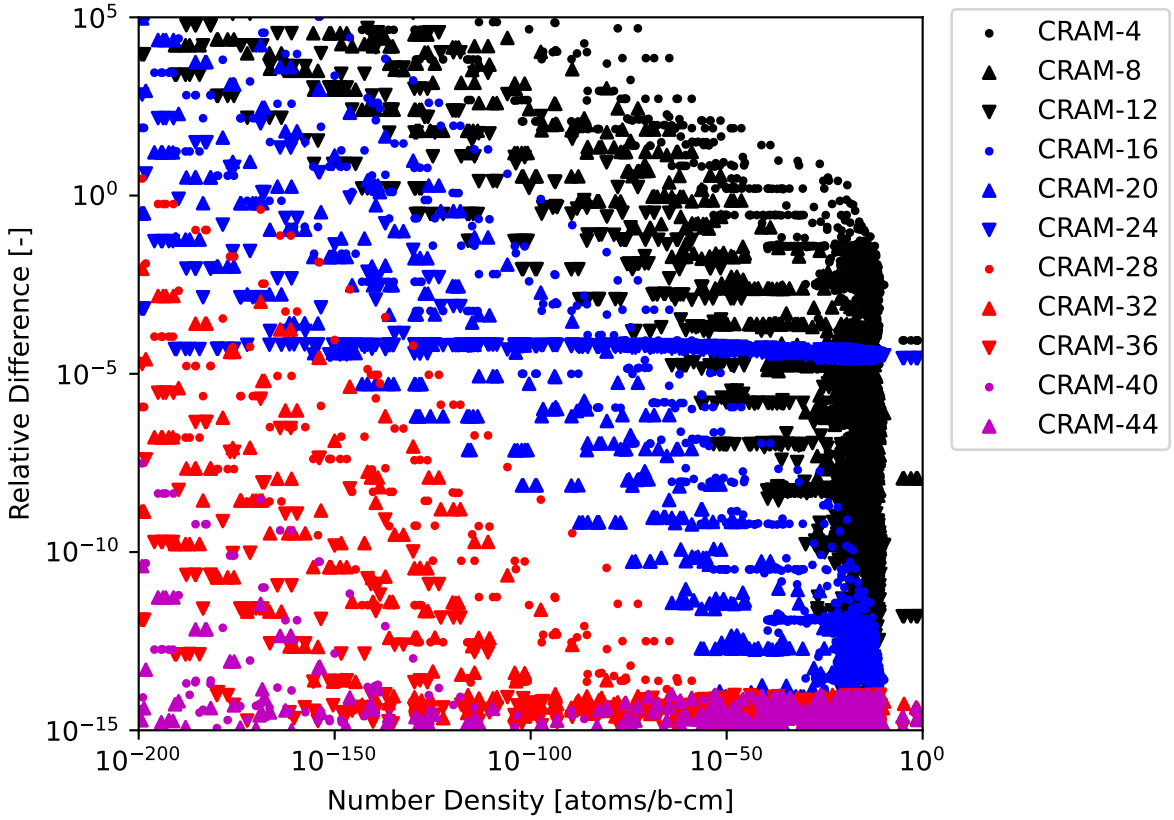

Figure 2.5: 1450-nuclide 1.0-s test case RDs computed for various CRAM approximation orders to the CRAM-48 solution.

2.6.2.2 ADM to CRAM comparison

We then compared ADM to the CRAM-48 result for the 1450-nuclide case using a 10^{-50} cutoff to maintain accuracy for nuclides with number densities greater than 10^{-30} $\frac{\text{atoms}}{\text{b·cm}}$. See Figure 2.6 and Table 2.13. 1165 nuclides have number densities above 10^{-50} $\frac{\text{atoms}}{\text{b·cm}}$, and 1026 nuclides have number densities greater than 10^{-30}

Order	Time [ms]	MNARD	ANARD	NNND
4	7.695 ± 0.323	2.56×10^{18}	3.97×10^{15}	210
8	10.976 ± 0.423	2.27×10^{11}	1.23×10^{9}	149
12	14.567 ± 0.402	4.74×10^{8}	7.84×10^{5}	144
16	17.897 ± 0.453	6.53×10^{6}	1.73×10^{4}	104
20	21.283 ± 0.524	9.32×10^{4}	2.26×10^{2}	50
24	25.081 ± 0.741	6.82×10^{2}	1.54×10^{0}	19
28	28.018 ± 0.576	3.00×10^{0}	6.41×10^{-3}	2
32	31.366 ± 0.687	8.82×10^{-3}	1.80×10^{-5}	0
36	35.200 ± 0.780	1.88×10^{-5}	3.70×10^{-8}	0
40	38.106 ± 0.668	3.08×10^{-8}	5.87×10^{-11}	0
44	41.362 ± 0.692	4.04×10^{-11}	7.64×10^{-14}	0
48	44.983 ± 0.630	-	-	0

Table 2.12: 1450-nuclide 1.0-s test case comparison of various approximation orders of CRAM to the CRAM-48 solution.

$\frac{\text{atoms}}{\text{b·cm}}$, as determined by the CRAM-48 solution. A ten digit agreement is achieved at Approximation Power 17 with a run time over four times as long as CRAM-48. Each additional matrix-matrix multiplication adds roughly 7.3 milliseconds to the ADM run time, and the matrix inversion takes roughly 80 milliseconds, once again about one-third of the ADM-17 run time.

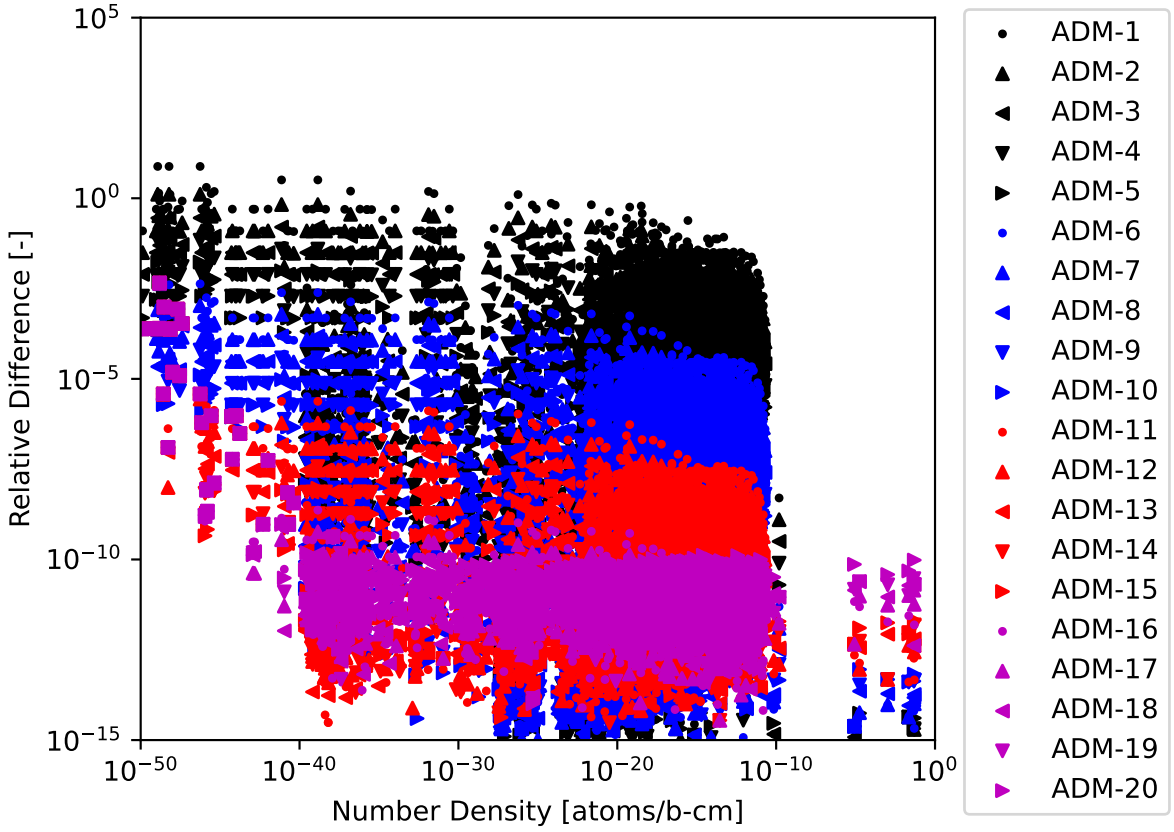

Figure 2.6: 1450-nuclide 1.0-s test case RDs computed for various ADM approximation powers with a cutoff of 10^{-50} to the CRAM-48 solution.

Power	Time [ms]	MNARD	ANARD	Power	Time [ms]	MNARD	ANARD
1	87.527 ± 3.245	1.26×10^{0}	1.69×10^{-2}	11	171.336 ± 1.837	1.06×10^{-6}	1.14×10^{-8}
2	97.568 ± 1.499	2.88×10^{-1}	3.37×10^{-3}	12	177.757 ± 2.024	2.65×10^{-7}	2.84×10^{-9}
3	106.814 ± 1.122	7.02×10^{-2}	7.47×10^{-4}	13	184.864 ± 1.944	6.64×10^{-8}	7.11×10^{-10}
4	115.902 ± 1.174	1.74×10^{-2}	1.86×10^{-4}	14	191.530 ± 2.048	1.66×10^{-8}	1.78×10^{-10}
5	124.660 ± 1.493	4.35×10^{-3}	4.66×10^{-5}	15	197.297 ± 1.780	4.15×10^{-9}	4.47×10^{-11}
6	133.319 ± 1.476	1.09×10^{-3}	1.17×10^{-5}	16	203.416 ± 1.711	1.04×10^{-9}	1.28×10^{-11}
7	141.832 ± 2.368	2.72×10^{-4}	2.91×10^{-6}	17	209.008 ± 1.493	2.59×10^{-10}	6.58×10^{-12}
8	148.941 ± 1.506	6.79×10^{-5}	7.29×10^{-7}	18	214.349 ± 1.892	6.84×10^{-11}	9.06×10^{-12}
9	156.760 ± 1.196	1.70×10^{-5}	1.82×10^{-7}	19	222.910 ± 6.465	6.40×10^{-11}	1.64×10^{-11}
10	163.923 ± 1.588	4.25×10^{-6}	4.55×10^{-8}	20	225.825 ± 1.937	1.30×10^{-10}	3.25×10^{-11}

Table 2.13: 1450-nuclide 1.0-s test case comparison of various approximation powers of ADM with a cutoff of 10^{-50} to the CRAM-48 solution for nuclides with number densities greater than 10^{-30} $\frac{\text{atoms}}{\text{b·cm}}$.

We then evaluated ADM-17 for varying m and v values. As shown in Table 2.14, a run time improvement is initially seen with an increasing v until $v = 7$, at which point run time degrades as the number of matrix-vector multiplications reaches into the thousands, while precision for nuclides with densities greater than 10^{-30} $\frac{\text{atoms}}{\text{b·cm}}$ is consistent. This is a similar v value that resulted in a maximum run time improvement for the 297 test case. Even with the run time improvement, ADM-17 is still roughly three times slower than CRAM-48. Based on these results and the 297-nuclide test case results, it appears that ADM performs worse than CRAM with an increasing matrix size.

m	v	Time [ms]	m	v	Time [ms]
17	0	209.008 ± 1.493	8	9	187.608 ± 1.666
16	1	195.543 ± 1.462	7	10	239.931 ± 1.727
15	2	185.906 ± 2.944	6	11	351.685 ± 1.954
14	3	176.691 ± 1.550	5	12	577.568 ± 2.041
13	4	168.687 ± 2.010	4	13	1028.398 ± 2.842
12	5	161.333 ± 1.298	3	14	1925.427 ± 4.519
11	6	156.377 ± 1.274	2	15	3688.520 ± 33.674
10	7	156.375 ± 1.264	1	16	7122.559 ± 142.493
9	8	167.378 ± 3.972	0	17	14333.752 ± 290.456

Table 2.14: 1450-nuclide 1.0-s run time comparisons of various m and v values for ADM-17 with a cutoff of 10^{-50}.

Now we once again considered the 3,600 and 3.6×10^{6} second depletion interval test cases for ADM-17 compared to CRAM-48.

The results of this comparison are shown in Figure 2.7 and Table 2.15. For the 3,600 second depletion interval, there were 1260 nuclides with number densities above 10^{-50} $\frac{\text{atoms}}{\text{b·cm}}$ and 1112 nuclides with number densities above 10^{-30} $\frac{\text{atoms}}{\text{b·cm}}$. For the 3.6×10^{6} second depletion interval, there were 1367 nuclides with number densities above 10^{-50} $\frac{\text{atoms}}{\text{b·cm}}$ and 1284 nuclides with number densities above 10^{-30} $\frac{\text{atoms}}{\text{b·cm}}$. Once again, there is a reduction in precision as the length of the depletion interval increases, but the decrease in precision is more severe for certain nuclides in the 3.6×10^{6} seconds. In this case, the maximum difference between ADM and CRAM solutions occurred for beryllium-8, which is a very short-lived nuclide. A short-lived nuclide should be the most difficult to calculate because of the stiffness it introduces to the depletion matrix, and that is reflected here.

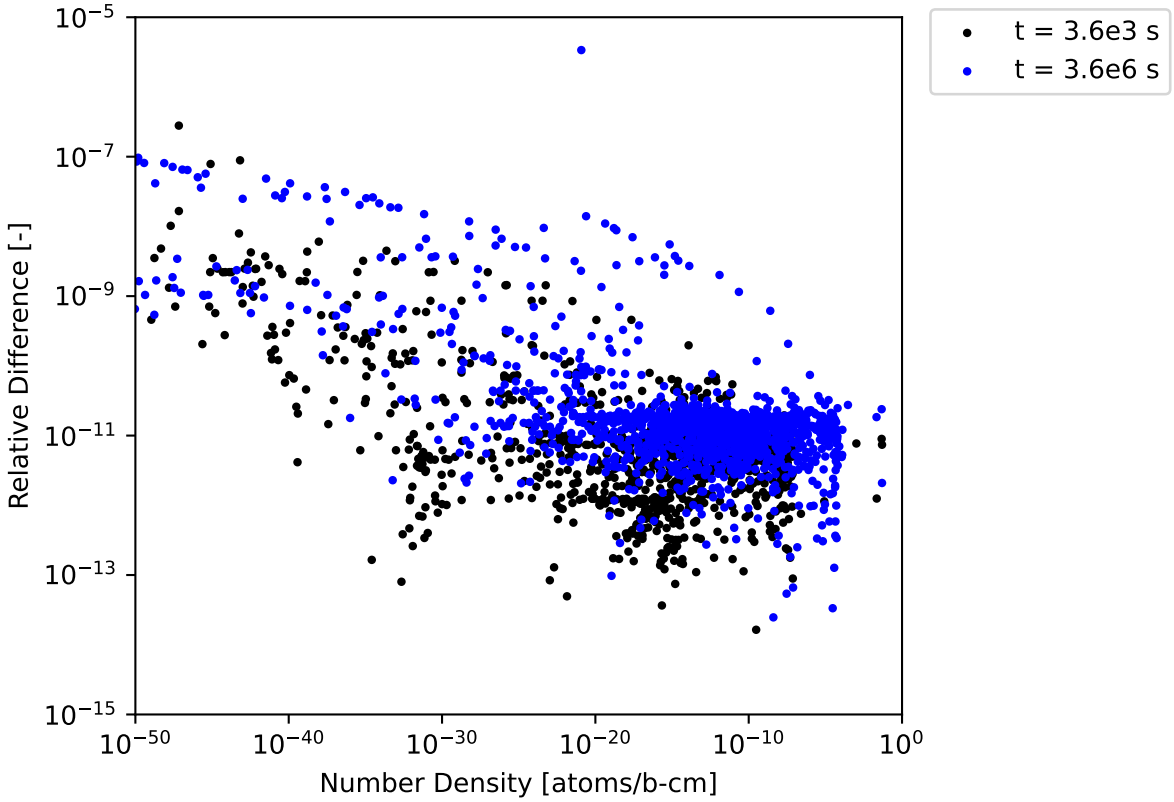

Figure 2.7: 1450-nuclide 3,600 and 3.6×10^6 second test cases RDs computed for ADM-17 with a cutoff of 10^{-50} to the CRAM-48 solution.

Depletion Interval [s]	MNARD	ANARD
3,600	3.21×10^{-9}	1.91×10^{-11}
3.6×10^6	3.38×10^{-6}	2.61×10^{-9}

Table 2.15: 1450-nuclide 3,600 and 3.6×10^6 second test cases comparison of ADM-17 with a cutoff of 10^{-50} to the CRAM-48 solution for nuclides with number densities greater than 10^{-30} $\frac{\text{atoms}}{\text{b·cm}}$.

2.6.3. 1599-Nuclide Test Case

We now considered a 1599-nuclide library, which is the same as the 1450-nuclide library except for the addition of 149 short-lived light nuclides. Because there are no decay or transmutation production pathways to these nuclides in the 1450-nuclide library, all of the added short-lived light nuclides are produced as fission products from uraniun-235 with a yield fraction of 10^{-7}.

2.6.3.1 CRAM at Different Approximation Orders

Once again we compared the results of various CRAM approximation orders to the CRAM-48 solution. The results are shown in Table 2.16 and Figure 2.8 and largely replicate the results from the 1450-nuclide test case. Interestingly, fewer nuclides have negative number densities for the 1599-nuclide test case compared to the 1450-nuclide test case. This implies that, even if the values for specific transmutation pathways are not altered, simply

adding more nuclides to the system may improve the behavior of CRAM. However, further investigation of this CRAM behavior is beyond the scope of this work.

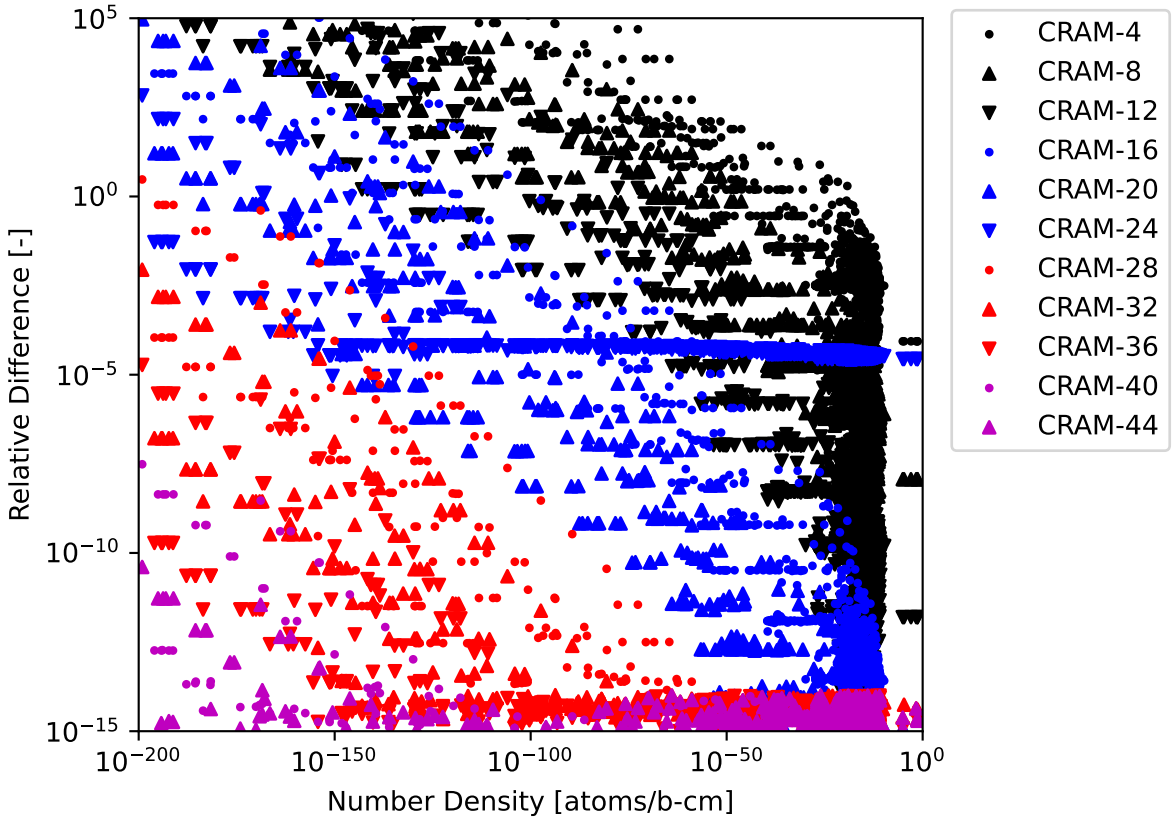

Figure 2.8: 1599-nuclide 1.0-s test case RDs computed for various CRAM approximation orders to the CRAM-48 solution.

Order	Time [ms]	MNARD	ANARD	NNND
4	8.482 ± 0.382	2.56×10^{18}	3.60×10^{15}	193
8	11.862 ± 0.359	2.27×10^{11}	1.11×10^{9}	137
12	15.419 ± 0.441	4.74×10^{8}	7.07×10^{5}	119
16	18.678 ± 0.468	6.53×10^{6}	1.56×10^{4}	88
20	22.072 ± 0.498	9.32×10^{4}	2.04×10^{2}	43
24	25.574 ± 0.593	6.82×10^{2}	1.39×10^{0}	18
28	29.179 ± 0.511	3.00×10^{0}	5.80×10^{-3}	2
32	32.891 ± 0.603	8.82×10^{-3}	1.63×10^{-5}	0
36	36.080 ± 0.751	1.88×10^{-5}	3.35×10^{-8}	0
40	39.386 ± 0.714	3.08×10^{-8}	5.32×10^{-11}	0
44	42.699 ± 0.778	4.04×10^{-11}	6.92×10^{-14}	0
48	46.326 ± 0.759	-	-	0

Table 2.16: 1599-nuclide 1.0-s test case comparison of various approximation orders of CRAM to the CRAM-48 solution.

2.6.3.2 ADM to CRAM comparison

We now considered ADM at various approximation powers and using a cutoff of 10^{-50} for the 1599-nuclide 1.0-s test case. 1338 nuclides have number densities above 10^{-50} $\frac{\text{atoms}}{\text{b·cm}}$, and 1200 nuclides have number densities above 10^{-30} $\frac{\text{atoms}}{\text{b·cm}}$. See Figure 2.9 and Table 2.17.

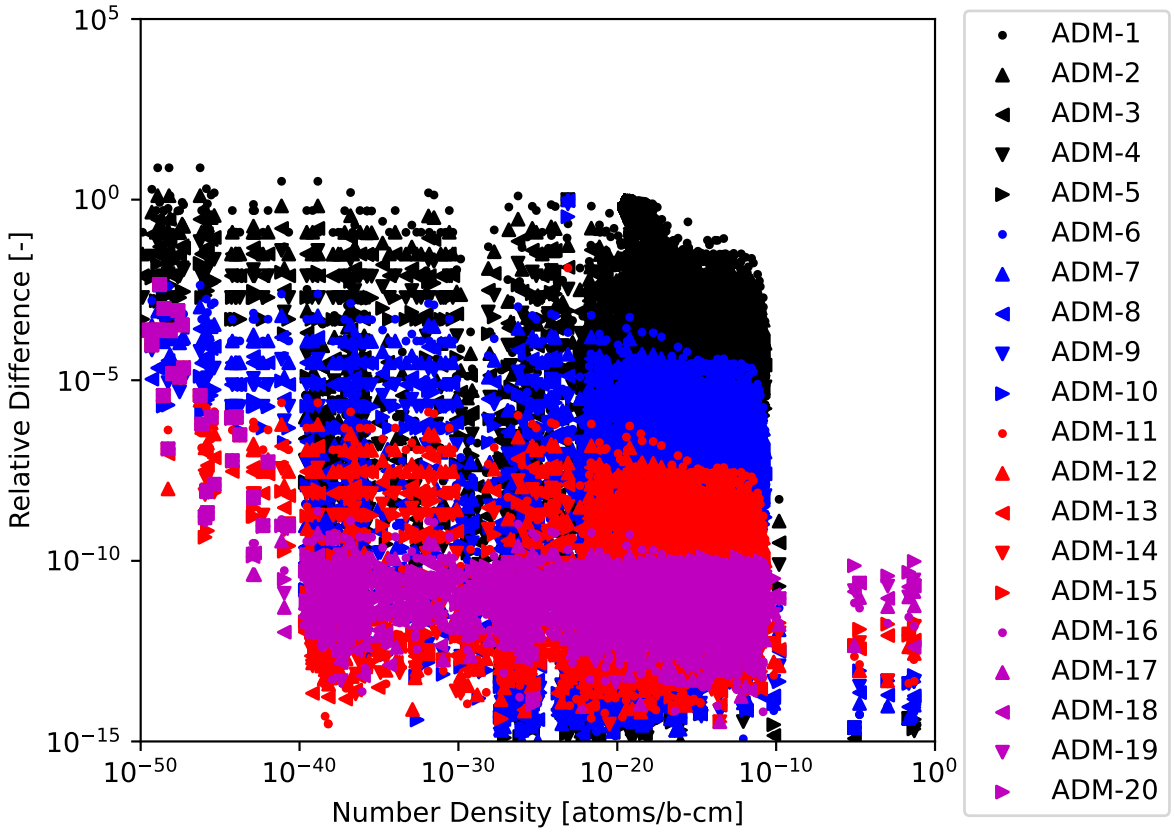

Figure 2.9: 1599-nuclide 1.0-s test case RDs computed for various ADM approximation powers with a cutoff of 10^{-50} to the CRAM-48 solution.

Power	Time [ms]	MNARD	ANARD	Power	Time [ms]	MNARD	ANARD
1	106.663 ± 7.069	1.26×10^{0}	8.39×10^{-2}	11	200.935 ± 6.343	1.28×10^{-2}	1.07×10^{-5}
2	117.649 ± 7.568	1.00×10^{0}	5.75×10^{-2}	12	209.311 ± 6.492	2.65×10^{-7}	2.69×10^{-9}
3	127.183 ± 5.396	1.00×10^{0}	3.78×10^{-2}	13	215.783 ± 6.615	6.64×10^{-8}	6.66×10^{-10}
4	138.153 ± 6.418	1.00×10^{0}	1.53×10^{-2}	14	224.172 ± 6.700	1.66×10^{-8}	1.67×10^{-10}
5	149.537 ± 7.497	9.99×10^{-1}	1.63×10^{-3}	15	231.779 ± 7.775	4.15×10^{-9}	4.20×10^{-11}
6	158.449 ± 7.637	9.96×10^{-1}	8.40×10^{-4}	16	238.346 ± 6.112	1.04×10^{-9}	1.21×10^{-11}
7	168.013 ± 6.623	9.83×10^{-1}	8.21×10^{-4}	17	244.053 ± 6.819	2.59×10^{-10}	6.39×10^{-12}
8	177.483 ± 7.421	9.34×10^{-1}	7.79×10^{-4}	18	249.185 ± 5.953	6.84×10^{-11}	9.03×10^{-12}
9	184.055 ± 6.217	7.62×10^{-1}	6.34×10^{-4}	19	256.358 ± 6.934	6.40×10^{-11}	1.68×10^{-11}
10	192.735 ± 6.577	3.36×10^{-1}	2.80×10^{-4}	20	262.023 ± 5.549	1.30×10^{-10}	3.27×10^{-11}

Table 2.17: 1599-nuclide 1.0-s test case comparison of various approximation powers of ADM with a cutoff of 10^{-50} to the CRAM-48 solution for nuclides with number densities greater than 10^{-30} $\frac{\text{atoms}}{\text{b·cm}}$.

ADM-17 provides the desired ten digits of precision with a five times greater run time than the CRAM-48 run time. Each additional matrix-matrix multiplication adds roughly 8.2 milliseconds to the ADM run time, and the matrix inversion takes roughly 98 milliseconds, slightly less than one-third of the ADM-17 run time. We

evaluated changing m and v, as shown in Table 2.18. Once again, $v = 7$ achieves the lowest possible run time, which is still almost four times larger than the run time for CRAM-48.

m	v	Time [ms]	m	v	Time [ms]
17	0	244.053 ± 6.819	8	9	204.485 ± 1.116
16	1	234.120 ± 12.414	7	10	258.295 ± 2.988
15	2	212.482 ± 6.629	6	11	367.385 ± 0.949
14	3	198.908 ± 1.089	5	12	593.511 ± 3.287
13	4	188.696 ± 1.460	4	13	1044.161 ± 2.669
12	5	181.396 ± 2.622	3	14	1956.950 ± 58.433
11	6	176.521 ± 2.888	2	15	3704.073 ± 14.029
10	7	175.256 ± 2.989	1	16	7180.476 ± 138.903
9	8	182.397 ± 3.520	0	17	13952.969 ± 137.753

Table 2.18: 1599-nuclide 1.0-s test case run time comparisons for various m and v values for ADM-17 with a cutoff of 10^{-50}.

Again we considered longer time steps for the 1599-nuclide test case, with results for ADM-17 shown in Figure 2.10 and Table 2.19. For the 3,600 second time step, there are 1432 nuclides with number densities greater than 10^{-50} $\frac{\text{atoms}}{\text{b·cm}}$ and 1287 nuclides with number densities greater than 10^{-30} $\frac{\text{atoms}}{\text{b·cm}}$. For the 3.6×10^6 second time step, there are 1548 nuclides with number densities greater than 10^{-50} $\frac{\text{atoms}}{\text{b·cm}}$ and 1457 nuclides with number densities greater than 10^{-30} $\frac{\text{atoms}}{\text{b·cm}}$. As expected, we saw a deterioration in precision across the board except for a select few nuclides, which have results incredibly diverged from the CRAM-48 solution. The largest difference corresponds to neon-33, a very short-lived nuclide, which should be difficult to model. Additionally, for the 3.6×10^6 second case, the neon-33 number density calculated by ADM-17 is negative, the first and only negative number density calculated by ADM.

Depletion Interval [s]	MNARD	ANARD	NNND
3,600	0.00704	4.92×10^{-6}	0
3.6×10^6	3.53	0.00228	1

Table 2.19: 1599-nuclide 3,600 and 3.6×10^6 second test cases comparison of ADM-17 with a cutoff of 10^{-50} to the CRAM-48 solution for nuclides with number densities greater than 10^{-30} $\frac{\text{atoms}}{\text{b·cm}}$.

Since we observed an unacceptable divergence from CRAM-48 in the ADM-17 results, we raised the approximation power of ADM to 25 to see if convergence can be achieved as expected. Results are shown in Figure 2.11 and Table 2.20 and demonstrate the expected behavior as the maximum and average differences between ADM and CRAM decrease to acceptable levels with the increase in approximation power. This indicates that ADM-17 was not an adequate approximation power for the time step considered for the 1599-nuclide case.

Depletion Interval [s]	MNARD	ANARD
3,600	3.63×10^{-9}	1.31×10^{-9}
3.6×10^6	4.55×10^{-9}	5.14×10^{-10}

Table 2.20: 1599-nuclide 3,600 and 3.6×10^6 second comparison of ADM-25 with a cutoff of 10^{-50} to the CRAM-48 solution for nuclides with number densities greater than 10^{-30} $\frac{\text{atoms}}{\text{b·cm}}$.

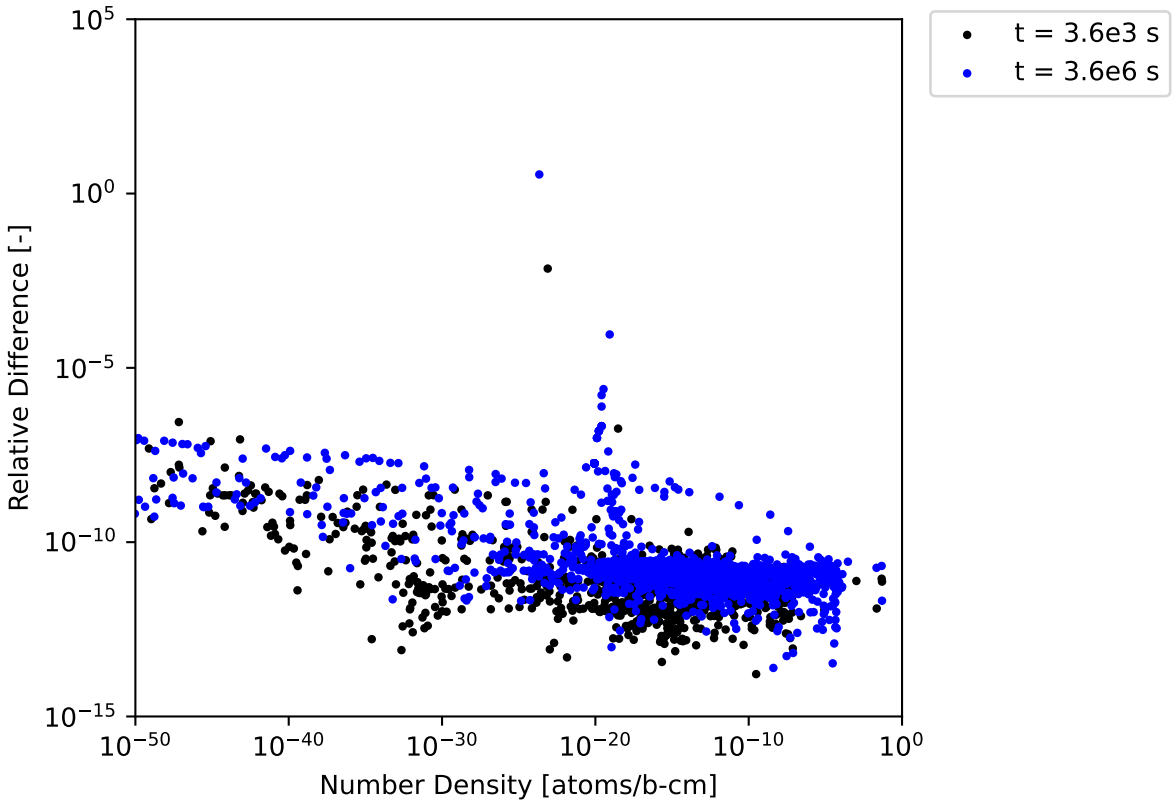

Figure 2.10: 1599-nuclide 3,600 and 3.6×10^{6} second test cases RDs computed for ADM-17 with a cutoff of 10^{-50} to the CRAM-48 solution.

2.6.4. 35-Nuclide Test Case

Since with an increasing number of nuclides the performance gap between ADM and CRAM increases, we considered a smaller test case for 35-nuclides taken from an OECD SFR benchmark report to see if ADM can outperform CRAM when the number of nuclides decreases.

2.6.4.1 Testing CRAM at Various Approximation Orders

We compared the various approximation orders of CRAM to the CRAM-48 solution for the 1 second depletion interval. Results are shown in Figure 2.12 and Table 2.21 with the results reflecting previously observed behavior.

2.6.4.2 ADM to CRAM comparison

Once again we compared various ADM approximation powers with a cutoff of 10^{-50} to the CRAM-48 solution for the 1 second depletion interval with the results shown in Figure 2.13 and Table 2.22. 30 nuclides had number densities above 10^{-50} $\frac{\text{atoms}}{\text{b·cm}}$, and 25 nuclides had number densities above 10^{-30} $\frac{\text{atoms}}{\text{b·cm}}$ as calculated by CRAM-48. Each additional matrix-matrix multiplication adds roughly 0.014 milliseconds to the ADM run time, and the matrix inversion takes roughly 0.047 milliseconds, about one-fifth of the ADM-16 run time.

A 10 digit agreement is achieved with ADM-16, and the run time of 0.263 milliseconds is less than the CRAM-48 run time of 0.317 milliseconds. However, CRAM-28 also achieves a 14 digit agreement with CRAM-48 and requires only 0.193 milliseconds, outperforming ADM-16. Next we considered varying m and v for ADM-16

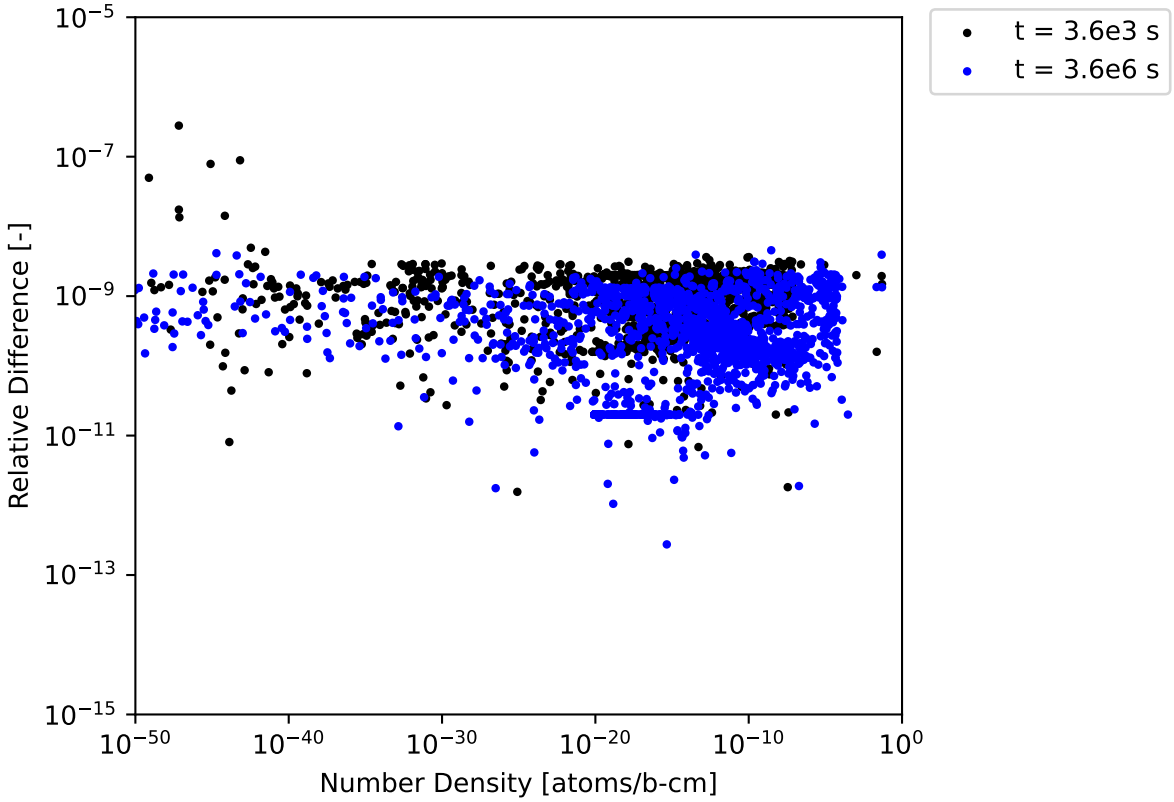

Figure 2.11: 1599-nuclide 3,600 and 3.6×10^6 second test cases RDs computed for ADM-25 with a cutoff of 10^{-50} to the CRAM-48 solution.

Order	Time [ms]	MNARD	ANARD	NNND
4	0.051 ± 0.006	5.19×10^{2}	2.49×10^{1}	9
8	0.076 ± 0.007	1.68×10^{1}	6.36×10^{-1}	2
12	0.106 ± 0.020	5.75×10^{-2}	1.99×10^{-3}	0
16	0.126 ± 0.012	8.56×10^{-5}	2.82×10^{-6}	0
20	0.154 ± 0.013	7.76×10^{-8}	2.48×10^{-9}	0
24	0.174 ± 0.012	6.20×10^{-5}	3.93×10^{-5}	0
28	0.193 ± 0.012	2.55×10^{-14}	2.14×10^{-15}	0
32	0.229 ± 0.014	9.48×10^{-15}	4.20×10^{-15}	0
36	0.248 ± 0.015	5.54×10^{-15}	1.11×10^{-15}	0
40	0.268 ± 0.022	4.36×10^{-15}	6.65×10^{-16}	0
44	0.301 ± 0.020	9.48×10^{-15}	2.01×10^{-15}	0
48	0.317 ± 0.018	-	-	0

Table 2.21: 35-nuclide 1.0-s test case comparison of various CRAM approximation orders to the CRAM-48 solution.

with the results shown in Table 2.23. Varying m and v results in an optimal value of $v = 5$ and reduces the run time of ADM-16 to 0.211 microseconds, still slightly more than CRAM-28.

Next we considered the comparison between ADM-16 with a cutoff of 10^{-50} to the CRAM-48 solution for the 3,600 and 3.6×10^6 second depletion intervals. For the 3,600 second depletion interval, CRAM-48 calculated that 30 nuclides had number densities greater than 10^{-30} $\frac{\text{atoms}}{\text{b·cm}}$ and 35-nuclides had number densities greater than

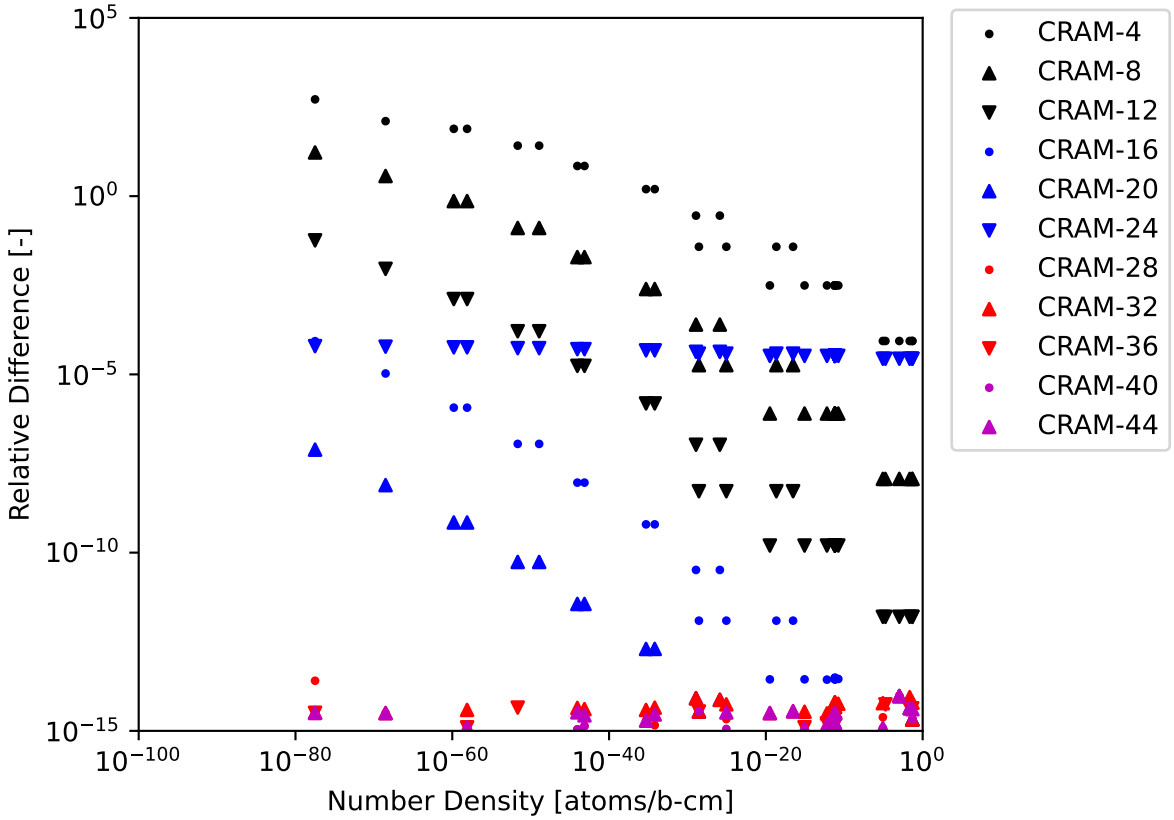

Figure 2.12: 35-nuclide 1.0-s test case RDs computed for various CRAM approximation orders relative to the CRAM-48.

Power	Time [ms]	MNARD	ANARD	Power	Time [ms]	MNARD	ANARD
1	0.061 ± 0.011	1.25×10^{-1}	1.00×10^{-2}	11	0.197 ± 0.015	1.19×10^{-7}	9.54×10^{-9}
2	0.078 ± 0.008	3.13×10^{-2}	2.50×10^{-3}	12	0.209 ± 0.013	2.98×10^{-8}	2.38×10^{-09}
3	0.087 ± 0.008	7.81×10^{-3}	6.25×10^{-4}	13	0.222 ± 0.017	7.45×10^{-9}	5.96×10^{-10}
4	0.106 ± 0.013	1.95×10^{-3}	1.56×10^{-4}	14	0.241 ± 0.020	1.86×10^{-9}	1.50×10^{-10}
5	0.118 ± 0.013	4.88×10^{-4}	3.91×10^{-5}	15	0.250 ± 0.015	4.65×10^{-10}	3.82×10^{-11}
6	0.129 ± 0.012	1.22×10^{-4}	9.77×10^{-6}	16	0.263 ± 0.018	1.19×10^{-10}	1.22×10^{-11}
7	0.140 ± 0.011	3.05×10^{-5}	2.44×10^{-6}	17	0.275 ± 0.014	3.27×10^{-11}	7.22×10^{-12}
8	0.155 ± 0.013	7.63×10^{-6}	6.10×10^{-7}	18	0.290 ± 0.021	2.00×10^{-11}	9.76×10^{-12}
9	0.167 ± 0.012	1.91×10^{-6}	1.53×10^{-7}	19	0.303 ± 0.019	4.86×10^{-11}	1.90×10^{-11}
10	0.187 ± 0.012	4.77×10^{-7}	3.81×10^{-8}	20	0.320 ± 0.023	8.70×10^{-11}	3.72×10^{-11}

Table 2.22: 35-nuclide 1.0-s test case comparisons for various approximation powers of ADM with a cutoff of 10^{-50} to the CRAM-48 solution for nuclides with number densities greater than 10^{-30} $\frac{\text{atoms}}{\text{b·cm}}$.

10^{-50} $\frac{\text{atoms}}{\text{b·cm}}$. For the 3.6×10^6 second depletion interval, CRAM-48 calculated that all 35-nuclides had number densities greater than 10^{-30} $\frac{\text{atoms}}{\text{b·cm}}$. The results are shown in Figure 2.14 and Table 2.24. Contrary to previous results, we see an expected degradation in precision for the 3,600 second depletion interval, but the degradation does not increase for the 3.6×10^6 second depletion interval with precision improving slightly compared to the 3,600 second depletion interval. This is attributed to the depletion matrix being significantly less stiff as the shortest-lived nuclide tracked is americium-242 with a decay constant of 1.2×10^{-5} s^{-1} and the neutron transmutation terms are smaller in magnitude since powerful neutron absorbers such as ^{135}Xe and ^{10}B are not tracked in the system. The less stiff the depletion matrix is the more precise ADM is expected to be for longer

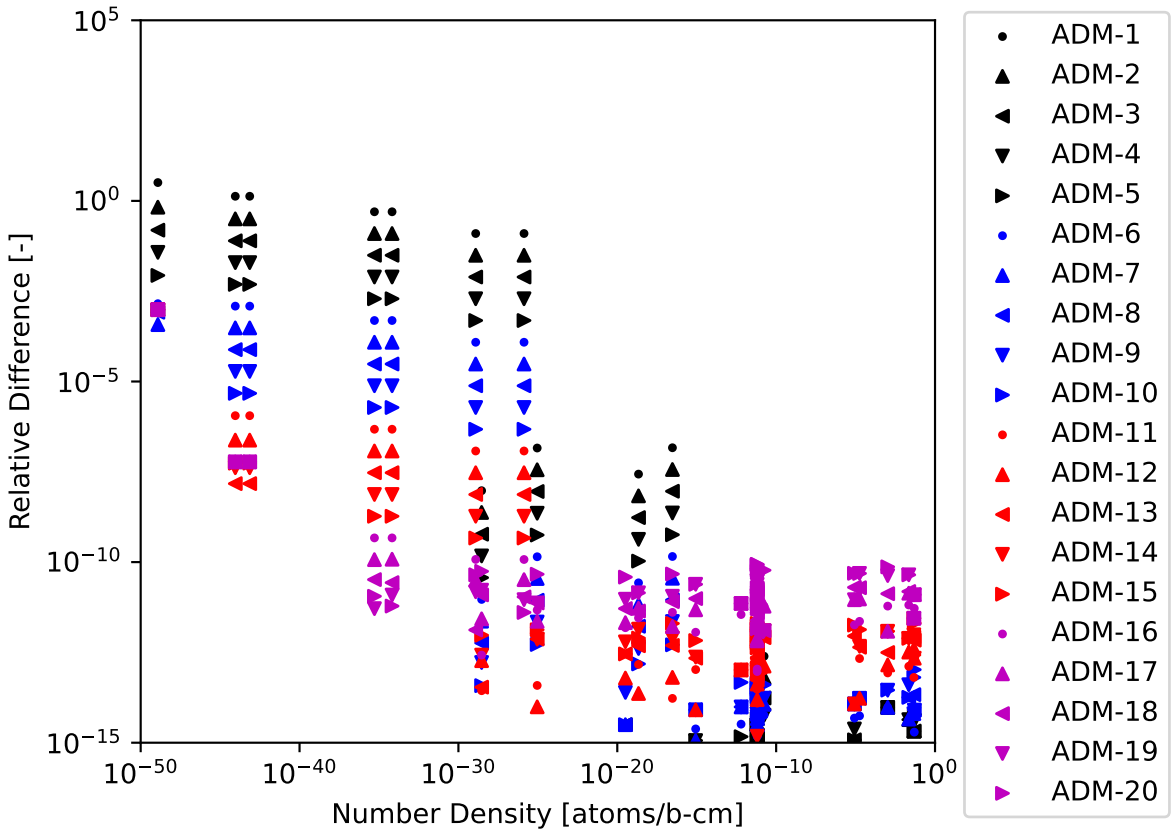

Figure 2.13: 35-nuclide 1.0-s test case RDs computed for various ADM approximation powers with a cutoff of 10^{-50} to the CRAM-48 solution.

m	v	Time [ms]	m	v	Time [ms]
16	0	0.263 ± 0.018	7	9	0.434 ± 0.032
15	1	0.272 ± 0.022	6	10	0.699 ± 0.034
14	2	0.245 ± 0.021	5	11	1.247 ± 0.058
13	3	0.234 ± 0.019	4	12	2.343 ± 0.076
12	4	0.223 ± 0.021	3	13	4.581 ± 0.150
11	5	0.211 ± 0.012	2	14	8.994 ± 0.306
10	6	0.218 ± 0.015	1	15	17.400 ± 0.312
9	7	0.240 ± 0.016	0	16	32.036 ± 0.489
8	8	0.298 ± 0.019	-	-	-

Table 2.23: 35-nuclide 1.0-s test case run time comparisons of various m and v values for ADM-16 with a cutoff of 10^{-50}.

depletion intervals. Consequently, the 3,600 and 3.6×10^6 second depletion interval results have a nearly identical level of precision.

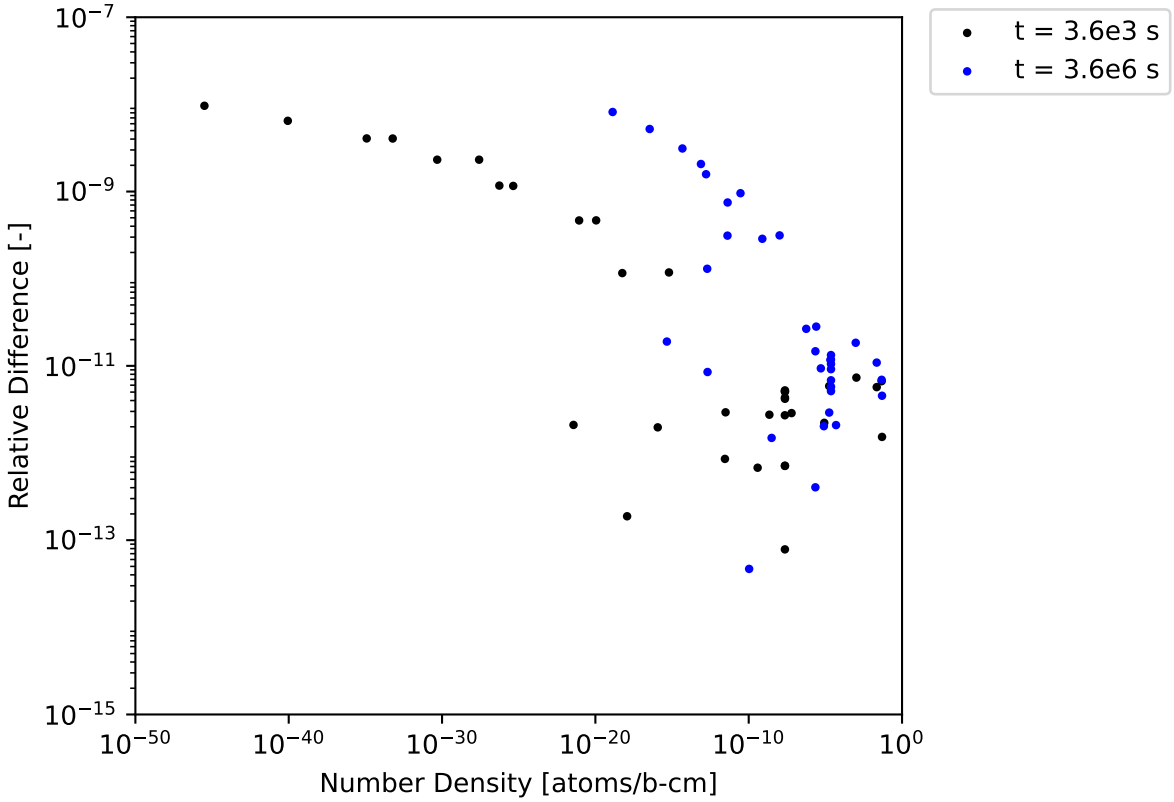

Figure 2.14: 35-nuclide 3,600 and 3.6×10^6 second test cases RDs computed for ADM-16 with a cutoff of 10^{-50} to the CRAM-48 solution.

Depletion Interval [s]	MNARD	ANARD
3,600	9.64×10^{-9}	9.27×10^{-10}
3.6×10^6	8.18×10^{-9}	6.62×10^{-10}

Table 2.24: 35-nuclide 3,600 and 3.6×10^6 second test case comparison of ADM-16 with a cutoff of 10^{-50} to the CRAM-48 solution for nuclides with number densities greater than 10^{-30} $\frac{\text{atoms}}{\text{b·cm}}$.

2.6.5. 693-Nuclide Test Case

For completeness, we lastly considered a 693-nuclide test case in order to better understand the increasing ADM and CRAM run times as the number of nuclides increases. The library is generated using the 1599-nuclide library and applying a decay constant cutoff of 10^{-4} s^{-1}, where nuclides with decay constants greater than this cutoff are removed from the library. Any instances where such a nuclide would be produced via transmutation or decay instead results in the production of the decay daughters of the removed nuclide.

2.6.5.1 Testing CRAM at Various Approximation Orders

We compared the various approximation orders of CRAM to the CRAM-48 solution, with the results shown in Figure 2.15 and Table 2.25. The behavior is expected based on the results of the previous test cases considered for the other libraries.

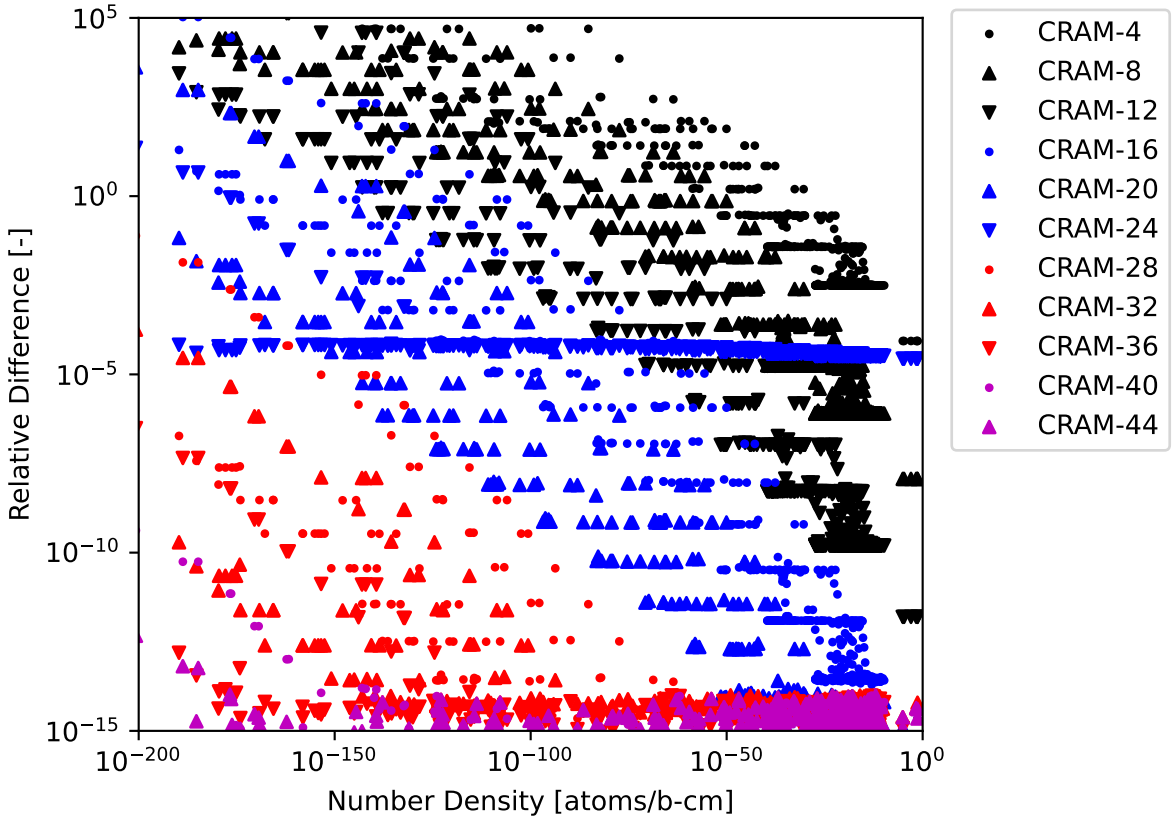

Figure 2.15: 693-nuclide 1.0-s test case RDs computed for various CRAM approximation orders to the CRAM-48 solution.

Order	Time [ms]	MNARD	ANARD	NNND
4	3.203 ± 0.154	1.14×10^{15}	3.27×10^{12}	122
8	5.048 ± 0.196	4.60×10^{10}	9.88×10^{7}	106
12	6.795 ± 0.280	8.06×10^{6}	2.94×10^{4}	75
16	8.702 ± 0.323	3.92×10^{5}	9.80×10^{2}	29
20	10.414 ± 0.324	4.100×10^{3}	9.47×10^{0}	13
24	12.360 ± 0.279	2.27×10^{1}	4.92×10^{-2}	3
28	13.956 ± 0.376	7.71×10^{-2}	1.60×10^{-4}	0
32	15.745 ± 0.310	1.80×10^{-4}	3.59×10^{-7}	0
36	17.429 ± 0.348	3.11×10^{-7}	6.00×10^{-10}	0
40	19.490 ± 0.444	4.19×10^{-10}	7.89×10^{-13}	0
44	20.636 ± 0.329	4.66×10^{-13}	2.06×10^{-15}	0
48	21.151 ± 0.269	-	-	0

Table 2.25: 693-nuclide 1.0-s test case comparison of various CRAM approximation orders to the CRAM-48 solution.

2.6.5.2 ADM to CRAM comparison

We observed that ADM-16 achieves 10 digits of agreement with CRAM-48 with a run time that is roughly three times greater. See Figure 2.16 and Table 2.26. Each additional matrix-matrix multiplication adds roughly 2.2 milliseconds to the ADM run time and the matrix inversion takes roughly 23 milliseconds, about one-third of

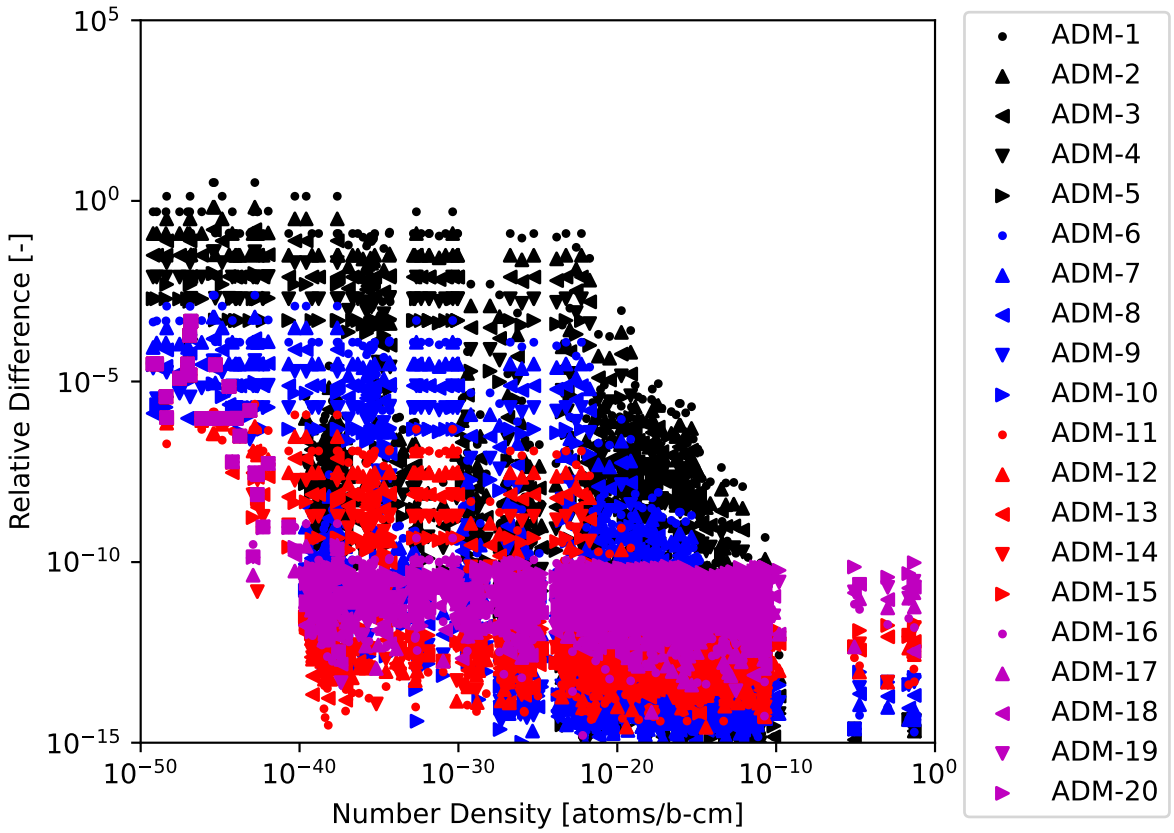

Figure 2.16: 693-nuclide 1.0-s test case RDs computed for various ADM approximation powers with cutoff of 10^{-50} to the CRAM-48 solution.

Power	Time [ms]	MNARD	ANARD	Power	Time [ms]	MNARD	ANARD
1	24.981 ± 1.129	1.25×10^{-1}	1.94×10^{-3}	11	50.984 ± 1.917	1.19×10^{-7}	1.85×10^{-9}
2	27.879 ± 1.182	3.13×10^{-2}	4.86×10^{-4}	12	52.586 ± 1.563	2.98×10^{-8}	4.63×10^{-10}
3	30.591 ± 1.325	7.81×10^{-3}	1.21×10^{-4}	13	56.029 ± 2.324	7.45×10^{-9}	1.16×10^{-10}
4	33.356 ± 1.729	1.95×10^{-3}	3.03×10^{-5}	14	56.882 ± 1.786	1.86×10^{-9}	2.94×10^{-11}
5	37.009 ± 2.186	4.88×10^{-4}	7.59×10^{-6}	15	58.338 ± 1.297	4.66×10^{-10}	8.15×10^{-12}
6	39.350 ± 2.037	1.22×10^{-4}	1.90×10^{-6}	16	60.555 ± 1.836	1.17×10^{-10}	3.82×10^{-12}
7	41.469 ± 1.609	3.05×10^{-5}	4.74×10^{-7}	17	62.926 ± 2.174	3.08×10^{-11}	4.06×10^{-12}
8	44.338 ± 2.290	7.63×10^{-6}	1.19×10^{-7}	18	64.077 ± 1.540	2.42×10^{-11}	8.01×10^{-12}
9	45.645 ± 1.003	1.91×10^{-6}	2.96×10^{-8}	19	66.941 ± 2.232	3.83×10^{-11}	1.51×10^{-11}
10	49.492 ± 2.171	4.77×10^{-7}	7.41×10^{-9}	20	67.366 ± 1.362	9.61×10^{-11}	3.32×10^{-11}

Table 2.26: 693-nuclide 1.0-s test case comparison of various approximation powers of ADM with a cutoff of 10^{-50} to the CRAM-48 solution for nuclides with number densities greater than 10^{-30} $\frac{\text{atoms}}{\text{b·cm}}$.

the ADM-16 run time. Varying v results in the optimal decrease in run time occurring at $v = 6$ with a run time roughly double the CRAM-48 solution as shown in Table 2.27.

Again we considered the comparison between ADM-16 with a cutoff of 10^{-50} to the CRAM-48 solution for the 3,600 and 3.6×10^6 second depletion intervals. For the 3,600 second depletion interval, CRAM-48 calculated that 475 nuclides had number densities greater than 10^{-30} $\frac{\text{atoms}}{\text{b·cm}}$ and 565 nuclides had number densities greater than 10^{-50} $\frac{\text{atoms}}{\text{b·cm}}$. For the 3.6×10^6 second depletion interval, CRAM-48 calculated that 590 nuclides had number densities greater than 10^{-30} $\frac{\text{atoms}}{\text{b·cm}}$ and 652 nuclide had number densities greater than 10^{-50} $\frac{\text{atoms}}{\text{b·cm}}$. The results are

m	v	Time [ms]	m	v	Time [ms]
16	0	60.555 ± 1.836	7	9	57.013 ± 0.923
15	1	56.369 ± 1.110	6	10	76.021 ± 0.762
14	2	53.203 ± 0.732	5	11	115.709 ± 1.302
13	3	50.530 ± 0.831	4	12	196.419 ± 1.969
12	4	48.084 ± 0.691	3	13	355.936 ± 3.382
11	5	46.024 ± 0.650	2	14	674.263 ± 2.653
10	6	45.036 ± 0.585	1	15	1312.431 ± 3.271
9	7	45.171 ± 0.808	0	16	2521.742 ± 6.839
8	8	48.311 ± 0.734	-	-	-

Table 2.27: 693-nuclide 1.0-s test case run time comparisons for various m and v values for ADM-16 with a cutoff of 10^{-50}.

shown in Figure 2.17 and Table 2.28 and once again demonstrate the loss of precision for ADM with an increasing time step length.

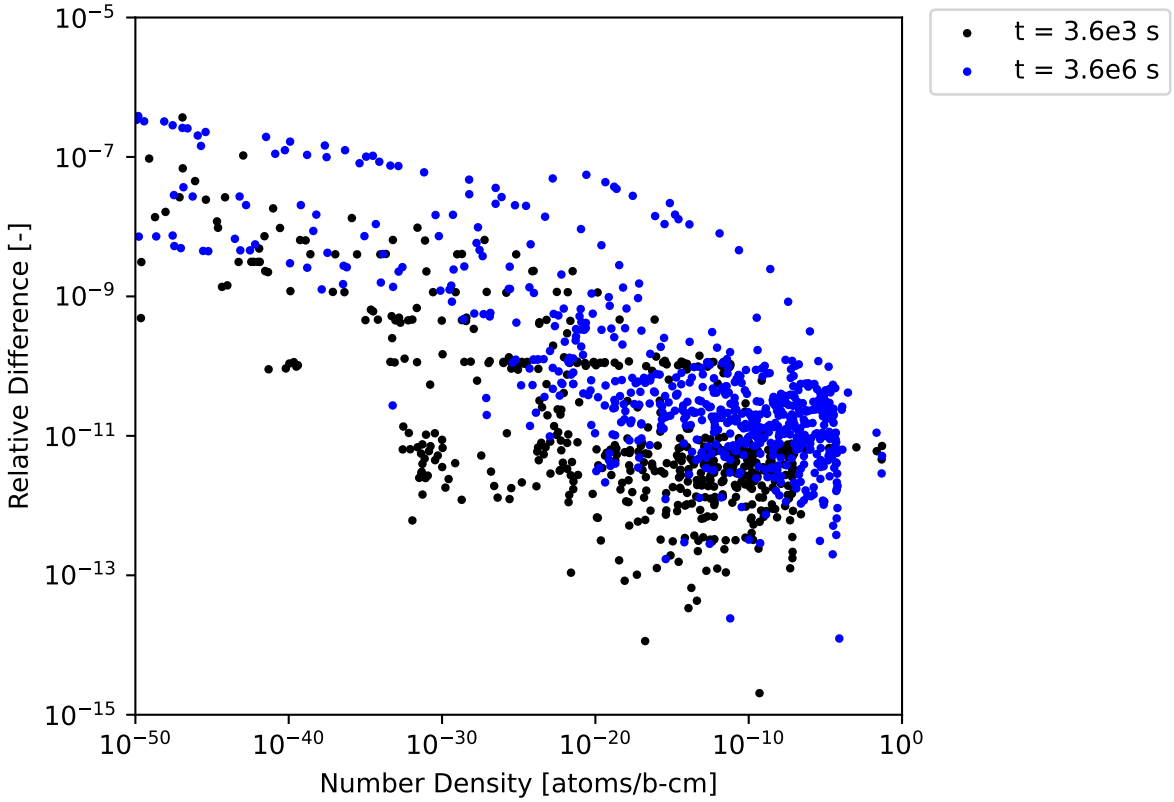

Figure 2.17: 693-nuclide 3,600 and 3.6×10^6 second test cases RDs computed for ADM-16 with a cutoff of 10^{-50} to the CRAM-48 solution.

Depletion Interval [s]	MNARD	ANARD
3,600	6.45×10^{-9}	9.71×10^{-11}
3.6×10^6	5.55×10^{-8}	1.15×10^{-9}

Table 2.28: 693-nuclide 3,600 and 3.6×10^6 second test cases comparison of ADM-16 with a cutoff of 10^{-50} to the CRAM-48 solution for nuclides with number densities greater than 10^{-30} $\frac{\text{atoms}}{\text{b·cm}}$.

2.6.6. Time-Independent Depletion Matrix with Fixed Depletion Step Size

So far we have considered solving the Bateman equations under the assumption that $\mathbf{A}$ or t may change from one depletion interval to the next, as shown for two hypothetical depletion intervals with lengths of t_1 and t_2.

$$\begin{aligned} \mathbf{A}(t_1) &\neq \mathbf{A}(t_2) \\ t_1 &\neq t_2 \end{aligned} \tag{2.27}$$

For most reactor analysis applications, this is necessary as, after each depletion interval, the change in nuclide number densities will result in the macroscopic cross sections of the materials in the reactor changing, which will consequently result in the flux profile of the reactor changing. If effects such as temperature are also being considered, the microscopic cross sections themselves will change because of Doppler broadening. All of these effects combined result in the depletion matrix $\mathbf{A}$ being time dependent for most analyses, as shown.

$$\begin{aligned} \mathbf{A}(t) &= \mathbf{D} + \mathbf{T}(t) \\ \mathbf{T}(t) &= \sum_{g=0}^{G} \Big(\sum_{r=0}^{R} \sigma_{g,r}(t) \Big) \phi_g(t) \end{aligned} \tag{2.28}$$

where

t	the length of the time step depletion is occurring over
$\mathbf{A}(t)$	the time-dependent depletion matrix
$\mathbf{D}$	the time-independent decay matrix
$\mathbf{T}(t)$	the time-dependent neutron transmutation matrix
G	the number of neutron energy groups
R	the number of neutron transmutation reactions
$\sigma_{g,r}(t)$	the time-dependent microscopic cross-section matrix for energy group g and neutron transmutation reaction r
$\phi_g(t)$	the time-dependent neutron flux for energy group g.

However, there are some applications where $\mathbf{A}$ may not change with time, two examples being a sample irradiated at a constant flux by a neutron generator with the sample undergoing no appreciable temperature change, which eliminates the time dependence of both ϕ and σ, or a pure decay analysis where the flux in the system is zero, meaning that $\mathbf{T}(t) = \mathbf{0}$ and $\mathbf{A} = \mathbf{D}$. If $\mathbf{A}t$ is constant for all depletion intervals considered for a given system, the response matrix for ADM, which is calculated using Eq. 2.14, only needs to be calculated once. Once the response matrix $\mathbf{P}_j(\mathbf{A}h(t,j))$, as defined in Eq. 2.18, is calculated for the depletion interval with length t, the number densities at the next depletion interval can be calculated via matrix-vector multiplications as shown provided that the next depletion interval has the same length t as the previous depletion interval.

$$\begin{aligned}
\mathbf{N}(t) &= \mathbf{P}_j(\mathbf{A}h(t,j))\mathbf{N}_0 \\
\mathbf{N}(2t) &= \mathbf{P}_j(\mathbf{A}h(t,j))\mathbf{N}(t) \\
\mathbf{N}(3t) &= \mathbf{P}_j(\mathbf{A}h(t,j))\mathbf{N}(2t) \\
\mathbf{N}(xt) &= \mathbf{P}_j(\mathbf{A}h(t,j))\mathbf{N}((x-1)t)
\end{aligned} \tag{2.29}$$

where

$\mathbf{P}_j(\mathbf{A}h(t,j))$	the final response matrix of ADM-j as defined by Eq. 2.18
$\mathbf{A}$	the time-independent depletion matrix
$h(t,j)$	the length of the time discretization defined as $h = \frac{t}{2^j}$
t	the fixed length in time of the depletion interval considered
$\mathbf{N}_0$	the initial nuclide number densities
x	the positive non-zero integer indicating the number of depletion intervals of length t which have been calculated
$\mathbf{N}(xt)$	the nuclide number densities at a point in time equal to xt.

For a large system with many depletion regions, such as a full-core decay heat calculation, the response matrix calculation time (which is less than 1 second for all systems we have considered) becomes negligible when compared to the potentially millions of Bateman equation solves that would be required. Thus we ignored the run time of the initial response matrix evaluation of $\mathbf{P}_j(\mathbf{A}h(t,j))$ and instead only considered the portion of ADM that will scale with an increasing number of regions and time steps.

We perform one final time comparison where we considered caching the response matrix $\mathbf{P}_j(\mathbf{A}h(t,j))$ of ADM and determined the run time for performing a single Bateman equation solve using the cached matrix. CRAM does not offer much in the way of caching potential since SGE involves matrix-vector operations that are dependent on the number densities at the given point in time, which are constantly updated after each depletion interval and will be unique to each reactor core region. The sparsity pattern for CRAM can be cached, and this does result in a small reduction in the run time of CRAM-48 for systems where $\mathbf{A}t$ is constant. We compare the time for performing the "cached Bateman solve" for ADM and CRAM for a depletion interval of 1 second and a total of 100 intervals occurring, which is identical to the parameters of the previous run time analyses.

Nuclides	ADM Power	ADM Time [ms]	CRAM-48 Time [ms]	ADM:CRAM-48 Ratio [-]
35	16	$7.24 \times 10^{-4} \pm 6.3 \times 10^{-5}$	0.292200 ± 0.019927	0.0025
297	16	0.017187 ± 0.003966	7.613530 ± 0.285358	0.0023
693	16	0.056262 ± 0.006114	20.326711 ± 0.498023	0.0028
1450	17	0.149685 ± 0.012129	39.862447 ± 0.661700	0.0038
1599	17	0.154266 ± 0.010152	40.856141 ± 0.659615	0.0038

Table 2.29: Run times of ADM at various approximation powers with a cutoff of 10^{-50} and CRAM-48 for all nuclide test cases assuming constant and cached $\mathbf{A}t$.

As shown in Table 2.29, ADM dramatically outperforms CRAM-48 for all systems we considered, with CRAM-48 taking over 250 times as long as ADM. We can conclude that, for systems where $\mathbf{A}t$ can be kept constant for each depletion interval, such as decay or sample neutron irradiation, ADM will outperform CRAM

in terms of run time. In terms of accuracy of results, since all prior test cases were evaluated using a constant $\mathbf{A}t$ system, just with the response matrix recalculated at each time step, the results produced here are identical to the ones produced for previous sections and are thus not repeated here.

Another thing to note when caching the response matrix is that $\mathbf{P}_j(\mathbf{A}h(t,j))$ has a dependency on both $\mathbf{A}$ and t, meaning both must be kept constant in order for caching to be valid, meaning each depletion interval must be of the same length t. This could be inconvenient, as an example, to perform a decay heat calculation every hour for a single day (24 depletion intervals) and then switch to performing a calculation for a single day for the remainder of the month (30 depletion intervals). CRAM would be able to solve this system in 54 solves. ADM with a cached response matrix would be forced to either solve 1 hour depletion intervals for the entire month (744 solves total) or the response matrix would need to be recalculated after the first 24 depletion intervals, reducing the performance advantage over CRAM because of the need to recalculate the response matrix $\mathbf{P}_j(\mathbf{A}h(t,j))$. However, it should be noted that, since cached ADM is over 250 times faster than CRAM-48 for all systems considered, needing to perform 30 times as many depletion solves would still result in ADM outperforming CRAM-48 in terms of run time.

2.7. Conclusion

We concluded that ADM, when coupled with the CNFD method, is an alternative method for solving the Bateman depletion equations with the ability to achieve a ten-digit agreement with CRAM-48 for all systems tested for nuclides with number densities greater than 10^{-30} $\frac{\text{atoms}}{\text{b·cm}}$ with a depletion interval of 1 second. As the length of the depletion interval increases, it necessitates an increase in the approximation power of ADM in order to maintain the desired precision, with the understanding that, as the approximation power of ADM increases, there is a compounding of numerical error introduced from double-precision arithmetic. We also conclude that ADM maintains a comparable performance to CRAM-48 for systems with 35 and 297-nuclides, with performance deteriorating as the number of nuclides and the size of the depletion matrix increases.

To reiterate, the best achieved run time ADM was able to obtain relative to CRAM-48 for each test case is shown in Table 2.30. We note that, because of the use of the dense matrix LAPACK routines [40] for the matrix inversion, an optimized sparse matrix inversion routine could reduce the ADM run time to make it more competitive with CRAM. However, for all cases considered, the matrix inversion takes at most one-third of the run time meaning that, even if the cost of the matrix inversion could be reduced to zero (which is not possible) ADM would still perform worse than CRAM for systems with more than 297-nuclides.

Nuclides	Power	m	v	ADM Time [ms]	CRAM-48 Time [ms]	ADM:CRAM-48
35	16	11	5	0.211 ± 0.012	0.317 ± 0.018	0.67
297	16	10	6	11.405 ± 0.389	8.499 ± 0.162	1.34
693	16	10	6	45.036 ± 0.585	21.151 ± 0.269	2.13
1450	17	10	7	156.375 ± 1.264	44.983 ± 0.630	3.48
1599	17	10	7	175.256 ± 2.989	46.326 ± 0.759	3.78

Table 2.30: Comparison of the run times of best performing versions of ADM with a cutoff of 10^{-50} to CRAM-48.

The benefits of ADM are its simplicity and ease of implementation and maintenance. ADM does not require support for complex number operations and does not require the use of pre-generated approximation coefficients. The final implementation of ADM required an additional 80 lines of code while the final version of CRAM-IPF-SGE required an additional 200 lines of code, ignoring the lines of code needed for the CRAM coefficient values, which add another 800 lines. It is for these reasons we recommend the implementation of ADM as, at a minimum,

a secondary method so that results produced by CRAM can be double-checked. As demonstrated in this work, CRAM can sometimes produce negative number densities at lower approximation orders, whereas ADM only does so in specific circumstances for very short-lived nuclides.

In terms of recommended approximation power of ADM to use, we recommend using an approximation power of 16 with the last five matrix-matrix and last matrix-vector multiplications substituted with 32 matrix-vector multiplications. Using the notation used previously in this paper, this would correspond to values of $j = 16$, $m = 11$, and $v = 5$. This should yield a run time improvement regardless of the size of the matrix, except for perhaps very small (2-by-2 and 3-by-3) matrices; however, the run times for such small systems would be negligible and not particularly practical for modeling any real-world nuclear system. ADM should also be implemented with the ability to vary the approximation power, while the ability to vary m and v is an optional implementation decision.

Lastly, ADM dramatically outperformed CRAM-48 in terms of run time for depletion systems where both $\mathbf{A}$ and t are constant at every depletion interval. While such systems are not particularly common, the dramatic performance improvement of ADM over CRAM for these systems merits acknowledgement.

2.8. Future Work

In terms of future work, there are several points of mathematical interest to be explored, namely a new set of comparisons of ADM and CRAM where the CRAM coefficients are calculated to quadruple-precision accuracy and all arithmetic is performed in quadruple-precision. However, such work would be more for the sake of intellectual curiosity rather than for practical modeling efforts, as the uncertainty associated with most forms of nuclear data renders the pursuit of quadruple-precision number densities unnecessary. Of greater interest would be the application of other methods used to solve the matrix exponential, many of which are outlined in Ref. [27], while exploiting properties of the depletion matrix, such as the ability to apply a numerical cutoff or the specific sparsity pattern the depletion matrix usually possesses.

Chapter 3: Evaluating Quantities of Interest Other than Nuclide Densities in the Bateman Equations

Olin W. Calvin, Micah D. Gale, and Sebastian Schunert, 2023. Evaluating Quantities of Interest Other Than Nuclide Densities in the Bateman Equations. Nuclear Science and Engineering. doi:10.1080/00295639.2022.2161802.

3.1. Abstract

Traditionally, analysts solve the Bateman depletion equations to calculate the NND of each nuclide since these densities impact other reactor parameters, such as reactivity, as they change. Many quantities of interest, such as radiation damage, are calculated using simple integration methods, assuming that the NNDs are constant over a given depletion interval. However, the NNDs are time-dependent, which can only be accurately represented by the Bateman depletion equations. We propose that these quantities can be calculated simultaneously with the NNDs within the Bateman depletion equations, preserving the coupled nature of these quantities to the time-dependent NNDs. We implemented this functionality in Griffin, demonstrating that only minor code modifications were necessary in order to accommodate an evaluation of these quantities in the Bateman depletion equations. The Chebyshev rational approximation method was used to successfully solve for these additional quantities in the Bateman depletion equations. For radiation damage, the results calculated by Griffin were very accurate, differing by less than 2.5% from an analytical benchmark. For other quantities, the discrepancy between quantities calculated by the Bateman depletion equations versus those calculated by the FE method exceeded 10% for decay energy and 2% for fissions per initial heavy metal atom and kinetic energy released per unit mass when few depletion intervals were used. As the number of depletion intervals increased, both methods began to converge as expected.

3.2. Introduction

The Bateman equations mathematically describe the NNDs in a given system as radioactive decay events occur, resulting in the production of the decay products of the nuclides originally present in the system [25]. The Bateman equations originally only accounted for radioactive decay since they were developed before the discovery of the neutron. However, it is simple to extend the Bateman equations to account for neutron transmutation, as shown in Eq. 3.1 adapted from Ref. [26].

$$\begin{aligned}\frac{dN_i(t)}{dt} = &\int_0^\infty \sum_j \gamma_{j\to i}(E)\sigma_{f,j}(E)N_j(t)\phi(E,t)dE \\ &+ \int_0^\infty \sum_k \Big(\sum_r \sigma_{r,k\to i}(E)N_k(t)\phi(E,t)\Big)dE \\ &+ \sum_l \lambda_{l\to i}N_l(t) - \int_0^\infty \sigma_{a,i}(E)N_i(t)\phi(E,t)dE - \lambda_i N_i(t)\end{aligned} \tag{3.1}$$

where

E	neutron kinetic energy
t	time

$\frac{dN_i(t)}{dt}$	time-dependent rate of change in the NND of nuclide i
$N_i(t)$	time-dependent NND of nuclide i
$\gamma_{j\rightarrow i}(E)$	energy-dependent probability that nuclide i will be produced as a fission product from the neutron-induced nuclear fission of nuclide j
$\sigma_{f,j}(E)$	energy-dependent microscopic fission cross section of nuclide j
$\phi(E,t)$	energy-dependent and time-dependent neutron flux within the system
$\sigma_{r,k\rightarrow i}(E)$	energy-dependent microscopic non-scattering, non-fission reaction cross section of reaction type r of nuclide k, which produces nuclide i
$\lambda_{l\rightarrow i}$	decay constant of nuclide l, which produces nuclide i
$\sigma_{a,i}(E)$	energy-dependent microscopic absorption (non-scattering) cross section of nuclide i
λ_i	decay constant of nuclide i.

Because of the large number of fission products produced in nuclear fission reactors, the number of nuclides to track using the Bateman equations can be on the order of hundreds or thousands. For such large numbers of nuclides, it becomes convenient to use matrix-vector notation.

$$\frac{d\mathbf{N}(t)}{dt} = \mathbf{A}(t)\mathbf{N}(t) \tag{3.2}$$

where

$\mathbf{N}(t)$	time-dependent vector of all NNDs in the system
$\frac{d\mathbf{N}(t)}{dt}$	time-dependent rate of change of the NNDs in the system
$\mathbf{A}(t)$	time-dependent matrix of the terms from Eq. 3.1 for each nuclide in the system also known as the "depletion matrix."

Eq. 3.2 enables the NNDs to be calculated at any point in time by solving the matrix exponential given the initial NNDs of $\mathbf{N}_0$. Typically, it is assumed that the depletion matrix $\mathbf{A}$ is constant for the length t of the depletion interval leading to

$$\mathbf{N}(t) = e^{\mathbf{A}t}\mathbf{N}_0 \tag{3.3}$$

The matrix exponential is formally defined as a power series

$$e^{\mathbf{A}t} = \sum_{i=0}^{\infty} \frac{(\mathbf{A}t)^i}{i!} \tag{3.4}$$

While it is appealing to solve the power series directly, the potential stiffness of the depletion matrix can prevent the power series solution from converging when working within double precision. This stiffness is driven by the orders of magnitude difference in the decay constants of various radionuclides, which can vary by over 40 orders of magnitude. Consequently, the CRAM was developed in order to efficiently and accurately solve the

matrix exponential [28] for nuclear reactor systems and is the method we used to solve the Bateman equations for all problems considered in this work.

While the Bateman equations can be used to accurately calculate the NNDs at any point in time, other quantities of interest are dependent upon the NNDs. However, these quantities are not evaluated as part of the Bateman equations in traditional analyses. Instead, these analyses rely on the assumption that the NNDs remain constant during a given depletion interval, an assumption that may not be appropriate depending on the system.

This work builds off of the work previously done analyzing the accumulation of radiation damage in the Bateman equations [43]. In this work we reiterate and expand on our work regarding the modeling of radiation damage in the Bateman equations and explore calculating the non-nuclide quantities of FIMA and KERMA in the Bateman equations.

3.2.1. Radiation Damage

Modeling displacement radiation damage, measured in DPA, has been of interest to the nuclear material science community for nearly 70 years [44]. Exothermic nuclear reactions and high-energy scattering reactions transfer enough energy to atoms in the crystal lattice of a material to displace some of these atoms from their lattice sites. This phenomenon is referred to as "displacement radiation damage" or simply "radiation damage." Radiation damage provides a better metric for developing material performance correlations for irradiated materials than fluence-based metrics because of the varying atomic displacement of different materials exposed to the same fluence [44].

At high neutron energies, a neutron scattering event transfers sufficient energy to cause these displacements, but a neutron at low energies cannot transfer enough energy to cause a displacement via scattering because of the kinematics of the reaction. At these low energies, all displacements are driven by exothermic capture reactions. In many of these reactions, the target nucleus will recoil with enough energy to cause displacements as well as produce a secondary particle with sufficient mass and energy to cause displacements. The minimum energy required to remove an atom from its lattice site in this way is referred to as the average threshold displacement energy (E_D). This value is generally on the order of 40 eV but can vary significantly between different elements (e.g., 17 eV for rubidium to 90 eV for tungsten [45]) and be a source of controversy because of conflicting models and experimental data, particularly for polyatomic materials [46]. Intuitively, this value is the property of a specific crystal lattice and crystal phase. Since measuring the difference between two crystal phases, say ferritic and martensitic steels, is beyond the current state-of-the-art technology, displacement energies are calculated on an elemental level. The first recoiling atom is referred to as the primary knock-on atom (PKA), and generally has kinetic energy between 1 and 100 keV in fission reactor applications for non-fuel materials. Reactor fuel materials, which experience the production of high-energy fission product nuclei with tens of MeV of kinetic energy, as well as materials used outside of fission reactors may experience PKAs with larger energies, but we are only concerned with non-fuel reactor materials in this work

All nuclides are capable of producing radiation damage. However, most analyses only consider the damage contribution from naturally occurring nuclides present at the beginning of irradiation, recent examples of this being found in Refs. [47] and [48]. There can be problematic transmutation products produced during irradiation which have a high probability of undergoing exothermic capture reactions which produce high-energy recoil nuclei that can cause significant amounts of radiation damage. One of the best examples of this is ^{59}Ni, which has a relatively high probability of undergoing an (n,α) reaction when irradiated by thermal neutrons. This reaction results in the production of a relatively high-energy iron-56 recoil nucleus with 340 keV of kinetic energy. Greenwood discussed how, in a mixed-spectrum reactor such as the High Flux Isotope Reactor (HFIR), this can

double the number of displacements in nickel and increase displacements by 13% in 316 stainless steel compared to displacement calculations performed without accounting for the ^{59}Ni(n,α) ^{56}Fe reaction [1]. A high-energy alpha particle (^{4}He nucleus) is also produced which does contribute to radiation damage, but because of the mass difference between ^{4}He and the nuclei of the bulk material, combined with losses from electronic interactions, the alpha particle produces significantly less damage than the iron-56 nucleus despite the alpha particle's much higher kinetic energy because the mass of the iron-56 nuclei is much closer to the mass of the nuclei of the bulk material which allows for more efficient energy transfer.

A correction factor accounting for the radiation damage produced by ^{59}Ni under thermal neutron irradiation was produced by Greenwood [1]. However, in reality this correction factor is seldom used by the analyst for reasons explained in Section 3.3.3. This paper proposes a way for transport codes to automatically calculate the radiation damage from all nuclides over all time steps. This can ensure that the analyst using these codes can calculate accurate results without being an expert in the minutia of radiation damage.

3.2.2. Additional Quantities of Interest

In addition to radiation damage, there are several other non-NND quantities of interest to analysts. Two we will consider are FIMA and KERMA. FIMA is a means of expressing the burnup level of nuclear fuel, with several metrics of fuel performance being dependent on its burnup. KERMA is also of interest when calculating burnup, in units such as megawatt-days per initial heavy metal kilogram ($\frac{\text{MWd}}{\text{kg}_{\text{HM}}}$), and is of interest in general since the total KERMA in a given reactor system should always equal the rated power the reactor system is operating at times the length of reactor operation (assuming no loss of heat to the surroundings). As is tradition, when we refer to KERMA we are referring to total *recoverable* kinetic energy released in the reactor, which excludes all energy released in the form of neutrinos.

3.3. Background

3.3.1. Radiation Damage Modeling in Monoatomic Materials

The computation of radiation damage in practical applications uses the damage-energy cross section, σ_D [eV-b], allowing the total damage-energy rate density, $\hat{e}$, defined as the amount of damage energy deposited per unit volume and time, to be computed by:

$$\hat{e}(t) = \int_0^\infty N(t)\sigma_D(E)\phi(E,t)dE, \tag{3.5}$$

where

$N(t)$	time-dependent number density of the monoatomic material
E	neutron kinetic energy
t	time
$\phi(E,t)$	energy- and time-dependent scalar neutron flux

Eq. 3.5 looks identical to the neutron transmutation terms in Eq. 3.1, allowing for an easy deployment in production code Bateman solvers. The displacement radiation damage, *RD*, measured in DPA can be computed as shown, adapted from Ref. [49]:

$$
\begin{aligned}
RD(t) &= \frac{0.8\hat{E}(t)}{2E_d N} \\
\hat{E}(t) &= \int_0^t \hat{e}(\tau) d\tau
\end{aligned}
\tag{3.6}
$$

where

$RD(t)$	time-dependent radiation damage in dpa
$\hat{E}(t)$	time-dependent damage-energy density in the material
E_d	threshold displacement energy of the material
N	number density of the material.

For reactor physics codes, the damage-energy cross sections are data that needs to be computed by a cross-section processor. One such code, the HEATR module of NJOY [50], computes damage-energy cross sections using the following expression:

$$
\sigma_D(E) = \sum_{r=1}^{R} \sigma_r(E) F_r(Z, A, E), \tag{3.7}
$$

where

r	index of a given reaction type (e.g. elastic scattering, inelastic scattering)
$\sigma_r(E)$	energy-dependent microscopic cross section of the nuclide which the monoatomic material is composed of
$F_r(Z, A, E)$	mean energy deposited as damage from reaction r by a neutron with kinetic energy E
Z	atomic number of the monoatomic material
A	mass number of the monoatomic material

The details of computing $\sigma_D(E)$ are described in the user manual for NJOY16 [51] which is publicly available on GitHub and will not be repeated here (note that the latest version of NJOY is NJOY21 [50]). However, it is worthwhile to consider the difference between computing standard neutron cross sections and damage-energy cross sections. Two additional pieces of information are required for the model: first, the amount of energy transferred to the nuclide and reaction products, and second, the fraction of energy deposited as damage energy for the given reaction products and recoil energies. The former information is obtained by considering the kinematics of the nuclear reaction and is generally provided in the evaluated nuclear data. The latter quantity is called the radiation damage efficiency or partition function and is computed using the Norgett, Robinson, and Torrens model [49]. This model is a numerical approximation to the statistical mechanics solutions to the theory first outlined by Kinchin-Pease [44] and built upon by others over the decades [52, 53]. The most significant difference

between the Norgett, Robinson, and Torrens model and the Kinchin-Pease model is that the former accounts for the dissipation of energy by electronic excitation.

Radiation damage does not only originate from neutron irradiation, even though that is generally the primary source. Radioactive decay can contribute to radiation damage if enough energy is transferred to the PKA to exceed the threshold displacement energy. Some radioactive decay reactions fit this criterion, with alpha emission being the most common example. It is not uncommon for alpha decays to create decay products with energies of multiple MeV. These alpha particles and recoil nuclei will cause radiation damage in exactly the same way alpha particles and recoil nuclei from (n,α) reactions would. This (n,α) reaction is explored in the Greenwood benchmark later on in Section 3.3.3. This decay radiation damage is calculated by:

$$\hat{e} = \sum_{i=1}^{I} \lambda_i \eta_i N_i, \tag{3.8}$$

where

λ_i	radioactive decay constant of nuclide i
η	decay radiation damage factor, or the average damage energy released by a single decay of nuclide i
N_i	NND of nuclide i.

There are currently no industry-accepted methods for calculating the decay radiation damage factor. In current practice, this contribution is entirely ignored (i.e., $\eta = 0$). The decay damage contribution is discussed here for completeness and will be integrated with new decay radiation damage models as they are developed.

3.3.2. Extension of Radiation Damage Modeling to Polyatomic Materials

Computing radiation damage in polyatomic materials is significantly more complex than in monoatomic materials, because damage efficiency becomes a function of both the lattice and PKA nuclides and because the damage cascade's kinematics are different since dissimilar nuclei are involved in elastic collisions. In general, the damage-energy cross section would depend on projectile and lattice nuclides (i.e., $\sigma_{D,p\to l}(E)$). However, the HEATR module of NJOY does not currently support the computation of $\sigma_{D,p\to l}(E)$.

Therefore, we propose a simple extension of the monoatomic approach to polyatomic materials:

$$\hat{e}_l(t) = \xi_l \sum_{p=1}^{P} \int_0^{\infty} N_p \sigma_{D,p}(E) \phi(E,t) dE, \tag{3.9}$$

where

l	index of a given nuclide l
p	PKA nuclide
ξ_l	partition function that we propose equals the atom fraction of nuclide l in the material

We tested this hypothesis for the polyatomic material $Si_{1-x}C_x$. The fraction of damage energy ξ_l is computed using the binary collision Monte Carlo (BCMC) code Magpie [54]. The Eq. (3.9) and BCMC methods computed fractional energy depositions that were well aligned, even though silicon and carbon differ significantly in atomic number, mass number, and threshold displacement energy ($E_{D,\mathrm{Si}} = 41$ eV and $E_{D,\mathrm{C}} = 16$ eV [55]). The robustness of the hypothesis across different polyatomic materials should be investigated.

The damage-energy cross section computed in the HEATR module of NJOY uses the Robinson partition function that supports different (Z, A) numbers for the PKA and lattice atoms, that is the partition function is $P(E_R,\ A_p,\ Z_p,\ A_l,\ Z_l)$. However, the HEATR module of NJOY only accepts a single (Z, A) pair and sets $A_p = A_l$ and $Z_p = Z_l$. This assumption works well where these atomic masses are close (e.g., with common steel alloying materials like iron and nickel). The damage-energy cross section for each nuclide is computed separately, essentially neglecting the presence of any other species in the radiation damage cascade.

Similar to how neutron reaction damage is generalized, decay damage given in Eq. (3.8) is extended to:

$$\hat{e}_l = \xi_l \sum_{p=1}^{P} \lambda_p \eta_p N_p. \tag{3.10}$$

3.3.3. The Current Approach to Radiation Damage Modeling

In Eq. (3.5), the dependence of $\hat{e}$ on the time variation of the nuclide concentration is apparent. However, in practice this time variation is commonly neglected to simplify the problem. The nuclide concentration and neutron flux are usually assumed to be constant throughout the time interval of interest so that a constant damage rate can be calculated, and the time integral simplifies to a simple multiplication of this constant damage rate with the length of the time interval.

The assumption of a constant damage-energy rate density breaks down when transmutation products produce a significant amount of radiation damage. As discussed in Section 3.2.1, the mass of the recoil nuclei produced by transmutation reactions is much closer to the mass of the constituent atoms in the bulk material then the secondary particles produced from transmutation reactions, such as alpha particles and protons, which results in a much more efficient transfer of energy from the recoil nuclei to the nuclei of the bulk material which much more readily produces radiation damage. The recoil nuclei produced from (n,γ) reactions will tend to have recoil energies on the order of hundreds of eV while the recoil nuclei produced by (n,α) and (n,p) reactions will have recoil energy on the order of tens or hundreds of keV. It is this several orders of magnitude difference in the energy of the recoil nuclei produced by (n,α) and (n,p) reactions compared to (n,γ) reactions that necessitates consideration of transmutation products which can undergo these (n,α) and (n,p) reactions. A method for accounting for ^{59}Ni damage was developed by Greenwood [1, 24]. It uses a correction factor based on the correlation of the amount of helium and hydrogen gas produced in a specimen to the additional damage caused by ^{59}Ni (n,α) and (n,p) reactions.

Greenwood's approach to account for additional damage caused by transmutation and decay products is problematic for at least two reasons. First, Greenwood's correlations are developed separately from the normal nuclear data library releases. If new nuclear data experiments refine the underlying data, the damage correlations are extremely unlikely to be updated. Second, this method is not easily extensible to other transmutation products, because each transmutation product of concern requires a manual correction factor and trackable reaction products may not exist, or may be obfuscated by other reactions. As mentioned by Greenwood, an alloy containing ^{59}Ni and contaminated with ^{10}B would result in both nuclides producing ^{4}He as the result of (n,α) reactions, meaning that simply measuring the ^{4}He concentration in the alloy and applying Greenwood's correction factor

using that ^{4}He concentration would not be appropriate, the ^{4}He contributed by ^{10}B would need to be excluded when using the correlation. Assuming the initial NND of ^{10}B, the neutron flux, and cross sections are well-known and that ^{10}B is not produced by other nuclides in the system then the ^{4}He contribution from ^{10}B in the system can be determined easily and the remaining ^{4}He contribution can be attributed to ^{59}Ni, since the NND of ^{59}Ni is strongly time-dependent because of its buildup from activation. However, if another helium producing nuclide is present which also has a strong time-dependent NND then this process becomes much more difficult to perform. An example of a nuclide which could fit this criteria is ^{33}S, which has an (n,α) cross section for thermal neutrons roughly an order of magnitude less than ^{59}Ni. ^{33}S may be present as a contaminant, but since most sulfur is ^{32}S it may buildup as a result of sulfur-32 activation. Accounting for helium production from two nuclides which have strongly time-dependent NNDs from the activation of other nuclides becomes much more challenging.

3.3.4. Modeling FIMA using Forward Euler

Unlike radiation damage, FIMA is calculated using data already expected to be present in any depletion-capable application. FIMA can be calculated using the FE method, as shown in Eq. 3.11.

$$\begin{aligned} f_j &= \sum_i^I N_{i,j} \int_0^\infty \phi_j(E)\sigma_{i,f}(E)dE \\ \Delta F_j &= f_j \cdot t_j \\ \text{FIMA}_j &= \frac{\Delta F}{N_{\text{IMA}}} + \text{FIMA}_{j-1} \end{aligned} \tag{3.11}$$

where

E	neutron kinetic energy
t_j	length of depletion interval j in time
$\sigma_{i,f}(E)$	energy-dependent microscopic fission cross section of nuclide i
N_i	NND of nuclide i at the beginning of depletion interval j
$\phi_j(E)$	energy-dependent scalar neutron flux calculated at the beginning of the depletion interval j
f_j	fission density rate at the beginning of depletion interval j
ΔF_j	change in fission density over depletion interval j
N_{IMA}	initial heavy metal atom density
FIMA_j	FIMA calculated after the j-th depletion interval.

Once again, the fission density rate term f is identical to the neutron transmutation terms in Eq. 3.1, indicating that it could easily be added to the Bateman equations. For the remainder of this work, we will focus on accurately calculating the fission density, F, with the understanding that F can easily be divided by the initial heavy metal atom density in order to calculate FIMA.

3.3.5. Modeling KERMA using Forward Euler

Similar to FIMA, calculating KERMA can be done with data already known to depletion-capable applications. However, typically when depletion is performed a constant power is assumed during each depletion interval, which we will refer to as the rated power. If a rated power is supplied, the neutron flux spectrum is calculated by the transport solution using the NNDs at the beginning of the depletion interval and is scaled in order to provide the rated power over the given depletion interval. We introduce the term κ_t, which corresponds to the average energy released per neutron interaction in [eV]. When multiplied by the total microscopic cross section σ_t, we obtain the average energy released per neutron interaction in units of [eV $\cdot$ b], or "kappa-total." This is similar to the well-known $\kappa_f \sigma_f$ or "kappa-fission" quantity, which is the average energy released per fission event multiplied by the microscopic fission cross section. The difference between kappa-total and kappa-fission is that kappa-total accounts for energy released via non-fission neutron interactions. With $\kappa_t \sigma_t$, the rated power at the beginning of each depletion interval is calculated as shown along with KERMA using FE. Since the rated power is user-supplied for the entire system we consider a system with non-uniform power density in order to better reflect the process of calculating the KERMA for a single region of a given system.

$$\begin{aligned} P_{\text{n},j}(\vec{r}) &= \sum_{i=1}^{I} N_{i,j}(\vec{r}) \int_0^\infty \phi_j(E,\vec{r}) \kappa_{i,t}(E) \sigma_{i,t}(E,\vec{r}) dE \\ P_{\text{d},j}(\vec{r}) &= \sum_{i=1}^{I} \lambda_i Q_i N_{i,j}(\vec{r}) \\ P_{\text{rated},j} &= \int_V P_{\text{d},j}(\vec{r}) + P_{\text{n},j}(\vec{r}) d\vec{r} \\ \text{KERMA}_j(\vec{r}) = K_j(\vec{r}) &= (P_{\text{d},j}(\vec{r}) + P_{\text{n},j}(\vec{r})) \cdot t_j + K_{j-1}(\vec{r}) \end{aligned} \tag{3.12}$$

where

E	neutron kinetic energy
t_j	length of depletion interval j in time
V	total volume of the system
$\vec{r}$	spatial position within volume V
$P_{\text{n},j}(\vec{r})$	neutron transmutation power density at the beginning of depletion interval j at spatial position $\vec{r}$
$\kappa_{i,t}(E)$	energy-dependent average energy released per neutron interaction with nuclide i
$\sigma_{i,t}(E,\vec{r})$	energy- and spatial-dependent total microscopic cross section of nuclide i
$N_{i,j}(\vec{r})$	NND of nuclide i at the beginning of depletion interval j at spatial position $\vec{r}$
$\phi_j(E,\vec{r})$	energy- and spatial-dependent scalar neutron flux at the beginning of depletion interval j
$P_{\text{d},j}(\vec{r})$	decay power density at the beginning of depletion interval j
λ_i	decay constant of nuclide i
Q_i	average energy released per decay of nuclide i
$P_{\text{rated},j}$	rated power at the beginning of depletion interval j

$K_j(\vec{r})$ KERMA at the end of depletion interval j at spatial position $\vec{r}$.

Note that, when performing neutron transport, the eigenvalue problem result is the scalar neutron flux spectrum, which is unscaled. When performing depletion, this unscaled neutron flux must be multiplied by a scaling factor in order to ensure that the power specified by the user is being produced by the system. The scaling factor is calculated using the NNDs at the beginning of the depletion interval, meaning the time-dependence of the NNDs over the depletion interval is ignored.

3.4. Calculating Non-Nuclide Quantities in the Bateman Equations

The main proposal of this work is to solve the Bateman equations with the non-nuclide quantities coupled directly, rather than computing non-nuclide quantities independently using simplifying assumptions. For radiation damage, Eqs. 3.9 and 3.10 can be rewritten as:

$$\frac{\partial \hat{E}_l}{\partial t} = \xi_l \sum_{p=1}^{P} \left(\lambda_p \eta_p N_p(t) + N_p(t) \int_0^\infty \sigma_{D,p}(E)\phi(E,t)dE \right) \tag{3.13}$$

where $\hat{E} = \sum_{l=1}^{L} \hat{E}_l$ and $\sum_{l=1}^{L} \xi_l = 1$ means that $\hat{E}_l = \xi_l \hat{E}$. Therefore, it is sufficient to only solve for $\hat{E}$:

$$\frac{\partial \hat{E}}{\partial t} = \sum_{p=1}^{P} \left(\lambda_p \eta_p N_p(t) + N_p(t) \int_0^\infty \sigma_{D,p}(E)\phi(E,t)dE \right) \tag{3.14}$$

For the fission density F used to calculate FIMA, we rewrite Eq. 3.11 as:

$$\frac{dF}{dt} = \sum_{i}^{I} N_i(t) \int_0^\infty \phi(E,t)\sigma_{i,f}(E)dE \tag{3.15}$$

And for KERMA, we rewrite Eq. 3.12 as:

$$\frac{dK}{dt} = \sum_{i=1}^{I} N_i(t) \Big(\int_0^\infty \phi(E,t)\kappa_{i,t}(E)\sigma_{i,t}(E)dE + \lambda_i Q_i \Big) \tag{3.16}$$

Written in these forms, it becomes apparent that Eqs. 3.14–3.16 look like any of the rows found in the Bateman system of equations. Recall from Eq. 3.2 that the Bateman equations can be expressed in matrix form where we will now assume that the depletion matrix $\mathbf{A}$ is constant over the given depletion interval being considered.

$$\frac{d\mathbf{N}}{dt} = \mathbf{A}\mathbf{N}, \tag{3.17}$$

where $\mathbf{N} = (N_1, \ldots, N_I)^T$ and I is the total number of nuclides tracked. We can simply define new nuclides to track the quantities of interest:

$$
\begin{aligned}
N_{I+1} &= \hat{E} \\
N_{I+2} &= F \\
N_{I+3} &= K
\end{aligned}
\tag{3.18}
$$

Given this, a slight modification to the depletion matrix can be defined as:

$$
\begin{aligned}
\tilde{\mathbf{N}} &= \left(N_1, \cdots, N_I, \hat{E}, F, K\right)^T \\
\frac{d\tilde{\mathbf{N}}}{dt} &= \tilde{\mathbf{A}}\tilde{\mathbf{N}}
\end{aligned}
$$

where $\tilde{\mathbf{A}}$ is the modified decay and transmutation matrix of the Bateman equations with the associated terms from Eqs. 3.14–3.16 added and $\tilde{\mathbf{N}}$ is the modified NND vector.

Eq. 3.19 can then be solved by the CRAM for the matrix exponential with excellent precision [28]. Alternatively, the Bateman equations can be solved in their original form, Eq. 3.17, and $\hat{E}$, F, and K can be accumulated at the end of each time step using a standard integration rule, such as FE. This modification to the depletion matrix does not violate the requirements of CRAM as the addition of each non-nuclide adds an eigenvalue of zero to the matrix without altering the non-zero eigenvalues of the depletion matrix without non-nuclides. Eigenvalues of zero can occur in "normal" depletion matrices when tracking ^{4}He which only builds up from (n,α) and α decay reactions and assuming ^{4}He has a cross section of zero. These conditions will also result in an eigenvalue of zero and a depletion matrix which CRAM is able to solve for. As a result, we did not experience any issues with using CRAM to solve these modified depletion matrices and, assuming the addition of the non-nuclide only adds eigenvalues of zero to the depletion matrix, we do not anticipate other researchers or analysts to have any difficulty using CRAM for these modified depletion matrices.

The proposed modification to the depletion matrix is similar to the modification proposed by Isotalo and Wieselquist [56] for modeling external feed in the Bateman equations. Indeed in Isotalo and Wieselquist's work the calculation of non-nuclide quantities in the form calculating source terms for the external production of given nuclides was considered. While we consider energy-related quantities which have no direct impact on the NNDs, in that the calculated KERMA, DPA, and FIMA values do not modify the production/destruction rates of nuclides in the depletion matrix, the similarities in our modification of the depletion matrix to previous work merits acknowledgement.

3.5. Implementation in Griffin

This functionality was implemented in the transport code Griffin [2], which is a neutronics application developed at both Idaho National Laboratory and Argonne National Laboratory based on the Multiphysics Object-Oriented Simulation Environment [57]. The implementation did not require major modifications to Griffin's transmutation and decay solver. Rather, most of the work was confined to allowing Griffin to read and process the necessary data, including damage threshold energies and damage-energy cross sections as the data required to calculate FIMA and KERMA was already present. By default, Griffin uses FE in order to calculate the quantities of FIMA and KERMA, thus FE is used as the basis of comparison to the proposed method in this work.

3.5.1. Data Needs

To calculate radiation damage, Griffin needed access to the threshold displacement energy, provided as either a single number for the entire material or as a different value for each nuclide, and the damage-energy cross sections for each nuclide. In order to calculate FIMA, the only quantities needed are the initial fissionable NNDs and the associated microscopic fission cross sections, while KERMA requires the average energy release per neutron interaction of all nuclides as well as the decay energies of all radionuclides. For FIMA and KERMA calculations, Griffin already possessed the required data and thus no modifications were required to calculate these values in the Bateman equations.

3.5.1.1 Threshold Displacement Energies

Threshold displacement energies are generally provided by the user on a nuclide basis in Griffin. Even though the estimated radiation damage is strongly dependent on the threshold displacement energy, the exact values used for the threshold displacement energy are a contentious topic [45, 49]. Therefore, it is crucial to offer a generic, flexible interface for comparing data sets (e.g., across codes or in comparison to old data) and allowing the user to use their preferred threshold displacement energies. Threshold displacement energies are usually given on an elemental basis. However, Griffin does not yet support elemental data, so the more general approach of providing them as isotopic data is used instead.

The second option for setting threshold displacement energies is to rely on Griffin's default values. Many users are unfamiliar with selecting threshold displacement energies, so Griffin provides default values for most elements. The values from Konobeyev et al.'s Table 4 [45] were implemented in Griffin as part of this work. Elements without specified threshold displacement energies (such as gases) are assumed to have a threshold displacement energy of zero with an error returned if an attempt is made to calculate radiation damage for a material calculated to have a threshold displacement energy of zero.

In this way, users have better control over how the material is modeled without requiring unnecessary data management that, while simple to perform, can be time-consuming. This is also useful when using the default threshold displacement energies taken from Konobeyev et al. [45] since this dataset is not exhaustive and does not provide threshold displacement energies for gases, higher actinides, and many other elements even though such elements will be present in materials deployed for nuclear applications and will experience damage since neutrons will interact with them.

The third option is to set a single threshold displacement value for all nuclides in a given material region. For problems with hundreds of nuclides, specifying the threshold displacement energy for each individual nuclide is an onerous task. Consequently, it may be convenient for the user to specify a threshold displacement energy that is effective for the entire material. This is ideal if the user is modeling a material with a threshold displacement energy value that is well understood, especially those that break some of the assumptions used when using a weighted-average for threshold displacement energies, such as high-entropy alloys.

Griffin allows mixing the first and second options for setting threshold displacement energies, enabling users to specify threshold displacement energies for a few nuclides while the rest of the nuclides in the system are assigned values from Konobeyev et al.'s Table 4 [45].

3.5.1.2 Total Energy Released per Reaction Event

While every neutron transmutation event releases some amount of energy, for simplicity we considered a system where the only energy released via (n,x) reactions comes from nuclear fission, with all fission events

releasing 200 MeV of prompt energy. While this is not true physically, for our purposes this is a satisfactory approximation. Decay energies and other cross section values were taken from the DRAGON5 code [41] for a pressurized-water reactor fuel pin. Griffin supports the specification of both $\kappa_t\sigma_t$ as well as $\kappa_f\sigma_f$; however, the data used from DRAGON5 did not include $\kappa_t\sigma_t$. While the DRAGON5 data provided κ_f for all fissionable nuclides, a fixed value of 200 MeV was assumed for κ_f for all fissionable nuclides in order to simplify consistency checks between the fission density and KERMA results calculated by Griffin using the new functionality.

3.5.2. Code Adaptation

Theoretically, the addition of non-nuclide tracking should not require any changes to existing transmutation solvers beyond adding the non-nuclides themselves, which track the quantities of interest in the system. However, since Griffin uses CRAM coupled with SGE [31] to solve the Bateman equations and SGE requires a specific sparsity pattern, some special requirements exist when adding these non-nuclides. SGE exploits the fact that depletion matrices are largely upper triangular (when nuclides are ordered from lightest to heaviest) with significant off-diagonals from fission product production and secondary hydrogen and helium production from (n,p) and (n,α) reactions, which are confined to the upper triangular region of the matrix. Since the non-nuclides of damage-energy and KERMA can be produced from any nuclide with the appropriate cross section, they are similar to hydrogen and helium in regards to how they affect the depletion matrix sparsity pattern. Consequently, appending the non-nuclides to the front of the NND vector and top of the depletion matrix (adjacent to hydrogen and helium) maintains the sparsity pattern required by SGE and results in CRAM providing its expected accuracy. If the non-nuclides are placed elsewhere then the sparsity pattern of SGE is violated. Appending a dense row to the bottom of an otherwise mostly upper triangular matrix can cause SGE in CRAM to fail or otherwise degrade in accuracy.

3.6. Results

3.6.1. Radiation Damage Benchmark

As a verification step for the radiation damage implementation in Griffin, the DPA calculations generated by the correction factor developed by Greenwood were reproduced in Griffin using the modified transmutation solver in Griffin [1].

Ideally this benchmark would be compared against experimental measurements. However, this is not practical due to the nature of the radiation damage cascade. This limitation has been apparent and a known limitation of the models since the foundational work of Kinchin and Pease [44]. This is due to the fact that during the initial damage cascade many atoms are displaced, forming a region of high-energy displaced atoms. Within picoseconds this region cools, and begins to recrystallize, and only a fraction of the initial displacements remains after this event as stable Frankel pairs [58]. The amount of stable Frankel pairs depends on many factors, and isn't practical to calculate currently. It should be noted that there has been recent advancements by Hirst, et al in measuring the amount of these of Frankel pairs post irradiation [59]. Though this is a very new approach with a low technology readiness level, and still suffers from the fundamental issue of correlating initial displacements to stable Frankel pairs. The goal of this benchmark is to show that this method performs the calculations as expected, and is able to replicate previous calculations performed with an alternative method, not necessarily to show that the underlying NRT methods are extremely accurate. That is an entirely different endeavour that is far beyond the scope of this research.

Table 3.1: Known values provided by Greenwood [1]

$\sigma_{D,\text{Ni}}$	2180 [eV-b]	$\sigma_{D,\gamma,\text{Ni}}$	2180 [eV-b]	$\sigma_{\alpha,^{59}\text{Ni}}$	11.6 [b]
$\sigma_{\gamma,\text{Ni}}$	4.43 [b]	$\sigma_{\gamma,^{58}\text{Ni}}$	4.6 [b]	$\sigma_{\gamma,^{59}\text{Ni}}$	80.4 [b]
$\sigma_{\gamma,^{60}\text{Ni}}$	2.8 [b]	$\sigma_{\gamma,^{61}\text{Ni}}$	2.4 [b]	$\frac{\hat{E}_{\alpha,^{59}\text{Ni}}}{\hat{E}_{\gamma,\text{Ni}}}$	349

Greenwood's 1983 correction factor calculated a fluence-dependent correlation between the helium produced by the (n,α) reaction for ^{59}Ni and the additional radiation damage that it created. This was intended to be used with the analyst performing a traditional radiation damage calculation by assuming the initial nuclide concentration remains constant during the irradiation. A transmutation solver then calculates the amount of helium produced by ^{59}Ni during the irradiation. The correction factor, dependent on the fluence the system experienced, would then be applied to the amount of helium produced to calculate the additional damage produced by the ^{59}Ni. This additional damage contribution from ^{59}Ni would then be added to the radiation damage calculated by the traditional radiation damage calculation resulting in the final total radiation damage experienced by the material. Of course, Greenwood's correlation is only applicable for the given neutron flux spectrum and neutron fluence levels provided by Greenwood as Greenwood noted that at very high fluences ($> 10^{24} \frac{\text{n}}{\text{cm}^2}$) the original nickel-58 and nickel-60 in the system will begin to heavily transmute into the heavier nickel isotopes and into copper, appreciably changing the radiation damage rate [1].

The primary challenge of recreating the results from Greenwood's 1983 work [1] via Griffin is the lack of damage-energy cross sections provided in Greenwood's work. Nevertheless, some assumptions could be made based on Greenwood's data in order to derive damage-energy cross sections for the nuclides under consideration. Conveniently, Greenwood assumed a mono-energetic neutron flux at a velocity of 2,200 $\frac{\text{m}}{\text{s}}$, making the implementation of the one-group damage-energy cross sections (once calculated) trivial. Greenwood explained in their original work that the correlation presented is only applicable for highly thermal neutron spectra and that, if considering non-thermal cases, the original equations used by Greenwood would need to be solved for again using the correct spectral-averaged cross sections for said non-thermal neutron flux and the correlation recalculated.

The known cross-section and damage-energy ratios provided by Greenwood are shown in Table 3.1. Note that the given damage-energy ratio is on a per reaction basis, meaning one ^{59}Ni(n,α) ^{56}Fe reaction releases $349\times$ the damage energy of one ^{x}Ni(n,γ) $^{x+1}$Ni reaction.

Based on these values, we made the following assumptions. We calculated a damage-energy (n,γ) cross section of ^{59}Ni using the damage energy and (n,γ) cross sections of natural nickel. We used the given ratio to determine the damage-energy cross section of ^{59}Ni(n,α) ^{56}Fe. We also assumed that the damage-energy cross section of the naturally occurring nickel isotopes (^{58}Ni and ^{60}Ni) are the same as natural nickel. Note that this assumption is not physical as Greenwood provides the (n,γ) cross section of ^{58}Ni and ^{60}Ni as different values, and both isotopes will have different γ-ray energies, changing the damage caused per (n,γ) reaction. The calculations for the assumed values are shown in Eq. 3.19.

Table 3.2: Data used by Griffin for the damage calculation to replicate Greenwood's 1983 work [1]. All data except for the damage-energy cross section for ^{59}Ni were collected from Greenwood's work [1]

Nuclide	Initial Abundance [-]	σ_γ [b]	σ_α [b]	σ_D [eV-b]
^{58}Ni	0.683	4.6	—	2,180
^{59}Ni	—	80.4	11.6	2,031,782
^{60}Ni	0.317	—	—	2,180
^{56}Fe	—	—	—	—

$$
\begin{aligned}
D_{\gamma,\text{Ni}} &= \frac{\sigma_{D,\gamma,\text{Ni}}}{\sigma_{\gamma,\text{Ni}}} = 492.1 \text{ [eV]} \\
\sigma_{D,\gamma,^{59}\text{Ni}} &= \sigma_{\gamma,^{59}\text{Ni}} D_{\gamma,\text{Ni}} = 39\,564.8 \text{ [eV-b]} \\
\sigma_{D,\alpha,^{59}\text{Ni}} &= D_{\gamma,\text{Ni}} \frac{D_{\alpha,^{59}\text{Ni}}}{D_{\gamma,\text{Ni}}} \sigma_{\alpha,^{59}\text{Ni}} = 1\,992\,217.6 \text{ [eV-b]} \\
\sigma_{D,^{59}\text{Ni}} &= \sigma_{D,\gamma,^{59}\text{Ni}} + \sigma_{D,\alpha,^{59}\text{Ni}} = 2\,031\,782 \text{ [eV-b]} \\
\sigma_{D,^{58}\text{Ni}} &= \sigma_{D,\text{Ni}} = 2180 \text{ [eV-b]} \\
\sigma_{D,^{60}\text{Ni}} &= \sigma_{D,\text{Ni}} = 2180 \text{ [eV-b]}
\end{aligned}
\tag{3.19}
$$

With the known Greenwood values and our assumed values, we now considered a sample of pure nickel with a fixed E_d of 40 eV. We tracked the buildup of ^{56}Fe in the material, from ^{59}Ni undergoing (n,α), but assumed that ^{56}Fe has cross sections of zero, meaning it does not activate, deplete, or produce radiation damage. We assumed that the pure nickel is initially only composed of ^{58}Ni and ^{60}Ni with the Greenwood-specified abundances. We tracked the production of ^{59}Ni from ^{58}Ni undergoing (n,γ) and ^{60}Ni production from ^{59}Ni undergoing (n,γ) but did not track the buildup of ^{61}Ni or the destruction of ^{60}Ni from (n,γ), treating ^{60}Ni as though it had an (n,γ) cross section of zero. Greenwood justified this because ^{60}Ni and ^{61}Ni have similar (n,γ) cross sections and thus would be expected to produce similar amounts of radiation damage under the same flux conditions. We ignored the decay of ^{59}Ni as Greenwood did, which is valid because the half-life of ^{59}Ni is almost 10^5 years and, on reactor material timescales, radioactive decay will not meaningfully impact its concentration. The data we used is shown in Table 3.2 [1].

Using these cross-section data and the initial isotopic concentrations of nickel, we performed several CRAM solves of the Bateman equations, applying a neutron flux of $10^{19} \frac{\text{n}}{\text{cm}^2-\text{s}}$ for sequential time steps, obtaining the isotopic concentrations and radiation damage values at the same neutron fluence levels listed by Greenwood. The accuracy of CRAM is well documented and extremely high when used at an appropriate approximation order, such as 16 [28] [36]. Because of the robust documentation of CRAM testing at approximation order 16, 16 was the approximation order we used for the CRAM solves performed in Griffin. Thus any error between our results and Greenwood's are a result of assumptions made to calculate the damage-energy cross sections.

For future comparison and reproducibility, we have provided the double-precision floating point result calculated by Griffin in Table 3.3, despite only being provided four significant figures at most in Greenwood's data and results. We observed a maximum RD of less than 2.5% between Griffin and Greenwood's results, which is satisfactory given the assumptions made, especially when considering that increases in the RD track the increasing concentration of ^{59}Ni where the most "egregious" assumptions were made. Greenwood also provided values for the ^{4}He concentration, which Griffin (when rounded to the same number of significant figures as Greenwood) matched exactly, as expected for CRAM, indicating once again that the difference in radiation damage is driven

by assumptions made regarding the damage-energy cross sections. The relative number fractions in the material are shown in Figure 3.1a as well as a plot showing the correlation between the absolute RD between the Griffin and Greenwood DPA and the number fraction of ^{59}Ni in Figure 3.1b. As can be seen in Figure 3.1b, the error in Griffin's modeling of the Greenwood problem is tightly correlated with the concentration of ^{59}Ni. This suggests that the error was caused by the assumptions and rounding error used in calculating the damage-energy cross section. While the two values are not perfectly correlated, portions of Greenwood's results were only reported to two significant figures, hence we consider a difference of less than 1% to be very good agreement, which is achieved whenever the ^{59}Ni concentration is relatively small.

Table 3.3: Total radiation damage values calculated by Griffin and Greenwood [2].

Fluence $\left[\frac{\text{n}}{\text{cm}^2-\text{s}}\right]$	Griffin [DPA]	Greenwood [DPA]	$\frac{\text{Griffin}-\text{Greenwood}}{\text{Greenwood}}$
1×10^{19}	$2.211\,872\,754\,137\,09 \times 10^{-4}$	2.232×10^{-4}	-0.9018%
5×10^{19}	$1.169\,579\,350\,675\,65 \times 10^{-3}$	1.180×10^{-3}	-0.8831%
1×10^{20}	$2.497\,805\,791\,475\,11 \times 10^{-3}$	2.520×10^{-3}	-0.8807%
5×10^{20}	$1.874\,387\,514\,104\,19 \times 10^{-2}$	1.890×10^{-2}	-0.8261%
1×10^{21}	$5.267\,949\,674\,369\,20 \times 10^{-2}$	5.300×10^{-2}	-0.6047%
5×10^{21}	$7.912\,613\,521\,088\,44 \times 10^{-1}$	8.090×10^{-1}	-2.1927%
1×10^{22}	$2.578\,587\,616\,834\,75$	2.641	-2.3632%
5×10^{22}	$2.582\,098\,709\,824\,75 \times 10^{1}$	2.642×10^{1}	-2.2673%
1×10^{23}	$5.270\,078\,422\,375\,55 \times 10^{1}$	5.401×10^{1}	-2.4240%
5×10^{23}	$1.451\,209\,971\,142\,76 \times 10^{2}$	1.476×10^{2}	-1.6795%
1×10^{24}	$1.694\,284\,618\,251\,51 \times 10^{2}$	1.698×10^{2}	-0.2188%

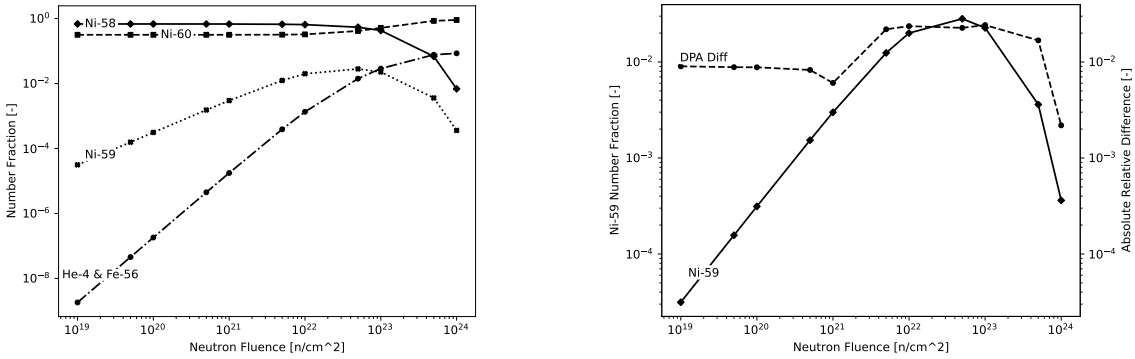

(a) Number fractions of nuclides calculated by Griffin. Note that ^{4}He and ^{56}Fe are exactly the same.

(b) Absolute RD in DPA between Griffin and Greenwood alongside ^{59}Ni fraction.

Figure 3.1: Number densities for Greenwood's test problem computed with Griffin and comparison between Griffin's and Greenwood's radiation damage [DPA] estimates [1].

3.6.2. FIMA and KERMA Comparison

For demonstrating the capabilities of computing FIMA and KERMA, we consider a simplified 2D quarter pressurized-water reactor fuel pin with initial NNDs, as shown in Table 3.4. Once again, we provide the exact numerical values for the NNDs used in the Griffin input file in order to simplify any future work seeking to verify or reproduce the results we have presented in this work.

1-group cross-section data was taken from DRAGON5 for the initial state of the fuel pin, and the microscopic cross sections were assumed to remain constant during the entire depletion. Once again, this is non-physical but

Table 3.4: Initial NNDs of the pressurized-water reactor quarter pin geometry in $\frac{\text{atoms}}{\text{b}\cdot\text{cm}}$.

Nuclide	Fuel	Cladding	Helium Gap	Coolant
H-1	–	–	–	$4.564\,169 \times 10^{-2}$
H-2	–	–	–	$6.847\,042 \times 10^{-6}$
He-4	–	–	$2.404\,4 \times 10^{-4}$	–
O16	$4.638\,898\,701\,695\,5 \times 10^{-2}$	–	–	$2.285\,945 \times 10^{-2}$
O17	$1.129\,998\,280\,333\,2 \times 10^{-4}$	–	–	$8.689\,893 \times 10^{-6}$
Zr-90	–	4.3×10^{-2}	–	–
U-234	$9.454\,705\,701\,002\,4 \times 10^{-6}$	–	–	–
U-235	$9.673\,255\,576\,522\,1 \times 10^{-4}$	–	–	–
U-238	$2.227\,421\,315\,914\,1 \times 10^{-2}$	–	–	–

serves our purposes of demonstrating the difference between calculating quantities via FE or tracking them in the Bateman equations. The quarter pin was depleted at a linear heat rate of 50 $[\frac{\text{W}}{\text{cm}}]$, which corresponds to a fuel rod linear heat rate of 20 $[\frac{\text{kW}}{\text{m}}]$, for a total length of 600 days.

We performed eight different coupled transport-depletion simulations, varying the number of depletion intervals over the course of the 600-day depletion. The 600-day period was divided into 1, 2, 4, 8, 16, 32, 64, and 128 depletion intervals of equal sizes. All fission events were assumed to release 200 MeV of energy with decay energies taken from DRAGON5 with non-fission neutron interactions (such as radiative capture) assumed to release no energy. Overall, the total number of nuclides tracked in the system was 297.

For the purposes of comparison, we introduced the terms interval difference (ID) and cumulative difference (CD) defined as:

$$\begin{aligned} \text{ID} &= \frac{X_{\text{Bateman}}(t_j) - X_{\text{Bateman}}(t_{j-1})}{X_{\text{FE}}(t_j) - X_{\text{FE}}(t_{j-1})} - 1 \\ \text{CD} &= \frac{X_{\text{Bateman}}(t_j)}{X_{\text{FE}}(t_j)} - 1 \end{aligned} \tag{3.20}$$

where X is some quantity evaluated at time t_j using either the Bateman equations or FE. Agreement between FE and the Bateman equations corresponds to a value of $\text{ID}, \text{CD} = 0$.

Note that for the first depletion interval, ID and CD will always equal one another.

FE calculated fission density and KERMA for each depletion interval using the NNDs calculated at the beginning of the current depletion interval, as shown in Eqs. 3.11 and 3.12. The results are shown in Figures 3.2 and 3.3 with similar results for both KERMA and fission density.

When calculating fission density or KERMA, the Bateman equations initially predict more KERMA and fissions than FE. This difference is attributed to the miscounting of decay heat by FE as the decay heat calculated at the very beginning of the first depletion interval is very close to zero when compared to the decay heat calculated at the beginning of all other depletion intervals. Consequently, the neutron flux is scaled such that fission provides almost the entirety of the rated power for the first depletion interval, when in reality as soon as fission begins decay heat from fission products will be released. This demonstrates that the Bateman equations more accurately calculate KERMA and fission density when depleting the system using the scaled flux solution during these initial depletion intervals.

To ensure that this is true, we also evaluated the decay energy density in the system using FE and the Bateman equations, as shown in Figure 3.4. Note that the ID and CD for the first depletion interval for all cases resulted in the Bateman equations calculating a value six orders of magnitude greater than FE. This is due to FE dramatically

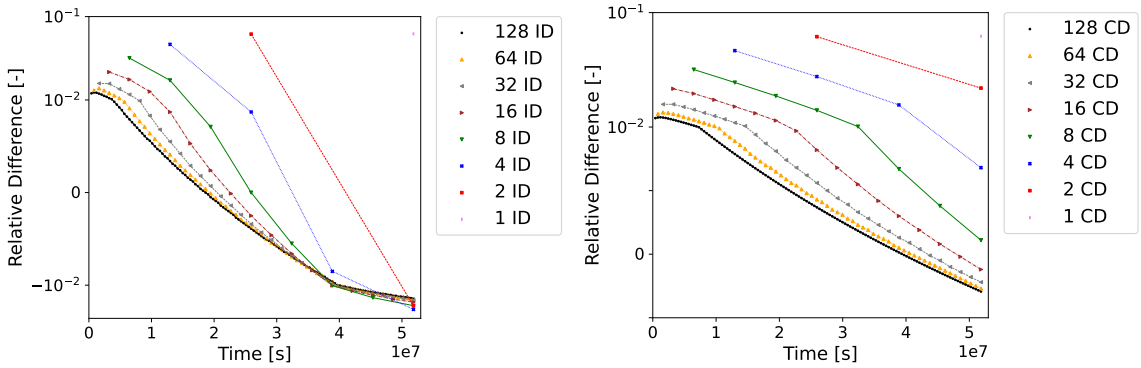

(a) (b)

Figure 3.2: Comparisons of KERMA differences to the Bateman equations: a ID, b CD.

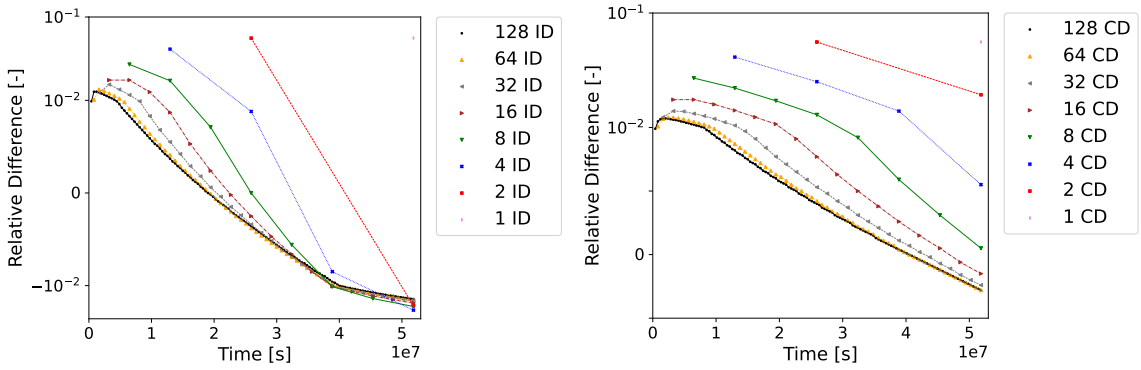

(a) (b)

Figure 3.3: Comparisons of fission density differences to the Bateman equations: a ID, b CD.

underpredicting the decay heat for the first depletion interval as mentioned previously. Overall, the decay energy density differences show that FE significantly underpredicts decay heat relative to the Bateman equations initially, with the underprediction decreasing over the course of the entire simulation. This is physically expected as the number of fissions remains relatively constant during the depletion, which results in a buildup of radioactive fission products. The short-lived fission products reach saturation and begin to provide a constant amount of decay heat while long-lived fission products steadily buildup, resulting in decay heat increasing during all depletion intervals. Since FE assumes the NNDs are constant during each depletion interval, FE fails to account for this increase in decay energy while the Bateman equations succeed.

However, Figure 3.4 does not explain the lower KERMA and fission density quantities calculated by the Bateman equations relative to FE in later depletion intervals. This is attributed to the decreasing macroscopic fission cross section of the fuel pin as depletion occurs and fissile nuclides are destroyed. As the macroscopic fission cross section decreases, the fission rate also decreases. Since the change in decay power released is minimal during these later depletion intervals, the decreased fission rate results in a subsequent decrease in KERMA over the course of each depletion interval. Once again, the Bateman equations account for these time-dependent effects while FE does not.

Both the Bateman equations and FE begin to converge as the number of depletion intervals increases and the length of each individual depletion interval decreases. This is to be expected based on the well understood

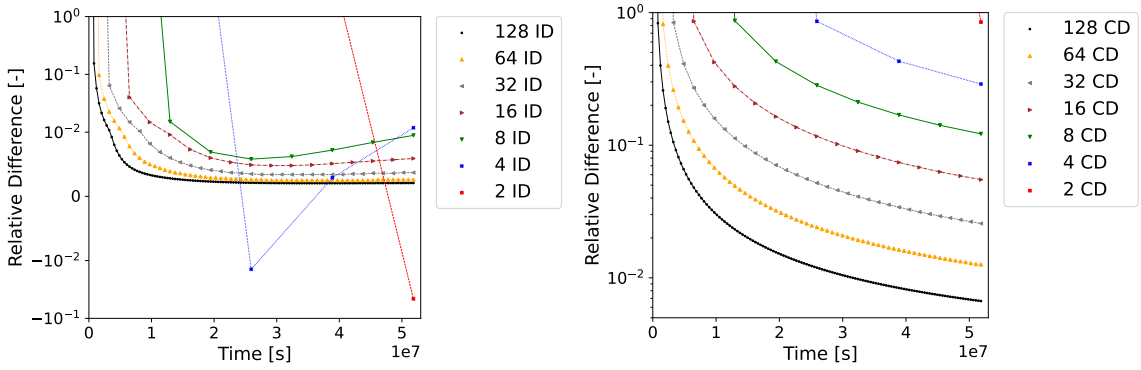

(a) (b)

Figure 3.4: Comparisons of decay energy density differences to the Bateman equations: a ID, b CD.

behavior of FE and serves as further evidence that the Bateman equations are accurately calculating the quantities of interest.

These results demonstrate that a difference of less than 7% for all tests can be observed when calculating FIMA or KERMA using FE versus the Bateman equations, with the differences decreasing to less than 2% if depletion intervals under 100 days are used. However, a quantity such as decay energy density can result in a greater than 10% difference at specific points in time for all depletion intervals tested. While other finite difference methods more accurate than FE could be used (e.g., Crank-Nicolson) and would be expected to yield better results than FE, these methods would still fail to fully account for the time-dependence of the NNDs. Since the time-dependence of the NNDs is explicitly modeled by the Bateman equations, calculating quantities of interest coupled to the NNDs in the Bateman equations is the more accurate method. The simplicity of calculating such values in the Bateman equations makes it relatively trivial to implement such functionality, which would then allow said quantities to benefit directly from any predictor-corrector methods implemented for the Bateman equations already.

3.7. Conclusions

The process of calculating non-nuclide quantities of interest to the Bateman equations is straightforward to implement into existing depletion codes. Quantities such as damage-energy, FIMA, and KERMA were calculated using the Bateman equations by modifications to Griffin. For quantities such as FIMA and KERMA, all data necessary to compute them is expected to already be present in any depletion-capable application. In the case of radiation damage, additional data, such as threshold displacement energies (E_d) and damage-energy cross sections (σ_D), must be made available to the code. This may present moderate challenges to existing codes that do not already have a data interface with NJOY [50].

When tracking non-nuclide quantities of interest in the Bateman equations, the sparsity pattern of the depletion matrix may change significantly if the additional rows and columns are not added to the "correct" positions in the matrix, which can cause a degradation in the accuracy of CRAM and potentially other Bateman equation solvers depending on the linear equation solvers used for these solvers, such as SGE. Code developers must be aware of the Bateman equation solver limitations since the calculation of non-nuclide quantities was likely not anticipated when existing methods were developed. Overall, no substantial changes to an existing code are necessary.

The advantage of the proposed method is that it improves radiation damage estimates when significant radiation damage from decay and transmutation products is expected. This problem was only solved for nickel-bearing

alloys using Greenwood's correction factors. However, the production of radiation damage by transmutation products is an often overlooked issue and Greenwood's correction factors for radiation damage in nickel-bearing alloys are rarely used in engineering analysis. In addition, Greenwood's correction factors only work for a single problematic nuclide, but as more materials are considered for existing and advanced reactors, the need for a method that fundamentally solves the problem without an excessive number of experiments or evaluations is growing. As interest in materials which experience very high levels of damage, such as those deployed in nuclear fusion or space applications increases, the ability to quickly and accurately calculate radiation damage in these materials as they undergo neutron transmutation is of great value. Furthermore, there is a lack of publicly available codes capable of calculating damage-energy cross sections for polyatomic materials. More research and development work is needed here.

For other quantities of interest, the advantage is less compelling for quantities such as FIMA and KERMA as the difference between calculating the quantities using FE versus the Bateman equations typically amounted to less than 1%, except when a very small number of depletion intervals were used. When considering the uncertainties introduced by manufacturing tolerances [60] in real-world materials and uncertainties in nuclear data [21] which can easily exceed 1%, a 1% difference in the calculated FIMA or KERMA values is within this uncertainty range. However, for quantities such as decay heat, which are much more sensitive to changes in NNDs, the differences between FE and the Bateman equations were much more significant with FE producing significantly less accurate results. Additionally, modifying the Bateman equations to compute non-nuclide number densities enables the computation of values that otherwise cannot be easily obtained via standard integration rules, such as FE. As an example, a non-nuclide representing the total number of fissions that come from only plutonium isotopes could be added, which would allow analysts and designers to easily discern what percent of their fissions are coming from specifically plutonium isotopes. Such a quantity would be challenging to accurately calculate using FE because of the time-dependent production and destruction of plutonium isotopes in uranium fuel. This is merely an example of what is possible when tracking non-nuclide quantities of interest in the Bateman equations.

Chapter 4: Depletion Chain Simplification Using Pseudo-Nuclides

4.1. Abstract

This paper introduces a method for simplifying the depletion chains and reducing the number of nuclides tracked in a given nuclear system while adding pseudo-nuclides in order to preserve decay heat. Pseudo-nuclides are demonstrated to preserve the decay heat effects of fission product irradiation with fewer nuclides tracked overall than decay heat precursors. The functionality is implemented and tested in the reactor physics application Griffin. Extensive testing is performed using the comprehensive ENDF-B/VIII.0 decay data and microscopic cross-section libraries from ORIGEN and MC^2-3. The impact on the number of nuclides that must be tracked based on effects such as changing cross-section data, changing energy group structure, changing neutron flux spectrum, and tracking decay energy release is explored in this work. Overall, the addition of pseudo-nuclides allows the number of nuclides tracked to be from 1,700 to 400 or fewer nuclides, based on the criteria used in this work.

4.2. Introduction

Nuclear fuel depletion calculations are a crucial component of nuclear engineering as the change in the NNDs of the fuel, control, and structural materials over time in a reactor impacts decay heat, reactivity, material performance, and many other quantities of interest. The Bateman equations [25] [26] can be solved to calculate the change in the NNDs of a system based on initial NNDs, the neutron flux experienced by the nuclides, the microscopic XSs of the nuclides, and the decay and transmutation data of each nuclide (such as decay products and FPYFs). The derivation of the Bateman equations into matrix exponential form has been widely published [29] [61] [28] and a detailed derivation of the Bateman equations is available in Ref. [62]. Consequently I will only consider the matrix exponential form of the Bateman equations as shown:

$$\mathbf{N}(t) = e^{\mathbf{A}t}\mathbf{N}_0 \tag{4.1}$$

where

t	time
$\mathbf{N}_0$	initial NND vector
$\mathbf{N}(t)$	time-dependent NND vector
$\mathbf{A}$	matrix containing the decay and transmutation coefficients

There are many well-established methods for solving matrix exponentials [27], and more specialized methods to solve Eq. 4.1 for real-world nuclear depletion systems have been developed as well [32] [63] [29]. In this work, I used the CRAM [28] already implemented in Griffin [2] at Approximation Order 16 to solve for the NNDs after each depletion interval. The total runtime of solving Eq. 4.1 using CRAM can be expressed using R as the seconds per Bateman equation solve for a given region for a single interval and X depletable regions per central processing unit (CPU) (assuming regions can be evenly distributed among CPUs and that there are many more regions than CPUs) and Y depletion intervals as shown in Eq. 4.2:

$$R\frac{\text{seconds}}{\text{region}\cdot\text{interval}}\times X\frac{\text{regions}}{\text{CPU}}\times Y\text{ intervals} \tag{4.2}$$

From Eq. 4.2 terms X and Y are dependent on the given system being analyzed and computational resources available. In Griffin using CRAM at Approximation Order 16, R is equal to 18.7 milliseconds per Bateman equation solve for a system with 1,600 nuclides and 3.2 milliseconds per Bateman equation solve for a system with 300 nuclides, when running in serial on a 12-core 2.70 GHz Intel Xeon E5-2697 [29]. A roughly linear reduction in runtime is observed as the number of nuclides tracked decreases.

Similarly, the amount of RAM needed, assuming that the NNDs are stored in double-precision, can be calculated as shown in Eq. 4.3. RAM usage does not depend on the number of CPUs or depletion intervals.

$$8\text{ bytes}\times N\text{ nuclides}\times Y\text{ regions} \tag{4.3}$$

As shown in Eqs. 4.2 and 4.3, there is a linear relationship between the number of depletable regions and runtime and RAM usage. If CRAM is used then both runtime and RAM usage scale linearly with the number of nuclides tracked. This presents a challenge to analysts. While it is possible to use CRAM to solve Eq. 4.1 for any number of nuclides, the computational costs in terms of runtime and RAM usage will be far greater if a large number of nuclides are tracked. Reducing the number of nuclides tracked will reduce the resources needed to model a given system and could free up computational resources enabling greater refinement of the depletion calculation. An increase in the number of depletable regions could result in better overall results than a system with fewer depletable regions but more nuclides tracked, depending on the system considered by the analyst.

An example of the total number of depletable regions in real-world reactor modeling include 215,988 [64], 500,000 [65], 909,330 [66], 2,042,712 [33]. Assuming 10^6 depletable regions which all contain fissioning fuel, this would correspond to a memory usage of 13.6 GB for a system with 1,700 nuclides and a runtime of approximately $\frac{5}{n}$ hours per depletion interval where n is the number of CPUs available. Depletion systems with even greater spatial refinement could see use in future analyses, and these systems could benefit significantly from reducing the number of nuclides tracked in the system. Even in the event where greater spatial refinement of the depletion calculation is unnecessary, reduction in memory usage can allow for greater analyst throughput by allowing more simulations to be run simultaneously as well as reductions in computational runtime allowing for greater turnaround time when performing reactor analysis.

4.2.1. Units

Before proceeding further, I will clarify the units used for quantities of interest in Table 4.1. These are commonly used units in the field of nuclear depletion but may be unfamiliar to some.

Quantity	Symbol	Unit	SI Equivalent
Microscopic XS	σ	barn (b)	10^{-28} m^2
Macroscopic XS	Σ	cm^{-1}	100 m^{-1}
NND	N	$\frac{\text{atoms}}{\text{b}\cdot\text{cm}}$	$10^{30}\,\frac{\text{atoms}}{\text{m}^3}$
Energy	E	eV	1.6022×10^{-19} J
Time	t	s	s
Decay Constant	λ	s^{-1}	s^{-1}
Neutron Flux	ϕ	$\frac{\text{neutrons}}{\text{cm}^2\cdot\text{s}}$	$10^4\,\frac{\text{neutrons}}{\text{m}^2\cdot\text{s}}$
Neutron Fluence	F	$\frac{\text{neutrons}}{\text{cm}^2}$	$10^4\,\frac{\text{neutrons}}{\text{m}^2}$

Table 4.1: Units used in this work and their SI equivalents for various physical quantities.

4.3. Background

Depletion chain simplification has been done since the beginning of nuclear engineering as the FPYFs for fissionable nuclides were not known. Once FPYFs for fissionable nuclides and decay data for short-lived FPs were measured, it became theoretically possible to solve Eq. 4.1 for all possible nuclides in a nuclear system. However, simplifications continued to be used to reduce the computational cost of depletion calculations. A common example of depletion chain simplification for fast reactor systems was the use of a pseudo-FP nuclide to model the neutronics impact of all FPs produced in the system [67]. This simplification was considered acceptable for fast reactor systems because of the much lower microscopic XS values of FPs in the fast neutron energy spectrum compared to the thermal neutron spectrum, which has powerful absorbers such as ^{135}Xe.

The need to simplify depletion chains because of mathematical difficulty has been reduced with the development of efficient and accurate methods for solving Eq. 4.1, such as CRAM. However, even with efficient mathematical methods increasing the number of nuclides can significantly increase computational resource usage as discussed in Section 4.2. Thus there remains a desire to reduce the number of nuclides tracked for depletion, and this has resulted in research interest in recent years.

Recent consideration of simplification methods include Chiba et al. [68], who used generalized perturbation theory to determine whether or not an FP could be removed from a given light water reactor (LWR) fuel pin-cell system. This successfully reduced the number of FPs tracked in the system from over 1,000 to 138 while preserving both the neutron multiplication factor and the target NNDs, which consisted of 33 target FP nuclides. Tran et al. [69] similarly considered the simplification of specifically the FPs tracked in the depletion system with the goal of preserving target NNDs. They used a much simpler criteria of simply directly commuting the decay and transmutation chains by removing short-lived intermediate nuclides from the system. This method was shown to reduce a library containing 1,284 FPs down to 193. Kajihara et al. [70] demonstrated the use of single value decomposition to reduce a 1,421 nuclide library down to 204 nuclides for a given LWR system once again seeking to preserve target NNDs and neutron multiplication factor. Zhang et al. [71] developed further on the work of Chiba et al. [68] by introducing an iterative process in addition to the generalized perturbation theory analysis of nuclide removal to achieve a larger reduction in the overall number of nuclides tracked in the simplified depletion library of roughly 8–31%. Once again the focus was on preserving target NNDs and neutron multiplication factor.

Huang et al. [72] and Li et al. [73] both introduced the concept of adding decay heat precursors (DHPs) to the system in order to model decay heat in addition to preserving target NNDs and k. This precursor system, similar to what is done in many reactor analysis applications for modeling delayed neutrons, successfully preserved the production of decay heat in the simplified nuclide library. In order to account for decay heat contributions from FP irradiation, additional target nuclides were added to the system in order to preserve the FP irradiation effect on decay heat for a PWR system [72]. Huang et al. reduced the total number of nuclides tracked in the system from 1,547 to compressed systems with nuclides ranging from 86 to 185 while Li et al. reduced the 1,547 nuclide system to libraries ranging from 182 to 233.

Because of the difficulty in modeling the FP irradiation effect impact on decay heat, the use of precursor groups is less appropriate for decay heat than it is for delayed neutrons. Additionally, the precursor method relies on the generation of DHPs for every fissionable nuclide. Since fissionable nuclides have different FPYFs for thermal and fast neutrons, different DHP yield fractions must be calculated for thermal and fast fissions for all fissionable nuclides of concern. I propose that PNs can be added to the depletion chains in order to account for the FP irradiation effect, as PNs can be added to the depletion library based on user-defined parameters and be produced as both FPs and as products from neutron transmutation or radioactive decay.

4.4. Data Used

This section includes important points regarding the ENDF [5], ORIGEN [38], and MC^2-3 [74] data used in this work and some modifications made to this data.

In Griffin, the decay and transmutation data is stored in a DecayTransmutationLibrary (DTL) while the XS data is stored in a MultigroupLibrary (MGL). Note that the MGL is the actual name of the data structure itself meaning a 1G XS library is still an MGL in Griffin. When performing depletion chain simplification, it is only the DTL in Griffin which is modified, not the MGL, as the DTL contains the actual decay and transmutation chains, the MGL only contains the XS data for nuclides with non-zero XS.

Griffin does not account for depletion caused by photons, with photoneutron and photofission events having microscopic XS on the order of millibarns [75] with most photon transmutation reactions having threshold energies in excess of 5 MeV while the yield of such high-energy photons is relatively low for nuclear fission systems [76]. As a result, no photon-related data is used in this work.

4.4.1. ENDF/B-VIII.0 Decay, Transmutation, and Fission Product Yield Data

The ENDF/B-VIII.0 data provides decay information for 3,820 nuclides as well as decay information for free neutrons [5]. Additionally, ENDF/B-VIII.0 provides FPYFs for many fissionable nuclides [5]. The ENDF/B-VIII.0 data does not provide neutron transmutation information for non-fission reactions. For simplicity, the DTL is loaded with all Griffin-supported transmutation reactions with the exception that only isotopes of radium (Z=88) and heavier elements are capable of undergoing fission. Since no specific non-fission transmutation information is available, Griffin automatically assumes that all transmutation products produced via non-fission transmutation reactions will be in the ground state. This is not physically true as there are several transmutation reactions which result in the significant production of nuclear isomers, some of which are very important to accurately model, such as the fissile ^{242m}Am. Since ORIGEN and MC^2-3 are used to solely provide XS data, they provide no information on whether or not a given transmutation product should be in the ground or metastable state. Consequently, I used the metastable branching ratios specified in the Serpent code [37], which could be easily implemented in the ENDF/B-VIII.0 DTL produced by Griffin. Strictly speaking, the metastable branching ratios for (n,x) reactions have an energy dependence associated with them, but this is not considered in the data provided by Serpent and is also not supported by the DTL format in Griffin thus the energy-dependence is not considered in this work.

When XS data is provided from a given MGL, Griffin automatically removes the neutron transmutation pathways which do not have non-zero XS values in the provided MGL. As an example of this, the ENDF decay data provides decay data for both ^{5}He and ^{6}He. Griffin, when loading the pure decay data from ENDF, assumes the ^{5}He(n,γ)^{6}He is possible. However, since neither of the MGLs used in this work provide non-zero XS data for ^{5}He, Griffin removes this transmutation pathway from the DTL when an MGL is provided. This can result in a reduction in the overall number of nuclides tracked in the depletion calculations because there is no possible production pathway for certain nuclides based on the initial NNDs of the system.

As mentioned previously, ENDF/B-VIII.0 provides FPYFs for neutron-induced fission events. ENDF/B-VIII.0 provides the incident fission-inducing neutron energy which results in the given FPYFs. Some fissionable nuclides have multiple sets of FPYFs which correspond to different incident neutron energies. Griffin supports specifying multiple FPYFs for different incident neutron energies for fissionable nuclides. If the neutron energy for each energy group is provided in the MGL then Griffin performs linear interpolation between provided FPYFs in the DTL in order to determine the FPYFs for fission from neutrons in each given energy group. If the neutron energy for an energy group in the MGL is outside of the range of the incident neutron energies specified in the

DTL for a given fissionable nuclide then the FPYFs corresponding to the nearest-neighbor incident neutron energy in the DTL are used. If neutron energy is not available in the MGL then Griffin uses the FPYFs corresponding to the lowest incident neutron energy for which FPYFs are provided in the DTL for each nuclide.

ENDF/B-VIII.0 does not provide FPYFs for all fissionable nuclides, some nuclides do not have neutron-induced FPYFs and many do not have spontaneous FPYFs. Griffin assumes that if no FPYFs are provided in the DTL then the fissioning nuclide is assumed to be destroyed with no FPs produced at all.

4.4.2. ORIGEN 1G XS Data

The ORIGEN XS data is a 1G library for a Westinghouse 17-by-17 PWR assembly at 5 wt% enrichment. In ORIGEN this library is one of the pre-generated "ARPLIBs" distributed with ORIGEN. The original library is indexed with burnup for the lifetime of an assembly; however, only the first set of values, representing the beginning-of-life for the PWR fuel, is used in this work for simplicity. The library consists of non-zero microscopic XSs for 675 nuclides, which is considered representative of the upper limit of available XS data. This XS data is converted from the ORIGEN-specific format into the Griffin-supported MGL format. For this library, the only two macroscopic XS values calculated and used in the simplification process are the total XS (Σ_t) and the fission XS (Σ_f) as no other XS values related to neutron transport or energy release are provided by the ORIGEN data. I do not consider depletion-specific macroscopic XS values, such as (n,γ), because these values are only relevant when it comes to accurately calculating the NNDs of nuclides of interest. Since accurately calculating the NNDs of the target nuclides will already serve as a constraint during the simplification process discussed in Section 4.5, preservation of these depletion-specific macroscopic XS values is considered redundant.

The ORIGEN XS data does not provide a characteristic neutron energy for the single neutron energy group, meaning that Griffin used the lowest-energy FPYFs from ENDF-B/VIII.0 when performing depletion calculations using the ORIGEN MGL.

4.4.3. MC^2-3 Multi-Group XS Data

The MC^2-3 application [74] (henceforth referred to as simply MC^2) can be used to generate XS data for up to 390 nuclides, with the caveat that three of these nuclides correspond to elemental XS data for carbon, vanadium, and zinc. Since Griffin does not support specifying elemental XS data while specifying decay and transmutation data on an isotopic basis, it is asserted that these microscopic elemental XS values are the same as the microscopic XS values for all naturally-occurring isotopes of each element even though physically all nuclides have unique XS values, even nuclides which are isotopes of the same element. Examples of this include ^{135}Xe being a powerful neutron absorber while other xenon isotopes are not nearly as significant and ^{13}C having a resonance peak in the 100-200 keV range in its XS [77] while ^{12}C does not [78]. The reason for this non-physical assumption is to increase the overall number of nuclides tracked by the system and because alternatives such as assuming the carbon XS provided was only applicable to ^{12}C would also be non-physical since the elemental carbon XS has a contribution from ^{13}C. This brings the total number of nuclides with non-zero XS data in Griffin using the MC^2 data to 396. MC^2 supports a wide range of neutron energy group structures from two to 2,082. Only a two-group (2G) library is generated for the purposes of demonstrating the impact of multiple energy groups on the simplification process.

MC^2 provides far more XS quantities than are provided in the ORIGEN XS data. For the simplification process, I only considered the macroscopic XS quantities listed in Table 4.2 as these are the quantities which will impact neutron transport and energy release. The exception to this is the omission of the scattering XS (Σ_s) which is omitted because, in Griffin, Σ_s is stored as a matrix which can be difficult to handle when determining how best

to preserve Σ_s, particularly when some values in the matrix may be quite small. It is anticipated that preserving other XS quantities such as Σ_t should result in preservation of Σ_s as a byproduct, but further research is needed. In Table 4.2, I provided the name of each XS quantity in Griffin and for the remainder of this work will refer to these XS quantities using the provided symbol for brevity.

Name	Symbol	Griffin Name
Total	Σ_t	Total
Fission	Σ_f	Fission
Transport	Σ_{tr}	Transport
Removal	Σ_r	Removal
Energy Release From All Reactions	Σ_{ed}	EnergyDeposition

Table 4.2: XS quantities provided by MC^2 used for the depletion chain simplification process in Griffin.

The XSs are generated in MC^2 with a temperature of 300 K and an infinite homogeneous region with all nuclides having an NND of 10^{-10} $\frac{\text{atoms}}{\text{b·cm}}$. As mentioned previously, in MC^2 some XS values are provided on an elemental basis, in which case it is assumed that the element has an NND of 10^{-10} $\frac{\text{atoms}}{\text{b·cm}}$. The NND values are simply chosen to be relatively small values such that the microscopic XS values will be generated for the simplification process rather than attempting to generate XS libraries that account for any physical effects seen in reactors, such as self-shielding or Doppler broadening. MC^2 provides incident neutron energies for each energy group meaning Griffin is able to perform linear interpolation to calculate FPYFs for fissionable nuclides with multiple sets of FPYFs for different incident neutron energies.

4.4.4. Data Pre-Processing

When considering the transmutation pathways for which there is non-zero XS data, an initial system fueled with UO_2 will only have decay and transmutation pathways to a total of 1,692 nuclides based on the ORIGEN XS data, while there are a total of 1,725 nuclides based on the MC^2 XS data for the 2G library.

As expected, different MGLs coupled with the same DTL result in varying numbers of nuclides to track. As more XS measurements are made for currently unmeasured nuclides, the theoretical maximum number of nuclides to track in a given nuclear system will increase. With the current data, I considered the ENDF-ORIGEN and ENDF-MC^2 DTLs to be quite comprehensive in terms of the upper limits of possible nuclides to track in a nuclear fission system.

I then considered the range of the non-zero decay constants in both DTLs. Both DTLs had the same maximum and minimum decay constants which corresponded to ^{8}Be with a decay constant of 8.47×10^{15} s^{-1} and ^{186}W with a decay constant of 1.29×10^{-28} s^{-1}. In particular, ^{8}Be was an extreme outlier with the next largest decay constant of 4.62×10^6 s^{-1} belonging to ^{72}Fe. Consequently the decay constants span about 44 orders of magnitude which could pose a challenge to some methods of generating pseudo-nuclides in Section 4.5.2. Thus some pre-processing is done to reduce the range of decay constants. The decay constant of ^{8}Be is set to 4.62×10^6 s^{-1}, the same as ^{72}Fe and all radionuclides with decay constants less than that of ^{238}U (4.92×10^{-18}) are assumed to be stable as these radionuclides will not decay in significant quantities on reactor timescales. These radionuclides which were assumed to be stable are shown in Table 4.3.

Preprocessing reduces the range of decay constants from 44 orders of magnitude to roughly 24 orders of magnitude, a significant reduction. The preprocessing also results in the loss of a production pathway for ^{228}Ra in both DTLs as it was only produced by the decay of ^{232}Th. The ENDF-MC^2 DTL loses an additional three nuclides, ^{49}Cr, ^{50}Cr, and ^{187}Os. The loss of these additional nuclides is the result of MC^2 not having microscopic XS data

Nuclide	λ [s^{-1}]	Nuclide	λ [s^{-1}]	Nuclide	λ [s^{-1}]
^{232}Th	1.56×10^{-18}	^{174}Hf	1.10×10^{-23}	^{150}Nd	2.78×10^{-27}
^{176}Lu	5.84×10^{-19}	^{186}Os	1.10×10^{-23}	^{128}Te	2.50×10^{-27}
^{187}Re	5.07×10^{-19}	^{144}Nd	9.59×10^{-24}	^{209}Bi	1.16×10^{-27}
^{87}Rb	4.57×10^{-19}	^{148}Sm	3.14×10^{-24}	^{96}Zr	1.10×10^{-27}
^{138}La	2.15×10^{-19}	^{113}Cd	2.73×10^{-24}	^{48}Ca	9.55×10^{-28}
^{147}Sm	2.07×10^{-19}	^{204}Pb	1.58×10^{-25}	^{116}Cd	7.09×10^{-28}
^{190}Pt	3.38×10^{-20}	^{50}V	1.57×10^{-25}	^{186}W	1.29×10^{-28}
^{152}Gd	2.03×10^{-22}	^{180}W	1.22×10^{-26}		
^{115}In	4.98×10^{-23}	^{100}Mo	3.01×10^{-27}		

Table 4.3: Decay constants of radionuclides with half-lives longer than ^{238}U.

for the production of these nuclides via transmutation, meaning that these nuclides lost production pathways when the nuclides in Table 4.3 were assumed to be stable. This reduces the ENDF-ORIGEN DTL to 1,691 nuclides and the ENDF-MC^2 DTL to 1,721 nuclides.

From testing, this preprocessing introduces minimal changes during depletion aside from the expected nine order of magnitude increase in the calculated NND of ^{8}Be, which is still quite small. As a result, these preprocessed DTLs will be used for the remainder of this work.

I briefly considered the recoverable decay energy released by each radionuclide. This is to determine if any radionuclides may require special treatment or handling when attempting to remove them from the depletion chains. A radionuclide which releases a significantly larger amount of decay energy and undergoes a significant amount of radioactive decay on reactor timescales could pose a challenge when attempting to remove said radionuclide from the system because of its unique contribution to decay heat. The recoverable decay energies of the radionuclides in both DTLs largely range from 1 keV to 10 MeV, with two major outliers. These outliers correspond to ^{250}Cm, which has an average recoverable decay energy of 141 MeV because of its high probability to undergo spontaneous fission, and ^{235m}U, which has an average recoverable decay energy of 56.8 eV as a very low-energy nuclear isomer. Despite these two outliers, the decay energies of all radionuclides span roughly six orders of magnitude, which is not expected to introduce any difficulties in modeling decay energy, thus no preprocessing is done with respect to decay energy. Additionally the outlier of ^{250}Cm has a half-life on the order of 8,000 years meaning it will not undergo significant radioactive decay on reactor timescales. The variation in the recoverable decay energies of the radionuclides is a further complication to how each radionuclide affects decay heat calculations, as the release of decay heat by a radionuclide is dependent on its NND, decay constant, and decay energy.

4.5. Heuristic Method

A heuristic trial-and-error method is used in order to determine the nuclides that should be tracked in order to accurately calculate certain quantities in a nuclear system under certain depletion conditions. In this work, a specified flux spectrum is used to deplete an infinite homogeneous region to the given points in time. After each depletion step, the NNDs and macroscopic XSs are computed using all nuclides in the reference DTL. I then iteratively removed individual nuclides from the reference DTL (excluding target nuclides), recalculated the NNDs of all remaining nuclides in the now-simplified DTL at all points in time, and checked to see if the results of the simplified DTL agree with the results from the reference DTL within a given tolerance.

4.5.1. Removing a Nuclide

In order to demonstrate the removal process, consider a restricted depletion chain consisting of ^{235}U undergoing fission and producing the FP ^{135}Te and ^{135}Xe capable of undergoing (n,γ) to produce ^{136}Xe or undergoing β^- decay to ^{135}Cs.

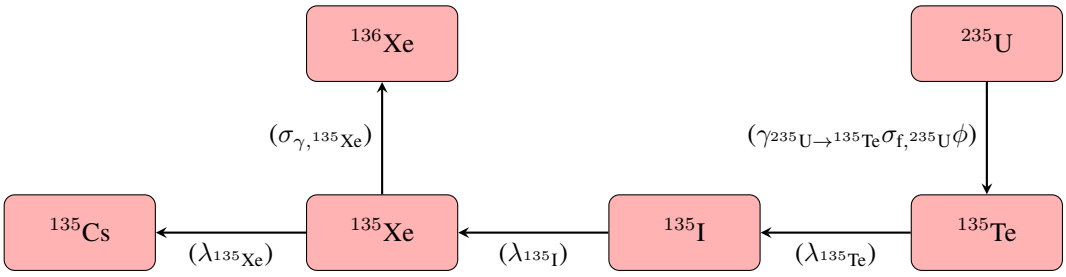

Figure 4.1: Hypothetical decay and transmutation diagram of a restricted depletion chain from the fission of ^{235}U.

With the values defined in Table 4.4 it becomes possible to solve the system analytically. In addition to the values provided it is assumed that ^{235}U, ^{136}Xe, and ^{135}Cs are all stable ($\lambda = 0$) and that all microscopic XS values for all reactions are zero except for $\sigma_{\mathrm{f},^{235}\mathrm{U}}$ and $\sigma_{\gamma,^{135}\mathrm{Xe}}$.

Quantity	**Value**	**Quantity**	**Value**	**Quantity**	**Value**
$N_{^{235}\mathrm{U}}$	$1\ \frac{\text{atoms}}{\text{b}\cdot\text{cm}}$	ϕ	$10^{14}\ \frac{\text{neutrons}}{\text{cm}^2\cdot\text{s}}$	$\sigma_{\mathrm{f},^{235}\mathrm{U}}$	20 b
$\lambda_{^{135}\mathrm{Te}}$	$0.04\ \text{s}^{-1}$	$\lambda_{^{135}\mathrm{I}}$	$2.9 \times 10^{-5}\ \text{s}^{-1}$	$\lambda_{^{135}\mathrm{Xe}}$	$2.1 \times 10^{-5}\ \text{s}^{-1}$
$\sigma_{\gamma,^{135}\mathrm{Xe}}$	10^5 b	$\gamma_{^{235}\mathrm{U}\rightarrow^{135}\mathrm{Te}}$	100%		

Table 4.4: Hypothetical quantities for solving the decay and transmutation system outlined in Figure 4.1.

I compute the analytic solution for the depletion chain in Figure 4.1 using the values defined in Table 4.4 for several points in time. Because of the values and assumptions used, the total NND of the system remains unchanged, meaning the sum of all NNDs should be the same at every point in time.

	NND at each point in time $[\frac{\text{atoms}}{\text{b}\cdot\text{cm}}]$					
Nuclide	0 s	60 s	3600 s	86400 s	864000 s	1728000 s
^{235}U	1.000	1.000	1.000	9.998×10^{-1}	9.983×10^{-1}	9.965×10^{-1}
^{135}Te	0	4.546×10^{-8}	5.000×10^{-8}	4.999×10^{-8}	4.991×10^{-8}	4.983×10^{-8}
^{135}I	0	7.449×10^{-8}	6.792×10^{-6}	6.332×10^{-5}	6.885×10^{-5}	6.873×10^{-5}
^{135}Xe	0	5.031×10^{-11}	3.452×10^{-7}	4.712×10^{-5}	6.441×10^{-5}	6.430×10^{-5}
^{135}Cs	0	1.746×10^{-14}	8.795×10^{-9}	4.220×10^{-5}	1.079×10^{-3}	2.247×10^{-3}
^{136}Xe	0	8.315×10^{-15}	4.188×10^{-9}	2.009×10^{-5}	5.139×10^{-4}	1.070×10^{-3}

Table 4.5: Analytic solution to the depletion chain presented in Figure 4.1.

When a nuclide is removed from the system, it is assumed that whenever the nuclide would have been produced it instead immediately produces its decay products. This can be visualized in Figure 4.2 where ^{135}Te is removed from the system.

The analytic solution to the new system without ^{135}Te can be calculated for the same points in time as shown in Table 4.6. For short periods of time, there is a large relative change in the NNDs of the remaining nuclides in the ^{135}Te decay chain as the removal of ^{135}Te from the system "accelerates" the production of its decay products. Since ^{135}Te is a short-lived nuclide, this effect is noticed when the NNDs of the subsequent members of the decay

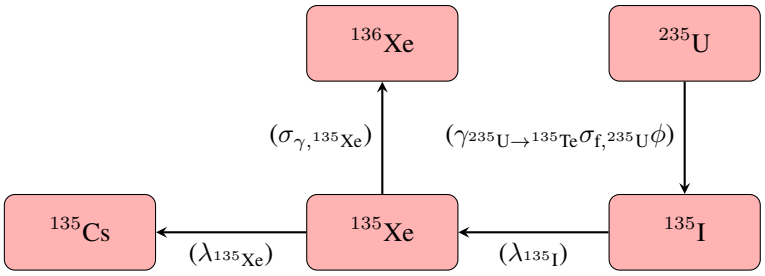

Figure 4.2: Hypothetical decay and transmutation diagram of a restricted depletion chain from the fission of ^{235}U with ^{135}Te removed from the system.

chain are less than the saturation density of ^{135}Te. Once the NNDs of the decay products of ^{135}Te begin to exceed the saturation density of ^{135}Te the relative impact of the removal of ^{135}Te on the NNDs of its decay products becomes less and less significant as the overall saturation densities of ^{135}I and ^{135}Xe are much larger than the saturation density of ^{135}Te and the removal of ^{135}Te does not have a significant impact on these quantities. Based on these results, an analyst may conclude that it is unnecessary to track ^{135}Te for the system they are analyzing.

	NND at each point in time [$\frac{\text{atoms}}{\text{b}\cdot\text{cm}}$]					
Nuclide	0 s	60 s	3600 s	86400 s	864000 s	1728000 s
^{235}U	1.000	1.000	1.000	9.998×10^{-1}	9.983×10^{-1}	9.965×10^{-1}
^{135}I	0	1.199×10^{-7}	6.837×10^{-6}	6.333×10^{-5}	6.885×10^{-5}	6.873×10^{-5}
^{135}Xe	0	1.043×10^{-10}	3.498×10^{-7}	4.713×10^{-5}	6.441×10^{-5}	6.430×10^{-5}
^{135}Cs	0	4.384×10^{-14}	8.976×10^{-9}	4.222×10^{-5}	1.079×10^{-3}	2.247×10^{-3}
^{136}Xe	0	2.088×10^{-14}	4.274×10^{-9}	2.011×10^{-5}	5.139×10^{-4}	1.070×10^{-3}

Table 4.6: Analytic solution to the depletion chain presented in Figure 4.2 where ^{135}Te has been removed.

In order to illustrate the limitations of the method of nuclide removal used in this work, I next considered the same depletion system as shown in Figure 4.2 except ^{135}Xe is also removed from the system. Since it is assumed that when a nuclide is removed from the system its decay products are produced, this results in the loss of the transmutation pathway for the production of ^{136}Xe as shown in Figure 4.3.

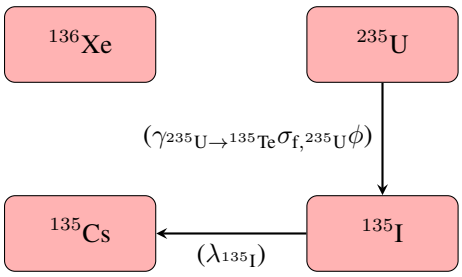

Figure 4.3: Hypothetical decay and transmutation diagram of a restricted depletion chain from the fission of ^{235}U with ^{135}Te and ^{135}Xe removed from the system.

Once again the analytic solution is calculated for the same points in time using the depletion chain in Figure 4.3 as shown in Table 4.7.

As expected, the NNDs of ^{135}Cs and ^{136}Xe deviate significantly as ^{136}Xe is no longer produced by the system and the loss of ^{135}Xe has resulted in a significant increase in the NND of ^{135}Cs as the neutron transmutation of

	NND at each point in time [$\frac{\text{atoms}}{\text{b}\cdot\text{cm}}$]					
Nuclide	0 s	60 s	3600 s	86400 s	864000 s	1728000 s
^{235}U	1.000	1.000	1.000	9.998×10^{-1}	9.983×10^{-1}	9.965×10^{-1}
^{135}I	0	1.199×10^{-7}	6.837×10^{-6}	6.333×10^{-5}	6.885×10^{-5}	6.873×10^{-5}
^{135}Cs	0	1.043×10^{-10}	3.631×10^{-7}	1.095×10^{-4}	1.658×10^{-3}	3.381×10^{-3}
^{136}Xe	0	0	0	0	0	0

Table 4.7: Analytic solution to the depletion chain presented in Figure 4.3 where ^{135}Te and ^{135}Xe have been removed.

^{135}Xe is no longer considered and the "delay" in the production of ^{135}Cs from ^{135}I decaying into ^{135}Xe which then decays into ^{135}Cs has been removed with ^{135}I decaying directly into ^{135}Cs. Since unlike ^{135}Te, ^{135}I and ^{135}Xe both had similar decay constants and similar saturation NNDs, the removal of ^{135}Xe has a significant impact on the production of ^{135}Cs, in addition to the loss of the transmutation pathway for ^{136}Xe. This demonstrates an instance where removing a nuclide is likely undesirable as the transmutation pathway from ^{135}Xe to ^{136}Xe was quite significant combined with the fact that ^{135}Xe is a powerful absorber of thermal neutrons which has a significant impact on the reactivity of a thermal reactor system.

Overall, the process of removing a nuclide and replacing it with its decay products is quite simple and relatively intuitive, particularly for short-lived nuclides for which there is no known XS data and thus the loss of production pathways via neutron transmutation is irrelevant. These short-lived nuclides without XS data are expected to make up most of the nuclides removed from the system during the simplification process. The loss of transmutation pathways during nuclide removal is a constraint which will ultimately result in more nuclides being tracked in order to preserve transmutation pathways which have a significant impact on the target NNDs and the macroscopic XSs of the system.

Theoretically, transmutation pathways could attempt to be preserved between nuclides using some sort of weighting based on the XS values of the removed nuclide, but this is not done for several reasons. The main reason being this would require replacing a removed nuclide with both its decay products and its transmutation products whenever the removed nuclide was produced. This is problematic when considering that nuclide production from radioactive decay is completely independent from the flux conditions experienced by the system. If the transmutation products of a removed nuclide can be produced whenever the removed nuclide's decay parent undergoes radioactive decay this could cause problems in instances where the flux in the system is zero, but transmutation products are still being produced via radioactive decay.

Another reason for the complete removal of the transmutation chains of removed nuclides is that the rate at which individual neutron transmutation reactions occur is dependent on the energy of the incident neutron causing the reaction. For most nuclides, at high incident neutron energies reactions such as (n,2n) and (n,p) are more likely to occur. By contrast, at lower incident neutron energies reactions such as (n,γ) are dominant. This means that any attempt to add the transmutation products of a removed nuclide to a simplified DTL would require the DTL to somehow account for the energy spectrum of the flux system during depletion, which is not desirable as the decay and transmutation pathways themselves should remain constant with any energy-dependence accounted for by the actual XS quantities in the MGL.

Because of the challenges mentioned above, transmutation pathways for removed nuclides are simply removed entirely which is the process followed by many of the authors mentioned in Section 4.3. Consequently, if a nuclide has a transmutation pathway of importance which may significantly impact either the macroscopic XS or the target NNDs then the nuclide will have to be preserved in the system in order to preserve this transmutation pathway.

The preservation of transmutation pathways when simplifying depletion chains is a potential research topic of interest for the future.

4.5.2. Adding Pseudo-Nuclides During Nuclide Removal

Griffin supports user-defined PNs, which can represent molecules, elements, or specific crystal structures of materials, typically to preserve the effect of chemical bonds on microscopic XS values. This functionality is used in Griffin to dynamically create PNs which can undergo radioactive decay in order to preserve the decay energy released during depletion.

Consider Figure 4.1 except that an entry has been added that represents the release of decay energy in the system from radionuclides undergoing radioactive decay as shown in Figure 4.4.

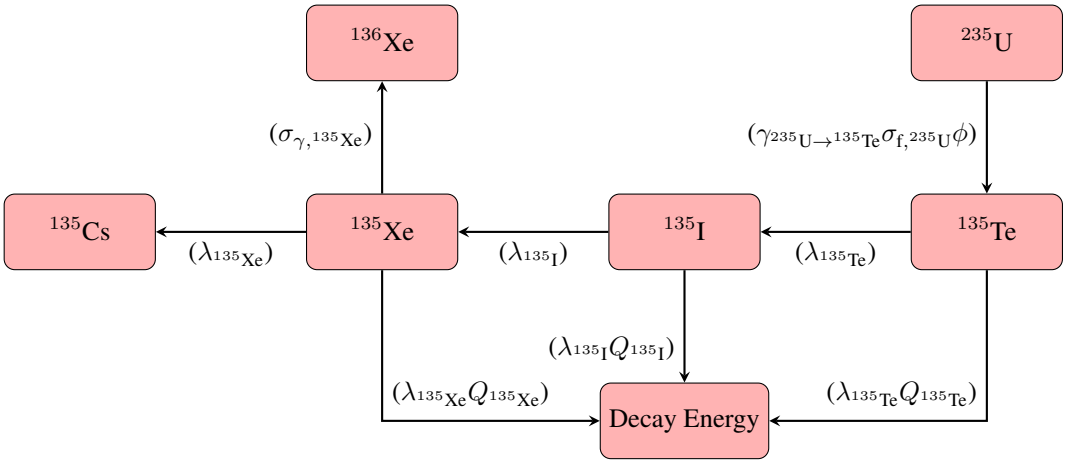

Figure 4.4: Figure 4.1 with the release of decay energy from radioactive decay included.

Note that while decay energy is tracked as though it were an NND it is physically not an NND but rather an energy density term Griffin tracks with units of $\frac{\mathrm{MeV}}{\mathrm{b\cdot cm}}$. When tracking decay energy release in the Bateman equations, Griffin refers to this quantity as "DecayEnergy," which will be used in this work when referring to the decay energy release calculated by Griffin. The ability of Griffin to calculate non-NND quantities, such as decay energy release, as part of the Bateman equations has been documented previously [79] and is not repeated here.

By asserting that ^{135}Te has a decay energy of 3 MeV, ^{135}I has a decay energy of 2 MeV and ^{135}Xe has a decay energy of 0.5 MeV, the total decay energy released by the system at any point in time can be calculated.

The addition of decay energy to the system now makes it more difficult to consider removing a radionuclide as this will overall reduce the amount of decay energy released by the system unless the decay energy release is somehow preserved. I considered two additional altered depletion chains from Figure 4.4, one in which ^{135}Te and ^{135}I are completely removed from the system and their contributions to the decay energy of the system are lost entirely as shown in Figure 4.5, and one in which ^{135}Te and ^{135}I are removed from the system, but two PNs are added to the system which have the same decay constants as ^{135}Te and ^{135}I and release the same amount of decay energy as ^{135}Te and ^{135}I as shown in Figure 4.6.

The analytic solution to the total decay energy released by the radionuclides at each point in time can be determined for all three systems considered as shown in Table 4.8.

It is clear that adding the PNs to the system significantly improves the overall modeling of decay energy release, however, the method is not perfect as even when PNs are added which have the exact same decay constant and decay energy release as the removed radionuclides, there is still a discrepancy introduced as a result of the

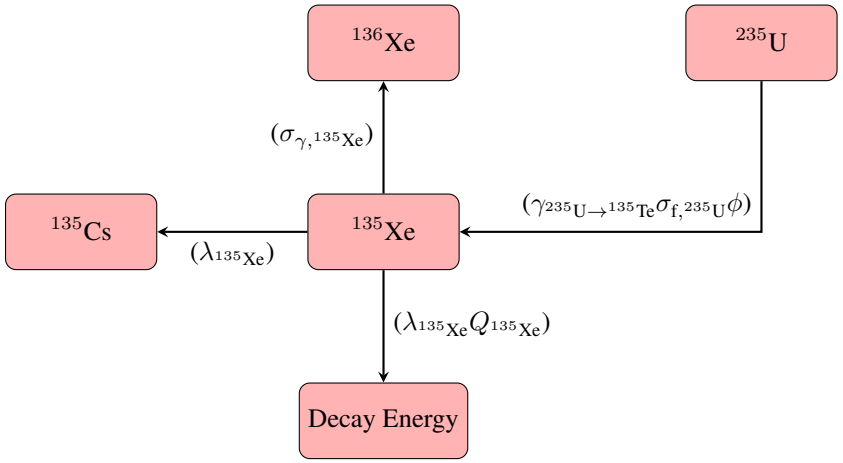

Figure 4.5: Figure 4.4 with ^{135}Te and ^{135}I removed from the system.

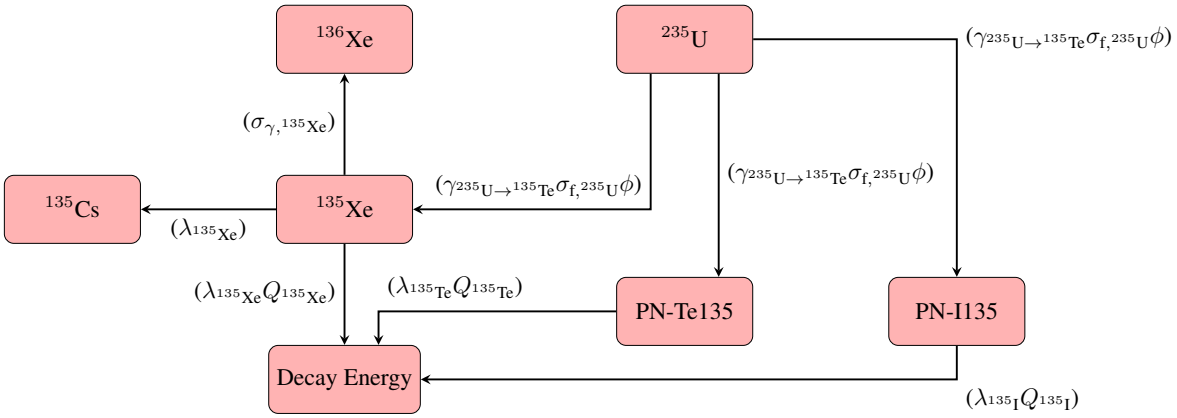

Figure 4.6: Figure 4.4 with ^{135}Te and ^{135}I removed from the system and replaced with PNs which model the decay energy they release.

	Density of decay energy released at each point in time [$\frac{\text{MeV}}{\text{b}\cdot\text{cm}}$]					
System	0 s	60 s	3600 s	86400 s	864000 s	1728000 s
Figure 4.4	0	2.237×10^{-7}	2.217×10^{-5}	7.581×10^{-4}	9.034×10^{-3}	1.824×10^{-2}
Figure 4.5	0	3.778×10^{-11}	1.312×10^{-7}	3.817×10^{-5}	5.630×10^{-4}	1.147×10^{-3}
Figure 4.6	0	2.239×10^{-7}	2.231×10^{-5}	7.753×10^{-4}	9.058×10^{-3}	1.826×10^{-2}

Table 4.8: Analytic solution to the depletion chain presented in Figure 4.3 where ^{135}Te and ^{135}Xe have been removed.

PNs not being produced in exactly the same way as the removed nuclide. In the case of the PNs which replaces ^{135}I, the PN-I135 in Figure 4.6 releases decay energy slightly faster than ^{135}I in Figure 4.4 because the production of ^{135}I is delayed by the decay of ^{135}Te while PN-I135 is produced directly from ^{235}U. Additionally, because ^{135}Xe is produced directly by ^{235}U in Figure 4.6, this will also result in ^{135}Xe releasing slightly more decay energy in this system than in Figure 4.4 because the ^{135}Xe is produced directly from ^{235}U and thus more ^{135}Xe undergoes radioactive decay and releases decay energy. Overall though, the PNs perform well for this small system considered.

In order to fully understand the process of adding PNs to the system a more complicated depletion chain is shown in Figure 4.7.

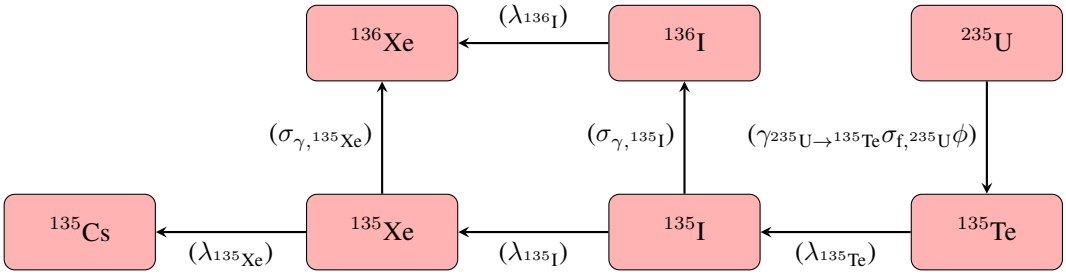

Figure 4.7: A more extensive ^{235}U depletion chain.

To demonstrate adding PNs as FPs, transmutation products, and decay products, I will remove ^{135}Te, ^{136}I, and ^{135}Xe from the system. Since removing ^{135}Xe will result in a dramatic underprediction in the NND of ^{136}Xe because of the loss of the (n,γ) transmutation pathway I do not calculate the analytic solution for Figure 4.7 or the simplified version. Additionally, I assume that ^{135}Te and ^{136}I have close enough decay constants that they can have their decay energy calculated by a single PN referred to as PN-1. ^{135}Xe has a smaller decay constant and thus will have its decay energy modeled by PN-2. The results of the simplification process are shown in Figure 4.8 with Decay Energy added to show the release of decay energy from the PNs in addition to its production via the remaining radionuclides in the system. ^{235}U produces PN-1 as a FP to model the decay energy of ^{135}Te, while ^{135}I produces PN-1 as a transmutation product to model the decay energy of ^{136}I, and ^{135}I produces PN-2 as a decay product to model the decay energy of ^{135}Xe.

For practical modeling purposes it is not feasible to add PNs with unique decay constants and decay energy for every single removed nuclide. Thus a restricted number of PNs must be added to the system which can model both the decay energy release and the decay constants of the removed nuclides. First, it is asserted that all PNs decay with an energy of 1 MeV with the rate of production of the PN scaled based on the actual decay energy Q of the removed radionuclide the PN is modeling the decay energy of. An example of this would be that in Figure 4.6 this would result in PN-Te135 being produced from ^{235}U at a rate of $3\gamma_{^{235}\mathrm{U}\rightarrow^{135}\mathrm{Te}}\sigma_{\mathrm{f},^{235}\mathrm{U}}\phi$ while contributing to overall decay energy release at a rate of $\lambda_{^{135}\mathrm{I}}1.0$ MeV, resulting in the same overall release of decay energy. While this accounts for the varying decay energy of each radionuclide, the decay constants of the PNs need to be determined.

After testing several different methods for calculating the decay constants of the PNs using the ENDF-ORIGEN DTL which involved dividing the non-zero decay constants into ordered sub-series and taking the arithmetic, geometric, harmonic, and logarithmic means and the median of each sub-series to determine the decay constants of the PNs with removed nuclides having their decay energy release modeled using the PN with the decay constant which was calculated from the sub-series that the removed nuclide was part of. Weighting with

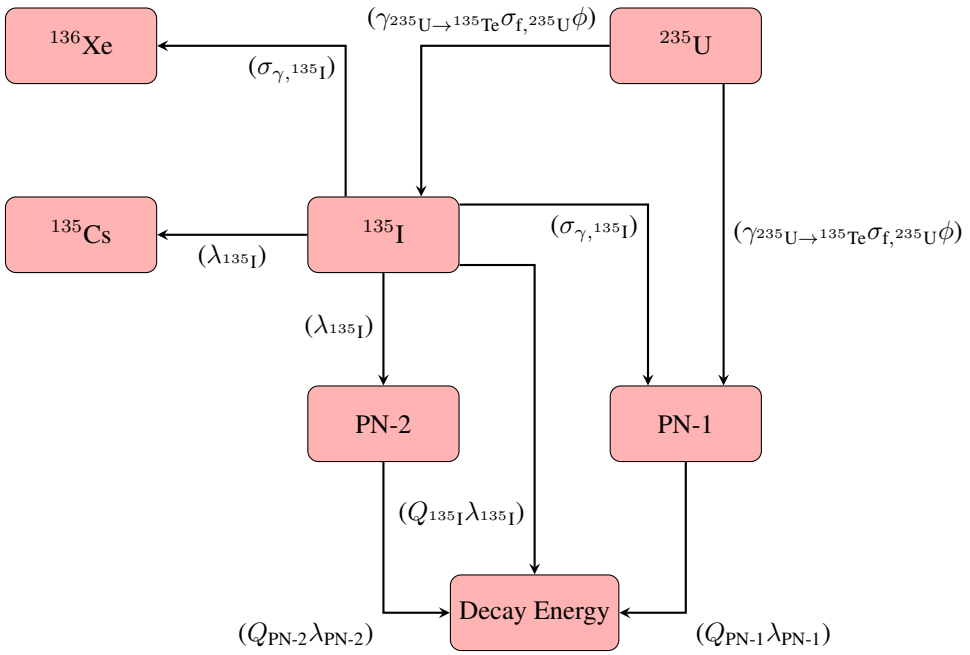

Figure 4.8: A more extensive ^{235}U depletion chain simplified with PNs.

decay energy release was also tested, but this did not result in a significant reduction in the overall number of nuclides tracked. Methods involving the arithmetic and harmonic means did not perform well as the distribution of decay constants resulted in both means being heavily biased to the upper or lower end of the sub-series. The geometric mean, logarithmic mean, and median methods all performed comparably, with the median sub-series method selected for the remainder of this work because of its simplicity and slightly fewer total nuclides tracked. More research regarding the calculation of optimized decay constants of the PNs is needed, but for the purposes of demonstrating the value of PNs for decay energy modeling in this work, the median sub-series method is considered satisfactory.

Overall, adding PNs for tracking decay energy release is similar to the DHP methodology introduced by Huang et al. [72] and Li et al. [73] with the primary difference being that PNs are able to account for the FP irradiation effect where FPs undergo neutron transmutation and produce radionuclides that can significantly contribute to decay heat. This is advantageous as this avoids needing to specify additional target nuclides in order to account for this irradiation effect.

4.5.3. Applying Tolerances

It is asserted that there are two tolerances to apply when performing depletion chain simplification: one for macroscopic XSs (T_Σ) and one for the NNDs of target nuclides (T_N). The reason for separating the two tolerances is that the macroscopic XS will impact reactivity and reactivity is expected to be modeled more accurately than the target NNDs.

$$\begin{aligned} \left| \frac{\Sigma^g_{\mathrm{R},r} - \Sigma^g_{\mathrm{S},r}}{\Sigma^g_{\mathrm{R},r}} \right| &\leq T_\Sigma \\ \left| \frac{N_{\mathrm{R},i} - N_{\mathrm{S},i}}{N_{\mathrm{R},i}} \right| &\leq T_N \end{aligned} \tag{4.4}$$

where

$\Sigma^g_{\mathrm{R},r}$	macroscopic XS value of reaction type r in energy group g calculated by the reference DTL
$\Sigma^g_{\mathrm{S},r}$	macroscopic XS value of reaction type r in energy group g calculated by the simplified DTL
$N_{\mathrm{R},i}$	NND of target nuclide i calculated by the reference DTL
$N_{\mathrm{S},i}$	NND of target nuclide i calculated by the simplified DTL.

For the simplification process, the user provides Griffin an MGL (containing the microscopic XS data), a DTL (containing the decay and transmutation data), a vector of multiple sequential depletion interval lengths ($\mathbf{t}$), a vector of the neutron flux spectrum at each depletion interval ($\boldsymbol{\phi}$), a vector of the target nuclides ($\mathbf{I}_N$), the tolerances T_Σ and T_N, and the initial NNDs ($\mathbf{N}_0$). The reference NNDs ($\mathbf{N}_\mathrm{R}$) are calculated using the reference DTL specified by the user where the group-dependent microscopic XS matrix ($\boldsymbol{\sigma}$) is provided by the given MGL and the decay matrix ($\mathbf{D}$) is provided by the given DTL.

$$\begin{aligned} \mathbf{A}_\mathrm{R}(t) &= \mathbf{D}_\mathrm{R} + \sum_{g=1}^{G} \boldsymbol{\sigma}^g_\mathrm{R} \phi^g(t) \\ \frac{d\mathbf{N}_\mathrm{R}(t)}{dt} &= \mathbf{A}_\mathrm{R}(t)\mathbf{N}_\mathrm{R}(t) \\ \mathbf{N}_\mathrm{R}(t) &= \mathbf{N}_{\mathrm{R},0} e^{\mathbf{A}_\mathrm{R} t} \end{aligned} \tag{4.5}$$

Once the reference NNDs are calculated using the reference DTL for every point in time specified by the user, the next step is to save the NNDs of all target nuclides specified by the user and calculate the reference macroscopic XS values at each point in time for all energy groups ($\boldsymbol{\Sigma}^g_\mathrm{R}$). Once the target NNDs and macroscopic XS values have been calculated using the reference DTL, I can begin the simplification process by removing nuclides using the process defined in Section 4.5.1. With this new simplified DTL, I recomputed the NNDs for all depletion intervals for all nuclides tracked in the simplified DTL. Eq. 4.5 is solved except that the simplified matrices and NNDs from the simplified DTL are used instead of using the reference matrices and NNDs from the reference DTL.

With the simplified NNDs calculated, the macroscopic XS values at each point in time based on the simplified NNDs are calculated. Griffin then compares the NNDs of target nuclides and the macroscopic XS values calculated by the simplified DTL to the values calculated by the reference DTL, as specified in Eq. 4.4. If the simplified values do not exceed the specified tolerances at all points in time specified by the user for all target nuclides and for all macroscopic XS values for all energy groups, the removed nuclide stays removed from the simplified DTL.

When it comes to the user determining the depletion conditions used to generate the simplified DTL, the neutron flux spectrum is the one which is likely to be the most difficult to determine. Assuming the user desires a

simplified DTL which can be applied to the entire reactor system being analyzed, the neutron flux spectrum will vary significantly throughout the reactor core both in terms of magnitude and in terms of energy distribution. As will be explained in later sections, using the largest neutron flux values which occur in the reactor core for each energy group are expected to yield a simplified DTL which can be accurately applied to the entire reactor core. If possible, the user can estimate these maximum neutron flux values, rather than perform a full-core depletion analysis themselves to determine the reference neutron flux spectrum after each depletion interval, and use them to generate a simplified DTL which can then be used to model the full core system.

4.5.4. Selecting Tolerances

In order to determine the potential impact of T_Σ on reactivity, I considered the neutron multiplication factor k and asserted that the system is critical. For the purposes of the depletion chain simplification, I have asserted an infinite medium. Additionally, I will first consider the system using the 1-group microscopic XS from ORIGEN. When calculating the neutron multiplication factor for an infinite region using 1-group XS, terms such as the fast fission factor (ϵ) and the resonance escape probability (p) are meaningless since all neutrons in the system are assumed to be in the same energy group and have the same behavior. Because of this, I consider the *infinite medium multiplication factor* of k_∞ presented in Eq. 3-13 of Ref. [22] and assert that the infinite medium is critical.

$$k_\infty = \eta f = 1 \tag{4.6}$$

where

k_∞	neutron multiplication factor of the infinite medium
η	number of fission neutrons produced per neutron absorbed in the fuel
f	probability of a neutron in the system being absorbed by the fuel

For simplicity, and with the understanding that the system considered in this work is an infinite medium, I will use k when referring to k_∞ for the remainder of this work. The impact of the depletion chain simplification on k is of interest as accurately modeling the neutron multiplication factor is of vital importance for nuclear reactors in order to ensure criticality accidents do not occur while also achieving the necessary reactivity to achieve a successful operational lifetime. Since nuclides will be removed from the system, η and f must be defined in terms relating to the NNDs, which is simple as both terms can be defined via the macroscopic XS of the system.

$$\begin{aligned} \eta &= \frac{\nu\sigma_{\mathrm{f}}^{\mathrm{F}}}{\sigma_{\mathrm{a}}^{\mathrm{F}}} = \frac{\nu N^{\mathrm{F}}\sigma_{\mathrm{f}}^{\mathrm{F}}}{N^{\mathrm{F}}\sigma_{\mathrm{a}}^{\mathrm{F}}} = \frac{\nu\Sigma_{\mathrm{f}}^{\mathrm{F}}}{\Sigma_{\mathrm{a}}^{\mathrm{F}}} \\ f &= \frac{\Sigma_{\mathrm{a}}^{\mathrm{F}}}{\Sigma_{\mathrm{a}}} \end{aligned} \tag{4.7}$$

where

ν	average number of neutrons produced per fission of a fuel atom
$\sigma_{\mathrm{f}}^{\mathrm{F}}$	average microscopic fission XS of the fuel

$\Sigma_{\mathrm{f}}^{\mathrm{F}}$	macroscopic fission XS of the fuel
$\sigma_{\mathrm{a}}^{\mathrm{F}}$	average microscopic absorption XS of the fuel
$\Sigma_{\mathrm{a}}^{\mathrm{F}}$	macroscopic absorption XS of the fuel
N^{F}	NND of fuel nuclides
Σ_{a}	macroscopic absorption XS of the homogenized reactor material

Multiplying η and f together simplifies the equation.

$$\eta f = \frac{\nu\Sigma_{\mathrm{f}}^{\mathrm{F}}}{\Sigma_{\mathrm{a}}^{\mathrm{F}}}\frac{\Sigma_{\mathrm{a}}^{\mathrm{F}}}{\Sigma_{\mathrm{a}}} = \frac{\nu\Sigma_{\mathrm{f}}^{\mathrm{F}}}{\Sigma_{\mathrm{a}}} \tag{4.8}$$

Because of the tolerance applied to the macroscopic XS values in Eq. 4.4, a maximum difference in the neutron multiplication factor will be observed if Σ_{f} is overpredicted and Σ_{a} is underpredicted or vice versa.

$$\begin{aligned}
(\eta f)_{\text{high}} &= \frac{\nu(1+T_\Sigma)\Sigma_{\mathrm{f}}^{\mathrm{F}}}{(1-T_\Sigma)\Sigma_{\mathrm{a}}} = \frac{1+T_\Sigma}{1-T_\Sigma}\eta f \\
(\eta f)_{\text{low}} &= \frac{\nu(1-T_\Sigma)\Sigma_{\mathrm{f}}^{\mathrm{F}}}{(1+T_\Sigma)\Sigma_{\mathrm{a}}} = \frac{1-T_\Sigma}{1+T_\Sigma}\eta f \\
k_{\text{high}} = (\eta f)_{\text{high}} &= \frac{1+T_\Sigma}{1-T_\Sigma}\eta f = \frac{1+T_\Sigma}{1-T_\Sigma}k \\
k_{\text{low}} = (\eta f)_{\text{low}} &= \frac{1-T_\Sigma}{1+T_\Sigma}\eta f = \frac{1-T_\Sigma}{1+T_\Sigma}k
\end{aligned} \tag{4.9}$$

The change in reactivity ρ is shown in Eq. 4.10, recalling that it is asserted that $k = 1$ for the given system.

$$\begin{aligned}
\rho_{\text{high}} &= \frac{k_{\text{high}} - 1}{k_{\text{high}}} = \frac{\frac{1+T_\Sigma}{1-T_\Sigma}k - 1}{\frac{1+T_\Sigma}{1-T_\Sigma}k} = \frac{2T_\Sigma}{1+T_\Sigma} \\
\rho_{\text{low}} &= \frac{k_{\text{low}} - 1}{k_{\text{low}}} = \frac{\frac{1-T_\Sigma}{1+T_\Sigma}k - 1}{\frac{1-T_\Sigma}{1+T_\Sigma}k} = \frac{-2T_\Sigma}{1-T_\Sigma}
\end{aligned} \tag{4.10}$$

In order to determine what is an acceptable change in reactivity, the effective delayed neutron fraction (β_{eff}) is considered. β_{eff} is dependent on the fissionable nuclides in the system, the neutron flux energy spectrum, and, in systems with non-static fuel, the fuel recirculation time. To be conservative, I took what is expected to be a real-world worst-case scenario based on existing reactor designs, a ^{233}U fueled MSR operating in the thermal spectrum with a recirculation time of a few seconds such that half of the delayed neutrons emitted by the FPs of ^{233}U are released outside of the active core region. ^{233}U undergoing fission by thermal neutrons has a delayed neutron fraction of roughly 0.3% [80]. The short recirculation time results in many of the delayed neutron precursor nuclides exiting the active core region before emitting their neutrons, resulting in β_{eff} being halved to 0.15% [81]. This is expected to be a worst-case scenario for existing reactor designs, noting that a lower value β_{eff} is undesirable as it reduces the size of the reactivity swing necessary to change the reactor from critical ($k = 1$) to prompt critical ($k - \beta_{\text{eff}} \geq 1$), with prompt criticality being a condition commercial power reactors avoid.

For $\beta_{\text{eff}} = 0.15\%$, this corresponds to 150 pcm of reactivity for a critical system. In typical reactor analysis the reactivity contribution of delayed neutrons is referred to as "one dollar" ($1) of reactivity, which for this system

considered means \$1 = 150 pcm. I assumed that any error introduced via the removal of nuclides is desired to be kept within a few percent of \$1. This is expected to be an overall conservative restriction. The reactivity changes in pcm for different values of T_Σ, assuming $k = 1$, are shown in Table 4.9.

T_Σ	ρ_{high} [pcm]	ρ_{low} [pcm]
10%	18,181.8	-22,222.2
1%	1,980.2	-2,020.2
0.1%	199.8	-200.2
0.01%	20.0	-20.0
0.001%	2.0	-2.0
0.0001%	0.2	-0.2

Table 4.9: Maximum and minimum reactivity changes introduced by the given T_Σ values to η and f terms for a critical infinite medium system.

As shown in Table 4.9, T_Σ values of 10% and 1% can introduce reactivity changes many times greater than \$1. $T_\Sigma = 10^{-5}$ achieves a reactivity change of about 1.33% of \$1. For the remainder of this work, $T_\Sigma = 10^{-5}$ is expected to cause a reactivity change of only a few percent of \$1. Recall that the effects of T_Σ on only the η and f for a 1G case were considered here. Changes to the macroscopic XS will impact all terms in the six-factor formula when considering real-world nuclear systems. Considering the diverse reactor designs under consideration around the world, changes to the macroscopic XS could have a larger effect on reactivity than those considered in Table 4.9. Conversely, when considering multigroup systems with a large number of energy groups, the enforcement of T_Σ across all neutron energy groups would be expected to result in only one energy group deviating by the absolute maximum possible value permitted by T_Σ at any point in time. Since the macroscopic XS values of other energy groups for the simplified library would be expected to be closer (in absolute terms) to the reference macroscopic XS values, this would reduce the overall impact of the simplification process on k.

In reality, while a cursory attempt to relate T_Σ to changes in reactivity, analysts will need to make the determination themselves how varying T_Σ impacts the reactivity of their system of interest. This will also be important for analysts to determine as, while I selected T_Σ such that any reactivity change is expected to be within a few percent of \$1, other analysis may be willing to tolerate far larger deviations in reactivity depending on the system being considered. This section should be interpreted not as the definitive method for determining T_Σ, but rather one example of how one could determine T_Σ.

T_N is much simpler to determine. Literature based on the experimental measurement of radionuclides, such as cesium-137 in pebble-bed reactors, indicate an experimental error of a few percent [82]. With this understanding of the limits of experimental measurement of NNDs during reaction operation, $T_N = 0.1\%$ is acceptable as any error introduced by the removal of nuclides from the system will likely be negligible compared to the experimental error in measuring NNDs for any practical purposes. T_N will also be applied to non-nuclide quantities that are evaluated as part of the Bateman equations, such as decay energy released.

4.6. Results

4.6.1. ENDF-ORIGEN 1G

I performed all testing using a 0D infinite homogeneous region with the initial non-zero NNDs specified in Table 4.10 representing pure UO_2 at a density of 10.97 $\frac{\text{g}}{\text{cm}^3}$ with 5 at% ^{235}U enrichment. Since the enrichment process also results in an increase in the concentration of ^{234}U present in natural uranium, the concentration of ^{234}U is increased 0.005 at% to 0.035 at%.

Nuclide	NND [$\frac{\text{atoms}}{\text{b}\cdot\text{cm}}$]
^{16}O	4.88428×10^{-2}
^{17}O	1.86055×10^{-5}
^{18}O	1.00372×10^{-4}
^{234}U	8.50031×10^{-6}
^{235}U	1.22404×10^{-3}
^{238}U	2.32483×10^{-2}

Table 4.10: Initial NNDs ($\mathbf{N}_0$) used for testing the simplification of the ENDF-ORIGEN dataset.

For a system containing the initial NNDs there are a total of 1,691 nuclides, which I divided into several different categories:

- Secondary: Nuclides which can be produced as a secondary particle from neutron transmutation and decay reactions (^{1}H, ^{2}H, ^{3}H, ^{3}He, and ^{4}He). Note that cluster decay is not accounted for in Griffin because of its low probability of occurrence and thus is not accounted for here.
- Light: Nuclides which are heavier than secondary nuclides, but belong to elements below titanium, which is the lightest FP in the ENDF/B-VIII.0, with the exception of ^{242}Am and ^{242}Cm capable of producing lighter FPs ranging from ^{1}H to ^{10}Be in what are presumably ternary fission events. Since titanium is the lightest FP produced from binary fission events, it is considered an appropriate boundary.
- FPs: Nuclides which are produced as a result of binary nuclear fission or are produced via the decay or transmutation of the binary nuclear fission products. For simplicity, this range is asserted to contain all isotopes of all elements from titanium to osmium which are the lightest and heaviest binary fission fragments, respectively, provided in the ENDF/B-VIII.0 decay data. Technically speaking, titanium and osmium isotopes could undergo decay or transmutation events to produce scandium or iridium isotopes, however, the FPYFs of titanium and osmium are quite low, on the order of 10^{-12}, thus titanium and osmium are considered acceptable boundaries.
- Heavy: Nuclides which belong to elements heavier than osmium but are not actinides. This encompasses all isotopes of all elements from iridium to radium.
- Actinides: Nuclides which belong to elements which are actinides, which includes all isotopes of elements from actinium to lawrencium. For both DTLs tested, no nuclides belonging to elements beyond actinides were present. Although the ENDF/B-VIII.0 data does provide decay information for nuclides up to roentgenium ($Z = 111$), the fermium gap prevents production of elements beyond actinides [83].

Based on the categories outlined above, the ENDF-ORIGEN DTL prior to simplification has: 5 secondary nuclides, 96 light nuclides, 1,417 FP nuclides, 87 heavy nuclides, and 86 actinides.

I then irradiated the region with a constant neutron flux of $10^{14}\,\frac{\text{neutrons}}{\text{cm}^2\cdot\text{s}}$ for 500 days, followed by a period of pure decay (zero neutron flux) for 500 days. During depletion, the NNDs and macroscopic XS values are calculated at multiple points in time, as indicated in Table 4.11. These are the conditions subsequently used to perform the iterative nuclide removal, as specified in Section 4.5.

Irr. Time (t) [s]	Δt [s]	ϕ $\left[\frac{\text{neutrons}}{\text{cm}^2\cdot\text{s}}\right]$	F $\left[\frac{\text{neutrons}}{\text{cm}^2}\right]$	Decay Time (t) [s]	Δt [s]	ϕ $\left[\frac{\text{neutrons}}{\text{cm}^2\cdot\text{s}}\right]$	F $\left[\frac{\text{neutrons}}{\text{cm}^2}\right]$
1.000	1.000	10^{14}	1.000×10^{14}	1.000	1.000	0	4.320×10^{21}
10.00	9.000	10^{14}	1.000×10^{15}	10.00	9.000	0	4.320×10^{21}
60.00	50.00	10^{14}	6.000×10^{15}	60.00	50.00	0	4.320×10^{21}
600.0	540.0	10^{14}	6.000×10^{16}	600.0	540.0	0	4.320×10^{21}
3,600	3,000	10^{14}	3.600×10^{17}	3,600	3,000	0	4.320×10^{21}
3.600×10^4	3.240×10^4	10^{14}	3.600×10^{18}	3.600×10^4	3.240×10^4	0	4.320×10^{21}
8.640×10^4	5.040×10^4	10^{14}	8.640×10^{18}	8.640×10^4	5.040×10^4	0	4.320×10^{21}
1.728×10^5	8.640×10^4	10^{14}	1.728×10^{19}	1.728×10^5	8.640×10^4	0	4.320×10^{21}
4.320×10^5	2.592×10^5	10^{14}	4.320×10^{19}	4.320×10^5	2.592×10^5	0	4.320×10^{21}
8.640×10^5	4.320×10^5	10^{14}	8.640×10^{19}	8.640×10^5	4.320×10^5	0	4.320×10^{21}
1.728×10^6	8.640×10^5	10^{14}	1.728×10^{20}	1.728×10^6	8.640×10^5	0	4.320×10^{21}
4.320×10^6	2.592×10^6	10^{14}	4.320×10^{20}	4.320×10^6	2.592×10^6	0	4.320×10^{21}
8.640×10^6	4.320×10^6	10^{14}	8.640×10^{20}	8.640×10^6	4.320×10^6	0	4.320×10^{21}
1.296×10^7	4.320×10^6	10^{14}	1.296×10^{21}	1.296×10^7	4.320×10^6	0	4.320×10^{21}
1.728×10^7	4.320×10^6	10^{14}	1.728×10^{21}	1.728×10^7	4.320×10^6	0	4.320×10^{21}
2.160×10^7	4.320×10^6	10^{14}	2.160×10^{21}	2.160×10^7	4.320×10^6	0	4.320×10^{21}
2.592×10^7	4.320×10^6	10^{14}	2.592×10^{21}	2.592×10^7	4.320×10^6	0	4.320×10^{21}
3.024×10^7	4.320×10^6	10^{14}	3.024×10^{21}	3.024×10^7	4.320×10^6	0	4.320×10^{21}
3.456×10^7	4.320×10^6	10^{14}	3.456×10^{21}	3.456×10^7	4.320×10^6	0	4.320×10^{21}
3.888×10^7	4.320×10^6	10^{14}	3.888×10^{21}	3.888×10^7	4.320×10^6	0	4.320×10^{21}
4.320×10^7	4.320×10^6	10^{14}	4.320×10^{21}	4.320×10^7	4.320×10^6	0	4.320×10^{21}

Table 4.11: Depletion intervals used during DTL simplification. The system is initially irradiated for 500 days before undergoing pure decay for 500 days. Note that the values are shown to an equal level of precision to the values specified for performing all calculations in Griffin.

4.6.1.1 Initial Simplification

I performed the initial ENDF-ORIGEN DTL simplification with Σ_t, and Σ_f preserved within the specified T_Σ of 10^{-5} and NNDs of the target nuclides are preserved within the specified T_N of 10^{-3}, with the assertion that the only target nuclides are those with initial non-zero NNDs in Table 4.10.

The initial simplification is able to reduce the number of nuclides tracked in the ENDF-ORIGEN system from 1,691 to 168. The nuclides remaining in the simplified DTL compared to the reference DTL are shown in Table 4.12. The RD of Σ_t and Σ_f are shown in Figure 4.9, where a positive value indicates that the simplified DTL overpredicts the given quantity and a negative value indicates an underprediction. Of the target NNDs, ^{234}U experiences the largest RD with an underprediction of 1.75×10^{-6} which is much lower T_N.

Type	**Reference**	**Simplified**
Secondary	5	0
Light	96	3
FP	1,417	141
Heavy	87	0
Actinide	86	24
Total	*1,691*	*168*

Table 4.12: The number of nuclides of each type (as defined in Section 4.6.1) tracked for the ENDF-ORIGEN reference and simplified DTLs.

As expected, the results from the simplified DTL are within the 10^{-5} tolerance set with Σ_t effectively reaching this tolerance at the final decay time, which indicates that more nuclides could have been removed if the tolerance was relaxed. Additionally, I notice that at several points in time the results from the simplified DTL oscillate between overprediction and underprediction of Σ_t and Σ_f. This is attributed to different nuclides contributing to the macroscopic XS at different points in time being removed from the simplified DTL.

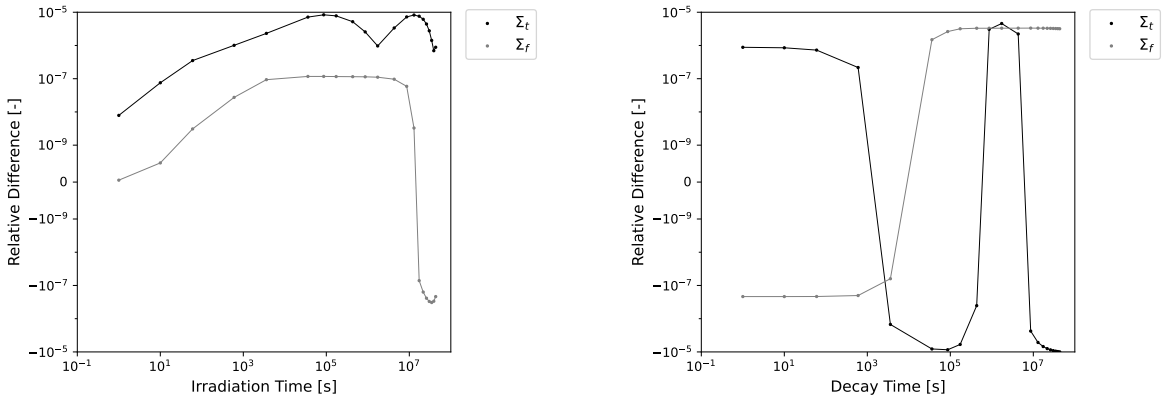

(a) Σ_t and Σ_f RDs during irradiation.

(b) Σ_t and Σ_f RDs during decay after irradiation.

Figure 4.9: Σ_t and Σ_f RDs between the results calculated by the 168 nuclide simplified DTL and 1,691 nuclide reference DTL for the ENDF-ORIGEN data using the depletion conditions specified in Table 4.11.

4.6.1.2 Simplified DTL at Varying Depletion Conditions

I now considered using the simplified DTL generated using the depletion conditions specified in Table 4.11 and using the simplified DTL to calculate Σ_t, Σ_f, and the target NNDs for systems with the same depletion intervals lengths, but halving or doubling the flux experienced by these systems ($\frac{1}{2}\phi$ and 2ϕ) and comparing the results to those generated by the reference DTL for the same flux conditions. The reason for a factor of two deviation in the flux is simply to determine the sensitivity of the simplified DTL to changing flux conditions.

Σ_t and Σ_f RDs for the simplified and reference DTLs for the varying flux conditions are shown in Figure 4.10. The maximum RD experienced by the target NNDs was for the 2ϕ condition for ^{234}U where the simplified DTL maximum RD was an underprediction of 4.92×10^{-6}. The results of both the macroscopic XS and the target NNDs indicate that the simplified DTL performs significantly worse when the flux conditions experienced by the system exceed those specified during the simplification process. Additionally, I note that the simplified DTL will also perform differently if the lengths of the depletion intervals are varied, however, analysts are expected to have a much better understanding and control of the lengths of the depletion intervals used in their models compared to the exact flux levels a given region in a given system may experience. As a result I have focused on varying the flux level, which is more likely to vary outside of the direct control of analysts.

4.6.1.3 Simplification with Additional Actinide Tracking

To test whether or not the loss of actinides is the source of the strong flux dependence of the simplified DTL, I considered the same problem but explicitly tracked all isotopes of uranium, neptunium, plutonium, americium, and curium with a σ_f greater than 10 b. Recall that this is using the MGL from the 1G ORIGEN XS data meaning there is only one σ_f value for each nuclide. These nuclides are: ^{233}U, ^{236}Np, ^{238}Np, ^{236}Pu, ^{237}Pu, ^{238}Pu, ^{239}Pu, ^{241}Pu, ^{243}Pu, ^{240}Am, ^{242}Am, ^{242m}Am, ^{244}Am, ^{241}Cm, ^{243}Cm, ^{245}Cm, ^{247}Cm, and ^{249}Cm. I did not consider fissile nuclides lighter than ^{233}U as the contributions of these nuclides to Σ_f is expected to be relatively small compared to the heavier actinides because of the much higher probability of nuclides to undergo (n,γ) reactions compared to reactions that produce lighter nuclides, such as (n,2n) and (n,α). Lighter actinides will also be produced as a result of α decay, but there are few fissile nuclides lighter than ^{233}U and the half-lives of many of the nuclides which would decay to these lighter fissile actinides are quite long relative to reactor timescales.

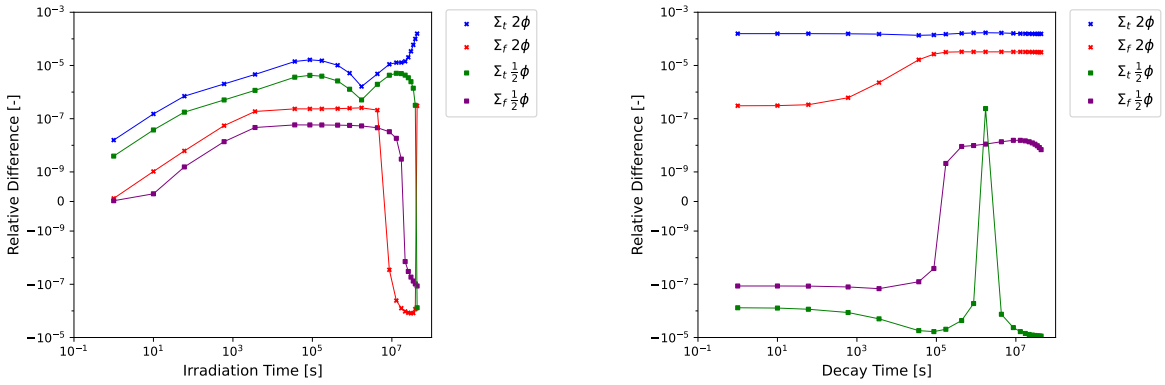

(a) Σ_t and Σ_f RDs during irradiation.

(b) Σ_t and Σ_f RDs during decay after irradiation.

Figure 4.10: Σ_t and Σ_f RDs between the simplified and reference ENDF-ORIGEN DTLs for the varying flux conditions.

Adding additional actinide tracking results in the number of nuclides in the simplified DTL increasing from 168 to 203 nuclides with the types of nuclides tracked shown in Table 4.13. Most of the additional nuclides tracked are actinides, which is expected as "adjacent" actinides (in terms of Z and A numbers) to the target actinides will undergo decay and transmutation events which produce the target actinides which, if significant, must be preserved. The number of FP nuclides also increases by 4, which is attributed to differences in the overall FPYFs since the tracking of additional actinides will result in a larger production of certain FPs which then have a significant contribution to Σ_t.

Type	**Reference**	**Simplified**	**Simplified with Actinides**
Secondary	5	0	0
Light	96	3	3
FP	1,417	141	145
Heavy	87	0	0
Actinide	86	24	55
Total	*1,691*	*168*	*203*

Table 4.13: The number of nuclides of each type (as defined in Section 4.6.1) tracked for the ENDF-ORIGEN reference, simplified without additional actinide tracking, and simplified with additional actinide tracking DTLs.

The Σ_t and Σ_f RDs between the results of the simplified DTL with additional actinide tracking and reference DTL are shown in Figure 4.11 for the depletion conditions used during the simplification process and for the varied flux conditions considered in Section 4.6.1.2. As expected, the RD of the Σ_f is reduced and also experiences fewer oscillations than in Figures 4.9 and 4.10. The RD of the Σ_t is reduced for certain points in time but still reaches the maximum allowable RD over the course of the simulation and is still exceeds T_Σ under the 2ϕ condition, reaching a maximum RD with an underprediction of 3.05×10^{-5}. This is expected as FPs have a significant impact on Σ_t and is the main limiting factor for removing additional nuclides.

I plotted the NND RDs of ^{233}U, ^{236}Pu, and ^{249}Cm as the RDs are much closer to T_N and ^{236}Pu exceeding T_N for the 2ϕ condition achieving a maximum RD overprediction of 0.128%. The results are shown in Figure 4.12. All other target nuclides had RDs below 10^{-5} for all flux conditions tested. These results confirm that the target NNDs are sensitive to the flux conditions and varying the flux conditions can result in a divergence from the

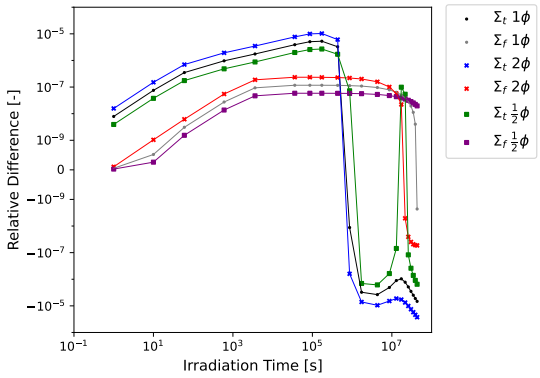

(a) Σ_t and Σ_f RDs during irradiation.

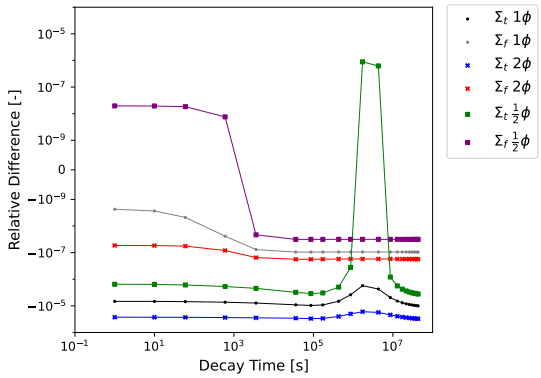

(b) Σ_t and Σ_f RDs during decay after irradiation.

Figure 4.11: Σ_t and Σ_f RDs between the simplified and reference ENDF-ORIGEN DTLs with additional actinide tracking.

reference solution in excess of the tolerance provided. Similar to the macroscopic XS, the target NNDs seem to be diverge specifically for increases in the flux of the system.

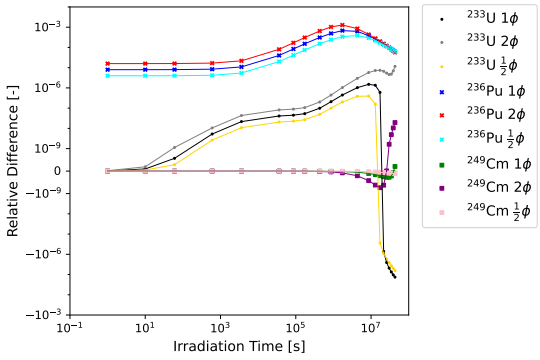

(a) NNDs RDs of select target nuclides during irradiation.

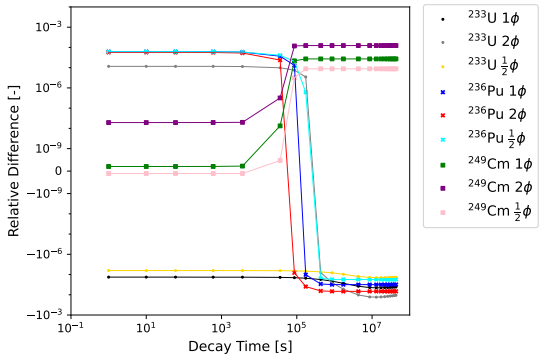

(b) NNDs RDs of select target nuclides during decay after irradiation.

Figure 4.12: Select target NNDs RDs between the simplified and reference ENDF-ORIGEN DTLs with additional actinide tracking for varying flux conditions.

Overall, tracking additional actinides improves modeling of Σ_f, which then reduces the overall divergence of Σ_f from the reference solution when the flux conditions differ from those used during the simplification process. As a result, additional actinides are tracked as part of the simplification process for the remainder of this work and is recommended for most fuel depletion analysis as the overall increase in the number of nuclides is considered a satisfactory trade-off for the improved modeling of Σ_f and its subsequent impact on reactivity.

4.6.1.4 Simplification with Decay Energy Tracking

I have demonstrated DTL simplification preserving macroscopic XS and target NNDs and now considered preserving decay energy released in the system (calculated in Griffin under the name "DecayEnergy") in addition to the previous values. Since DecayEnergy is calculated as part of the Bateman equations as if it were a nuclide [79], I applied the 10^{-3} NND tolerance. Instead of tracking DecayEnergy, another option would be to evaluate the decay power based on the NNDs of radionuclides and compare the decay power calculated after

each depletion interval. However, this would only account for the instantaneous decay power after each depletion interval rather than the total decay energy released during each depletion interval. Since the total decay energy released determines the amount of heat which must be removed from a reactor after shutdown, I consider this the more appropriate quantity to track, with the understanding that it is also quite trivial to calculate the instantaneous decay power using the calculated NNDs at each point in time. No PNs have been added to improve the modeling of DecayEnergy, the analysis performed in this section is only meant to determine how many nuclides must be tracked to model DecayEnergy without any PNs in order to serve as a reference to later determine the effectiveness of adding PNs.

The overall number of nuclides tracked increases from 203 in Section 4.6.1.3 to 695 nuclides, with the types of nuclides shown in Table 4.14. Overall, the number of FPs tracked increases significantly, which is to be expected as many short-lived FPs without XS data could be removed when DecayEnergy was not tracked, but now must be tracked as the total decay energy release must be retained within T_N. An additional actinide is also tracked, which is not surprising as short-lived actinides can decay with significant energy release. Since DecayEnergy will be present for both the reference and simplified DTLs whenever it is tracked, it is excluded from the nuclide counts in Table 4.14 and all subsequent tables.

Type	**Reference**	**Simplified with Actinides**	**Simplified with Actinides and DecayEnergy**
Secondary	5	0	0
Light	96	3	3
FP	1,417	145	636
Heavy	87	0	0
Actinide	86	55	56
Total	*1,691*	*203*	*695*

Table 4.14: The number of nuclides of each type (as defined in Section 4.6.1) tracked for the ENDF-ORIGEN reference, simplified with additional actinide tracking, and simplified with additional actinide and DecayEnergy tracking DTLs.

The results are shown in Figures 4.13 and 4.14. I only consider the macroscopic XS and DecayEnergy RDs as the higher actinide target NNDs largely exhibit the same behavior as shown in Section 4.6.1.3. Σ_t still reaches T_Σ despite the increased number of nuclides tracked; however, the overall shape of the Σ RDs is different from the results in Figure 4.11, and this change is attributed to the increased number of nuclides modeled. The RD of DecayEnergy in Figure 4.11 is underpredicted and very near T_N for all depletion intervals. This is to be expected, as removing nuclides from the system, typically short-lived radionuclides, will ultimately result in less decay energy being released by the system overall. This also demonstrates why so many nuclides must be tracked by the system in order to keep the DecayEnergy within T_N.

4.6.1.5 Simplified DTL with Decay Energy Tracking and Pseudo-Nuclides

In Section 4.5.2, the methodology of adding PNs for modeling decay energy release from removed nuclides was discussed and a method of determining PN decay constants was proposed using the median sub-series method. Based on testing, ten PNs achieves a balance between removing most of the radionuclides which were added when tracking DecayEnergy in Section 4.6.1.4 without adding too many PNs as it is expected that for analysts it is preferable to track say 300 physical nuclides and 10 PNs instead of 250 physical nuclides and 50 PNs.

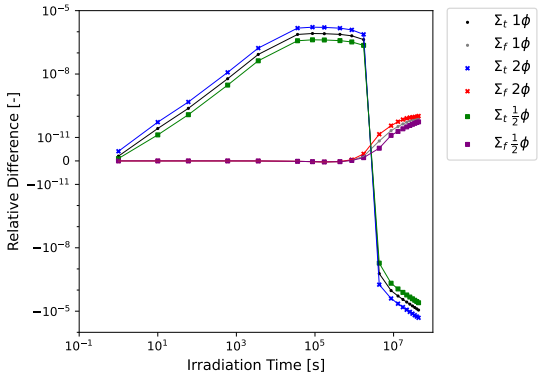

(a) Σ_t and Σ_f RD during irradiation.

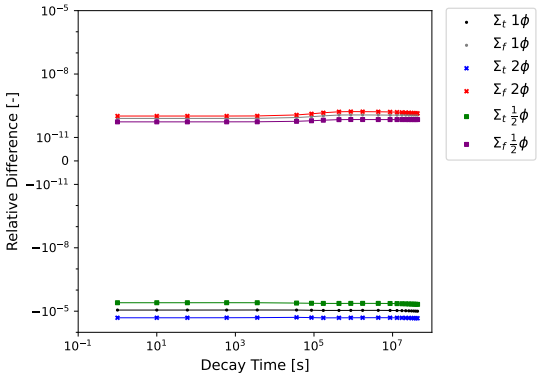

(b) Σ_t and Σ_f RD during decay after irradiation.

Figure 4.13: Σ_t and Σ_f RDs between the simplified and reference ENDF-ORIGEN DTLs with additional actinide and DecayEnergy tracking for varying flux conditions.

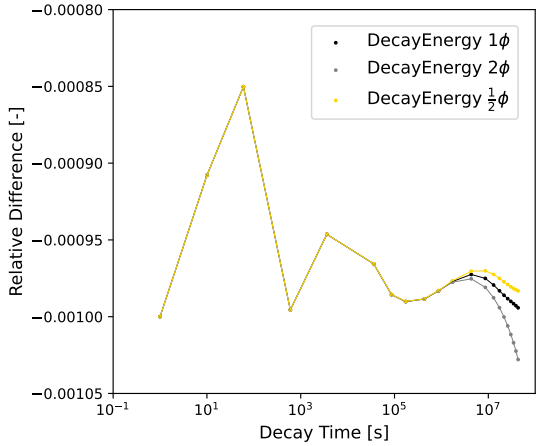

(a) DecayEnergy RD during irradiation.

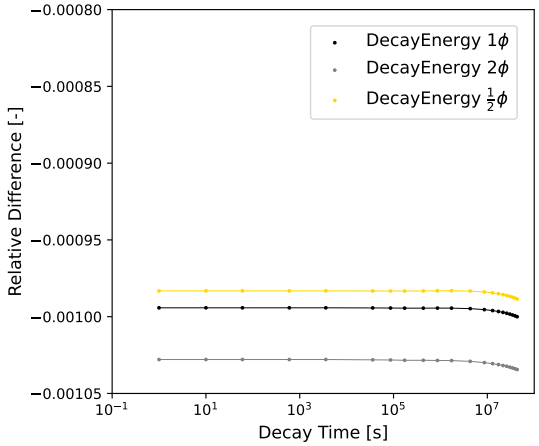

(b) DecayEnergy RD during decay after irradiation.

Figure 4.14: DecayEnergy RD between the simplified and reference ENDF-ORIGEN DTLs with additional actinide and DecayEnergy tracking for varying flux conditions.

Additionally, Li et al. proposed ten DHPs [73] meaning the number of PNs is consistent with the number of DHPs proposed previously.

Adding ten PNs significantly reduces the number of nuclides tracked from 695 to 342, a 50% reduction, though still significantly larger than the 203 nuclides for the DTL without DecayEnergy tracked. The types of nuclides tracked are shown in Table 4.15.

Type	**Reference**	**Simplified with Actinides and DecayEnergy**	**Simplified with Actinides and DecayEnergy and 10 PNs**
Pseudo	0	0	10
Secondary	5	0	0
Light	96	3	3
FP	1,417	636	273
Heavy	87	0	0
Actinide	86	56	56
Total	*1,691*	*695*	*342*

Table 4.15: The number of nuclides of each type (as defined in Section 4.6.1) tracked for the ENDF-ORIGEN reference, simplified with additional actinide and DecayEnergy tracking, and simplified with additional actinide and DecayEnergy tracking with 10 PNs DTLs.

Once again I plotted the results of the RDs of Σ_t and Σ_f and the DecayEnergy RD between the simplified DTL with 10 PNs and the reference DTL for varying flux conditions as shown in Figures 4.15 and 4.16. The Σ_t and Σ_f results in Figure 4.15 are largely identical to those from Figure 4.13 with the exception of a few increased oscillations in Σ_t which is attributed to the removal of additional radionuclides which no longer need to be tracked because of the added PNs, but their removal results in changes to the overall Σ_t at various points in time. The divergence from the reference solution is once again observed when the flux increases for the macroscopic XS, but DecayEnergy seems largely insensitive to the increased flux conditions. This is attributed to the additional PNs largely preserving the significant decay energy production pathways, meaning that as the neutron flux increases, the increased decay energy from the increase in FP concentration can still be accounted for relatively accurately.

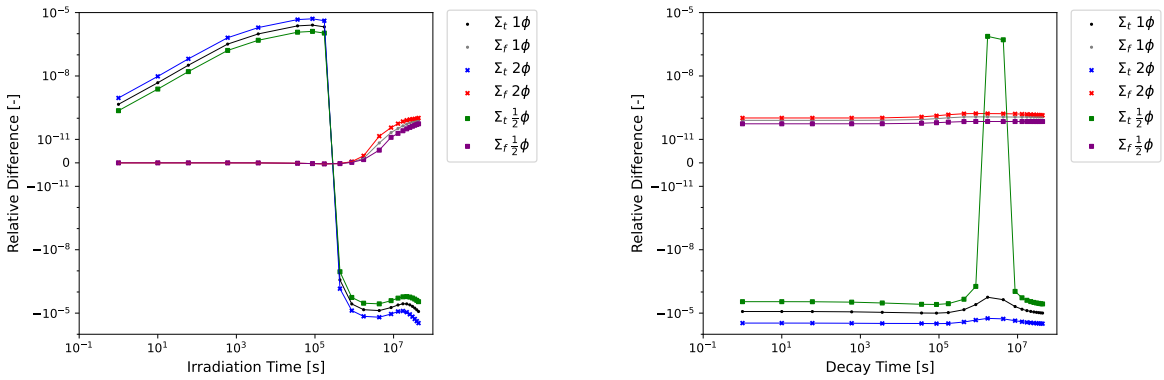

(a) Σ_t and Σ_f RD during irradiation.

(b) Σ_t and Σ_f RD during decay after irradiation.

Figure 4.15: Σ_t and Σ_f RDs between the simplified and reference ENDF-ORIGEN DTLs with additional actinide and DecayEnergy tracking with 10 PNs for varying flux conditions.

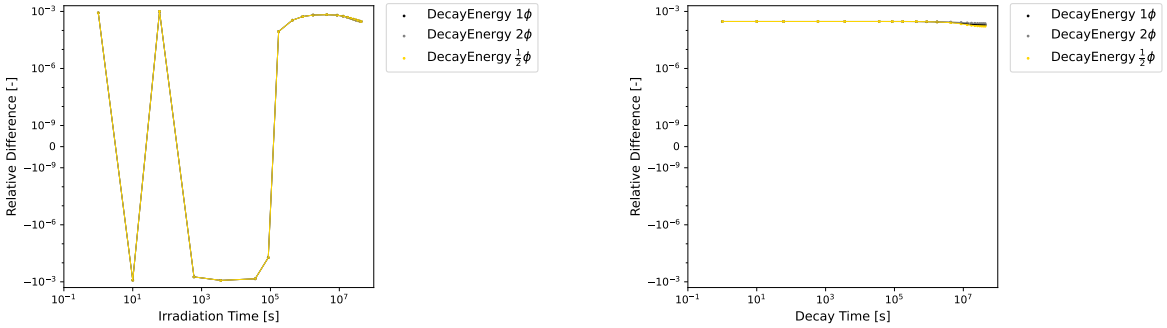

(a) DecayEnergy RD during irradiation.

(b) DecayEnergy RD during decay after irradiation.

Figure 4.16: DecayEnergy RD between the simplified and reference ENDF-ORIGEN DTLs with additional actinide and DecayEnergy tracking with 10 PNs for varying flux conditions.

4.6.1.6 Comparing the Heuristic Method to Other Simplification Methods

I briefly compare between the simplification method proposed in this work and other published methods mentions in Section 4.3. Overall, these methods typically used coarser reactivity thresholds than I have used in this work so far and most of these works were not concerned with decay energy tracking. As a result, I first consider the number of nuclides tracked in the simplified ENDF-ORIGEN DTL for varying T_Σ with additional actinide tracking without decay energy tracking or PNs as shown in Table 4.16.

Type	**Reference**	**Simplified with Actinides** $T_\Sigma = 10^{-5}$	**Simplified with Actinides** $T_\Sigma = 10^{-4}$	**Simplified with Actinides** $T_\Sigma = 10^{-3}$
Secondary	5	0	0	0
Light	96	3	3	0
FP	1,417	145	122	73
Heavy	87	0	0	0
Actinide	86	55	55	55
Total	*1,691*	*203*	*180*	*131*

Table 4.16: The number of nuclides of each type (as defined in Section 4.6.1) tracked for the ENDF-ORIGEN reference DTL and simplified with additional actinide tracking DTLs with $T_N = 10^{-3}$ and varying T_Σ.

Based on the values in Table 4.9, $T_\Sigma = 10^{-3}$ corresponds to a reactivity change on the order of hundreds of pcm and $T_\Sigma = 10^{-4}$ corresponds to a reactivity change on the order of tens of pcm.

The number of nuclides in the simplified libraries generated by similar publications is shown in Table 4.17. The publications which reported reactivity differences based on their simplified libraries were on the order of tens to hundreds of pcm different from their reference depletion libraries. Considering the variety of differences between the simplification processes of these various publications, including, but not limited to, the data used, the simplification criteria, and the simplification methodologies themselves, it would be inappropriate to state that one published method is superior to another based on the available information. However, what can be stated is that for the ENDF-ORIGEN dataset used in this work with criteria similar to previously published works, the number of nuclides tracked is similar to those of previous publications and thereby competitive with them from the perspective of the number of nuclides tracked.

Publication	FP Nuclides	Total Nuclides
Chiba et al. [68]	138	
Tran et al. [69]	193	
Kajihara et al. [70]		204
Zhang et al. [71]		127-185
Huang et al. [72]		86-185
Li et al. [73]		182-233

Table 4.17: The number of total or FP nuclides used in simplified depletion libraries in other depletion chain simplification publications.

4.6.2. ENDF-MC^2-3 Multigroup

In order to consider how an increase in the number of energy groups and changes in the flux energy spectrum may impact the depletion chain simplification process, the ENDF-MC^2 DTL with a 2G MGL is used. Since the simplification process seeks to preserve the macroscopic XS within T_Σ for all XS reaction types for all energy groups it is expected that the more energy groups present in the system will increase the number of nuclides tracked. Additionally, recall that the MC^2-3 data contains incident neutron energy information which will be used to perform linear interpolation on the ENDF FPYFs which will impact which nuclides are tracked.

I kept the same depletion intervals as specified in Table 4.11, except that, instead of a total neutron flux of 10^{14} $\frac{\text{neutrons}}{\text{cm}^2\cdot\text{s}}$ during the first half of the depletion intervals, the total neutron flux is increased by an order of magnitude to 10^{15} $\frac{\text{neutrons}}{\text{cm}^2\cdot\text{s}}$. The overall increase in the neutron flux is done in order to represent the higher neutron fluxes experienced in fast reactors, which MC^2 is designed to provide XS data for, compared to thermal reactors, the increased neutron flux being necessary to achieve comparable power density as in thermal reactors because of the reduced fission XS of fissile nuclides in the fast energy region compared to thermal energy region.

Additionally, I varied the initial NNDs of the system to represent UO_2 fuel with 20 at% ^{235}U and a subsequent increase in the ^{234}U concentration as well, as shown in Table 4.18. Once again, this is done in order to better represent the fast reactor conditions that MC^2 is designed to produce XS libraries for. The target NNDs include additional actinides as specified in Section 4.6.1.3 in order to better model Σ_f.

Nuclide	NND [$\frac{\text{atoms}}{\text{b}\cdot\text{cm}}$]
^{16}O	4.88428×10^{-2}
^{17}O	1.86055×10^{-5}
^{18}O	1.00372×10^{-4}
^{234}U	3.40012×10^{-5}
^{235}U	4.89618×10^{-3}
^{238}U	1.95507×10^{-2}

Table 4.18: Initial NNDs ($\mathbf{N}_0$) used for testing the simplification of the ENDF-MC^2 dataset.

Lastly, I used the same tolerances T_Σ and T_N as used in the previous sections for the same reasons mentioned in Section 4.5.4.

4.6.2.1 Simplification with Varying Flux Energy Spectra

In order to investigate the impact of varying the energy spectrum of the neutron flux used during the depletion chain simplification process, I considered three different spectra, a thermal spectrum where 99% of the flux is in the thermal group and 1% in the fast group, a flat spectrum where 50% of the flux is in the thermal group and 50%

in the fast group, and a fast spectrum where 99% of the flux is in the fast group and 1% in the thermal group. The nuclides tracked by the reference DTL and simplified DTLs with varying flux conditions are shown in Table 4.19.

Type	Reference	Simplified Thermal Flux	Simplified Flat Flux	Simplified Fast Flux
Secondary	5	1	1	1
Light	95	3	4	4
FP	1,417	240	188	136
Heavy	99	0	0	0
Actinide	105	62	59	55
Total	*1,721*	*306*	*252*	*196*

Table 4.19: The number of nuclides of each type (as defined in Section 4.6.1) tracked for the ENDF-MC^2 reference and simplified DTLs with varying flux energy spectra applied during the simplification process.

Based on the results in Table 4.19 it can be seen that the overall number of nuclides tracked increases the more "thermal" the neutron flux is as significantly more FPs must be tracked. This is to be expected as the fission rate is expected to increase for a more thermal flux compared to a faster flux, which will result in both the concentration of FPs being higher and a reduction in the overall concentration of actinides. Thus the relative contribution of the FPs to the macroscopic XS of the system increases the more thermal the flux experienced by the depletion system is.

Overall, this confirms what was already expected, the neutron flux energy spectrum used during the simplification process impacts what nuclides are tracked in the simplified DTL and thus when generating a simplified DTL it is imperative to use a flux energy spectrum which is representative of the system which the simplified DTL will be applied to. For the remainder of this section the "flat" flux energy spectrum (where both flux energy groups have the same magnitude) is used as this is expected to be somewhat more representative of real-world reactor conditions than the fast or thermal flux cases considered.

4.6.2.2 Simplification with Decay Energy Tracking and 10 PNs

As was previously demonstrated for the 1G case in Section 4.6.1.5, adding PNs to the simplified DTL can allow significantly more radionuclides to be removed from the system while preserving decay energy release. The simplification process is performed for the ENDF-MC^2 DTL using the depletion conditions defined in Section 4.6.2 with DecayEnergy tracked with and without PNs. The number of nuclides tracked in the simplified DTLs are shown in Table 4.20. The addition of PNs results in a similar reduction in the number of nuclides tracked in the simplified DTL while preserving decay energy release for the 2G case as for the 1G case.

For the 10 PN case, the RDs of macroscopic XSs between the simplified DTL and the reference DTL are considered for the same varying flux conditions as the 1G case. Since the halved flux condition results in better agreement between the simplified DTL solution and the reference DTL solution, it is omitted from Figure 4.17. Since MC^2 provides additional XS quantities, the removal, total, and transport XS are considered as the fission and energy deposition XSs did not exceed T_Σ. Griffin orders neutron energy groups from fastest to slowest in descending order, meaning Σ_t^1 corresponds to the Σ_t in the fast energy group while Σ_t^2 is the thermal energy group. Aside from Σ_r^1, the XS quantities largely follow the same behavior. I did not consider any changes to the target NNDs as the absolute RD of all target nuclides remained an order of magnitude below T_N except for DecayEnergy which has similar behavior as in Figure 4.16. These results demonstrate The simplification process has no immediate issues handling multigroup XS data.

Type	Reference	Simplified with DecayEnergy	Simplified with DecayEnergy and 10 PNs
Pseudo	0	0	10
Secondary	5	1	1
Light	95	4	4
FP	1,417	665	288
Heavy	99	0	0
Actinide	105	59	58
Total	*1,721*	*729*	*361*

Table 4.20: The number of nuclides of each type (as defined in Section 4.6.1) tracked for the ENDF-MC^2 reference and simplified DTLs for the flat flux energy spectrum applied during the simplification process with DecayEnergy tracking.

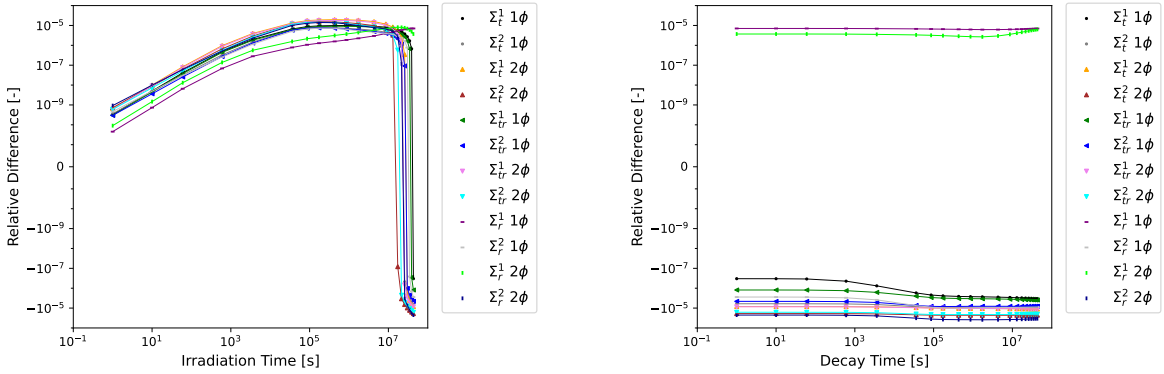

(a) Σ_t, Σ_{tr}, and Σ_r RD during irradiation.

(b) Σ_t, Σ_{tr}, and Σ_r RD during decay after irradiation.

Figure 4.17: Σ_t, Σ_{tr}, and Σ_r RDs between the simplified and reference ENDF-MC^2 DTLs with DecayEnergy tracking and 10 PNs for regular and double flux conditions.

4.6.2.3 Comparing PNs to DHPs

As mentioned in Section 4.3, the method of adding PNs to the simplified DTL is similar to the DHP methodology proposed by Huang et al. [72] and Li et al. [73]. The PN method can be converted into effectively a DHP method by asserting that PNs can only be produced as FPs and not as decay or neutron transmutation products. With this adaptation, the PN method and the DHP method can be compared in terms of the number of nuclides tracked by each method for the simplification of the ENDF-MC^2 DTL. While Li et al. published an example of DHP decay constants for several fissionable nuclides, these decay constants cannot be easily applied to the ENDF-MC^2 DTL satisfactorily for several reasons, the primary one being that the depletion intervals used in this work cannot have their decay energy release preserved by the published DHP values for very short timesteps on the order of seconds. Second, the exact depletion chain library used by Li et al. differs from the ENDF-MC^2 DTL. Third, no DHP information is provided for several actinides which will appreciably contribute FPs. As a result, the process of adapting PNs to serve as DHPs is considered the simplest and most straight-forward method of comparison.

The results of using PNs as DHPs is shown in Table 4.21. As anticipated, the PNs perform better than DHPs as they can be used to model the FP irradiation effect better than DHPs because the PNs can be produced as decay and transmutation products in addition to being produced as FPs.

Type	Reference	Simplified with 10 DHPs	Simplified with 10 PNs
Pseudo	0	10	10
Secondary	5	1	1
Light	95	4	4
FP	1,417	354	288
Heavy	99	0	0
Actinide	105	58	58
Total	*1,721*	*427*	*361*

Table 4.21: The number of nuclides of each type (as defined in Section 4.6.1) tracked for the ENDF-MC^2 reference simplified DTLs with 10 DHPs, and simplified with 10 PNs.

I note that while this initial comparison demonstrates the superiority of adding PNs instead of DHPs to the depletion chain for preserving decay energy release, this should not be interpreted as the PN method being wholly superior to the DHP method. In this comparison, the median sub-series method mentioned earlier is used to calculate the decay constants of both the PNs and the DHPs. A more optimized method could be used for calculating the DHP and PN decay constants based on the depletion conditions experienced by the system which would alter the number of nuclides tracked for both methods. Additionally, if the goal is to use DHPs to wholly model the decay energy released by FPs, rather than explicitly modeling the decay energy released by some FP nuclides with additional decay energy released by DHPs, then DHPs could be employed to theoretically eliminate the need to track any FP nuclides for the purposes of decay energy modeling, functioning similar to a decay heat standard [84]. This is something that only DHPs could achieve as the PNs main advantage is modeling the FP irradiation effect which becomes impossible if no FPs are explicitly tracked in the simplified depletion library. Once again, it is up to the analyst modeling a given system to determine what must be accurately calculated and the best method to achieve said calculation accurately and efficiently.

4.7. Conclusion

Several conclusions regarding the simplification of depletion chains in order to reduce the number of nuclides tracked in a given depletion system are:

1. When preserving macroscopic XS quantities, the number of nuclides tracked in the depletion library experienced reductions from roughly 1,700 nuclides to anywhere between 165 to 361 nuclides when applying relatively strict macroscopic XS and NND tolerances. In particular, almost all non-actinide, non-FP nuclides were always removed from the simplified DTLs unless these nuclides had an initial non-zero NND.

2. Additional actinides should usually be tracked in fission reactor system because of their significant contribution to the macroscopic XS and the relatively small number of nuclides this adds to the system.

3. Simplified depletion libraries generated using specific flux conditions will generate worse results as the flux conditions increase from those used during the simplification process. If a single simplified depletion library is desired for depleting a large system where different regions experience different depletion conditions, the highest flux experienced in the system for each energy group is recommended for generating the simplified depletion library.

4. Accurately tracking decay energy release requires significantly more nuclides to be tracked in the simplified system with roughly 700 nuclides required for all depletion libraries tested.

5. Adding PNs for decay energy tracking can significantly reduce the number of nuclides needed by the simplified depletion library with reductions from roughly 700 to 350 nuclides achieved for the systems tested when adding 10 PNs.

For developers of depletion analysis tools that do not currently provide users the ability to generate simplified depletion chains based on user-defined thresholds, the heuristic simplification method with PNs introduced in this work is recommended to be implemented because of its overall simplicity and the potential for significant cost savings in terms of runtime and RAM usage of the depletion calculations by using a simplified depletion chain [65] [85].

4.8. Future Work

There is significantly more work to be performed in terms of evaluating depletion chain simplification, including:

1. Neutron transport calculations performed using a simplified depletion library and observing how the macroscopic XS tolerance impacts real-world neutron multiplication factors and power densities.
2. Testing to determine if full-core analysis can be performed using a single simplified depletion library or if multiple simplified depletion libraries should be generated for different core regions.
3. Scaling studies to determine the trade-off between reducing the number of nuclides and increasing the spatial resolution of a given reactor geometry.
4. Usage of PNs for modeling decay particle emission (such as decay photons and neutrons), which requires the preservation of both the energy released in the form of the given particle type and the overall energy spectrum of the decay particles.
5. Exploration of various optimization schemes for adding PNs to the simplified DTL.
6. Investigation of preserving transmutation chains when nuclides in the chain are removed.
7. Comprehensive comparison of the various published depletion chain simplification methods and their performance for various fast and thermal reactor systems.

Chapter 5: Pseudo-Nuclides for Modeling Decay Photon Emission

5.1. Abstract

This paper introduces using pseudo-nuclides for preserving the overall decay photon activity of a two dimensional sodium fast reactor (SFR). Decay photons in nuclear reactors result in a nonlocal decay heat deposition as well as a unique radiological hazard for spent nuclear fuel, both of which are dependent on the photon energy. Despite the challenges introduced by the need to preserve the energy spectra of these decay particles, pseudo-nuclides are able to achieve a 50% reduction in the number of nuclides tracked while preserving decay photon activity within the tolerances used in this work. The introduced method is flexible depending on the specific needs of the analyst, allowing it to be adapted for novel reactor designs and simulations.

5.2. Introduction

Nuclear fuel depletion calculations are vital for understanding the operational parameters of a nuclear reactor, such as fuel cycle length and decay heat. Physically, depletion involves calculating the NNDs of thousands of nuclides because of the wide spectrum of FPs produced from actinides in the reactor fuel undergoing neutron-induced nuclear fission. The FPs can then undergo radioactive decay or neutron activation, resulting in the need to track even more nuclides. Additionally, because of the spatial and energy dependence of the neutron flux in a reactor system, it is necessary to track the NNDs separately for different regions that experience different neutron fluxes. Effects such as self-shielding, burnup, temperature, and density all impact the neutron flux a given spatial region of the reactor experiences, and thus impact the depletion of the fuel in that region.

The need to consider both thousands of nuclides and potentially millions of spatial depletion zones [33, 64–66] demands significant computational resources. As a result, any way to reduce the overall computational cost of a given model is desirable. One option is to reduce the number of nuclides tracked in the system. While not a strictly physical assumption, many of the radionuclides, particularly the immediate FPs, produced in a nuclear reactor are very short-lived nuclides that rapidly decay and do not reach significant quantities in the fuel. Previous research has demonstrated that many nuclides can be removed while still preserving the neutronic properties of the system, reducing the overall number of nuclides from roughly 1,700 to 200 [68, 70]. However, the removal of short-lived radionuclides can result in a dramatic underprediction of decay-related quantities, such as decay heat, with previous research demonstrating that the use of decay heat precursors [72, 73] or PNs [86] can preserve the release of decay energy from the removed radionuclides, while only requiring tracking a total of 300 or fewer nuclides.

In this work, the use of PNs to model the decay photon activity of a SFR is investigated, as modeling decay photon activity introduces additional challenges because of the need to preserve the energy spectrum of the decay photons emitted by the radionuclides. Additionally, the simplification process can be tested against a more realistic reactor model as opposed to the infinite homogeneous regions it was previously tested against [86].

5.3. Data Used

The ENDF VIII.0 decay data [5] and 33-group neutron XS data from MC^2-3 [74] (henceforth referred to as simply MC^2) is used. 1,738 nuclides are tracked in the reference ENDF-MC^2 DTL used by Griffin [2], which is representative of the upper limit of the nuclides tracked during depletion calculations.

ENDF provides both discrete and continuous photon energy spectra for photon-emitting radionuclides. For simplicity, the continuous photon energy spectra are converted to discrete photon spectra, with the discrete energy of each continuous energy bin being the midpoint between the energy bounds of the continuous energy bin. For example, if 25% of photons have a continuous energy distribution between 10 and 25 keV, this energy bin is represented in Griffin as 25% of photons being produced with a discrete energy of 17.5 keV. As will be discussed in Sec. 5.4, Griffin will need to "bin" photons into energy groups anyways, so the simplification of continuous spectra to discrete spectra is acceptable.

The same preprocessing from prior work [86] is leveraged to consider nuclides with half-lives longer than ^{238}U as stable, and ^{8}Be as having the same decay constant as the next shortest-lived radionuclide, ^{72}Fe. This preprocessing can improve the numerical accuracy of the Chebyshev rational approximation method [28, 31, 36], which Griffin uses to solve the Bateman equations [39], and can also make it easier to add PNs to the system by removing outlier decay constants without significantly impacting the overall results of the system [86].

5.4. Photon Energy Group Structure

The primary challenge associated with modeling decay photons instead of overall decay energy release is the energy-dependent nature of photon transport. Similar to how neutrons interact with matter differently depending on the energy of the neutron [22], the energy of the photon determines how it interacts with matter and, for the purposes of photon heating, determines how and where the photon heats a material within a given system [87]. Additionally, in some reactor systems, high-energy photons can cause photonuclear reactions that must be accounted for. The most common example of this reaction is the production of photoneutrons when high-energy photons interact with deuterium, which is a significant source of delayed neutrons in heavy-water reactors [88]. The equation for photoneutron emission from deuterium is:

$$^{2}\mathrm{H} + \gamma \rightarrow {}^{1}\mathrm{H} + {}^{1}\mathrm{n}. \tag{5.1}$$

These photonuclear reactions can only be caused by photons of sufficient energy [75]. As a result, while it was possible to simply model decay energy release by asserting that a given PN releases 1 MeV per decay and then simply alter the yield fraction of the given PN based on the actual amount of decay energy released by the radionuclide the PN was attempting to model, this is not appropriate for decay photons. Replacing photon-emitting nuclides with PNs, which emit 1 MeV photons with the yield fraction of the PN modified based on both the photon yield fraction and the photon energy of the replaced nuclide, would not be appropriate as this would misrepresent the actual photon interactions that occur for photons with varying energies. An obvious example of this problem is once again the photoneutron production from deuterium. The energy threshold for this reaction is 2.225 MeV [75], meaning if only 1 MeV photons are produced in the system, no photoneutrons will be produced from deuterium, which is untrue for real-world reactor systems. More broadly, photon transport, as mentioned previously, is energy dependent similar to neutron transport. Thus in order to account for this energy dependence, Griffin applies the multigroup approximation to photons similar to neutrons.

Defining the energy group structure for photons depends on the level of detail desired by the analyst as well as the specific interest motivating photon transport. If the analyst is primarily concerned with photonuclear reactions, they will primarily be concerned with accurately modeling high-energy photons, as most photonuclear reactions require photons with energies over 2.225 MeV and the photonuclear cross sections are energy dependent, meaning the probability of a given photonuclear interaction occurring changes as the energy of the photon above the cutoff changes [75]. On the other hand, much of the energy released in the form of decay photons is carried by low-

energy photons incapable of causing photonuclear reactions. An analyst concerned with modeling photon heating in a system will require detailed modeling of low-energy and high-energy photons, with photons over 8 MeV generally being of less interest simply because so few photons with that energy are produced, meaning their overall heating effect is low compared to lower-energy photons.

An 18 energy group stucture for photons is considered, with the energy bounds defined in Table 5.1, which are largely taken from Ref. [89] except that the highest energy group has an unbounded maximum energy and the lowest energy group has a lower bound of 0 instead of 1 keV. The energy bounds are changed to account for the production of decay photons outside the original energy bounds. Additionally a midpoint energy is calculated for each energy group, except for the unbounded Group 1, which uses its lower bound as its midpoint. This midpoint allows the decay photon spectrum of each nuclide to be described as a discrete photon spectrum producing photons with the midpoint energies of each energy group in Griffin. For the highest and lowest energy groups, the photon yields are weighted based on the midpoint energy of their energy group. For the upper bound region, this is to better preserve the total energy released by high-energy photons since a midpoint cannot be calculated for an unbounded group. Thus if a radionuclide produces one photon with an energy of 12 MeV, it will instead be assumed to produce 1.5 photons of 8 MeV, thereby conserving the total photon energy released by the radionuclide. Similarly, the lowest energy group is weighted by the midpoint energy, and this is motivated by the very low energy of some photons emitted by radionuclides, namely characteristic x-rays.

Group Number	Lower Bound [eV]	Upper Bound [eV]	Midpoint [eV]
1	8.00×10^6	∞	8.00×10^6
2	6.50×10^6	8.00×10^6	7.25×10^6
3	5.00×10^6	6.50×10^6	5.75×10^6
4	4.00×10^6	5.00×10^6	4.50×10^6
5	3.00×10^6	4.00×10^6	3.50×10^6
6	2.50×10^6	3.00×10^6	2.75×10^6
7	2.00×10^6	2.50×10^6	2.25×10^6
8	1.67×10^6	2.00×10^6	1.83×10^6
9	1.33×10^6	1.67×10^6	1.50×10^6
10	1.00×10^6	1.33×10^6	1.17×10^6
11	8.00×10^5	1.00×10^6	9.00×10^5
12	6.00×10^5	8.00×10^5	7.00×10^5
13	4.00×10^5	6.00×10^5	5.00×10^5
14	3.00×10^5	4.00×10^5	3.50×10^5
15	2.00×10^5	3.00×10^5	2.50×10^5
16	1.00×10^5	2.00×10^5	1.50×10^5
17	5.00×10^4	1.00×10^5	7.50×10^4
18	0	5.00×10^4	2.50×10^4

Table 5.1: Energy bounds of photon energy group structure.

The resulting photon yield spectrum using the energy group bounds defined in Table 5.1 is shown in Figure 5.1.

5.5. Methodology

While previous research determined that 10–20 PNs were sufficient for modeling the decay heat emitted by radionuclides removed from a simplified depletion chain [86], the energy-dependence of decay photon emission means more PNs will likely be needed as each PN will need to correspond to a given decay constant and photon energy group.

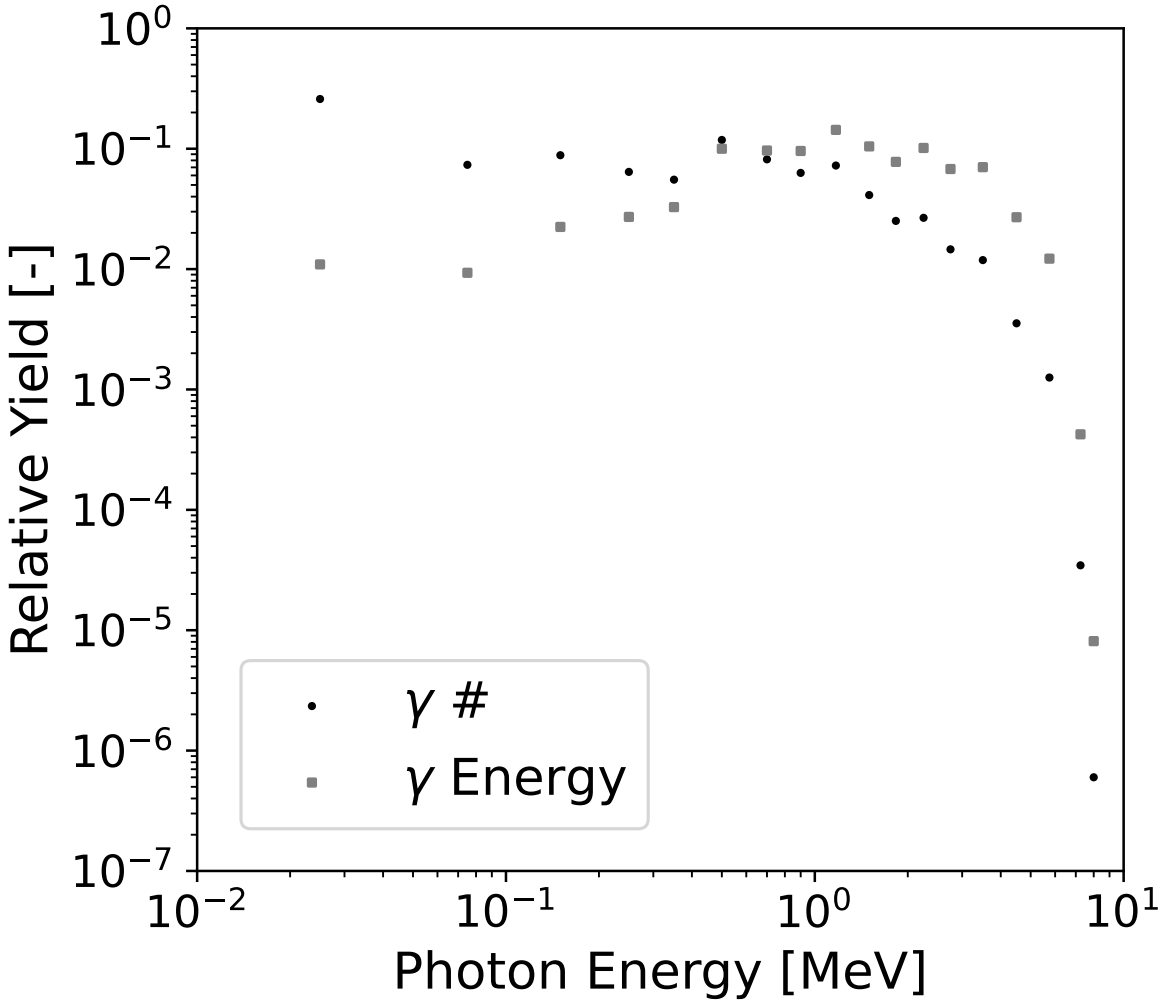

Figure 5.1: The averaged group-wise relative decay photon yield in terms of number of photons and total photon energy. This can be interpreted as the relative yields expected if all photon-emitting radionuclides had the same activity in a given system.

To determine the initial NNDs of the system, Table 2.29 from Ref. [42] was used, which provided burned-in NNDs for an inner core fuel pin of a medium-sized oxide SFR core. In order to estimate fresh fuel NNDs, I assumed that uranium oxide (UO_2) enriched to 20.000 at% ^{235}U is used with the enrichment increasing the concentration of ^{234}U to 0.139 at% and the remaining 79.861 at% as ^{238}U. The NNDs of the other materials in the SFR core were calculated assuming natural abundance of the isotopes for which only elemental number densities were provided. The results of the calculated NNDs for all nuclides present in all homogenized assemblies regions at the beginning of the simulation are shown in Table 5.2. For simplicity, all nuclides within the homogenized fuel assemblies are permitted to deplete while the NNDs of all other assemblies are kept constant.

5.5.1. Spatial Refinement

The geometry of the SFR core used is largely identical to the medium oxide core in Ref. [42] except that corner absorber assemblies were added, shown in Figure 5.2.

Nuclide	Fuel NND	Empty Duct NND	Radial Reflector NND	Radial Shield NND
^{10}B	0	0	0	7.99258×10^{-3}
^{11}B	0	0	0	3.38527×10^{-2}
^{12}C	0	0	0	1.08705×10^{-2}
^{13}C	0	0	0	1.09804×10^{-4}
^{16}O	1.69558×10^{-2}	0	0	0
^{23}Na	7.40989×10^{-3}	2.02096×10^{-2}	3.45216×10^{-3}	3.80851×10^{-3}
^{50}Cr	1.15483×10^{-4}	4.17073×10^{-5}	3.80590×10^{-4}	1.33680×10^{-4}
^{52}Cr	2.22698×10^{-3}	8.04284×10^{-4}	7.33930×10^{-3}	2.57788×10^{-3}
^{53}Cr	2.52522×10^{-4}	9.11993×10^{-5}	8.32218×10^{-4}	2.92311×10^{-4}
^{54}Cr	6.28580×10^{-5}	2.27014×10^{-5}	2.07157×10^{-4}	7.27623×10^{-5}
^{55}Mn	1.17741×10^{-4}	4.25228×10^{-5}	3.88032×10^{-4}	1.36294×10^{-4}
^{54}Fe	1.04568×10^{-3}	3.77653×10^{-4}	3.44619×10^{-3}	1.21045×10^{-3}
^{56}Fe	1.64002×10^{-2}	5.92302×10^{-3}	5.40492×10^{-2}	1.89844×10^{-2}
^{57}Fe	3.78948×10^{-4}	1.36859×10^{-4}	1.24887×10^{-3}	4.38658×10^{-4}
^{58}Fe	5.00498×10^{-5}	1.80757×10^{-5}	1.64946×10^{-4}	5.79360×10^{-5}
^{58}Ni	7.50283×10^{-5}	2.70968×10^{-5}	2.47266×10^{-4}	8.68503×10^{-5}
^{60}Ni	2.89006×10^{-5}	1.04376×10^{-5}	9.52458×10^{-5}	3.34544×10^{-5}
^{61}Ni	1.25641×10^{-6}	4.53756×10^{-7}	4.14065×10^{-6}	1.45437×10^{-6}
^{62}Ni	4.00507×10^{-6}	1.44645×10^{-6}	1.31992×10^{-5}	4.63613×10^{-6}
^{64}Ni	1.02055×10^{-6}	3.68577×10^{-7}	3.36337×10^{-6}	1.18136×10^{-6}
^{92}Mo	1.84070×10^{-5}	6.64779×10^{-6}	6.06628×10^{-5}	2.13074×10^{-5}
^{94}Mo	1.15438×10^{-5}	4.16910×10^{-6}	3.80442×10^{-5}	1.33627×10^{-5}
^{95}Mo	1.99451×10^{-5}	7.20324×10^{-6}	6.57315×10^{-5}	2.30877×10^{-5}
^{96}Mo	2.09503×10^{-5}	7.56629×10^{-6}	6.90444×10^{-5}	2.42513×10^{-5}
^{97}Mo	1.20402×10^{-5}	4.34836×10^{-6}	3.96799×10^{-5}	1.39373×10^{-5}
^{98}Mo	3.05239×10^{-5}	1.10238×10^{-5}	1.00595×10^{-4}	3.53334×10^{-5}
^{100}Mo	1.22437×10^{-5}	4.42187×10^{-6}	4.03508×10^{-5}	1.41729×10^{-5}
^{234}U	1.17749×10^{-5}	0	0	0
^{235}U	1.69559×10^{-3}	0	0	0
^{238}U	6.77053×10^{-3}	0	0	0

Table 5.2: NNDs of the various homogenized assembly regions in units of $\frac{\text{atoms}}{\text{b}\cdot\text{cm}}$.

Four different levels of spatial refinement for the SFR geometry were tested. The same level of refinement is used for both neutronics and depletion, with the understanding that only fuel assemblies experience depletion.

The runtime and memory usage should be expected to scale linearly with the number of elements per assembly with the results of the more refined spatial geometries expected to be more physical than the results generated by coarser geometries.

5.5.2. Temporal Refinement

In order to perform a comprehensive depletion analysis of the SFR core, a set of temporal points to deplete the system to are selected. The points are selected such that the system will deplete to a subcritical state. Whenever it is specified that the SFR core was depleted, the temporal points used for the depletion calculation are those in Table 5.3. Shorter intervals are used during the beginning of the depletion calculation in order to ensure that the buildup of short-lived FPs during the initial depletion process can be accounted for by the simplified DTLs.

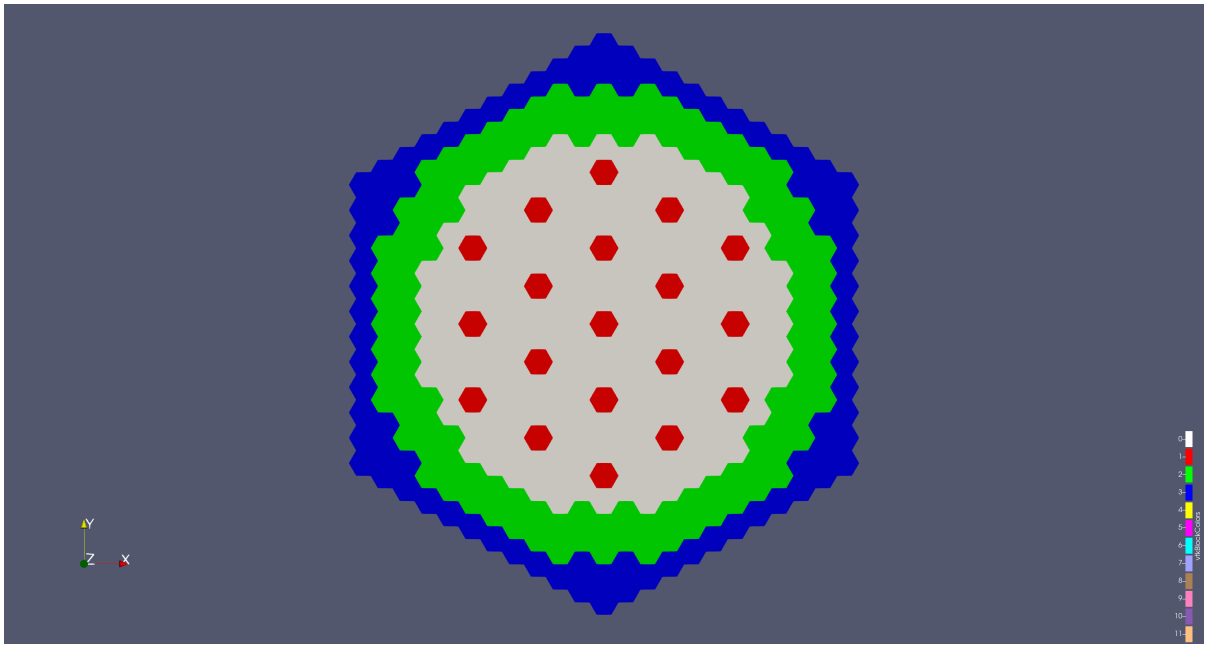

Figure 5.2: Assembly map of the SFR, where red corresponds to empty control assemblies, grey corresponds to fuel assemblies, green corresponds to reflector assemblies, and blue corresponds to absorber assemblies.

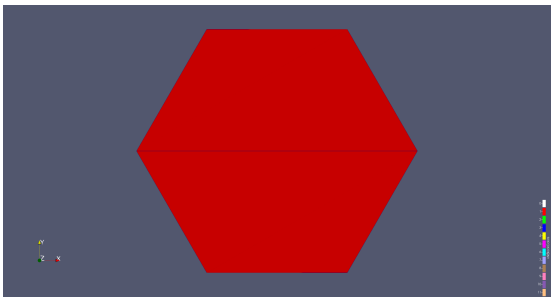

(a) Two element assembly (2EA)

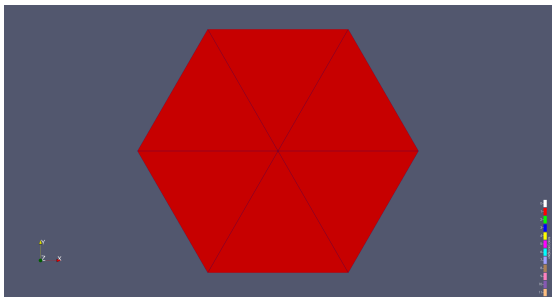

(b) Six element assembly (6EA)

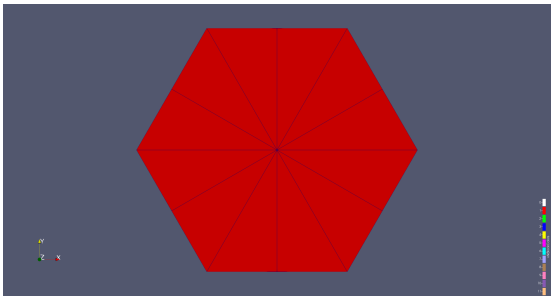

(c) 12 element assembly (12EA)

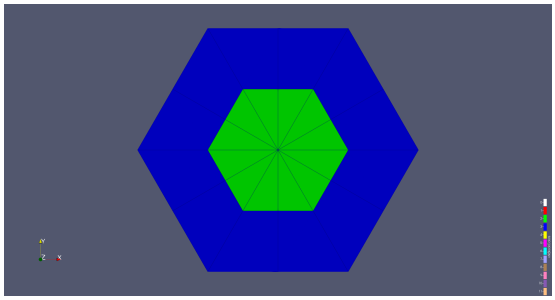

(d) 24 element assembly (24EA)

Figure 5.3: Various spatial resolutions of each assembly. Note that, since 24EA contains both triangular and quadrilateral elements, two different identifiers are required, but both element types represent the same material within each assembly.

Time [s]			
3,600	33,696,000	85,536,000	137,376,000
7,200	36,288,000	88,128,000	139,968,000
21,600	38,880,000	90,720,000	142,560,000
86,400	41,472,000	93,312,000	145,152,000
172,800	44,064,000	95,904,000	147,744,000
432,000	46,656,000	98,496,000	150,336,000
864,000	49,248,000	101,088,000	152,928,000
1,728,000	51,840,000	103,680,000	155,520,000
2,592,000	54,432,000	106,272,000	158,112,000
5,184,000	57,024,000	108,864,000	160,704,000
7,776,000	59,616,000	111,456,000	163,296,000
10,368,000	62,208,000	114,048,000	165,888,000
12,960,000	64,800,000	116,640,000	168,480,000
15,552,000	67,392,000	119,232,000	171,072,000
18,144,000	69,984,000	121,824,000	173,664,000
20,736,000	72,576,000	124,416,000	176,256,000
23,328,000	75,168,000	127,008,000	178,848,000
25,920,000	77,760,000	129,600,000	181,440,000
28,512,000	80,352,000	132,192,000	184,032,000
31,104,000	82,944,000	134,784,000	186,624,000

Table 5.3: Points in time where NNDs of the fuel regions were calculated in Griffin.

5.6. Results

5.6.1. Simplification Process

For the simplification process, the entire SFR core was modeled using the 6EA geometry from Figure 5.3 and depleted the homogenized fuel assemblies system using the reference DTL until the system went subcritical. The maximum flux levels for each energy group at each temporal point, as specified in Table 5.3, in the fuel region were extracted. These maximum flux levels were used during the simplification process, where the NNDs of the homogenized fuel assembly from Table 5.2 were assigned to a 0D infinite homogeneous region and depleted for the same depletion intervals used during the reference calculation with a linear heat rate of $1.165 \times 10^7 \ \frac{\text{W}}{\text{cm}}$ with continuous finite element diffusion [90] used for calculating the neutron multiplication factor and neutron flux distribution in the system. While diffusion is not the most accurate method to evaluate the neutronic properties of the given core, these data provide a basis of comparison between the results calculated by the reference DTL and those calculated by the simplified DTLs. This is the simplification process performed whenever a simplified DTL is mentioned as being generated in the subsequent sections. Additionally, for all simplified DTLs, it is assumed that the target nuclides include actinides with significant fission XSs as well as the decay energy density (calculated by Griffin as "DecayEnergy") with 20 PNs added to preserve the decay energy release of the system. The actinides tracked are: ^{233}U, ^{236}Np, ^{238}Np, ^{236}Pu, ^{237}Pu, ^{238}Pu, ^{239}Pu, ^{241}Pu, ^{243}Pu, ^{240}Am, ^{242}Am, $^{242\text{m}}$Am, ^{244}Am, ^{241}Cm, ^{243}Cm, ^{245}Cm, ^{247}Cm, and ^{249}Cm as well as all nuclides with initial non-zero NNDs in the fuel region as shown in Table 5.2.

In order to calculate the decay constants of the PNs, the decay constants of all radionuclides in the reference DTL are placed into an ordered set S. The set is then divided into ordered subsets of equal sizes based on the number of decay constants needed for the PNs. If two decay constants are needed, the ordered set is divided into two ordered subsets S_1 and S_2, with all of the values in one of the subsets less than any of the values in the other

subset. The median of each of these subsets is then taken, with the two median values calculated serving as the decay constants for the PNs, $\lambda_1 = \text{median}(S_1)$ and $\lambda_2 = \text{median}(S_2)$. If a radionuclide is removed from the system and a PN added to model the decay effects of the removed radionuclide, the decay constant of the PN used is equal to the decay constant calculated from the ordered subset the radionuclide's decay constant belonged to. Meaning that if a radionuclide with a decay constant in S_1 is removed from the system, a PN with a decay constant of λ_1 will be used to model its decay effects. This is the same process that was used previously for generating the decay constants of PNs.

5.6.2. Reference Results

The results calculated for each level of spatial refinement (Figure 5.3) are first considered. The reactivity results of the varying spatial refinement cases are shown in Figure 5.4, which demonstrate that the calculated reactivity of the system increases with increasing spatial refinement. Since increasing spatial refinement results in increased computational costs, reducing the size of the DTL could reduce the computational cost of a given spatial refinement, thereby allowing for more accurate spatial geometries, which could provide better results than the highest level of refinement achievable with the reference DTL. A total of 1,738 nuclides are present in the reference DTL.

5.6.3. Simplification Without Decay Photon Tracking

Next, the results calculated for each level of spatial refinement specified in Figure 5.4 are considered. The simplification process was performed using a macroscopic XS tolerance (T_Σ) of 10^{-5} and a target NND tolerance (T_N) of 10^{-3}, which was used in previous work [86]. The target nuclides specified are: ^{233}U, ^{236}Np, ^{238}Np, ^{236}Pu, ^{237}Pu, ^{239}Pu, ^{241}Pu, ^{243}Pu, ^{242}Am, ^{242m}Am, ^{244}Am, ^{244m}Am, ^{241}Cm, ^{243}Cm, ^{245}Cm, ^{247}Cm, and ^{249}Cm, as well as all nuclides with nonzero initial NNDs in the homogenized fuel region, as specified in Table 5.2. The "DecayEnergy" non-nuclide quantity is tracked in the Bateman equations by Griffin [79] and 20 PNs are used to preserve DecayEnergy within T_N. This results in a total of 300 nuclides to track in the simplified depletion library.

As shown in Figure 5.5, the simplified DTL differences are less than 1 pcm from the reference DTL results for each considered spatial resolution and the difference is identical for all considered spatial resolutions. This indicates that the simplified DTL can reproduce k_{eff} results relatively well regardless of the spatial refinement level specified.

DecayEnergy and ^{249}Cm experience the greatest divergence from the reference results for all spatial geometries, as shown in Figs. 5.6 and 5.7. Both quantities are within T_N of the reference solution for all depletion zones at all points in time, which was anticipated based on previous results. Additionally, all spatial resolutions have similar behavior.

Next, the overall decay photon activity of the system is considered. For simplicity, the RDs of all photon energy groups are considered simultaneously, and the mean, median, maximum OP, and maximum UP across all photon energy groups were calculated, shown in Figure 5.8. The behavior is somewhat similar to behavior observed when performing simplification without considering DecayEnergy, and the quantity is wholly underpredicted during the entire simulation, with the average decay photon activity for all energy groups in all depletion zones underpredicted by over 60%. This is unacceptable for applications that require accurate modeling of decay photon emission, such as nonlocal heating during shutdown and the radiological hazard of spent fuel. Consequently, it is necessary to modify the simplification process to preserve decay photon activity.

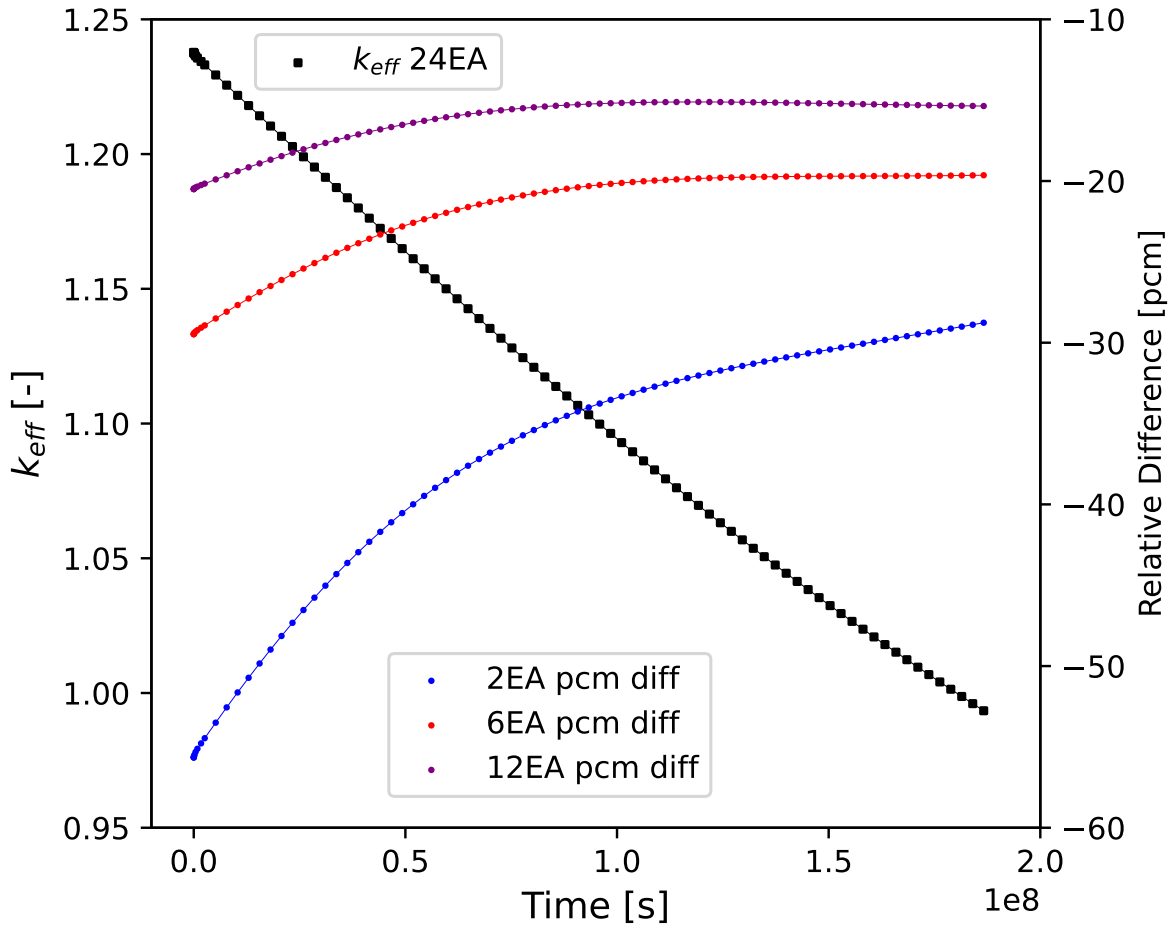

Figure 5.4: k_{eff} result for the 24EA case and the reactivity difference of the 2EA, 6EA, and 12EA cases relative to the 24EA case using the reference DTL.

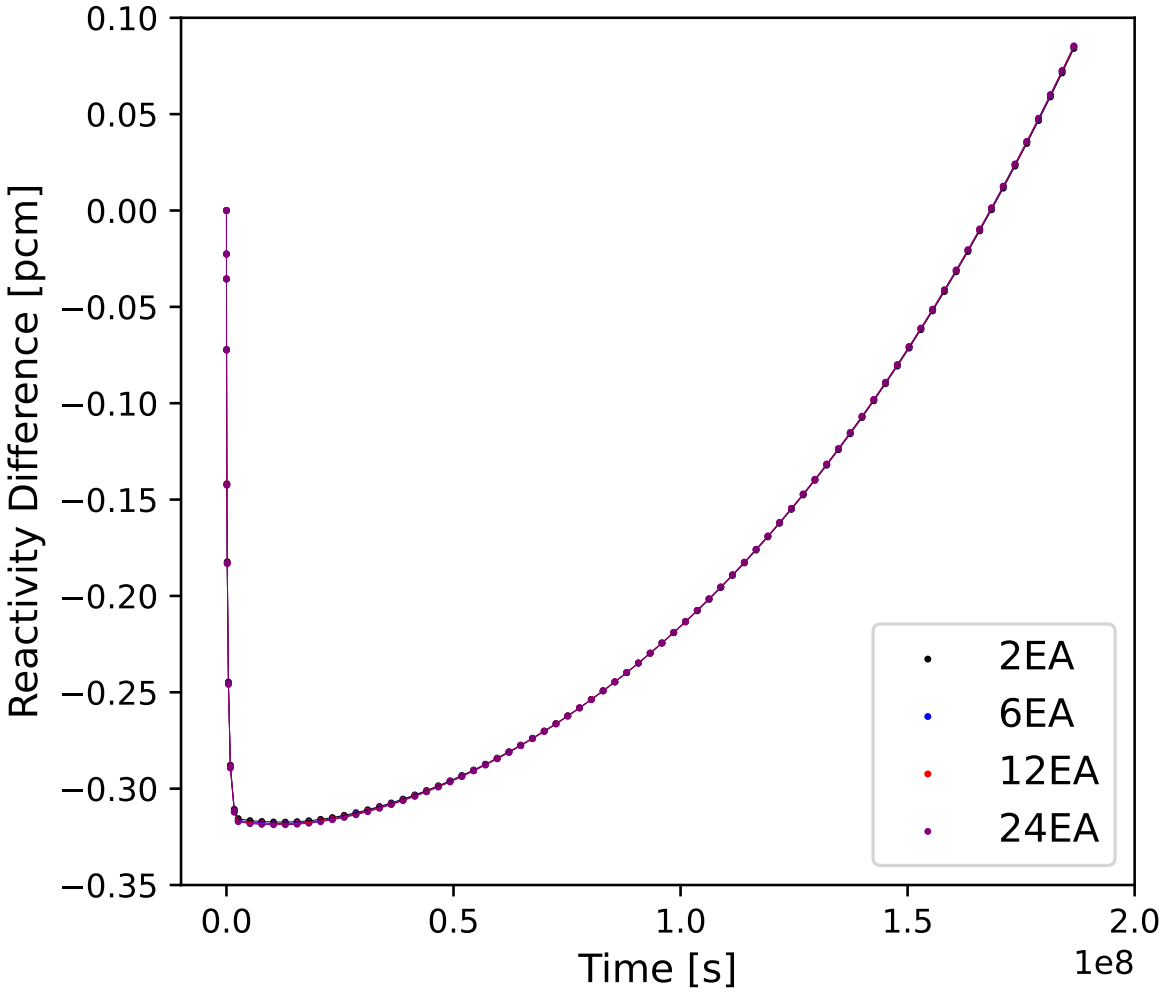

Figure 5.5: Reactivity differences between the simplified DTL and the reference DTL for the various spatial resolutions in Figure 5.3.

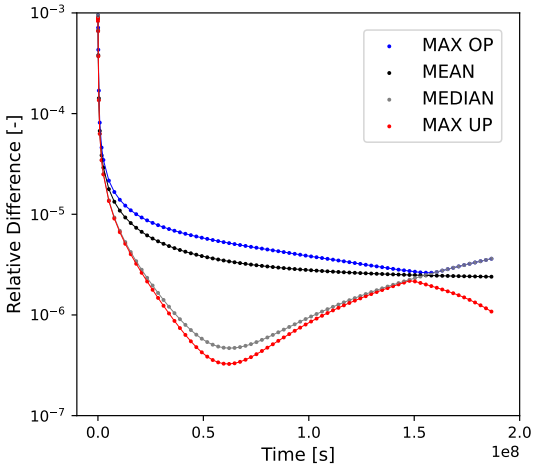

(a) 2EA

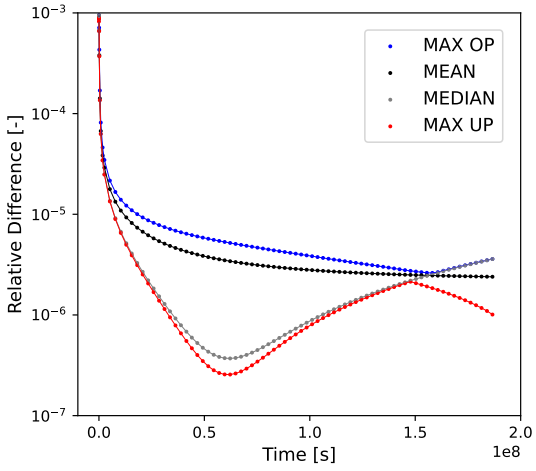

(b) 6EA

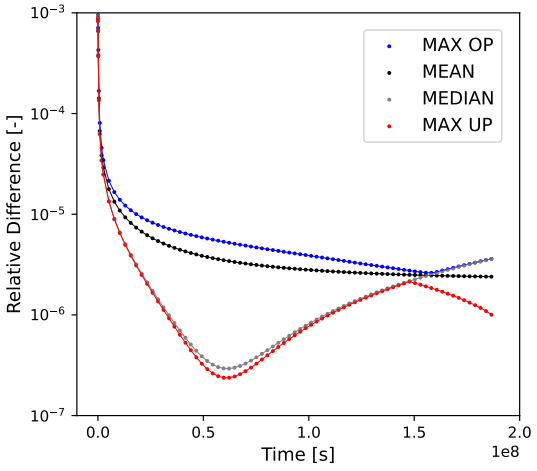

(c) 12EA

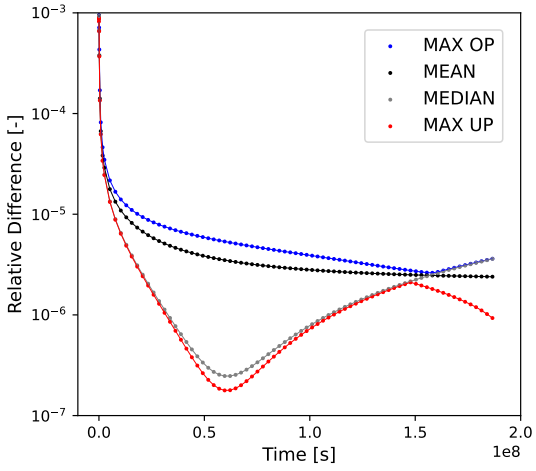

(d) 24EA

Figure 5.6: RDs between the DecayEnergy calculated by the reference DTL compared to the simplified DTL. The maximum overprediction (OP), maximum underprediction (UP), mean, and median RDs at each timestep across all depletion zones are shown.

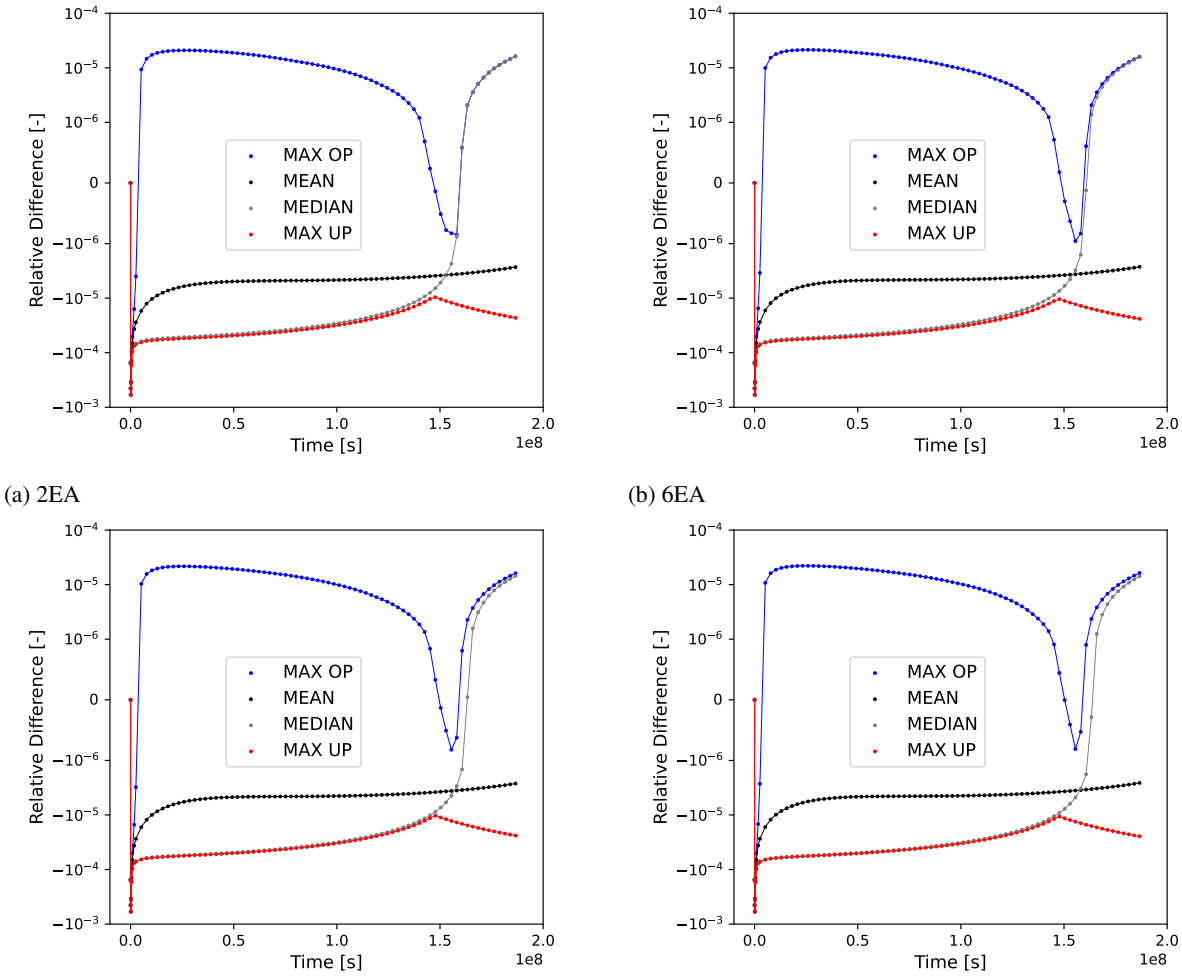

(a) 2EA

(b) 6EA

(c) 12EA

(d) 24EA

Figure 5.7: RDs between the ^{249}Cm NND calculated by the reference DTL compared to the simplified DTL. The maximum OP, maximum UP, mean, and median RDs at each timestep across all depletion zones are shown.

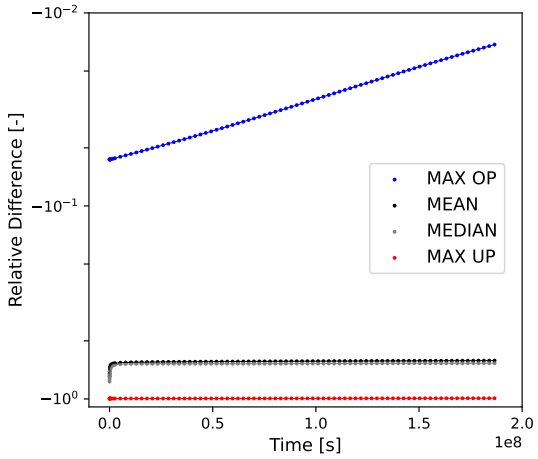

(a) 2EA

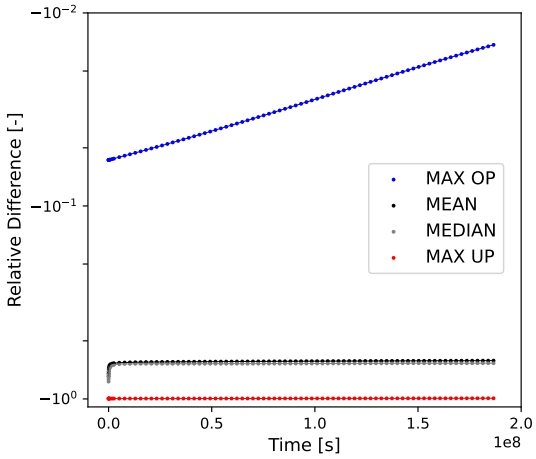

(b) 6EA

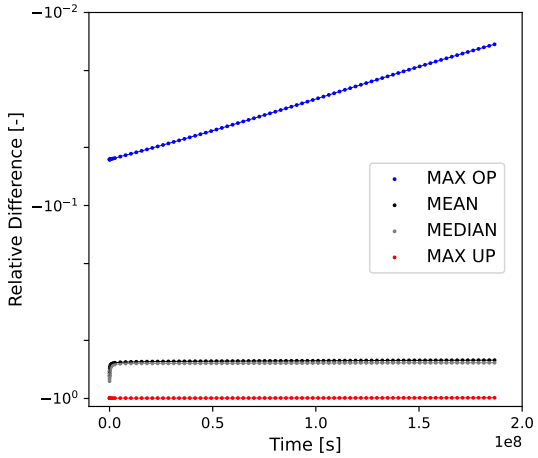

(c) 12EA

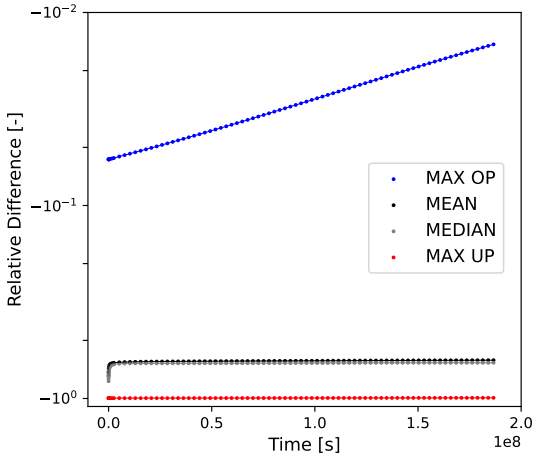

(d) 24EA

Figure 5.8: RDs between the decay photon activity for all groups calculated by the reference DTL compared to the simplified DTL. The maximum OP, maximum UP, mean, and median RDs at each timestep across all depletion zones and all photon energy groups are shown.

5.6.4. Simplification with Decay Photon Tracking

The first step is to simply add the decay photon activity across all energy groups as a quantity to preserve during the simplification process within T_N. This increases the number of nuclides tracked in the system to 751 and produces the decay photon activity results shown in Figure 5.9. As expected, the results are significantly improved; however, the decay photon activity is underpredicted at all points in time for all depletion zones and all energy groups and slightly exceeds T_N, though this difference is quite small and an overall improvement compared to Figure 5.8. The overall increase from 300 nuclides in Section 5.6.3 to 751 nuclides is an increase of 150%, thus PNs may be able to reduce the overall number of nuclides tracked.

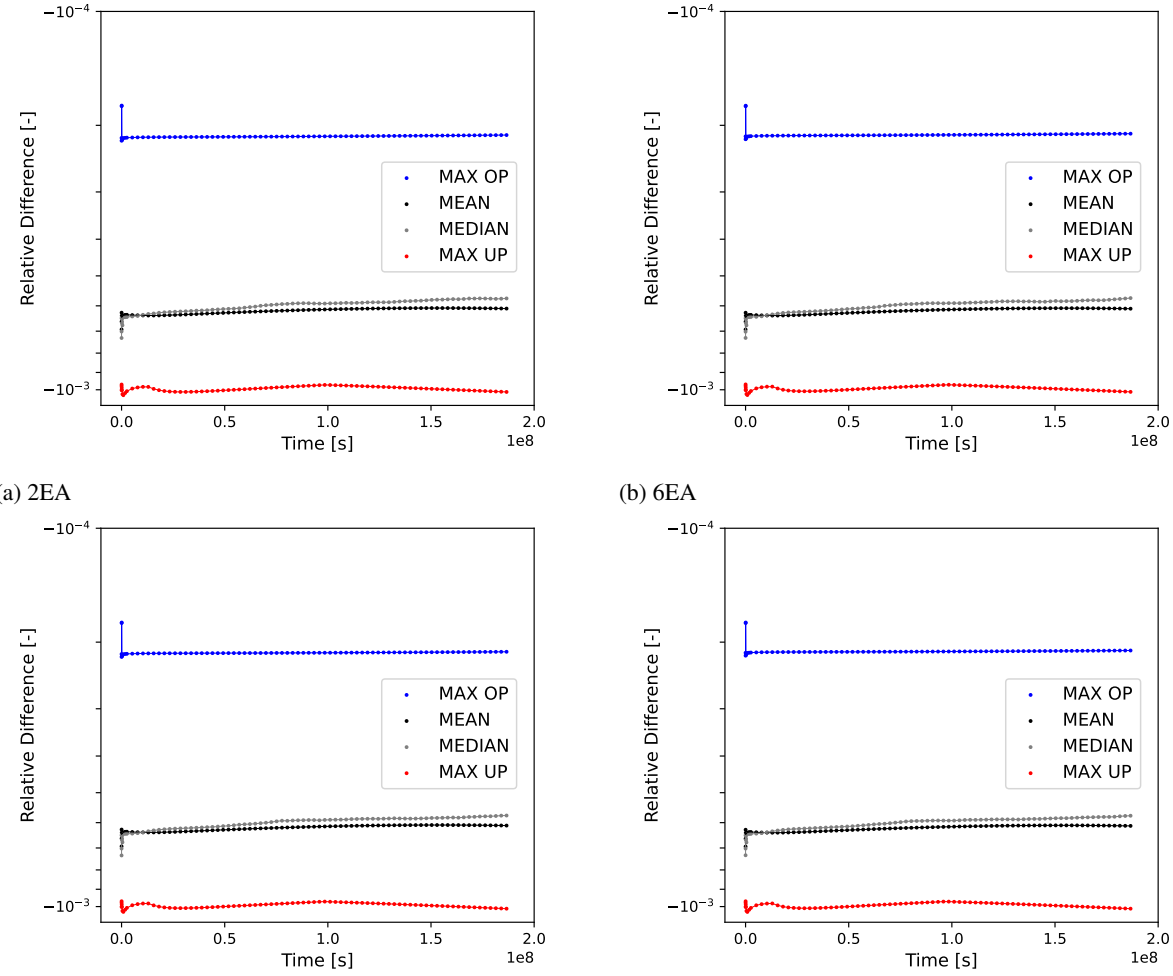

(a) 2EA

(b) 6EA

(c) 12EA

(d) 24EA

Figure 5.9: RDs between the decay photon activity for all groups calculated by the reference DTL compared to the simplified DTL with decay photon activity tracking. The maximum OP, maximum UP, mean, and median RDs at each timestep across all depletion zones and all photon energy groups are shown.

5.6.5. Simplification with Decay Photon Tracking and PNs

To preserving modeling of decay photon activity in each energy group while using fewer nuclides overall, the addition of PNs was considered. As the spatial geometries all had similar results, only the outcomes of the

24EA case are considered for the remainder of this work. As there are 18 photon energy groups, the number of PNs added for photon tracking was always a multiple of 18. When adding 18 PNs, all PNs have the same decay constant, which is the median of all nonzero decay constants in the reference DTL, with each PN emitting one photon per decay in one of the 18 energy groups. When adding 36 PNs, two different decay constants are calculated by dividing the nonzero decay constants from the reference DTL into two ordered subsets and taking the medians of each subset, following the process mentioned in Section 5.6 as the number of PNs increases.

The initial short timesteps all experience the maximum divergence from the reference results, which is expected, as during the initial depletion intervals the decay photon activity is dominated by many short-lived FPs which rapidly reach their saturation NNDs, while longer-lived FPs require more time to build up to significant quantities where their activity is comparable to that of the short-lived FPs. As the number of PNs increases, the overall calculation of photon activity improves. However, as shown in Table 5.4, the increasing accuracy with increasing PNs comes at the cost of more nuclides to model in the system. If the tolerance of T_N is acceptable, all simplified DTLs with decay photon activity tracking meet the criteria, with 36 PN DTL requiring the fewest overall nuclides. It is also worth noting that the number of PNs for each simplified DTL is not always exactly 20 plus the number of decay photon tracking PNs. This is because not all radionuclides in a given decay constant range emit photons in all energy groups, particularly the high-energy photon groups. As a result, sometimes PNs may be added to the system but are then automatically removed by Griffin since no production pathway exists for those PNs.

Simplified	—	✓	✓	✓	✓	✓	✓	✓	✓
Photon Tracking	—	—	✓	✓	✓	✓	✓	✓	✓
Photon PNs	0	0	0	18	36	54	72	90	180
Pseudo	0	20	20	38	53	69	84	101	177
Secondary	5	5	5	5	5	5	5	5	5
Light	105	7	9	8	8	8	8	8	8
FP	1,424	217	666	393	261	278	263	253	238
Heavy	99	0	0	0	0	0	0	0	0
Actinide	105	51	51	51	51	51	51	51	51
Total	*1,738*	*300*	*751*	*495*	*378*	*411*	*411*	*418*	*479*

Table 5.4: The number of nuclides of each type tracked for various simplified libraries with the given parameters. Recall that in this work all simplified libraries have 20 PNs to assist in modeling decay energy release.

5.7. Conclusion

The results of this work demonstrate that, similar to decay energy, significantly more nuclides must be tracked in simplified depletion libraries to accurately calculate decay photon activity. While the energy spectrum of the decay photons does present a new challenge, PNs are able to significantly reduce the overall number of nuclides tracked in a simplified library while still preserving decay photon activity for an 18-group photon spectrum. The reduction of 751 to 378 nuclides is a reduction of almost 50% and would be expected to reduce the runtime and memory usage of a given depletion calculation by roughly 50%.

Additionally, as shown in Figs. 5.4 and 5.5, system spatial refinement has a much larger impact on the reactivity of the system than the simplification process with the criteria used in this work. While not every reactor model will see a significant change in the reactivity or other reactor parameters by increasing spatial refinement, some reactor models may benefit from using a simplified DTL as errors introduced by the simplification process may be less significant than the error introduced by using a coarser geometry.

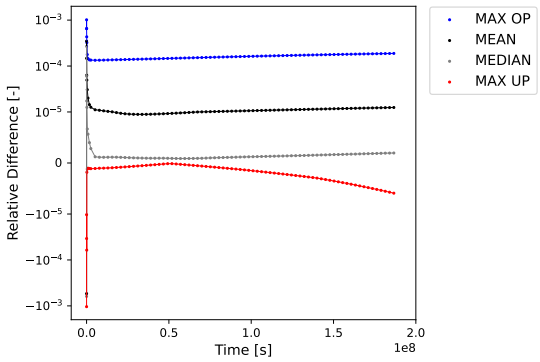

(a) 18 PNs for decay photon tracking

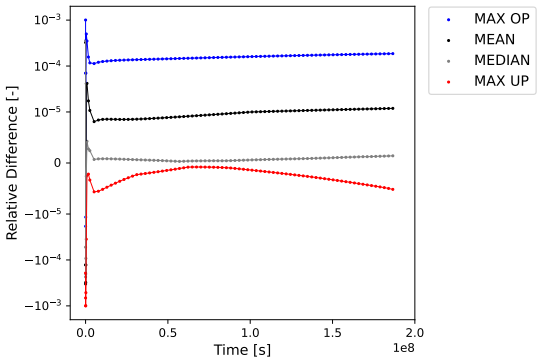

(b) 36 PNs for decay photon tracking

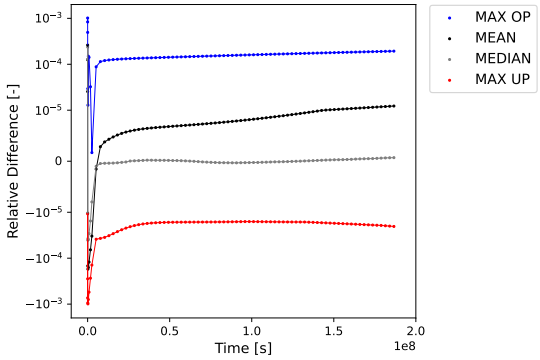

(c) 54 PNs for decay photon tracking

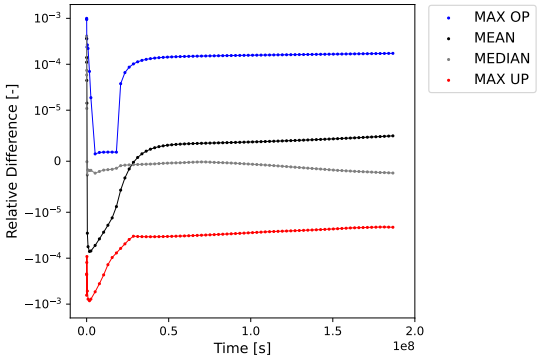

(d) 72 PNs for decay photon tracking

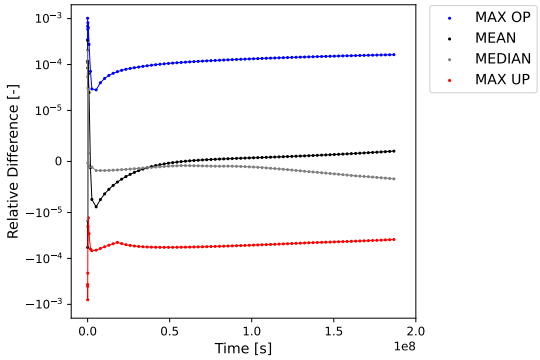

(e) 90 PNs for decay photon tracking

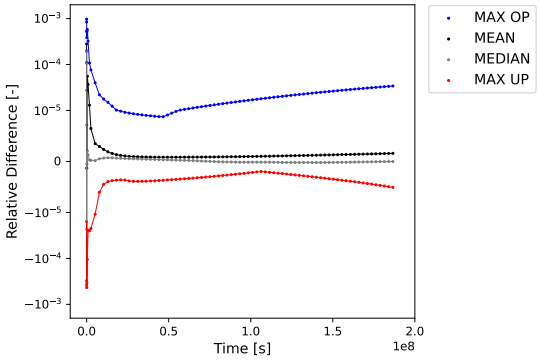

(f) 180 PNs for decay photon tracking

Figure 5.10: RDs between the decay photon activity for all groups calculated by the reference DTL compared to the simplified DTLs with varying numbers of PNs.

Even for models with sufficient spatial refinement, the simplification process can significantly reduce the overall computational resources required while preserving quantities of interest within a given criteria. As a result, it may still be of interest for analysts to use simplified depletion libraries in order to reduce the overall computational costs that may enable running multiple models in parallel or a greater turnaround time when performing multiple iterations of reactor analysis, both of which may offset any error introduced by the simplification process, an error that may be well within experimental uncertainty for many reactors [82].

5.8. Future Work

This work has expanded upon previous work [86]; however, significant areas of research interest remain, including:

- Optimizing the decay constants of the PNs added to the simplified depletion library.
- Determining if PNs with specific decay particle spectra could result in a need for fewer PNs overall rather one PN for each decay constant and decay particle energy group, which could result in hundreds of PNs for more refined group structures.
- Completing a comprehensive review and comparison of existing depletion library simplification methods for various reactor benchmarks.

Chapter 6: Conclusion

Several novel methods are proposed and tested in this work, the conclusions of which are presented in this chapter.

6.1. The Adding and Doubling Method

ADM was developed in an effort to create a faster method than CRAM for solving the depletion matrix exponential. While ADM is only competitive with CRAM in terms of run time for systems with less than 300 nuclides, there are still several advantages of ADM. The first is the ease of implementation of ADM in depletion applications because of the simplicity of the method. This reduces the burden on developers regarding the implementation and maintenance of the method as well as being a more transparent and easy to understand method. ADM is also a completely independent method compared to CRAM for solving the matrix exponential and is theoretically agnostic to the sparsity of the depletion matrix. By comparison, CRAM when implemented with SGE expects a certain sparsity pattern from the depletion matrix which can cause CRAM to give erroneous results if this expected sparsity pattern is violated. Consequently, ADM has value as a method which can be used to verify the results produced by CRAM with a larger, but still acceptable, run time for the purposes of verification.

ADM does provide a dramatic performance improvement over CRAM in the niche instance where the depletion matrix and the length of the depletion interval are constant for multiple depletion intervals. In this instance, ADM can cache the response matrix in order to solve the Bateman equations for multiple regions while performing a single matrix-vector multiplication, which is significantly faster than solving the CRAM equations for a given depletion region. However, this use case is expected to only be applicable for real-world systems if attempting to perform decay heat analysis, in which case the depletion matrix remains constant because there is no transmutation component meaning the depletion matrix is equal to the decay matrix, which is constant. If transmutation is occurring, then this condition cannot likely be applied because the rate of transmutation will fluctuate over time as the neutron flux distribution and the microscopic XSs of the system vary as depletion occurs.

Regarding the implementation of ADM, it is recommended to be implemented alongside CRAM as a means of verifying CRAM, but if an existing depletion application already has a method which can be used to verify CRAM then the implementation of ADM is likely redundant.

6.2. Non-Nuclide Quantities in the Bateman Equations

Chapter 3 demonstrated the utility of calculating non-nuclide quantities in the Bateman equations instead of using traditional finite difference methods, such as FE. Such quantities do not appreciably alter the sparsity pattern of the depletion matrix or alter the eigenvalues of the depletion matrix, meaning CRAM and other methods of solving the Bateman equations can be used to solve these augmented systems. The reason for evaluating these non-nuclide quantities in the Bateman equations is driven by the dependence of quantities such as FIMA and KERMA on the NNDs of the system. Since the NNDs are time-dependent because of depletion, the time-dependence of these quantities can best be accounted for by simultaneously solving for these quantities in the Bateman equations alongside the NNDs. Because of the relative simplicity of tracking non-nuclide quantities in the Bateman equations, and the fact that depletion-capable applications likely already handle the data necessary for calculating quantities such as KERMA, it is recommended that this functionality be implemented in all depletion-capable applications.

6.3. The Heuristic Simplification Method

A relatively simple heuristic method is proposed in order to perform the depletion chain simplification process using user-defined depletion conditions, tolerances for quantities of interest, and a reference depletion library. The user defines the flux conditions and depletion intervals which the 0D infinite homogeneous region will experience. The reference library is then used to calculate reference values for the quantities of interest, namely macroscopic XS and target NND, but other target quantities such as decay energy release and decay photon activity can also be specified. These reference values are calculated for each depletion interval specified by the user. The simplification process, as outlined in Section 4.5, then recalculates all quantities of interest as nuclides are removed from the system, preserving nuclides whose removal causes the quantities of interest to diverge by more than the user-specified tolerance.

The heuristic method depends on calculating the macroscopic XS with the expectation that preserving the accuracy of the macroscopic XS after each depletion interval will result in a similar preservation of accuracy when calculating the neutron multiplication factor k. As shown in Table 4.9 and Figure 5.5, k is well-preserved in the simplification process for the SFR system tested. It is also determined that the results calculated by the simplified depletion library are sensitive to increases in the magnitude of the neutron flux relative to the neutron flux specified during the simplification process as determined in Section 4.6.1.2. As a result, it is recommended to use the largest anticipated flux levels for the given system when performing the simplification process as this is expected to improve the performance of the simplified depletion library which was demonstrated for the SFR system tested in Section 5.6.3. Additionally, it is recommended to always consider all actinides with high fission probabilities as target nuclides to preserve the NNDs of, as this will significantly improve modeling of the macroscopic fission XS and thus k. Since there are only a few dozen higher actinides to track, this has a relatively small impact on the total number of nuclides in the simplified depletion library. However, if very small depletion libraries are desired, this recommendation can be ignored so long as the drawbacks of doing so are understood.

While the heuristic method is demonstrated as capable of reducing the number of nuclides tracked from roughly 1,700 to 200 nuclides in Section 4.6.1.3 or 300 nuclides in Table 5.4 while preserving macroscopic XS and target NNDs for the systems tested, this number increases dramatically if preserving decay-related effects are desired as shown in Sections 4.6.1.4 and 5.6.4, with the number of nuclides tracked increasing to 700 or more. A cursory comparison of the heuristic method to recently published methods in Section 4.6.1.6 indicates that the overall reduction in the number of nuclides tracked is comparable to that of other published methods.

6.4. Pseudo-Nuclides

The significant increase in the number of nuclides tracked when tracking decay-related quantities motivated the addition of PNs to the system in order to model these decay-related effects. PNs are introduced as similar to the previously published method of DHPs [72, 73] with the difference being that PNs can be produced as a result of fission, radioactive decay, or non-fission transmutation while DHPs can only be produced as a result of fission. This allows PNs to account for the fission product irradiation effect better than DHPs.

When applied to modeling decay energy release, which is equivalent to the time integral of decay power, PNs achieve significant reductions in the overall number of nuclides tracked with the number of nuclides tracked reduced by 50% with PNs compared to the simplified depletion libraries without PNs as shown in Sections 4.6.1.5 and 4.6.2.2. When applied to modeling decay photon activity, a comparable 50% reduction can be achieved as shown in Table 5.4 for the given SFR system with 18 photon energy groups. It is expected that as the number of photon energy groups increases, the total number of PNs needed will increase, increasing the total number of

nuclides tracked. With a fine enough photon energy group structure, the number of PNs needed may become so large that there is no benefit to using PNs during the simplification process as the number of PNs added may be larger than the number of nuclides removed during the simplification process.

In order to generate the decay constants for the PNs, the median subseries method described in Section 4.5.2 was used and performed well. While more optimization is possible, for the cases considered here this method of calculating decay constants for the PNs was sufficient.

A cursory comparison between PNs and DHPs in Section 4.6.1.6 indicates that the number of nuclides tracked when using PNs is less than the number needed when using DHPs for the specific system tested.

6.5. Depletion Simplification Recommendations

6.5.1. For Analysts

For reactor analysts performing depletion modeling where it is necessary to accurately model decay effects, or potentially esoteric nuclides which are not typically tracked in simplified depletion libraries distributed by depletion-capable applications, it is recommended to adopt the methodology introduced in this work to generate simplified depletion libraries. These simplified depletion libraries can significantly reduce the computational cost of depletion calculations by over 80% when compared to reference depletion libraries based off of the ENDF/B-VIII.0 data [5]. These reductions in computational costs can allow the analyst to increase the spatial refinement of their model, which could result in a net improvement in the accuracy of their results similar to what was shown in Section 5.6.2. However, if further spatial refinement is not desired, the reduction in the computational costs of the depletion model is still desirable as it will enable results to be generated sooner and allow for more variations of the model to be run in parallel. However, it is incumbent on the analyst to understand the depletion conditions the system will experience, and to perform the simplification process with the understanding the simplified depletion library is only meant to model a system experiencing the given depletion conditions and only preserving the quantities of interest defined during the simplification process.

While it cannot be stated that the simplification method introduced in this work is wholly superior to other simplification methods which have been published, the heuristic method introduced in this work is relatively simple and thus considered a possibility for analysts to utilize themselves in order to accelerate their workflow with simplified depletion libraries.

6.5.2. For Developers

For developers of depletion-capable applications such as Serpent, OpenMC, ORIGEN, and others, it is recommended to implement some form of depletion library simplification capability. As mentioned previously, the method presented in this work is relatively simple to implement, from a developer's perspective, and simple to use, from a user's perspective. However, other published simplification methods, such as those mentioned in Section 4.6.1.6, have also demonstrated good performance and could also be considered for implementation in depletion-capable applications. The usage of PNs for modeling decay effects when performing the simplification process is recommended, as PNs provide a great degree of flexibility in terms of what decay effects they are capable of modeling.

The simplification process introduces significantly smaller changes in k than varying the spatial refinement of the system as shown in Figure 5.4. Based on the computational costs associated with varying the number of nuclides and/or the number of spatial depletion zones as shown in Eqs. 1.12 and 4.3, this indicates that the error introduced by the simplified depletion libraries can be less than the error introduced by a coarser spatial

refinement of the system. Since the advantages of using simplified depletion libraries, and the disadvantages of using a reference depletion library, have been previously published by the developers of OpenMC [85], the advantages of providing depletion library simplification functionality are apparent to developers.

Chapter 7: Future Work

Numerous potential future research topics are introduced as a result of this work and are outlined in this section.

7.1. Additional Tracking of Non-Nuclide Quantities

In this work the tracking of non-nuclide quantities was limited to the evaluation of DPA, FIMA, and KERMA. It is possible that there are other non-nuclide quantities of interest which could be evaluated in the Bateman equations and may be difficult to calculate via other methods. A potential quantity of interest to evaluate would be the ratio of fissions from uranium relative to fissions from plutonium as this can inform optimization of the fuel cycle and improve fuel utilization. It can be difficult to determine the number of fissions which are from a given nuclide, particularly if the NND of the nuclide has a strong time-dependence and varies significantly over a depletion interval. An estimate of the number of fissions that occur for a given nuclide over a given depletion interval can be obtained by Eq. 7.1.

$$\#\text{ Fissions of Nuclide X} = \frac{N_{\text{X}}(t_0) + N_{\text{X}}(t_1)}{2}(t_1 - t_0)\sum_{g=1}\sigma_{\text{X,f},g}\phi_g \tag{7.1}$$

However, this may not be a valid estimate if the NND is not changing linearly with respect to time. Since radioactive decay results in an exponential decay in the NND of radionuclides, nonlinear changes in NNDs are entirely possible. Even if the estimate in Eq. 7.1 is suitable for analysis purposes, it can be tedious to perform this analysis after the Bateman equations results have been generated, particularly for systems with a large number of depletion regions. While it would be possible to modify a depletion-capable application to estimate this quantity using Eq. 7.1, Chapter 3 demonstrated that it would not be a significant amount effort to instead simply calculate this quantity as part of the Bateman equations, which would be expected to yield a more accurate result.

7.2. Application of Neural Networks to the Simplification Process

One of the most interesting future research topics regarding depletion chain simplification is the application of neural networks to the depletion chain simplification process. In theory, it should be possible to train a neural network using the depletion chain simplification process to predict which nuclides should be tracked based on which quantities of interest the user wants to preserve for a given reactor design (e.g., SFR, PWR, etc.).

One potential advantage of a neural network over a user running the simplification process themselves is that a user may not have a good understanding of the depletion conditions their system will experience. Or the system may need to be designed to accommodate a variety of depletion conditions, such as a research reactor which is designed to be able to sustain several different power levels for irradiation experiments while simultaneously being capable of briefly pulsing to extremely high power and flux levels. With the depletion chain simplification methodology outlined in this work, this would likely require the user to generate several different simplified depletion libraries using the various unique depletion conditions the reactor is expected to experience and then taking a superset of all the nuclides which occur at least once in each simplified library. If a neural network is trained on a wide variety of depletion conditions then it should be able to generate a simplified depletion library which can accommodate several different depletion condition ranges specified by a user.

Another potential advantage of a neural network is that a user may not have easy access to depletion-ready XS data which is appropriate for the given reactor system they intend to model and generation or acquisition of this

XS data will likely be a more time-consuming process than the simplification process itself. If a neural network is trained on the simplification process using a wide range of XS data from various sources such as ENDF [5], JEFF [18], and JENDL [17], for a wide range of flux spectra then it should be able to produce a simplified depletion library of sufficient quality provided that the user as a relatively general knowledge of the anticipated temperature and flux energy spectrum the system should experience.

The final potential advantage considered here is that a neural network would be expected to understand the optimal number of PNs needed for the user to preserve decay-related quantities within tolerances specified by the user. This optimization would likely outperform any standardized method of generating PNs as different methods of generating PNs are likely more or less optimal depending on the depletion conditions and data provided. An extensively trained neural network should understand which method to generate PN decay constants or PN decay particle energy spectra is optimal for the user-specified depletion conditions.

However, despite the many advantages of using a neural network for depletion chain simplification, there are also challenges which would need to be addressed. The primary challenge of using a neural network for depletion chain simplification, particularly a neural network using the heuristic method presented in this work, is the computational resources necessary to train a neural network. As mentioned in Eq. 1.12, the CRAM run time for a system with 1600 nuclides is 19 ms, which will vary depending on individual processor performance relative to the processor used to generate this number. This means that to solve CRAM for 50 depletion intervals would take roughly 1 s. When performing iterative nuclide removal, the depletion calculation needs to be performed for all 50 depletion intervals every time a nuclide is removed. If perfectly efficient nuclide removal is performed such that a nuclide is always removed this will reduce the run time of CRAM when removing future nuclides since the number of nuclides tracked has decreased. However, this would still result in a run time of at least 800 s or about 13 minutes. While this is not particularly expensive if the simplification process only needs to be performed once, when training a neural network it is possible that the simplification process will need to be performed millions or potentially billions of times depending on the range of depletion conditions and depletion data the system is to be trained for.

Should the calculation need to be performed a million times, the training process would take almost three years. The training process could be parallelized, but even with thousands of processors the training process could take weeks, which is a significant computational expense. This is also ignoring the time which would need to be spent gathering data for the training process, which would require an extensive literature search on existing and proposed reactor designs and their anticipated depletion conditions as well as processing available XS data into a form usable by the neural network during the training process.

Such a comprehensive neural network is likely impractical with current computational resources, however, a more narrow and specialized neural network can likely be trained using existing simplification methods and computational hardware. The main drawback of this being that the more specialized a neural network is, the more likely a user may prefer to perform the simplification process themselves and have a better understanding of how the simplified depletion library was generated. Further research on this topic is necessary in order to truly understand the value of applying neural networks to depletion libraries both with current computational resources and computational resources which may be available in the future.

7.3. Comparison of Simplification Methods

As mentioned previously in this work, many different methods of simplifying depletion chains have been introduced, however, no comprehensive comparison of these methods has been performed. In order to better determine which method is “superior” it would be necessary to implement all methods in a single depletion-

capable application, such as Griffin, and generate multiple simplified depletion libraries, using the same criteria for all methods, for various reactor models, preferably full-core models. This would enable each method to be compared based on the time needed to generate the simplified depletion library, the number of nuclides in each simplified library, and the accuracy of the results using the simplified depletion libraries.

Ideally, a comprehensive review paper would generate depletion libraries from multiple datasets such as ENDF [5], JEFF [18], JENDL [17] and test the simplification process for pressurized heavy water reactors (PHWRs), gas reactors, lead fast reactors, LWRs, SFRs, and MSRs, as each of these reactor systems will experience significantly different flux spectra and have significantly different initial nuclear fuel compositions. Indeed each individual reactor type could be fueled with different initial fuel compositions and fuel cycles as a PHWR initially fueled with natural uranium will experience a significantly different depletion conditions than a PHWR fueled with a mix of enriched uranium and reactor-grade plutonium.

Similarly, the various simplification methods could also each be tested using PNs or DHPs to model decay effects and determine how well each method performs when it comes to modeling decay effects.

7.4. Pseudo-Nuclide Decay Particle Energy Spectra

In this work, the multigroup approximation applied to photons enabled the assumption that each photon-emitting PN only emitted photons in a distinct energy group. While the number of PNs needed to preserve decay photon activity based on the system considered in Section 5.6.4 was not particularly large relative to the total number of nuclides in the simplified library, this assumption could rapidly breakdown if the number of photon energy groups is much larger or a continuous photon energy spectrum is used. In order to accommodate these potential challenges, one possibility is to give each photon-emitting PN an energy spectrum, such that fewer PNs are necessary in order to reproduce the same decay photon activity and spectrum. Determining the best energy spectrum for each PN would be challenging as the decay photon energy spectrum of every photon-emitting radionuclide is different and changing depletion conditions will strongly impact the overall NNDs of various photon-emitting radionuclides. However, many photon-emitting radionuclides have similar spectra particularly when it comes to low-energy photons emitted as characteristic x-rays from internal conversion and electron capture which could make the approach viable.

7.5. Optimizing the Decay Constants of Pseudo-Nuclides

In this work the decay constants of PNs were generated by dividing the decay constants of radionuclides into ordered subsets equal to the number of PN decay constants needed and then taking the median of each subset and using those medians as the decay constants for the PNs. When considering decay heat, all radionuclides were used for this process while when considering decay photon activity only radionuclides which emitted decay photons were considered.

This process can likely be optimized. One potential optimization would be to still take the median of ordered subsets containing decay constants, but only consider the decay constants of radionuclides which have been removed from the system, rather than all radionuclides, some of which will not be removed from the system and thus should not impact the values of the PNs. The challenge in implementing this is that, for the heuristic method proposed in this work, this introduces another iterative loop. Currently, the heuristic method attempts to remove each nuclide in the system (except for those designated as target nuclides) and solves the Bateman equations for the modified system, recalculating the reference quantities and determining if the values are within the specified tolerances relative to the reference quantities calculated with the reference DTL. As nuclides are removed from

the system, PNs are added to the DTL as PNs become potential decay, transmutation, and fission products. If the decay constants of the PNs added to the system are dependent on the radionuclides which have been removed from the system, then after a nuclide has been successfully removed from the system the decay constants of the PNs will need to be adjusted, potentially requiring another calculation of the Bateman equations in order to ensure that the change in the decay constants of the PNs did not cause a quantity such as decay photon activity to result in a divergence from the reference solution which exceeds the given tolerance.

7.6. Irradiation-Dependent Pseudo-Nuclides

Pseudo-nuclides have previously seen extensive use in numerous reactor applications with pseudo fission products generated in an attempt to collectively represent the effect of FPs on reactivity [67]. As mentioned previously in this work, both the generation of FPs and the subsequent irradiation of said FPs impact quantities of interest, such as reactivity and decay heat. Consequently, one potential area of investigation is the development of irradiated pseudo fission products which are produced as pseudo fission products undergo neutron irradiation.

Consider a system where ^{235}U undergoes both neutron-induced fission from both fast and thermal neutrons, where PNs are used to model the buildup of FPs for the purposes of modeling the impact of FPs on reactivity as shown in Figure 7.1.

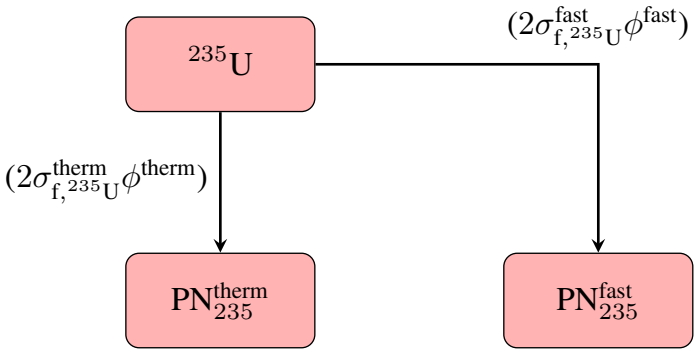

Figure 7.1: Hypothetical decay and transmutation diagram of ^{235}U undergoing fission to produce PNs.

$\text{PN}^{\text{therm}}_{235}$ and $\text{PN}^{\text{fast}}_{235}$ can capture the reactivity effect of the FPs produced by ^{235}U without explicitly modeling the hundreds of potential FP nuclides. However, the addition of PNs produced from the irradiation of $\text{PN}^{\text{therm}}_{235}$ and $\text{PN}^{\text{fast}}_{235}$ could better capture the reactivity effect of irradiated FPs as shown in Figure 7.2.

The main advantage of producing an irradiated PN from the FP PNs is the ability to better capture the potentially significant production of certain irradiated FPs. As an example, in thermal reactors there will be a significant production of ^{136}Xe and ^{150}Sm from the ^{135}Xe(n,γ)^{136}Xe and ^{149}Sm(n,γ)^{150}Sm reactions. The resulting buildup of ^{136}Xe and ^{150}Sm could have a reactivity impact which is better modeled with a separate PN compared to the normal lumped FP PNs. For fast reactors this is expected to be more relevant as the disparity between XS values for fast reactors is significantly less than the disparity present in thermal reactors.

The challenges of using an irradiated PN, such as $\text{PN}^{\text{irr}}_{235}$, would be determining the production XS of $\text{PN}^{\text{irr}}_{235}$, which is represented by $\sigma_{\text{a,PN}^{\text{therm}}_{235}}$ and $\sigma_{\text{a,PN}^{\text{fast}}_{235}}$ in Figure 7.2. There are multiple approaches that could be made when determining this XS, namely attempting to account for the energy-dependence of the XS or assuming the XS is energy-independent and constant regardless of incident neutron energy. This XS may need to then be calculated for every single PN FP, of which there could be a dozen or more.

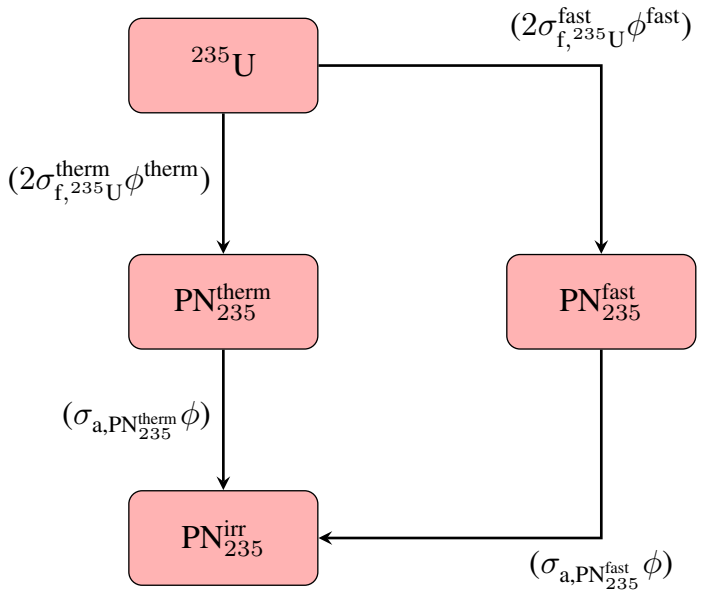

Figure 7.2: Hypothetical decay and transmutation diagram of ^{235}U undergoing fission to produce PNs which can then produce a PN via irradiation.

Rather than attempt to calculate an optimal XS for the production of $\text{PN}^{\text{irr}}_{235}$, it may instead be preferred to allow the simplification method to attempt to optimize the XS values of the PNs, however this would be expected to result in an increased computational cost because of the significant increase in the number of iterations needed by the method.

7.7. Solving Depletion Matrices for Coupled Regions

There is significant research interest in MSRs with liquid-fuel designs. One of the benefits of the liquid-fuel MSR design is the ability to alter the NNDs of the fuel salt via online extraction from and addition to the fuel salt stream.

These extraction and addition processes can pose challenges depending on the system considered. Consider a simplified two-region system where region C corresponds to the active core region and region O corresponds to an out-of-core region where only radioactive decay occurs. The Bateman equations for each region in Griffin can be written as shown in Eq. 7.2, adapted from Eq. 1.7, assuming no coupling between the two regions.

$$\begin{aligned}\frac{dN_{\text{C},i}}{dt} &= \sum_{j\neq i} b_{j\rightarrow i}\lambda_j N_{\text{C},j}(t) + \sum_{g=1}^{G}\sum_{j\neq i}\sigma_{g,j\rightarrow i}\phi_g(t)N_j(t) + \sum_{g=1}^{G}\sum_{j\neq i}\sigma_{\text{f},g,j}\gamma_{\text{f},g,j\rightarrow i}\phi_g(t)N_{\text{C},j}(t) \\ &\quad + \sum_{j\neq i}\lambda_{\text{sf},j}N_{\text{C},j}(t)\gamma_{\text{sf},j\rightarrow i} - \lambda_i N_{\text{C},i}(t) - \sum_{g=1}^{G}\sigma_{\text{a},g,i}\phi_g(t)N_i(t) \\ \frac{dN_{\text{O},i}}{dt} &= \sum_{j\neq i} b_{j\rightarrow i}\lambda_j N_{\text{O},j}(t) + \sum_{j\neq i}\lambda_{\text{sf},j}N_{\text{O},j}(t)\gamma_{\text{sf},j\rightarrow i} - \lambda_i N_{\text{O},i}(t)\end{aligned} \tag{7.2}$$

Without coupling, the two regions can each be solved via matrix exponential methods with the order of each matrix dependent on the number of nuclides in each matrix, which is $n \times n$ where n is the number of nuclides

in the region. However, if coupling is considered Eq. 7.2 becomes Eq. 7.3 (adapted from Ref. [91]), where it is assumed that a given nuclide i is removed from region C at a constant rate L_i and added to region O at the same rate.

$$\begin{aligned}
\frac{dN_{\mathrm{C},i}(t)}{dt} &= \sum_{j\neq i} b_{j\to i}\lambda_j N_{\mathrm{C},j}(t) + \sum_{g=1}^{G}\sum_{j\neq i}\sigma_{g,j\to i}\phi_g(t)N_j(t) + \sum_{g=1}^{G}\sum_{j\neq i}\sigma_{\mathrm{f},g,j}\gamma_{\mathrm{f},g,j\to i}\phi_g(t)N_{\mathrm{C},j}(t) \\
&\quad + \sum_{j\neq i}\lambda_{\mathrm{sf},j}N_{\mathrm{C},j}(\vec{r},t)\gamma_{\mathrm{sf},j\to i} - \lambda_i N_{\mathrm{C},i}(t) - \sum_{g=1}^{G}\sigma_{\mathrm{a},g,i}\phi_g(t)N_i(t) - L_i N_{\mathrm{C},i}(t) \\
\frac{dN_{\mathrm{O},i}(t)}{dt} &= \sum_{j\neq i} b_{j\to i}\lambda_j N_{\mathrm{O},j}(t) + \sum_{j\neq i}\lambda_{\mathrm{sf},j}N_{\mathrm{O},j}(t)\gamma_{\mathrm{sf},j\to i} - \lambda_i N_{\mathrm{O},i}(t) + L_i N_{\mathrm{C},i}(t)
\end{aligned} \tag{7.3}$$

While the change in Eq. 7.3 is subtle, the implications are significant as while the NNDs of region C are still independent from those of region O, the same is not true of region O, which now has a dependency on the NNDs in both region O and region C. Because the NNDs of region C are time-dependent, the most accurate method of solving for the NNDs in region O is to solve for the NNDs of both regions simultaneously. This can be accomplished via the formation of a coupled depletion matrix.

$$\begin{aligned}
\mathbf{L} &= \begin{bmatrix} L_1 & 0 & 0 & \cdots & 0 \\ 0 & L_2 & 0 & \cdots & 0 \\ 0 & 0 & L_3 & \cdots & 0 \\ \vdots & \vdots & \vdots & \ddots & 0 \\ 0 & 0 & 0 & 0 & L_n \end{bmatrix} \\
\mathbf{X} &= \begin{bmatrix} \mathbf{A}_{\mathrm{O}} & \mathbf{L} \\ \mathbf{0} & \mathbf{A}_{\mathrm{C}} - \mathbf{L} \end{bmatrix}
\end{aligned} \tag{7.4}$$

where

$\mathbf{A}_{\mathrm{O}}$	depletion matrix of region O without coupling terms
$\mathbf{A}_{\mathrm{C}}$	depletion matrix of region C without coupling terms
$\mathbf{L}$	matrix of the nuclide rates of transfer from region C to region O
$\mathbf{X}$	coupled depletion matrix.

Once matrix $\mathbf{X}$ is known, the Bateman equations can be solved using the matrix exponential as described in Section 1.3.2.

$$\begin{aligned} \vec{N}_{\mathrm{O+C}}(t) &= \begin{bmatrix} \vec{N}_{\mathrm{O}}(t) \\ \vec{N}_{\mathrm{C}}(t) \end{bmatrix} \\ \frac{d\vec{N}_{\mathrm{O+C}}(t)}{dt} &= \mathbf{X}\vec{N}_{\mathrm{O+C}}(t) \\ \vec{N}_{\mathrm{O+C}}(t) &= \vec{N}_0 e^{\mathbf{X}t} \end{aligned} \tag{7.5}$$

While it is possible to solve Eq. 7.5 using existing depletion solvers such as CRAM, the order of the coupled depletion matrix becomes $(n_{\mathrm{O}} + n_{\mathrm{C}}) \times (n_{\mathrm{O}} + n_{\mathrm{C}})$, where n is the number of nuclides tracked in a given region. The increased size of the depletion matrix will increase the cost of the depletion solvers, such as CRAM.

Strictly speaking, there is no limit to the number of coupled regions that may be present in a given reactor system. While a two-region coupled system is considered here, it is entirely possible for the number of coupled regions to be quite large, resulting in a comparable increase in the size of the coupled region matrix. The use of PNs to reduce the overall number of nuclides tracked in each region could become quite valuable as the size reduction in absolute terms could be quite large. As an example, a 6-region coupled system tracking 1700 nuclides in each region would result in a coupled depletion matrix of order 10200×10200. If PNs can reduce the system to 300 nuclides tracked in each region the subsequent coupled depletion matrix would only be of order 1800×1800, which is much more reasonable. Aside from the computational cost advantages of PNs, reducing the size of the depletion matrices and the number of nuclides tracked can be beneficial for analysts and developers as debugging and manual analysis of results becomes much more feasible.

However, there are challenges to using PNs in coupled region systems. If PNs are used to replace nuclides which are being removed from the one region and added to another, a single PN may not be able to model multiple nuclides if those nuclides each have different transfer rates from one region to another. This could potentially be resolved by using an averaged transfer rate, which would be similar to the process of calculating the decay constants of the PNs for modeling decay-related effects.

7.8. Multiple Simplified Depletion Libraries for a Single Reactor System

In this work, a single simplified depletion library was considered sufficient for the purposes of modeling an entire reactor system with the flux conditions used during the simplification process taken as the maximum flux level which occurred anywhere in the reactor system for each energy group. While a single simplified depletion library was considered sufficient for that system, other reactor systems may have significantly different depletion conditions because of the flux energy spectrum in a given region, different initial NNDs in different regions, and different temperatures which cause the microscopic XSs of nuclides to vary because of Doppler broadening [23].

In the event that there are significant differences between the depletion conditions experienced in different spatial regions of the reactor, this could result in a significant increase in the number of nuclides tracked in a single simplified depletion library because different nuclides have a larger relative impact on reactor parameters, such as the macroscopic XSs, in different regions, which must be tracked. This increase in the size of the simplified depletion library would subsequently result in an increase in the computational resources needed for the depletion calculation as shown in Eqs. 1.12 and 1.13. The use of multiple simplified depletion libraries which are restricted to different spatial regions of the reactor could reduce these computational costs, however, these computational costs would likely be relatively modest as based on the research presented in this work, typically 300 nuclides are considered sufficient for modeling purposes. If the reactor experiences very different depletion conditions

spatially, then it is possible that a single simplified depletion library would require 400 nuclides instead of 300. By using two different simplified depletion libraries in different spatial regions which both have 300 nuclides, this would be expected to reduce the overall computational cost of the depletion calculation by 25%. While a sizable reduction, it is possible the benefit does not outweigh the increased burden for analysts in generating multiple simplified depletion libraries and ensuring that the use of said libraries are restricted to the appropriate spatial regions.

7.9. Scaling Studies Between Spatial Refinement and Nuclide Simplification

As shown in Figures 5.4 and 5.5, the spatial refinement of a given reactor system can have a larger impact on the reactivity of the system than using a simplified depletion library. However, it would be expected that there comes a point in any reactor system where increasing the spatial refinement of the computational model impacts reactivity and other reactor parameters less than the use of a simplified depletion library. Because of the significant differences between various reactor designs in terms of flux energy spectrum, initial fuel NNDs, fuel cycle lengths, operating temperatures, and other key design features, the level of spatial refinement needed such that the use of simplified depletion library has a comparable impact on reactivity compared to further increasing the spatial refinement likely varies significantly between a PWR and an SFR, as an example. As a result, scaling studies could be performed for a variety of reactor designs where the simplification tolerances and spatial refinements of the reactor models are varied and the impacts of reactivity on both systems can be determined. These scaling studies could then be used by analysts, who should already have an idea of the level of spatial refinement required by their model, to inform whether or not the use of a simplified depletion library is acceptable if said depletion library will introduce a relatively small change in reactor parameters, while reducing computational costs such that a higher level of spatial refinement can be used which could result in a net improvement to the results of the model. Alternatively, an analyst may currently be using a simplified depletion library on a model which is very refined spatially, when the scaling studies may reveal that it would be more accurate to slightly coarsen the model in order to use a more comprehensive depletion library, which will have a larger impact on reactor parameters.

Such scaling studies would be very beneficial for the reactor analysis community; however, the challenge of these scaling studies is both the time required by analysts to develop multiple reactor models with varying levels of spatial refinement for testing purposes as well as the computational resources required to run said models. The VERA benchmark has two million depletion regions [33] which in Griffin would be expected to require roughly 10 core-hours to perform a single depletion calculation if 1600 nuclides are tracked using CRAM, with fifty or more depletion calculations likely necessary for modeling an entire fuel cycle, which would correspond to 500 core-hours. The RAM usage would also correspond to 25.6 GB for the duration of the benchmark. If, hypothetically, five different levels of spatial refinement and five different depletion simplification tolerances are used, this would result in 25 permutations of the VERA benchmark to test which, if all permutations average to have the same resource usage as the original benchmark, would result in a total core walltime of almost one and a half years. If potentially a dozen or more reactor benchmarks are to be considered with a similar number of permutations, this could result in total core walltime of decades. Even if thousands of cores are available, the overall simulation cost could take months, not to mention the time required to analyze the results after the simulations have finished. Once again, the limits of currently available computational resources may prohibit such scaling studies at this time, but as available computational resources increase [13] these studies become increasingly more viable as well as more relevant to the reactor analysis community as an increase in computational resources available inevitably leads to increases in the complexity of reactor models and simulations.

Appendix A: Equation Derivations

A.1. Neutron Transport Equation Simplification

A step-by-step simplification of the NTE presented in Eq. 1.4 (and repeated as Eq. A.1) to the infinite medium multiplication factor in Eq. 1.5 is presented in this section.

$$\begin{aligned}\frac{1}{v(E)}\frac{\partial\psi(\vec{r},E,\vec{\Omega},t)}{\partial t} = &-\vec{\Omega}\cdot\vec{\nabla}\psi(\vec{r},E,\vec{\Omega},t) - \sum_i N_i(\vec{r},t)\sigma_{\mathrm{t},i}(E)\psi(\vec{r},E,\vec{\Omega},t)\\ &+ \sum_i N_i(\vec{r},t)\int_0^\infty dE'\int_{4\pi} d\vec{\Omega}'\sigma_{\mathrm{s},i}(E'\to E,\vec{\Omega}'\to\vec{\Omega})\psi(\vec{r},E',\vec{\Omega}',t)\\ &+ \frac{1}{4\pi}\sum_i N_i(\vec{r},t)\int_0^\infty dE'\nu_{\mathrm{p},i}(E')\sigma_{\mathrm{f},i}(E')\chi_{\mathrm{p},i}(E'\to E)\phi(\vec{r},E',t)\\ &+ \frac{1}{4\pi}\sum_i \nu_{\mathrm{d},i}\lambda_{\mathrm{d},i}N_i(\vec{r},t)\chi_{\mathrm{d},i}(E)\\ &+ S_{\text{ext}}(\vec{r},E,\vec{\Omega},t)\end{aligned} \tag{A.1}$$

where

$\vec{r}$	spatial position vector
E	kinetic energy of the neutron
t	time
$\vec{\Omega}$	neutron direction
v	neutron velocity
ψ	angular neutron flux
ϕ	scalar neutron flux
N_i	position-dependent and time-dependent NND of nuclide i
$\sigma_{\mathrm{t},i}$	microscopic total XS of nuclide i
$\sigma_{\mathrm{s},i}$	microscopic scattering XS of nuclide i
$\nu_{\mathrm{p},i}$	average number of prompt neutrons produced from the neutron-induced fission of nuclide i
$\sigma_{\mathrm{f},i}$	microscopic fission XS of nuclide i
$\chi_{\mathrm{p},i}$	prompt neutron energy spectrum from the neutron-induced fission of nuclide i
$\nu_{\mathrm{d},i}$	average number of neutrons emitted per delayed neutron emission of nuclide i
$\lambda_{\mathrm{d},i}$	decay constant of delayed neutron emission of nuclide i
$\chi_{\mathrm{d},i}$	delayed neutron energy spectrum from the delayed neutron emission of nuclide i
S_{ext}	external neutron source term.

The first assumptions applied are those that allow terms to be zeroed out and removed from Eq. A.1 entirely. It is assumed that: there is no external source term ($S_{\text{ext}} = 0$), the system is infinite meaning there is no boundary

condition to apply to consider neutrons streaming into or out of the system ($\vec{\Omega} \cdot \vec{\nabla}\psi = 0$), and no delayed neutrons are produced ($\nu_{\mathrm{d}} = 0$). Applying these assumptions to Eq. A.1 yields Eq. A.2.

$$\begin{aligned}\frac{1}{v(E)}\frac{\partial\psi(\vec{r},E,\vec{\Omega},t)}{\partial t} = &-\sum_i N_i(\vec{r},t)\sigma_{\mathrm{t},i}(E)\psi(\vec{r},E,\vec{\Omega},t) \\ &+\sum_i N_i(\vec{r},t)\int_0^\infty dE'\int_{4\pi} d\vec{\Omega}'\sigma_{\mathrm{s},i}(E'\to E,\vec{\Omega}'\to\vec{\Omega})\psi(\vec{r},E',\vec{\Omega}',t) \\ &+\frac{1}{4\pi}\sum_i N_i(\vec{r},t)\int_0^\infty dE'\nu_{\mathrm{p},i}(E')\sigma_{\mathrm{f},i}(E')\chi_{\mathrm{p},i}(E'\to E)\phi(\vec{r},E',t)\end{aligned} \tag{A.2}$$

The next set of assumptions deals with applying the removal of dependencies from individual terms. It is assumed that all neutrons which exist and are produced in the system are monoenergetic which removes the energy dependencies of E and E'. A consequence of this assumption is the removal of the scattering term as assuming all neutrons maintain a constant single energy means that scattering is impossible ($\sigma_{\mathrm{s}} = 0$). It is also assumed and the system is homogeneous which removes directional dependence ($\vec{r}$). Lastly, it is assumed that specifically the NNDs of the system will remain constant with time, removing the time-dependence t from N. Applying these assumptions to Eq. A.2 yields Eq. A.3.

$$\frac{1}{v}\frac{\partial\psi(\vec{\Omega},t)}{\partial t} = -\sum_i N_i\sigma_{\mathrm{t},i}\psi(\vec{\Omega},t) + \frac{1}{4\pi}\sum_i N_i\nu_{\mathrm{p},i}\sigma_{\mathrm{f},i}\phi(t) \tag{A.3}$$

Next, the macroscopic XS term Σ is used and $\nu_{\mathrm{p},i}$ is replaced with simply ν, which represents the average number of neutrons released per fission event in the material.

$$\begin{aligned}\Sigma &= \sum_i N_i\sigma_i \\ \nu &= \frac{\sum_i N_i\nu_{\mathrm{p},i}}{\sum_i N_i} \\ \frac{1}{v}\frac{\partial\psi(\vec{\Omega},t)}{\partial t} &= -\Sigma_{\mathrm{t}}\psi(\vec{\Omega},t) + \frac{1}{4\pi}\nu\Sigma_{\mathrm{f}}\phi(t)\end{aligned} \tag{A.4}$$

The next assumption is isotropic production of neutrons, meaning all neutrons have the same probability of being produced in any given direction which allows the relationship between the angular flux ψ and the scalar flux ϕ to be expressed as $\psi = \frac{\phi}{4\pi}$. ϕ is used in Eq. A.5 as it is the scalar neutron flux which determines the neutron-nuclei reaction rates of interest.

$$\frac{1}{v}\frac{\partial\phi(t)}{\partial t} = -\Sigma_{\mathrm{t}}\phi(t) + \nu\Sigma_{\mathrm{f}}\phi(t) \tag{A.5}$$

Since the scattering XS is assumed to be zero, the total XS is equal to the absorption XS, meaning $\Sigma_{\mathrm{t}} = \Sigma_{\mathrm{a}}$.

$$\frac{1}{v}\frac{\partial\phi(t)}{\partial t} = -\Sigma_{\mathrm{a}}\phi(t) + \nu\Sigma_{\mathrm{f}}\phi(t) \tag{A.6}$$

For clarity, v and ϕ are rearranged in the equation. Additionally, the time-dependence of ϕ is omitted for simplicity and $\frac{\partial\phi}{\partial t}$ is replaced with $\Delta\phi$ and Δt to represent the change in the scalar neutron flux over a given period of time.

$$\frac{\Delta\phi}{\Delta t} = v\phi(\nu\Sigma_{\mathrm{f}} - \Sigma_{\mathrm{a}}) \tag{A.7}$$

Now the neutron multiplication factor k is introduced, which represents the change in the neutron population from one distinct neutron generation to the next.

$$\begin{aligned} k &= \frac{\Delta\phi + \phi}{\phi} \\ k &= v\Delta t(\nu\Sigma_{\mathrm{f}} - \Sigma_{\mathrm{a}}) + 1 \end{aligned} \tag{A.8}$$

Recall that velocity is length over time and the macroscopic XS has units of inverse length. Consequently, the velocity term can be refactored in terms of Σ_{a} and Δt.

$$\begin{aligned} v &= \frac{\frac{1}{\Sigma_{\mathrm{a}}}}{\Delta t} = \frac{1}{\Delta t\Sigma_{\mathrm{a}}} \\ k &= \frac{1}{\Delta t\Sigma_{\mathrm{a}}}\Delta t(\nu\Sigma_{\mathrm{f}} - \Sigma_{\mathrm{a}}) + 1 \\ k &= \frac{1}{\Sigma_{\mathrm{a}}}(\nu\Sigma_{\mathrm{f}} - \Sigma_{\mathrm{a}}) + 1 = \frac{\nu\Sigma_{\mathrm{f}}}{\Sigma_{\mathrm{a}}} - \frac{\Sigma_{\mathrm{a}}}{\Sigma_{\mathrm{a}}} + 1 \\ k &= \frac{\nu\Sigma_{\mathrm{f}}}{\Sigma_{\mathrm{a}}} \end{aligned} \tag{A.9}$$

Δt now serves as the neutron generation time, which is the time it takes for the neutron population to vary by a factor of k. Consequently, both the neutron velocity and Σ_{a} determine the generation time. Σ_{a} is the probability that the neutron is absorbed by the material after traveling some distance in the material and the velocity determines how quickly the neutron travels through the material.

Appendix B: Depletion in Griffin

B.1. Particle Names

Griffin uses several particle names and symbols which are mostly common throughout the nuclear industry and are also used in this work. These names and symbols are shown in Table B.1.

Name	Symbol	Nuclide
Alpha	α	^{4}He
Helion	—	^{3}He
Neutron	n	^{1}n
Proton	p	^{1}H
Deuteron	d	^{2}H
Triton	t	^{3}H

Table B.1: Particle names, symbols, and nuclide identifiers used in Griffin and this work.

B.2. Decay Modes

Not all modes of the potential radioactive decay modes nuclides can undergo are supported by Griffin, however, the most important decay modes encountered in traditional reactor analysis are supported, with a "generic" decay mode allowing some level of support for unspecified decay modes. The various decay modes supported in Griffin are shown in Table B.2 and are sufficient to support all decay modes currently provide by the ENDF/B-VIII.0 decay data [5].

An important note to consider is that decay modes delayed by another decay mode involve an intermediate (but short-lived) nuclide while non-delayed decay modes (such as double beta minus decay) involve the spontaneous release of one or more particles. Various examples of the decay modes listed in Table B.2 are shown below.

Alpha decay:

$$^{238}\mathrm{U} \rightarrow {}^{234}\mathrm{Th} + {}^{4}\alpha \tag{B.1}$$

Beta minus decay:

$$^{135}\mathrm{Xe} \rightarrow {}^{135}\mathrm{Cs} + {}^{0}\beta^{-} + {}^{0}\overline{\nu} \tag{B.2}$$

Beta plus decay, also known as positron emission:

$$\begin{aligned} {}^{18}\mathrm{F} &\rightarrow {}^{18}\mathrm{O} + {}^{0}\beta^{+} + {}^{0}\nu \\ {}^{0}\beta^{+} + {}^{0}e &\rightarrow 2\,{}^{0}\gamma \end{aligned} \tag{B.3}$$

Beta minus-delayed neutron emission:

$$\begin{aligned} {}^{87}\mathrm{Br} &\rightarrow {}^{87}\mathrm{Kr}^{*} + {}^{0}\beta^{-} + {}^{0}\overline{\nu} \\ {}^{87}\mathrm{Kr}^{*} &\rightarrow {}^{86}\mathrm{Kr} + {}^{1}\mathrm{n} \end{aligned} \tag{B.4}$$

Name	Symbol	Griffin Name
alpha decay	α	Alpha
beta minus decay	β^-	BetaMinus
beta minus-delayed alpha emission	$\beta^-\alpha$	BetaMinusAlpha
beta minus-delayed neutron emission	β^-n	BetaMinusNeutron
beta minus-delayed double neutron emission	β^-2n	BetaMinus2Neutron
beta minus-delayed triple neutron emission	β^-3n	BetaMinus3Neutron
beta minus-delayed quadruple neutron emission	β^-4n	BetaMinus4Neutron
electron capture	ε or EC	BetaPlus
beta plus decay or positron emission	β^+	BetaPlus
beta plus-delayed alpha emission	$\beta^+\alpha$	BetaPlusAlpha
electron capture-delayed alpha emission	$\varepsilon\alpha$	BetaPlusAlpha
beta plus-delayed proton emission	β^+p	BetaPlusProton
electron capture-delayed proton emission	εp	BetaPlusProton
beta plus-delayed double proton emission	β^+2p	BetaPlus2Proton
electron capture-delayed double proton emission	ε2p	BetaPlus2Proton
double beta minus decay	$2\beta^-$	DoubleBetaMinus
double neutron emission	2n	DoubleNeutron
double proton emission	2p	DoubleProton
isomeric transition	IT	IsomericTransition
neutron emission	n	Neutron
proton emission	p	Proton
spontaneous fission	SF	SpontaneousFission
—	GD	GenericDecay

Table B.2: Decay modes supported by Griffin. Note that there is no distinction in Griffin between electron capture and positron emission, which is a convention also followed by the ENDF-6 data format [3].

Beta minus-delayed double neutron emission:

$$\begin{aligned} {}^{11}\text{Li} &\rightarrow {}^{11}\text{Be}^* + {}^0\beta^- + {}^0\overline{\nu} \\ {}^{11}\text{Be}^* &\rightarrow {}^{9}\text{Be} + 2\,{}^1\text{n} \end{aligned} \tag{B.5}$$

Beta minus-delayed triple neutron emission:

$$\begin{aligned} {}^{11}\text{Li} &\rightarrow {}^{11}\text{Be}^* + {}^0\beta^- + {}^0\overline{\nu} \\ {}^{11}\text{Be}^* &\rightarrow {}^{8}\text{Be} + 3\,{}^1\text{n} \end{aligned} \tag{B.6}$$

Beta minus-delayed quadruple neutron emission:

$$\begin{aligned} {}^{17}\text{B} &\rightarrow {}^{17}\text{C}^* + {}^0\beta^- + {}^0\overline{\nu} \\ {}^{17}\text{C}^* &\rightarrow {}^{13}\text{C} + 4\,{}^1\text{n} \end{aligned} \tag{B.7}$$

Beta minus-delayed alpha emission:

$$\begin{aligned} {}^{11}\mathrm{Li} &\rightarrow {}^{11}\mathrm{Be}^{*} + {}^{0}\beta^{-} + {}^{0}\overline{\nu} \\ {}^{11}\mathrm{Be}^{*} &\rightarrow {}^{7}\mathrm{He} + {}^{4}\alpha \end{aligned} \tag{B.8}$$

Beta plus-delayed proton emission:

$$\begin{aligned} {}^{47}\mathrm{Fe} &\rightarrow {}^{47}\mathrm{Mn}^{*} + {}^{0}\beta^{+} + {}^{0}\nu \\ {}^{47}\mathrm{Mn}^{*} &\rightarrow {}^{46}\mathrm{Cr} + {}^{1}\mathrm{p} \end{aligned} \tag{B.9}$$

Beta plus-delayed double proton emission:

$$\begin{aligned} {}^{22}\mathrm{Al} &\rightarrow {}^{22}\mathrm{Mg}^{*} + {}^{0}\beta^{+} + {}^{0}\nu \\ {}^{22}\mathrm{Mg}^{*} &\rightarrow {}^{20}\mathrm{Ne} + 2\,{}^{1}\mathrm{p} \end{aligned} \tag{B.10}$$

Beta plus-delayed alpha emission:

$$\begin{aligned} {}^{113}\mathrm{Xe} &\rightarrow {}^{113}\mathrm{I}^{*} + {}^{0}\beta^{+} + {}^{0}\nu \\ {}^{113}\mathrm{I}^{*} &\rightarrow {}^{109}\mathrm{Sb} + {}^{4}\alpha \end{aligned} \tag{B.11}$$

Double beta minus decay:

$${}^{48}\mathrm{Ca} \rightarrow {}^{48}\mathrm{Ti} + 2\,{}^{0}\beta^{-} + 2\,{}^{0}\overline{\nu} \tag{B.12}$$

Double neutron emission:

$${}^{5}\mathrm{H} \rightarrow {}^{3}\mathrm{H} + 2\,{}^{1}\mathrm{n} \tag{B.13}$$

Double proton emission:

$${}^{45}\mathrm{Fe} \rightarrow {}^{43}\mathrm{Cr} + 2\,{}^{1}\mathrm{p} \tag{B.14}$$

Electron capture:

$${}^{18}\mathrm{F} + {}^{0}\mathrm{e}^{-} \rightarrow {}^{18}\mathrm{O} + {}^{0}\nu \tag{B.15}$$

Isomeric transition:

$${}^{24\mathrm{m}}\mathrm{Na} \rightarrow {}^{24}\mathrm{Na} + {}^{0}\gamma \tag{B.16}$$

Neutron emission:

$${}^{5}\mathrm{He} \rightarrow {}^{4}\mathrm{He} + {}^{1}\mathrm{n} \tag{B.17}$$

Proton emission:

$$^{151}\mathrm{Lu} \rightarrow {}^{150}\mathrm{Yb} + {}^{1}\mathrm{p} \tag{B.18}$$

Spontaneous fission:

$$^{235}\mathrm{U} \rightarrow {}^{97}\mathrm{Y} + {}^{135}\mathrm{I} + 3\,{}^{1}\mathrm{n} \tag{B.19}$$

Note that fission produces a FP spectrum, the above is only an example of one possible fission product pathway.

B.3. Transmutation Reactions

Griffin assumes that all transmutation occur as a result of neutron-nuclei interactions. While transmutation can also be caused by photons, protons, alphas, fusion, and other effects, neutron transmutation is by far the dominant process in fission reactors and thus is the only particle for which transmutation reactions are currently supported in Griffin. The neutron transmutation reactions supported by Griffin are listed in Table B.3. Note that Griffin does support other XS quantities, such as the total XS (σ_t) and scattering XS (σ_s), however, these XS quantities do not describe XSs quantities which are related to depletion, they are purely used in neutron transport calculations and thus are not mentioned in Table B.3.

Symbol	Griffin Name
(n,γ)	NGamma
(n,α)	NAlpha
(n,2α)	N2Alpha
(n,2n)	N2N
(n,3n)	N3N
(n,4n)	N4N
(n,p)	NProton
(n,n+p)	NNProton
(n,d)	NDeuteron
(n,t)	NTriton
(n,^{3}He)	NHelion
(n,f)	Fission

Table B.3: Neutron transmutation reactions supported by Griffin. Unlike decay modes, most transmutation reactions are referred to by their symbolic notation.

Various examples of the transmutation reactions listed in Table B.3 are shown below.
(n,2n):

$$^{238}\mathrm{U} + {}^{1}\mathrm{n} \rightarrow {}^{239}\mathrm{U}^{*} \rightarrow {}^{237}\mathrm{U} + 2\,{}^{1}\mathrm{n} \tag{B.20}$$

(n,3n):

$$^{238}\mathrm{U} + {}^{1}\mathrm{n} \rightarrow {}^{239}\mathrm{U}^{*} \rightarrow {}^{236}\mathrm{U} + 3\,{}^{1}\mathrm{n} \tag{B.21}$$

(n,4n):

$$^{238}\mathrm{U} + {}^{1}\mathrm{n} \rightarrow {}^{239}\mathrm{U}^{*} \rightarrow {}^{235}\mathrm{U} + 4\,{}^{1}\mathrm{n} \tag{B.22}$$

(n,p):

$$^{238}\mathrm{U} + {}^{1}\mathrm{n} \rightarrow {}^{239}\mathrm{U}^{*} \rightarrow {}^{238}\mathrm{Pa} + {}^{1}\mathrm{p} \tag{B.23}$$

(n,n+p):

$$^{238}\mathrm{U} + {}^{1}\mathrm{n} \rightarrow {}^{239}\mathrm{U}^{*} \rightarrow {}^{237}\mathrm{Pa} + {}^{1}\mathrm{p} + {}^{1}\mathrm{n} \tag{B.24}$$

(n,d):

$$^{238}\mathrm{U} + {}^{1}\mathrm{n} \rightarrow {}^{239}\mathrm{U}^{*} \rightarrow {}^{237}\mathrm{Pa} + {}^{2}\mathrm{d} \tag{B.25}$$

(n,t):

$$^{238}\mathrm{U} + {}^{1}\mathrm{n} \rightarrow {}^{239}\mathrm{U}^{*} \rightarrow {}^{236}\mathrm{Pa} + {}^{3}\mathrm{t} \tag{B.26}$$

(n,^{3}He):

$$^{238}\mathrm{U} + {}^{1}\mathrm{n} \rightarrow {}^{239}\mathrm{U}^{*} \rightarrow {}^{236}\mathrm{Th} + {}^{3}\mathrm{He} \tag{B.27}$$

(n,α):

$$^{238}\mathrm{U} + {}^{1}\mathrm{n} \rightarrow {}^{239}\mathrm{U}^{*} \rightarrow {}^{235}\mathrm{Th} + {}^{4}\alpha \tag{B.28}$$

(n,2α):

$$^{238}\mathrm{U} + {}^{1}\mathrm{n} \rightarrow {}^{239}\mathrm{U}^{*} \rightarrow {}^{231}\mathrm{Ra} + 2\,{}^{4}\alpha \tag{B.29}$$

(n,γ) or radiative capture:

$$\begin{aligned} ^{241}\mathrm{Am} + {}^{1}\mathrm{n} &\rightarrow {}^{242}\mathrm{Am}^{*} \\ ^{242}\mathrm{Am}^{*} &\rightarrow {}^{242}\mathrm{Am} + {}^{0}\gamma \end{aligned} \tag{B.30}$$

(n,f) or neutron-induced fission:

$$^{235}\mathrm{U} + {}^{1}\mathrm{n} \rightarrow {}^{236}\mathrm{U}^{*} \rightarrow {}^{135}\mathrm{I} + {}^{98}\mathrm{Y} + 3\,{}^{1}\mathrm{n} \tag{B.31}$$

Note that fission produces a FP spectrum, the above is only an example of one possible fission product pathway.

Appendix C: Acronyms and Abbreviations

ADM Adding and Doubling Method

ANARD average nuclide absolute relative difference

ANL Argonne National Laboratory

BE binding energy

BOL beginning-of-life

BORAX Boiling Water Reactor Experiment

BWR boiling water reactor

CD cumulative difference

CNFD Crank-Nicolson Finite Difference

CPU central processing unit

CRAM Chebyshev rational approximation method

CSEWG Cross Sections Evaluation Working Group

DHP decay heat precursor

DMI direct matrix inversion

DPA displacements per atom

DTL DecayTransmutationLibrary

EBR-I Experimental Breeder Reactor-I

ENDF Evaluated Nuclear Data File

FE forward Euler

FIMA fissions per initial heavy metal atom

FP fission product

FPIE fission product irradiation effect

FPYF fission product yield fraction

HCP heavy charged particle

IAEA International Atomic Energy Agency

ID interval difference

INL Idaho National Laboratory

IPF incomplete partial fraction

KERMA kinetic energy released per unit mass

LMFR liquid metal fast reactor

LWR light water reactor

MGL MultigroupLibrary

MNARD maximum nuclide absolute relative difference

MSR molten salt reactor

NND nuclide number density

NNND negative nuclide number density

NPP nuclear power plant

NTE neutron transport equation

OECD Organization of Economic Co-operation and Development

OP overprediction

ORIGEN Oak Ridge Isotope Generation

ORNL Oak Ridge National Laboratory

pcm per cent mille

PFD partial fraction decomposition

PHWR pressurized heavy water reactor

PKA primary knock-on atom

PN pseudo-nuclide

PWR pressurized water reactor

RAM random-access memory

RD relative difference

RMS root mean square

SCWR supercritical water reactor

SF spontaneous fission

SFR sodium fast reactor

SGE sparse Gaussian elimination

UP underprediction

XS cross section

Appendix D: Glossary

A-number The total number of nucleons (protons and neutrons) a nuclide has. Equal to the sum of the Z-number and the N-number ($A = Z + N$).

cross section In nuclear engineering, the cross section of a nuclide refers to the probability of a given reaction occurring between an incident particle and the nucleus of the nuclide. Typically only neutron cross sections are considered, but photon cross sections are sometimes considered as well. Cross sections are dependent on the incident particle energy relative to the nucleus, which results in a dependence on both the kinetic energy of the incident particle and on the temperature of nuclei via Doppler broadening [23]. The microscopic neutron cross section refers to the probability of a neutron interacting with a single nucleus of a given nuclide and has units of area, typically barns or cm^2 and is represented by the symbol σ. The macroscopic cross section refers to probability of neutron interaction within the bulk material and has units of inverse length, typically $\frac{1}{\text{cm}}$ and is represented by the symbol Σ. The macroscopic cross section of a given reaction x can be calculated as shown for a system with I nuclides.

$$\Sigma_{\text{x}} = \sum_{i}^{I} N_i \sigma_{\text{x},i} \tag{D.1}$$

Because of the large number of both neutrons and nuclei in a given reactor system, good statistical convergence is achieved via the law of large numbers [20] which is why neutron cross sections, which are units of probability, can be expressed as a unit of area.

decay energy The amount of energy released in the form of kinetic energy of various particles (e.g. α, γ, the recoil nucleus) as the result of radioactive decay of a given radionuclide. With the exception of the energy released in the form of antineutrinos and neutrinos, all decay energy is recoverable in a reactor. Decay energy carried by photons and neutrons may be deposited non-locally in a given reactor system or may leak out of the system entirely because of the range of said particles. Other particles may deposit their kinetic energy non-locally, but it is often assumed that these particles deposit their energy at or near where they were produced for modeling purposes. The average decay energy released per decay of a given radionuclide is well-known for most radionuclides although it is important to consider that some radionuclides can have multiple decay modes with each mode releasing significantly different quantities of energy. The highest energy decay event is spontaneous fission, which releases roughly 200 MeV, while the lowest energy decay event tends to be a low energy isomeric transition, which may release as little as 100 eV.

decay heat The release of energy (heat) from radioactive decay. Decay heat is based off of both the half-life of the nuclide decaying as well as the decay energy of the radionuclide. Nuclides with high decay energies and short half-lives release a larger amount of thermal power on a per atom basis than nuclides with low decay energies and long half-lives. Because of the numerous short-lived, radionuclides produced by nuclear fission, a significant portion of the heat released from a reactor at steady-state comes from radioactive decay, on the order of 5% of the total heat produced. Consequently, when nuclear reactors are shutdown via control rod insertion or other methods the rate of nuclear fission rapidly drops to zero as the inserted neutron poisons rapidly reduce the neutron multiplication factor of thge reactor. While this reduces the thermal power produced by fission and other transmutation reactions to zero, it is impossible to halt the

radioactive decay of the FPs in the nuclear fuel. Thus a reactor that was producing 3 GW of heat may still produce roughly 60 MW of heat immediately after shutdown. This residual decay heat is a major safety concern and significant effort is spent designing reactors to be able to handle this decay heat in accident scenarios.

Doppler broadening Doppler broadening is the phenomenon by which the microscopic XSs of a given nuclide change as the temperature of the nuclide increases. Since the nuclei in a given material are moving in the material with a given speed based on their temperature, this vibration can alter the relative energy of an incident neutron when it collides with a nucleus [23]. If the nucleus is moving away from the neutron the effective incident energy of the neutron will be slightly lower than the actual kinetic energy of the neutron. If the nucleus is moving towards the neutron, the effective incident energy of the neutron will be slightly higher than the actual kinetic energy of the neutron. While this effect can be considered negligible for continuous regions, this has a significant impact on the resonance region since resonances are sharp peaks that occur for specific neutron energies. As the temperature of the material increases these peaks effectively broaden as neutrons of a wider energy range can undergo the resonant reaction because of the thermal motion of the nuclei at the higher temperatures. In general, Doppler broadening results in a negative reactivity effect with increasing temperature as the probability of a neutron undergoing (n,γ) with a nucleus increases.

element Nuclides which all have the same number of protons all belong to the same element. What element a given atom or nucleus belongs to is determined by the number of protons in the nucleus. The number of protons determines how many electrons an atom has when in an electrically-neutral state as well as the configuration of said electrons. This electron configuration determines the chemical properties of the element, consequently, all isotopes of a given element have the same chemical properties.

fertile A nuclide is considered fertile if it can undergo (n,γ), and possibly subsequent radioactive decays, in order to transform into a fissile nuclide. The most relevant fertile nuclides in nuclear reactor engineering are ^{232}Th, ^{238}U, and ^{240}Pu.

fissile A nuclide is considered fissile if it is capable of sustaining a nuclear fission chain reaction. The most relevant fissile nuclides in nuclear reactor engineering are ^{233}U, ^{235}U, ^{239}Pu, and ^{241}Pu.

fission The process of a nucleus splitting into two (or more) fission products which usually results in the release of several free neutrons. Fission can be induced by both neutrons and photons, or can occur via radioactive decay, which is referred to as spontaneous fission. Fission can also be induced by other particles, such as protons, however, the repulsion charged particles experience from nuclei significantly limits their importance to nuclear engineers.

fission product A fission product is a nuclide which is heavier than an α that is produced via fission. Because the neutron-to-nucleon ratio for stability is lower for lighter nuclides like fission products than for heavier nuclides like fissionable nuclides, fission products are typically neutron-rich relative to their total number of nucleons and consequently are unstable and undergo radioactive decay. The decay of FPs is the primary source of decay heat in a nuclear reactor.

fissionable A nuclide is considered fissionable if it is physically capable of undergoing nuclear fission via neutron-induced fission or spontaneous fission. If there is even a small chance of the nuclide undergo-

ing nuclear fission then it is considered fissionable. Traditionally, all isotopes of radium (Z=88) and heavier elements are considered fissionable.

fusion The process of two nuclei fusing into a single nuclei. Currently, there are no commercial reactors which operate via nuclear fusion.

Griffin Reactor analysis application which is being jointly developed by INL and ANL for advanced reactor modeling [2].

half-life The half-life of a radionuclide corresponds to the amount of time after which half of a given quantity of a radionuclide is expected to have undergone radioactive decay. While radioactive decay occurs based on given probabilities, the large (in absolute terms) number of nuclei necessary to make measurement of radioactivity important for practical purposes means that the law of large numbers allows for the half-life to be calculated.

isotope Isotopes are nuclides which have the same number of protons and thus are all the same element but have different numbers of neutrons. All isotopes of an element have the same chemical behavior since they all have the same number of protons and electrons in the same configuration. However, because the number of nucleons is different for each isotope of a given element the nuclear properties of isotopes of the same element can vary wildly. ^{1}H and ^{2}H are both isotopes of hydrogen with identical chemical behavior but very different nuclear properties. In general, isotopes should only be referenced when referring to isotopes of a specific element, otherwise the term is meaningless. If it is desired to refer to multiple isotopes of multiple elements than the more accurate term "nuclide" should be used instead.

multigroup Refers to the division of the neutron flux and XSs into discrete energy groups. This results in neutrons being tracked in energy "bins" rather than tracking neutrons using the exact energy carried by each particle (which is the physical reality).

N-number The total number of neutrons a nuclide has.

neutron Particle with no electric charge that is found in the nuclei of most atoms and has a slightly larger mass than the proton. Neutrons released from nuclear fission are what makes the fission chain reactions in nuclear reactors possible. Neutrons in a nuclear reactor can be divided into different categories based on their source as well as their kinetic energy.

neutron multiplication factor The neutron multiplication factor (k) is the factor by which a the population of neutrons changes from one neutron generation to another as shown.

$$k = \frac{\text{\# of neutrons from next generation}}{\text{\# of neutrons from current generation}} \tag{D.2}$$

The neutron multiplication factor is one of the most important values in nuclear engineering as it determines whether a given nuclear system is subcritical ($k < 1$), critical ($k = 1$), or supercritical ($k > 1$).

nuclide A nuclide refers to a distinct nuclear configuration of nucleons such that all nuclei which share the same configuration of nucleons share the same nuclear properties. The result is that in order for two nuclei to be the same nuclide they must have the same number of protons, the same number of neutrons, and the same

ground or metastable state. The term nuclide is sometimes conflated with the term isotope, however the two terms do have distinct definitions.

photofission Photofission is a photon-nucleus interaction where a photon is absorbed by the nucleus which results in the nucleus entering an excited state and undergoing nuclear fission. A potential photofission of ^{235}U is shown.

$$^{235}\mathrm{U} + {}^{0}\gamma \rightarrow {}^{235}\mathrm{U}^{*} \rightarrow {}^{97}\mathrm{Y} + {}^{135}\mathrm{I} + 3\,{}^{1}\mathrm{n} \tag{D.3}$$

Photofission is abbreviated as a (γ,f) reaction.

photon A photon is a neutral and massless particle which carries some amount of energy. Photons of various energies form the electromagnetic spectrum from low energy radio waves to high energy gamma rays. In this work, photons are typically represented by γ.

photoneutron A photoneutron is a neutron emitted by a nucleus after a nucleus absorbs a photon and enters an excited state which enables it to emit a neutron. Photoneutrons are largely ignored in most reactor systems because of the high energy photons required to cause most nuclides to emit photoneutrons, the population of which is quite low in a nuclear reactor. The exception is in PHWRs where a relatively low photon energy of about 2.225 MeV [88] is required to cause photoneutron emission from the deuterium present in heavy water. The photoneutron emission from deuterium is shown.

$$^{2}\mathrm{H} + {}^{0}\gamma \rightarrow {}^{2}\mathrm{H}^{*} \rightarrow {}^{1}\mathrm{H} + {}^{1}\mathrm{n} \tag{D.4}$$

Photoneutron emission is abbreviated as a (γ,n) reaction.

radioactive decay Radioactive decay is the process by which unstable nuclides emit energy, which comes from mass lost by the unstable nucleus, in order to approach stability. The emitted energy is carried by one or more particles which tend to interact with the surrounding material depositing their kinetic energy into the bulk material in the form of heat. Any given nuclide which undergoes radioactive decay does so with a constant probability of decay occurring at any given point in time. Nuclides which undergo radioactive decay are referred to as radioactive or unstable while nuclides which do not undergo radioactive decay are referred to as stable. Occasionally nuclides which are radioactive but have a very low probability of undergoing radioactive decay are referred to as stable because for practical purposes they can be treated as stable.

radionuclide Radionuclides are nuclides which undergo radioactive decay. All nuclides are either radionuclides or stable nuclides.

stable Stable nuclides are nuclides which do not undergo radioactive decay. When nuclides are energetically capable of undergoing radioactive decay but have never been observed of doing so are referred to as observationally stable. Nuclides which have been observed to decay but decay extremely slowly with half-lives greater than the age of universe are frequently treated as stable.

transmutation Nuclear transmutation is the process by which a nuclide transforms from one nuclide to another. While this technically includes transformations which result from radioactive decay it is typically used to refer to transmutation initiated by an incident particle, such as a neutron or photon. Neutrons can cause

transmutation via a myriad of non-scattering reactions such as (n,γ) and (n,f). Photons can also induce transmutation via photoneutron emission or photofission. For typical depletion analysis, only transmutation caused by neutrons (referred to as "neutron transmutation") is considered.

Z-number The total number of protons a nuclide has.

References

[1] Greenwood, L.R., 1983. A new calculation of thermal neutron damage and helium production in nickel. Journal of Nuclear Materials 115(2), 137. ISSN 00223115. doi:10.1016/0022-3115(83)90302-1.
URL https://doi.org/10.1016/0022-3115(83)90302-1

[2] Lee, C H et al., 2021. Griffin Software Development Plan. Research Report INL/EXT-21-63185, ANL/NSE-21/23, Idaho National Laboratory and Argonne National Laboratory.

[3] Cross Sections Evaluation Working Group (CSEWG), 2018. ENDF-6 Formats Manual: Data Formats and Procedures for the Evaluated Nuclear Data Files ENDF/B-VI, ENDF/B-VII and ENDF/B-VIII. Technical Report BNL-203218-2018-INRE, Brookhaven National Laboratory.
URL https://www-nds.iaea.org/exfor/x4guide/manuals/endf-manual.pdf

[4] IAEA. Power Reactor Information System. Accessed on 11-12-2022.
URL https://pris.iaea.org/pris/

[5] Brown, D. A. et al., 2018. ENDF/B-VIII.0: The 8th Major Release of the Nuclear Reaction Data Library with CIELO-project Cross Sections, New Standards and Thermal Scattering Data. Nuclear Data Sheets 148, 1. ISSN 0090-3752. doi:10.1016/j.nds.2018.02.001. Special Issue on Nuclear Reaction Data.
URL https://www.sciencedirect.com/science/article/pii/S0090375218300206

[6] ANL. EBR-I (Experimental Breeder Reactor-I). Accessed on 09-12-2022.
URL https://www.ne.anl.gov/About/reactors/frt.shtml

[7] ANL. The Chicago Pile 1 Pioneers. Accessed on 09-12-2022.
URL https://www.ne.anl.gov/About/cp1-pioneers/

[8] ANL. STR (Submarine Thermal Reactor). Accessed on 09-12-2022.
URL https://www.ne.anl.gov/About/reactors/lwr3.shtml

[9] Rao, M. V. Bhaskara et al., 11 2008. Nuclear Energy Scenario of Asian Developing Countries. In: Proceedings of the 3rd International Solar Energy Society Conference - Asia Pacific Region 2008 (ISES-AP-08). International Solar Energy Society, 1–9.

[10] US Nuclear Regulatory Commission. History of Emergency Preparedness. Accessed on 09-12-2022.
URL https://www.nrc.gov/about-nrc/emerg-preparedness/history.html

[11] Ritchie, Hannah, et al., 2022. Energy. Our World in Data. Accessed on 11-12-2022.
URL https://ourworldindata.org/energy

[12] ANL. Light Water Reactor Technology Development. Accessed on 04-09-2023.
URL https://www.ne.anl.gov/About/reactors/lwr3.shtml

[13] Mack, Chris A., 2011. Fifty Years of Moore's Law. IEEE Transactions on Semiconductor Manufacturing 24(2), 202. doi:10.1109/TSM.2010.2096437.

[14] Zhang, Tengfei et al., 2022. Variational nodal methods for neutron transport: 40 years in review. Nuclear Engineering and Technology 54(9), 3181. ISSN 1738-5733. doi:https://doi.org/10.1016/j.net.2022.04.012.
URL https://www.sciencedirect.com/science/article/pii/S1738573322002157

[15] Sanchez, R. et al., 1982. A review of neutron transport approximations. Nuclear Science and Engineering 80(4), 481. doi:10.13182/NSE80-04-481.

[16] Chadwick, M. B. et al., 2006. ENDF/B-VII.0: Next Generation Evaluated Nuclear Data Library for Nuclear Science and Technology. Nuclear Data Sheets 107(12), 2931. ISSN 0090-3752. doi:10.1016/j.nds.2006.11.001. Evaluated Nuclear Data File ENDF/B-VII.0.
URL https://www.sciencedirect.com/science/article/pii/S0090375206000871

[17] Shibata, Keiichi et al., 2011. JENDL-4.0: A New Library for Nuclear Science and Engineering. Journal of Nuclear Science and Technology 48(1), 1. doi:10.1080/18811248.2011.9711675.

[18] Glinatsis, Georgios et al., 2022. An investigation of the JEFF 3.2 nuclear data library. Annals of Nuclear Energy 168, 108885. ISSN 0306-4549. doi:10.1016/j.anucene.2021.108885.
URL https://www.sciencedirect.com/science/article/pii/S0306454921007623

[19] Wackeroth, Doreen, 2006. Cross Section. High Energy Physics Made Painless .
URL https://ed.fnal.gov/painless/pdfs/cross.pdf

[20] Etemadi, Nasrollah, 1981. An elementary proof of the strong law of large numbers. Zeitschrift für Wahrscheinlichkeitstheorie und verwandte Gebiete 55(1), 119.

[21] Aliberti, G. et al., 2006. Nuclear data sensitivity, uncertainty and target accuracy assessment for future nuclear systems. Annals of Nuclear Energy 33(8), 700. ISSN 0306-4549. doi:10.1016/j.anucene.2006.02.003.

[22] Duderstadt, James J. et al., 1981. Nuclear Reactor Analysis. John Wiley & Sons, Inc. ISBN 0-471-22363-8.

[23] Walsh, Jonathan A. et al., 2017. On-the-fly Doppler broadening of unresolved resonance region cross sections. Progress in Nuclear Energy 101, 444. ISSN 0149-1970. doi:https://doi.org/10.1016/j.pnucene.2017.05.032. Special Issue on the Physics of Reactors International Conference PHYSOR 2016: Unifying Theory and Experiments in the 21st Century.
URL https://www.sciencedirect.com/science/article/pii/S0149197017301373

[24] Greenwood, L.R. et al., 1996. Hydrogen generation arising from the ^{59}Ni(n, p) reaction and its impact on fission—fusion correlations. Journal of Nuclear Materials 233-237, 1530. ISSN 00223115. doi:10.1016/S0022-3115(96)00264-4.
URL https://doi.org/10.1016/S0022-3115(96)00264-4

[25] Bateman, H., 1910. Solution of a system of differential equations occurring in the theory of radioactive transformations. Proceedings of the Cambridge Philosophical Society, Mathematical and physical sciences 15, 423.

[26] Bell, G. I. et al., 1970. Nuclear Reactor Theory. Litton Educational Publishing, Inc., 1st edition.

[27] Moler, Cleve et al., 2003. Nineteen dubious ways to compute the exponential of a matrix, twenty-five years later. Society for Industrial and Applied Mathematics Review 45(1), 3.

[28] Pusa, Maria et al., 2010. Computing the Matrix Exponential in Burnup Calculations. Nuclear Science and Engineering 164(2), 140. doi:10.13182/NSE09-14.

[29] Calvin, Olin W., et al., 2022. Introduction of the adding and doubling method for solving bateman equations for nuclear fuel depletion. Nuclear Science and Engineering 0(0), 1. doi:10.1080/00295639.2022.2129950.
URL https://www.tandfonline.com/doi/full/10.1080/00295639.2022.2129950

[30] Pusa, Maria, 2011. Rational Approximations to the Matrix Exponential in Burnup Calculations. Nuclear Science and Engineering 169, 155. doi:10.13182/NSE10-81.
URL https://doi.org/10.13182/NSE10-81

[31] Pusa, Maria et al., 2013. Solving Linear Systems with Sparse Gaussian Elimination in the Chebyshev Rational Approximation Method. Nuclear Science and Engineering 175(3), 250. doi:10.13182/NSE12-52.

[32] Pusa, Maria, 2016. Higher-Order Chebyshev Rational Approximation Method and Application to Burnup Equations. Nuclear Science and Engineering 182(3), 297. doi:10.13182/NSE15-26.

[33] Kochunas, Brendan et al., 2017. VERA Core Simulator Methodology for Pressurized Water Reactor Cycle Depletion. Nuclear Science and Engineering 185(1), 217. doi:10.13182/NSE16-39.
URL https://www.tandfonline.com/doi/full/10.13182/NSE16-39

[34] ORNL. Frontier supercomputer debuts as world's fastest, breaking exascale barrier. Accessed on 04-09-2022.
URL https://www.ornl.gov/news/frontier-supercomputer-debuts-worlds-fastest-breaking-exascale-barrier

[35] Szames, Esteban, 07 2020. Few group cross section modeling by machine learning for nuclear reactor. Ph.D. thesis, Université Paris-Saclay.

[36] Calvin, Olin et al., 2021. Global error analysis of the chebyshev rational approximation method. Annals of Nuclear Energy 150. ISSN 0306-4549. doi:https://doi.org/10.1016/j.anucene.2020.107828.
URL https://www.sciencedirect.com/science/article/pii/S0306454920305260

[37] Leppänen, J., et al., 2015. The Serpent Monte Carlo Code: Status, Development and Applications in 2013. Annals of Nuclear Energy 82, 142.

[38] Hermann, O. W. et al., 2000. SCALE: A Modular Code System for Performing Standardized Computer Analyses for Licensing Evaluation. ORIGEN-S: SCALE system module to calculate fuel depletion, actinide transmutation, fission product buildup and decay, and associated radiation source terms. Technical Report NUREG/CR-0200, Oak Ridge National Laboratory.

[39] Calvin, Olin et al., 8 2019. Implementation of Depletion Architecture in the MAMMOTH Reactor Physics Application. In: Proceedings of the 2019 International Conference on Mathematics and Computational Methods Applied to Nuclear Science and Engineering. American Nuclear Society, 2806–2815.

[40] Anderson, E., et al., 1999. LAPACK Users' Guide. Philadelphia, PA: Society for Industrial and Applied Mathematics, third edition. ISBN 0-89871-447-8 (paperback).

[41] Marleau, G. et al., 2018. A User Guide for DRAGON Version 5. User Manual IGE-355, Ecole Polytechnique de Montreal.

[42] OECD, 2016. Benchmark for Neutronic Analysis of Sodium-cooled Fast Reactor Cores with Various Fuel Types and Core Sizes. Technical Report 9, Organization for Economic Co-operation and Development Nuclear Energy Agency.

[43] Gale, Micah et al., 5 2022. Using Griffin's Transmutation Solver to Calculate Radiation Damage. In: Proceedings of the International Conference on Physics of Reactors (PHYSOR) 2022. American Nuclear Society, 836–845.

[44] Kinchin, G. H. et al., 1955. The displacement of atoms in solids by radiation. Reports on Progress in Physics 18(1), 1. doi:10.1088/0034-4885/18/1/301.

[45] Konobeyev, A.Yu. et al., 2017. Evaluation of effective threshold displacement energies and other data required for the calculation of advanced atomic displacement cross-sections. Nuclear Energy and Technology 3(3), 169. ISSN 24523038. doi:10.1016/j.nucet.2017.08.007.

[46] Juslin, N. et al., 2007. Simulation of threshold displacement energies in FeCr. Nuclear Instruments and Methods in Physics Research Section B: Beam Interactions with Materials and Atoms 255(1), 75. ISSN 0168-583X. doi:10.1016/j.nimb.2006.11.046. Computer Simulation of Radiation Effects in Solids.

[47] Mascitti, J. A. et al., 01 2011. Method for the Calculation of DPA in the Reactor Pressure Vessel of Atucha II. Science and Technology of Nuclear Installations 2011. doi:10.1155/2011/534689.

[48] Chen, Shengli et al., 2019. Calculation and verification of neutron irradiation damage with differential cross sections. Nuclear Instruments and Methods in Physics Research Section B: Beam Interactions with Materials and Atoms 456, 120. ISSN 0168-583X. doi:10.1016/j.nimb.2019.07.011.

[49] Norgett, M.J., et al., 1975. A proposed method of calculating displacement dose rates. Nuclear Engineering and Design 33(1), 50. ISSN 00295493. doi:10.1016/0029-5493(75)90035-7.

[50] Conlin, Jeremy Lloyd et al., 2017. NJOY21: Next generation nuclear data processing capabilities. EPJ Web of Conferences 146, 09040. ISSN 2100-014X. doi:10.1051/epjconf/201714609040.

[51] MacFarlane, R E et al., 2019. The njoy nuclear data processing system version 2016. User Manual LA-UR-17-20093, Los Alamos National Laboratory.

[52] Linhard, J et al., 1963. Integral Equations Governing Radiation Effects. Matematisk-fysiske Meddelelser udgivet af Det Kongelige Danske Videnskabernes Selskab 33(10).

[53] Robinson, M.T., 1969. THE ENERGY DEPENDENCE OF NEUTRON RADIATION DAMAGE IN SOLIDS. UKAEA Culham Laboratory, 364–378.
URL https://www.osti.gov/biblio/4019582

[54] Schwen, Daniel et al., 2021. Evolution of microstructures in radiation fields using a coupled binary-collision monte carlo phase field approach. Computational Materials Science 192, 110321. ISSN 0927-0256. doi:10.1016/j.commatsci.2021.110321.

[55] Li, Weimin et al., 2019. Threshold displacement energies and displacement cascades in 4h-SiC: Molecular dynamic simulations. AIP Advances 9(5), 055007. ISSN 2158-3226. doi:10.1063/1.5093576.

[56] Isotalo, A. E. et al., 2015. A method for including external feed in depletion calculations with CRAM and implementation into ORIGEN. Annals of Nuclear Energy 85, 68. ISSN 0306-4549. doi:10.1016/j.anucene.2015.04.037.

[57] Permann, Cody J. et al., 2020. MOOSE: Enabling massively parallel multiphysics simulation. SoftwareX 11, 100430. ISSN 23527110. doi:10.1016/j.softx.2020.100430.

[58] Nordlund, Kai et al., 2015. Primary Radiation Damage in Materials Review of Current Understanding and Proposed New Standard Displacement Damage Model to Incorporate in Cascade Defect Production Efficiency and Mixing Effects. Technical report, Nuclear Energy Agency of the OECD (NEA). NEA-NSC-DOC–2015-9.

[59] Hirst, Charles A. et al., 2022. Revealing hidden defects through stored energy measurements of radiation damage. Science Advances 8(31), eabn2733. doi:10.1126/sciadv.abn2733.

[60] Liang, Yuxuan et al., 8 2022. PRELIMINARY SENSITIVITY AND UNCERTAINTY ANALYSIS OF ACCIDENT TOLERANT FUEL IN SMR. In: Proceedings of the 2022 29th International Conference on Nuclear Engineering (ICONE29). American Society of Mechanical Engineers.

[61] Levy, Edmond, 2018. A matrix exponential approach to radioactive decay equations. American Journal of Physics 86(12), 909. doi:10.1119/1.5064446.
URL https://aapt.scitation.org/doi/citedby/10.1119/1.5064446

[62] Cetnar, Jerzy, 2006. General solution of Bateman equations for nuclear transmutations. Annals of Nuclear Energy 33(7), 640. ISSN 0306-4549. doi:10.1016/j.anucene.2006.02.004.
URL https://www.sciencedirect.com/science/article/pii/S0306454906000284

[63] Kawamoto, Yosuke et al., 2015. Numerical solution of matrix exponential in burn-up equation using minimax polynomial approximation. Annals of Nuclear Energy 80, 219. ISSN 0306-4549. doi:10.1016/j.anucene.2015.02.015.
URL https://www.sciencedirect.com/science/article/pii/S0306454915000729

[64] Nguyen, Tung Dong Cao et al., 8 2019. APR-1400 Whole-Core Depletion Analysis with MCS. In: Proceedings of the 2019 International Conference on Mathematics and Computational Methods Applied to Nuclear Science and Engineering. American Nuclear Society, 485–494.

[65] Robert, Yves et al., 08 2021. Evaluation of Serpent Capabilities for Hyperfidelity Depletion of Pebble Bed Cores. In: Proceedings of the International Conference on Nuclear Engineering. volume Volume 1: Operat-

ing Plant Challenges, Successes, and Lessons Learned; Nuclear Plant Engineering; Advanced Reactors and Fusion; Small Modular and Micro-Reactors Technologies and Applications. doi:10.1115/ICONE28-65810.V001T04A016.

[66] García, Manual et al., 2021. Validation of Serpent-SUBCHANFLOW-TRANSURANUS pin-by-pin burnup calculations using experimental data from the Temelín II VVER-1000 reactor. Nuclear Engineering and Technology 53(10), 3133. ISSN 1738-5733. doi:10.1016/j.net.2021.04.023.
URL https://www.sciencedirect.com/science/article/pii/S1738573321002424

[67] Aldama, D. L., et al., 2003. WIMS-D Library Update, Final Report of a Coordinated Research Project. Technical report, International Atomic Energy Agency.

[68] Chiba, Go, et al., 2015. Important fission product nuclides identification method for simplified burnup chain construction. Journal of Nuclear Science and Technology 52(7-8), 953. doi:10.1080/00223131.2015.1032381.

[69] Tran, V. P., et al., 2017. Automated generation of burnup chain for reactor analysis applications. Kerntechnik 82(2), 196. doi:10.3139/124.110671.
URL https://doi.org/10.3139/124.110671

[70] Kajihara, Takanori, et al., 2016. Automatic construction of a simplified burn-up chain model by the singular value decomposition. Annals of Nuclear Energy 94, 742. ISSN 0306-4549. doi:10.1016/j.anucene.2016.04.034.
URL https://www.sciencedirect.com/science/article/pii/S0306454916301979

[71] Zhang, Yunfei, et al., 2020. Problem-dependent compression method for burnup library. Annals of Nuclear Energy 140, 107287. ISSN 0306-4549. doi:10.1016/j.anucene.2019.107287.
URL https://www.sciencedirect.com/science/article/pii/S0306454919307972

[72] Huang, Kai, et al., 2017. Depletion system compression method with treatment of decay heat. Progress in Nuclear Energy 101, 476. ISSN 0149-1970. doi:10.1016/j.pnucene.2017.03.022. Special Issue on the Physics of Reactors International Conference PHYSOR 2016: Unifying Theory and Experiments in the 21st Century.
URL https://www.sciencedirect.com/science/article/pii/S0149197017300677

[73] Li, Yunzhao, et al., 2017. A depletion system compression method based on quantitative significance analysis. Nuclear Science and Engineering 187(1), 49. doi:10.1080/00295639.207.1297079.

[74] Lee, Changho et al., 2017. MC^2-3: Multigroup Cross Section Generation Code. Nuclear Science and Engineering 187(3), 268. doi:10.1080/00295639.2017.1320893.
URL https://doi.org/10.1080/00295639.2017.1320893

[75] Dietrich, Samuel S. et al., 1988. Atlas of photoneutron cross sections obtained with monoenergetic photons. Atomic Data and Nuclear Data Tables 38(2), 199. ISSN 0092-640X. doi:10.1016/0092-640X(88)90033-2.
URL https://www.sciencedirect.com/science/article/pii/0092640X88900332

[76] Peelle, R. W. et al., Jan 1971. Spectrum of Photons Emitted in Coincidence with Fission of ^{235}U by Thermal Neutrons. Phys. Rev. C 3, 373. doi:10.1103/PhysRevC.3.373.
URL https://link.aps.org/doi/10.1103/PhysRevC.3.373

[77] Cohn, H. O. et al., Apr 1961. Carbon-13 Neutron Total Cross Section. Phys. Rev. 122, 534. doi:10.1103/PhysRev.122.534.
URL https://link.aps.org/doi/10.1103/PhysRev.122.534

[78] Smith, A. et al., 1979. Neutron Interaction with Carbon-12 in the Few-MeV Region. Nuclear Science and Engineering 70(3), 281. doi:10.13182/NSE79-A20149.
URL https://www.tandfonline.com/doi/abs/10.13182/NSE79-A20149

[79] Calvin, Olin W. et al., 2023. Evaluating quantities of interest other than nuclide densities in the bateman equations. Nuclear Science and Engineering 0(0), 1. doi:10.1080/00295639.2022.2161802.
URL https://www.tandfonline.com/doi/full/10.1080/00295639.2022.2161802

[80] Nagaya, Yasunobu, et al., 2010. Comparison of Monte Carlo calculation methods for effective delayed neutron fraction. Annals of Nuclear Energy 37(10), 1308. ISSN 0306-4549. doi:10.1016/j.anucene.2010.05.017.
URL https://www.sciencedirect.com/science/article/pii/S0306454910001957

[81] Aufiero, Manuele, et al., 2014. Calculating the effective delayed neutron fraction in the Molten Salt Fast Reactor: Analytical, deterministic and Monte Carlo approaches. Annals of Nuclear Energy 65, 78. ISSN 0306-4549. doi:10.1016/j.anucene.2013.10.015.
URL https://www.sciencedirect.com/science/article/pii/S0306454913005458

[82] Yan, Wei-Hua, et al., 2014. Prototype studies on the nondestructive online burnup determination for the modular pebble bed reactors. Nuclear Engineering and Design 267, 172. ISSN 0029-5493. doi:10.1016/j.nucengdes.2013.12.036.
URL https://www.sciencedirect.com/science/article/pii/S0029549313007176

[83] Zagrebaev, V. I. et al., Oct 2011. Production of heavy and superheavy neutron-rich nuclei in neutron capture processes. Phys. Rev. C 84, 044617. doi:10.1103/PhysRevC.84.044617.
URL https://link.aps.org/doi/10.1103/PhysRevC.84.044617

[84] ANSI, February 2019. Decay heat power in light water reactors. American National Standard ANSI/ANS-5.1-2014-R2019, American Nuclear Society, La Grange Park, IL, U.S.A.

[85] Romano, Paul K. et al., 2021. Depletion capabilities in the openmc monte carlo particle transport code. Annals of Nuclear Energy 152, 107989. ISSN 0306-4549. doi:10.1016/j.anucene.2020.107989.
URL https://www.sciencedirect.com/science/article/pii/S030645492030685X

[86] Calvin, Olin W., 2023. Depletion Chain Simplification Using Pseudo-Nuclides. Annals of Nuclear Energy (ANUCENE-D-22-01197R1). PREPRINT.

[87] Lamarsh, John R. et al., 2001. Introduction to Nuclear Engineering. Prentice-Hall Inc. ISBN 9780201824988.

[88] Setiawan, Yanaur Ady et al., 2022. Beta-Ray-Bremsstrahlung Contributions to Short-Lived Delayed Photoneutron Groups in Heavy Water Reactors. Nuclear Science and Engineering 0(0), 1. doi:10.1080/00295639.2022.2103341.
URL https://www.tandfonline.com/doi/full/10.1080/00295639.2022.2103341

[89] Kim, Kyeongwon, et al., 2020. Generation of a multigroup gamma production and photon transport library for STREAM. In: Transactions of the Korean Nuclear Society Virtual Spring Meeting, Spring.

[90] Wang, Yaqi et al., 2021. Rattlesnake: A MOOSE-Based Multiphysics Multischeme Radiation Transport Application. Nuclear Technology 207(7), 1047. doi:10.1080/00295450.2020.1843348.
URL https://www.tandfonline.com/doi/full/10.1080/00295450.2020.1843348

[91] Walker, Samuel et al., 11 2022. Implementation of Isotopic Removal Capability in Griffin for Multi-Region MSR Depletion Analysis. In: Transactions of the American Nuclear Society. American Nuclear Society, volume 127, 976–979.